A Unified Framework Which Uses Multi-Scale Microstructural Information for Modeling Dynamic Failure in Brittle Materials

by

Andrew L. Tonge

A dissertation submitted to The Johns Hopkins University in conformity with the requirements for the degree of Doctor of Philosophy.

Baltimore, Maryland

June, 2014

Abstract

Developing improved armor ceramic materials necessitates an understanding of the active failure mechanisms during an impact event and the interactions between these mechanisms that lead to material failure. Similarly, within planetary science, the mechanisms active within impact events provide insight into the origin, evolution, and internal structure of asteroids and other planetary bodies. While careful experiments interrogate the true physical process, real time, high resolution data in three dimensions needed for investigating the competition between dynamic deformation mechanisms is not yet available. Simulations provide a vehicle for testing our understanding of the physical processes, evaluating the effectiveness of experiments, and illuminating the competition between deformation mechanisms.

We develop a material model that includes physically based material variability, micromechanics-based damage growth, granular flow, compaction of the granular material, and a Mie-Grüneisen equation of state. Using this new modeling framework, we simulate three experimental configurations including Edge On Impact, dynamic uniaxial compression, and simplified ballistic loading. Using simulations of Edge On

ABSTRACT

Impact experiments in AlON, we demonstrate that the failure front observed in experiments propagates as a result of stress waves interacting with the free surfaces favoring damage growth on the interior of the tile (consistent with experimental observations). In simulations of simplified ballistic impact on boron carbide, we demonstrate that the extent of granular flow and material microcracking is linked to the slope of the granular flow surface, suggesting that materials capable of forming larger, high aspect ratio fragments may provide better resistance to penetration.

Finally, we demonstrate the versatility of the model by investigating the collisional evolution of the near Earth asteroid Eros. Using two different potential internal flaw distributions, we demonstrate that the stronger of the two flaw distributions creates a heterogeneous damage and granular flow pattern within the asteroid (which is consistent with observations). Once this network of highly damaged material develops, subsequent impacts of similar severity do not significantly alter the orientation of the failure zones.

Thesis Advisor and Primary Reader: K.T. Ramesh

Secondary Readers: Lori Graham-Brady and Robert McMeeking

Acknowledgments

This thesis would not have been possible without the patient mentorship and guidance of my thesis advisor Professor K.T. Ramesh. He taught me to think about research problems in terms of the mechanisms that are active and the processes that those enable. This is an approach that will allow me to look at many types of problems throughout my research career.

I attribute my appreciation for the importance of variability and how one addresses that variability in computational settings to the discussions and training that I received as an NSF IGERT trainee. I would like to thank all of the IGERT faculty for providing insight into their areas of expertise and introducing me to the variety of experts here at Hopkins that have looked at similar problems through the lens of different disciplines. I would like to especially thank Profesor Lori Graham-Brady for her insights and discussions on approaches to and the implications of creating realizations of material microstructures.

Within Professor Ramesh's lab I am especially grateful for the help and guidance that former postdoc and now Professor at The New Mexico Institute of Mining and

ACKNOWLEDGMENTS

Technology Jamie Kimberley provided while I was a new graduate student. He was always helpful either in explaining additional concepts in continuum mechanics and wave propagation or in helping me understand experiments in greater detail. There have been many useful conversations on numerical methods and computational approaches with Nitin Daphalapurkar, for which I am grateful. The remaining members (both current and former) of the Ramesh lab all helped me at various points through out this journey and without them it would have been a much more difficult and arduous journey.

Professor Rebecca Brannon's willingness to share her insights into computational methods and particularly what seems to work and what does not has been extremely helpful. I have also benefited from conversations with colleagues in the MEDE CRA both at the Army Research Laboratory and at other academic institutions, especially Professor Bob McMeeking's group at UCSB.

Developing and implementing a material model for dynamic failure is a difficult task, but I would not have been able to get as far as I did without the support of the Uintah development community. I am grateful that the developers of the Uintah framework decided to make their capable and flexible numerical solver available to the public as open source software. Finding a good, efficient, massively parallel continuum mechanics code that could solve the impact problems that I look at in this work was essential to being able to complete the work that I have done. I am especially thankful for the responsiveness that Jim Guilkey, John Schmidt, and Alan

Humphrey provided when I had a question related to their areas of expertise.

Additionally, I would like to thank my readers K.T. Ramesh, Lori Graham-Brady, and Bob McMeeking for taking the time to read this document and provide their feedback.

This work could not have been completed without the funding support that I have received over the years. My first year I was supported through a departmental fellowship. After that, I was supported by the NSF IGERT Modeling Complex Systems (IGERT 0801471) program. My final two years have been supported by the Army Research Laboratory and was accomplished under Cooperative Agreement Number W911NF-12-2-0022. The views and conclusions contained in this document are my own and should not be interpreted as representing the official policies, either expressed or implied, of the Army Research Laboratory or the U.S. Government. The U.S. Government is authorized to reproduce and distribute reprints for Government purposes notwithstanding any copyright notation herein.

Finally I would like to thank my wonderful wife Theresa who has been an essential companion on the journey in completing this work. Her support and understanding have been gratefully appreciated.

Dedication

This thesis is dedicated to my family. Particularly my wife Theresa, who shared the Ph.D. journey with me and whom will continue to support my endeavors throughout our lives, and my grandparents especially Russ Haris and Bob Koucky who from a young age always encouraged me to explore the natural world and seek to understand it through the eyes of an engineer.

Contents

List of Tables

List of Figures

Chapter 1

Introduction

Even with all of the advances in computing capabilities it is likely that we will never design structures (bridges, planes, cars, or body armor) by simulating the location of every atom in the system. The process of building a model to simplify the physical problem and extract the important physical processes is essential to the art and science of modeling. The goal of modeling is to keep the minimal amount of complexity necessary to gain the physical insights needed to evaluate a situation and make a decision. One problem that is particularly interesting in this regard is high velocity impact. The nature of the impact event exercises a large range of length and timescales, which cannot all be resolved explicitly. In this work, we develop a material model for use in simulations of brittle failure during impact loading. We present an approach to multi-scale modeling where analytical models and statistical sampling are used to represent subscale processes and a conventional continuum me-

chanics code is used to solve the macro-scale problem. This approach is applicable to many physical systems, not just brittle materials: the particular physical processes that we model would change as the type of system changes.

We consider two classes of problem: ballistic impact on ceramics and impacts on rocky asteroids. When modeling ballistic impact on ceramic armor, the impact conditions and material are relatively well defined and one hopes to develop quantitative predictions of the impact outcome. Since the range of model applications is within the range of conditions that can be reached through experiments, it is possible to develop material models for these materials using an empirical approach. However, a purely empirical approach leads to a long design-build-test cycle when attempting to develop either a new material or use existing materials in a different configuration. Models that account for the physical processes that occur during these impact events have the potential to shorten this design cycle and reduce the amount of time it takes from discovery of a new material to implementation of that material for a particular application. Our interest in modeling ballistic impacts on ceramics is in developing a framework that can couple the different energy dissipation mechanisms in these materials under relavent impact conditions both to illustrate which loading regiemes are of particular interest for further research and to suggest possible research directions for producing materials with improved performance.

An interesting multi-scale modeling problem is that of predicting the outcome of impacts on planetary bodies, because it is a problem that cannot be experimentally

examined at the same scales. Therefore, insights into physical process must rely on some sort of modeling to bridge the gap between the laboratory scale and the planetary scale of interest. Small bodies in planetary science are kilometers in size. In the asteroid belt, these kilometer sized objects collide at relative velocities on the order of 5 kilometers per second (hyper-velocity impact). These impacts present two separate modeling challenges. First, the orders of magnitude that separate experiments from the application size scale require physics based models, since extrapolation without a physical basis is highly uncertain. Second, the condition of the bodies prior to impact and history of the bodies since the impact occurred are uncertain. For most small bodies in the solar system the only information that we have about the body is mass, approximate shape, and surface composition.

There are many physical processes that occur during a hyper-velocity impact event. These processes cover the range of scales from atomic scales, where extreme energy density can cause ionization or the formation of plasma, up to the geometric shape of the target body, which affects the propagation and focusing of elastic waves and sets the gravitational potential. With all of these length-scales there are also a variety of timescales associated with these processes. Like the length-scales, these timescales range from timescales associated with atomic vibrations and the time it takes an elastic wave to propagate across the body (several seconds) up to the time it takes for complete formation of a crater in low gravity (several minutes). Although all of these processes provide valuable information about impact processes, we restrict

our focus to keep the problem tractable.

We first restrict the impact velocity range to between 100 m/s and 5 km/s. Additionally, we limit ourselves to considering brittle materials such as rocks and structural ceramics. Within this impact velocity range for these classes of materials thermodynamic effects are present, however high pressure and temperature equations of state are not critical. At these velocity ranges, we do not expect significant contributions from atomic scale effects such as ionization. We limit the velocity range of interest to a range where the Mie-Grüneisen equation of state is acceptable.

This reduced problem of interest amounts to developing a framework for predicting the result of a high velocity impact on a brittle material. We look at both geologic materials such as basalt and structural ceramics such as Aluminum Oxynitride (AlON) and boron carbide in order to demonstrate the versatility of the modeling approach. Because structural ceramics tend to be more homogeneous with controlled manufacturing procedures, they are attractive for model validation purposes because the experiments have less scatter than geologic materials. AlON has the added benefit that it is transparent, and as a result, experiments can visualize the development of internal damage within the material, not just the expression of damage on the surface.

Within this reduced problem the key physical processes are

- boundary conditions, such as contact, free surfaces, and resolved cracks
- rearrangements of the internal structure, such as classical plasticity and pressure

dependent granular flow,

- the development and growth of subscale defects, such as microcracks, that affects the homogenized material behavior through elastic softening or activation of other mechanisms, and
- homogenized atomic level behavior captured through the elastic response and the equation of state.

In addition to these different scales of physical response, brittle materials are inherently statistical in nature. Since their strength is controlled by defects, and these defects are rare, the spatial distribution of these defects leads to spatial variability in the local strength.

1.1 Models and Experiments: Two Essential Pieces to Understanding Material Behavior

An essential procedure when developing a model (both the constitutive model and the computational framework that solves an initial boundary value problem) for a physical process (such as an impact on an armor ceramic tile) is demonstrating that the model describes the correct physical process. The testing procedure is for-

mally referred to as model validation. As discussed in [6], verification is the proof that the computational model is solving the equations in the associated conceptual or mathematical model correctly, while validation is the ongoing process of establishing confidence in a mathematical model of a process through comparison to experiments. In this work, we will present an approach to integrating physical observations from experiments, theoretical analysis of various process, and computations within a framework. Using this framework, one can look at problems ranging from the design of armor ceramic materials to understanding the consequences of asteroid impact events.

In solid mechanics, the distinction between a constitutive description that is valid at a material point (an arbitrarily small volume) and a relationship between the average deformation and the average stress in a volume is often not explicitly acknowledged. Many traditional constitutive models assume that they describe the behavior of a material point at all times. For some models this is a very reasonable assumption. For example, elasticity can be derived from atomic interactions when the atoms are confined to a crystal lattice and the averaging volume is sufficiently large that individual atomic vibrations are ignored. The transition from atomic springs to continuum elasticity occurs over many orders of magnitude in scale separation and therefore it is generally reasonable to apply elasticity theory at a point in a continuum.

Failure processes in materials, such as the development of shear bands or large scale cracks leading to fragmentation, are (by definition) processes that occur over some interval in time and space. If the timescales and length-scales involved in these

processes are small compared to the structural problem of interest, then one may develop additional equations that describe the behavior of these features. For example when analyzing the propagation of a crack using either the extended finite element method (XFEM)[7] or the cohesive zone approach[8], one must specify a model for either the crack propagation behavior or the traction separation rules. In many problems involving the dynamic failure of brittle materials under impact loading, the time and length-scales associated with the material failure process are on the same order of magnitude as the computational discretization applied to solve the problem. In these cases, it becomes important to recognize that computational approaches divide space up into finite volumes and therefore constitutive models must describe the behavior of a finite volume of material (which may contain subscale failure processes).

1.1.1 Homogeneous Stress States With Simple Loading

Experiments are designed to subject a material to a specific stress state in a specific manner. For example, uniaxial compression experiments attempt to apply a uniform traction to the boundary of a specimen and measure the motion of that boundary. The experiment is designed such that the rate at which the load is applied is small compared to the time it takes information to travel within the specimen. This results in a uniaxial stress state while the deformation in the material is uniform.

Once the specimen begins to fail and the deformation field is no longer uniform, the boundary traction and displacement are not representative of the material behavior in the specimen; however, *the experiment is still measuring what occurs in the physical problem*. The physical problem has just become more complicated than the one used for the initial design of the experiment. This illustrates the importance of coupling experiments and computational models in order to extract more information from each.

1.1.2 Even Simple Experiments Benefit From Coupling to Simulations to Understand Effects of Imperfections

In a uniaxial compression test, the experimental data is typically a relationship between the applied displacement at the boundary and the force required to cause this displacement. In this experiment, it is common to extract the elastic modulus of the material and a strength. In order to extract any of these quantities, one must make an assumption about the behavior of the material (an elastic modulus is a model parameter and therefore defining one is implicitly using a model to interpret the experiments). This assumption of material behavior amounts to defining a model for the material. Models provide a mechanism to interpret the experimental data and ultimately can help justify or reinforce the observed behavior.

One example of the synergy between experiments and modeling is the work on unloading failure in quartz crystals [9]. In this work the authors demonstrated that the experimentally observed self selection of preferential cleavage planes during load removal resulted from the frictional interface and the elastic anisotropy of the quartz specimen. Without the additional modeling work, one may have interpreted the preferential selection of the specific failure plane as evidence that the particular plane is a weaker cleavage plane than other similar planes; however the modeling demonstrates that this is not the case. The modeling shows that the selection of the particular plane is a result of the loading orientation and that a different loading orientation could have produced a different crack growth plane.

Based on this simple example, it is clear that more complex experiments can benefit from modeling efforts both in the experimental design phases and when interpreting the experimental results. Experiments provide real measurements of a physical event, but insights arrise from the interpretation of experimental results using a model.

1.2 Background

Dynamic failure of brittle materials is a large field and this work builds upon the work of many researchers before us. In developing a modeling approach for simulating the failure of brittle materials subjected to impact loading we combine a micromechanics based constitutive model with a computational approach that is suitable for large

deformation problems. Before delving into the details of our approach, we provide some context by reviewing some recent work both in the development of constitutive models for dynamic brittle failure and in the computational schemes used to solve the related initial boundary value problems. Additional background that is relavant to the particular chapter is included at the beginning of those chapters.

1.2.1 Models for the Failure of Quasi-Brittle Materials Through Microcracking

A number of researchers have approached the process of microcrack growth through the use of micromechanics based damage models [10–19]. Many of the micromechanics models for failure under compressive loading are based on the work of Ashby and Hallam [16] or Nemat-Nasser and Horii [17]. At the most basic level, these micromechanics damage models provide for the growth of a subscale population of cracks based on some measure of the crack tip driving force and a crack kinetics law. The models differ in how crack interactions are handled. This is typically done either through the use of a crack array [20] or through an effective medium approach as in [10]. Additionally, the Paliwal and Ramesh [10] model addresses a dynamically interacting distribution of microcrack sizes instead of using a single crack size. The distribution of cracks is important for capturing the correct scaling response of strength with strain rate [21].

As the microcracks continue to grow and develop, they will eventually intersect. The behavior of the material once these microcracks begin to link up depends on the stress state applied to the material. Low confinement or tensile stresses favors the development of a few dominant cracks. In contrast, high confinement, which is the initial loading condition in impact events, promotes the activation of many small cracks. When many microcracks have intersected and created many small fragments of material, the material is reasonably described as a granular material [22]. The behavior of granular materials has been extensively studied in the context of soil mechanics. There are classic models such as the Mohr-Coulomb, Drucker-Prager, and Cam-Clay models that can be used to treat the granular material as a continuum solid (for reference see a standard geotechnical engineering reference such as [23]). More recent research has focused on developing constitutive equations for an effective homogenized granular material from the results of simulations that treat each grain as a discrete element (e.g. Andrade et al. [24]). The granular flow contributes two key aspects during an impact event[25]. First, as the granular material is sheared, it bulks and increases the pressure on the surrounding material. Second, it provides a mechanism for dissipating additional energy as the material is excavated.

Over the years researchers have developed a number of models that incorporate internal variables that are directly related to microstructural features (e.g. [10, 18, 26–29]). In all of these models the key microstructural feature is a distribution of cracks.

Dienes [26] developed a material model for the failure of rocks under high loading

rates in the mid 1980's. The model included an effective inelastic rate of deformation associated with crack opening, sliding, nucleation, and growth as well as a degraded elastic response. This model explicitly tracked a number of crack orientations and defined an effective crack length based on an exponential distribution of crack sizes. The author also used a stability criterion to determine the limit stress to activate crack growth. The focus of this work was the collective failure behavior of network of cracks, with applications to oil and natural gas extraction. Gailly and Espinosa [27] developed a model for the microcracking and granular flow of the comminuted material for brittle materials subjected to penetration loading that captured similar physical processes as the work by Dienes [26]; however, the model developed by Gailly and Espinosa [27] used a more complicated flow model for the comminuted material.

The model developed by Clayton [29] uses a similar approach to describing the activation and growth of microcracks and eventual granular flow of the material; however the model is developed in a finite deformation framework using a homogenization approach to connect the micro- and macro-scales. Clayton [29] concluded that for the geologic material granite only 9 effective crack families were needed to properly describe the material behavior, which is consistent with the earlier work by Dienes [26].

Dienes et al. [28] extended earlier work to develop a mechanism based damage model for investigating the detonation of polymer bonded explosives due to local in-homogeneities. This model incorporated both an orientation distribution and size

distribution of cracks. The crack growth rate was computed using an energy release rate argument and crack coalescence was handled using a statistical argument. Since the primary focus of this work was on estimating the stability of explosive materials, the author focused on the thermodynamics and the associated heating.

Nemat-Nasser and Horii [17] approached the brittle material failure problem by computing the effective stress intensity factor associated with an inclined crack under compressive loading. The wing cracking mechanism was experimentally demonstrated by creating inclined slit cracks in PMMA[16]. These cracks kinked from their initial orientation and grew with their normals perpendicular to the applied compression direction.

The experimental observation of the wing-cracking mechanism lead to the development of a number of material models based on this mechanism. Nemat-Nasser and Obata [15] used kinematic arguments to compute the effective stress-strain response of a material containing an isolated wing crack. Deng and Nemat-Nasser developed a series of arguments for the behavior of an array of cracks[20]. They later extended the work to account for the dynamic growth of cracks in both tension[30] and compression[31]. The microcrack interaction ideas were reformulated in the context of internal state variable (as opposed to kinematic arguments) in [14]. Using a kinematics and wing cracking based micromechanics damage model Huang and Subhash [12] investigated the criterion for failure of brittle materials subjected to dynamic loading at different levels of confinement. They observed that material fail-

ure occurred when the damage growth rate tended to infinity and that the time (or strain) associated with the rapid increase in the damage growth rate increased with increasing confinement. Paliwal and Ramesh [10] extended these ideas by using the self consistent approach to capture the effective interactions of a population of micro-cracks that interact during dynamic loading. This model was not implemented into a continuum mechanics code to investigate the coupling between local damage growth, the surrounding material, and the structural response.

The model developed by Deshpande et al. [18] also uses a wing cracking mechanism with crack interactions addressed through a crack array approach to compute the evolution and growth of damage within the material. The model developed in 2009 [32] included elastic softening of the damage material; however, a more recent model in 2011 [18] replaced the elastic softening with a Drucker-Prager type granular flow surface that evolved with the damage parameter. As these cracks grow, they cause a reduction in the stiffness of the material [32] or an evolution of the yield surface of the material [18].

Although these micromechanics based damage models have the potential to introduce physically based variability into the constitutive response, they stop short of introducing this important element. There has been some efforts to link the physical variability observed in brittle materials to the process of sampling flaws in a material and interactions of these flaws with a micro-mechanical damage model [33]. However these efforts did not look at the implications of the variability for structural prob-

lems. Variability is a key feature of brittle materials. Introducing this variability has the added benefit of stabilizing the damage problem and providing natural initiation sites for damage [34–36]. In this work, we present a mechanism based material model that incorporates variability for use in high rate simulations. A key component of the model is the use of a micromechanics based damage model with the incorporation of macroscopic material variability.

1.2.2 Computational Approaches for Dealing With Localized Failure

Although the initial loading in impact events is in the form of compressive loading, it is likely that some regions of the material are exposed to tensile loading. As discussed above tensile loading is often unstable and the largest microcracks quickly grow and become macro scale cracks. Once the microcracks coalesce into a macro scale crack, a new surface is introduced into the continuum body. In order to deal with the topological change and apply the appropriate traction boundary conditions, a number of methods have been developed to enrich the solution space and explicitly track the crack front and path including the cohesive element method [8] and the extended finite element method [37]. These methods are very effective for tracking a few dynamically interacting cracks; however, they get expensive when many dynamically interacting cracks are considered and some have poor scaling performance in parallel

environments [38]. Techniques such as element deletion [39] can provide successful representations of regions that look like, and behave similar to, explicit cracks at a much lower computational cost. A similar approach is to define a different material behavior for the fully damaged material, such as granular flow, and not delete the material points (thus conserving mass). This approach is used in the Kayenta model [22] and the brittle material models by Johnson and coworkers [40–42].

The combination of a flexible and robust computational technique with a material model that is motivated by the relavent subscale physical processes provides a powerful tool for looking at the dynamic failure processes in both armor ceramics and geologic materials such as rocks. In this work we adopt an existing computational approach and focus on developing and testing a material model that can be used to look at these problems.

1.3 Organization of This Thesis

The following chapters are organized as follows. We begin by discussing how one develops statistical realizations of a flaw distribution within a volume of material to define the initial conditions for an initial boundary value problem in chapter 2. This is followed by a discussion of the material point method in chapter 3. In this work we use the material point method to solve a given initial boundary value problem instead of other methods such as the finite element method. In chapter 4 we present the material

model that was developed as part of this work. In this chapter the model is applied to the transparent ceramic material Aluminum Oxynitride (AlON) and used to simulate the Edge-On Impact experiments[43]. We also discuss the verification testing that was done to insure that the model was correctly implemented in the computational framework and the Mie-Grüneisen equation of state. After applying the model to AlON, it is applied to boron carbide in chapter 5. In the context of boron carbide, we examine additional parameters in the model by simulating dynamic uniaxial stress compression and simplified ballistic loading configurations. In chapter 6 we extend the material model to very large scales and look at the evolution of the asteroid Eros. This chapter shifts the focus from model development and validation to using the model to gain insights into the behavior of the natural world. It is particularly useful to stretch the model and apply it to a problem where the application area is far removed from any possible calibration experiments. The final chapter provides a summary of the work and thoughts on future work.

Chapter 2

Simulating Flaw Distributions in Brittle Materials

2.1 Addressing Flaws Across Many Orders of Magnitude

Computational resources have reached the point where it is possible to discretize a material on a length scale that approaches the microstructural length scales. In this work, when we discuss microstructure we are referring specifically to the local distribution of crack like flaws within the material. We assume that the other microstructural features such as grain boundaries and crystal structure are homogenized into effective subscale properties, which include the stiffness, fracture toughness, and

the crack growth laws. These effective properties are assumed to be constant through out the material. In this work, therefore, capturing the microstructure amounts to capturing the effects of a flaw population defined by flaw statistics in a representative volume. However, since the computational discretization is typically determined by the geometry, macroscopic loading conditions, and computational cost, the discretization volume may not be commensurate with a statistically representative volume. It thus becomes important to use models that can explicitly account for the effects of statistical sampling on the initial boundary value problem of interest.

For example, consider a tile of armor ceramic. The materials processing procedures are typically designed to place an upper bound on the flaw size in the tile ($s_{\max}$). At the same time, the activation of other deformation mechanisms (e.g. plasticity, twinning, crack nucleation, etc.) place lower bound on the flaw size ($s_{\min}$) that can be activated prior to triggering these other mechanisms. If other mechanisms are triggered at stresses lower than the stress required to activate a crack of size $s_{\min}$ than flaws smaller than $s_{\min}$ will not contribute to microcracking. For some materials $s_{\min}$ when defined in this manner may be on the order of the atomic spacing in the material. In principle, this distribution of flaws could extend from a few microns up through many millimeters. There are many small flaws and a few large flaws in most real flaw size distributions in advanced ceramics [44].

In some problems, the length scale introduced by the computational discretization h may fall within the range of this distribution and effectively divides the distribution

into subscale flaws and explicit flaws. Flaws that are much larger than h are resolved explicitly by the computational mesh and grow by concentrating stresses around them, possibly leading to activation of the surrounding microcracks. Flaws smaller than h cannot be resolved by the computational mesh and therefore are homogenized in some way (in this case, they are represented using a damage model). Flaws larger than h change the boundary value problem and must be accommodated by the computational scheme used to solve the problem. The separation between explicit flaws and subscale flaws introduces a separation in the mechanism of crack growth in addition to the way that the cracks are represented.

Explicit flaws grow by activating smaller (subscale) flaws in a damage zone around the parent crack (figure 2.1). Generally, the size of this damage zone is rate and crack-size dependent as well as statistical because there is a distribution of subscale flaws. Since the size of the damage zone can vary, the energy release rate per unit area of crack extension (G_c) may be both crack-size-dependent and rate-dependent for explicit cracks growing through a statistical and rate sensitive elastic damaging material.

An analytic self consistent approximation for treating subscale flaws (as in [10]) assumes that the subscale flaws grow based on a subscale linear elastic fracture mechanics calculation. An assumption in this calculation is that the cracks are growing through an elastic brittle material, the fracture toughness of which is rate independent as well as deterministic. Note that while it is possible for flaws with sizes near

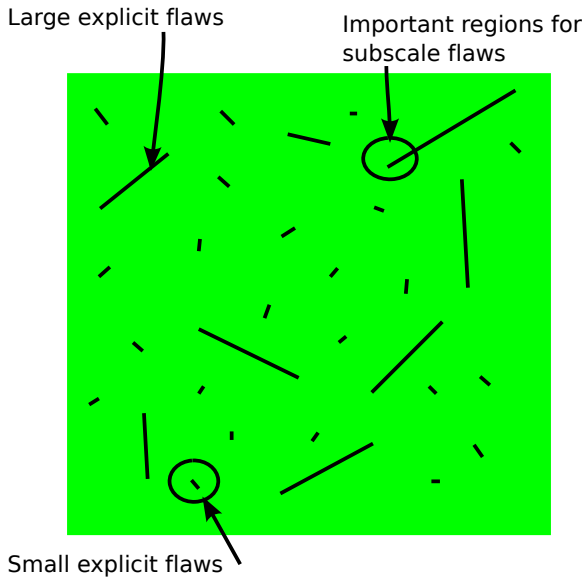

Figure 2.1: Natural separation of flaws into subscale and explicit based on probability of finding subscale flaws in the vicinity of explicit flaws

$s_{\max}$ to grow through microcrack activation, flaws with sizes near $s_{\min}$ may not be able to grow by activating smaller flaws because there are no sufficiently small flaws. As a result, the stress required to grow flaws below a critical flaw size may become sufficiently high that other physical processes (not considered here) are activated.

In order to better illustrate the distinction between these two populations of flaws, consider two additional length-scales h_l and h_h defined such that $s_{\min} < h_l << h << h_h < s_{\max}$ (shown schematically in figure 2.2). We choose h_h so that flaws larger than h_h can be accurately represented explicitly with the numerical discretization. This population of flaws will cause locally elevated stresses that activate subscale flaws and lead to failure of the structure (figure 2.1). Although there are more flaws in the size range between h and h_h, these flaws are too small to provide a large contribution to

the structural failure (if this is not true than the analyst must change h by using a different discretization size and possibly modeling approach). These flaws are unlikely to activate because the stresses required to activate these flaws are much larger than the stresses required to activate the population of larger flaws. The flaws in the size range h_l to h are by definition considered subscale flaws, and they would be the first subscale flaws activated; however, they are also the most scarce subscale flaws. When there are explicit flaws, the most important subscale flaws are the subscale flaws that are abundant enough that there is a high probability that they exist near an explicit flaw. When the discretization scale falls within the range of flaw sizes that are present in the material, this argument suggests these difficult to represent flaws near the mesh size (between h_l and h_h) can be neglected because they are too small to be activated as an explicit flaw and too scarce to contribute significantly to the subscale damage.

In this work we have chosen the problems such that all of the initial flaws are subscale flaws much smaller than the mesh size and therefore they can be represented through the micromechanics approach. Naturally, as these subscale flaws interact and grow they will eventually cause the local material to lose its ability to sustain tensile or shear loading. This transition and the treatment of connected damaged regions is discussed within the full material model description (see chapter 4). In the next section we present a detailed discussion of how one approaches the problem of defining a particular realization of a material microstructure (distribution of subscale cracks) for use as initial conditions in a simulation.

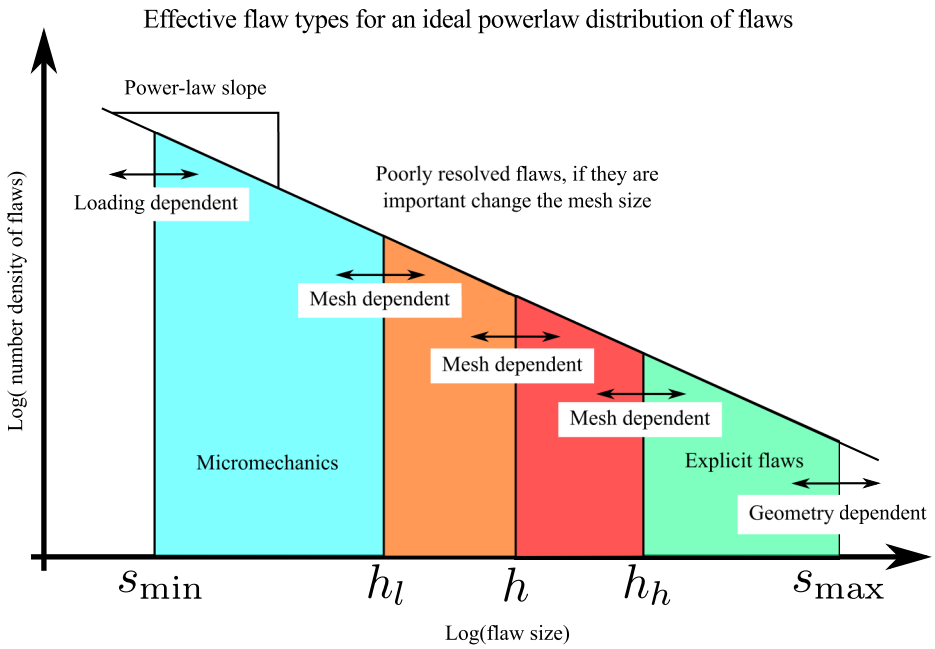

Figure 2.2: For a power-law distribution of flaw sizes flaws could exist at all scales. The problem geometry places an effective upper bound on the flaw size ($s_{\max}$) and the loading conditions place a lower bound on the flaws that can be activated ($s_{\min}$). The discretization length scale h may fall between these two limits. Flaws between h_l and h_h are too small to be resolved explicitly but to large to be effectively homogenized. If these flaws are important for the problem of interest then the mesh size must be changed. In this work, we only consider flaw distributions that fall completely into the blue micromechanics region.

2.2 Realizations of Flaw Distributions

In any specific specimen, the local flaw population is a function of the spatial position. We approach the statistical problem of dynamic brittle failure through a Monte-Carlo approach, where we generate a discrete number of realizations of the specimen of interest and then use a deterministic material model to calculate the solution to a given initial boundary value problem. In this section, we describe our approach to generating a realization of a specimen. We begin by discussing how one defines the statistical distribution of flaws within a sampled volume ($\hat{V}$) of material.

We start by defining a joint probability distribution function $f(n, a, \boldsymbol{x})$, which describes the probability $P_{n,a}$ that there are between n_l and n_h flaws with sizes between s_l and s_h in the local volume of material V_0. One obtains this probability by integrating the probability distribution over the allowable values:

$$P_{n,a}(n_l < n < n_h, s_l < a < s_h) = \iiint_{V_0} \left(\int_{n_l}^{n_h} \int_{s_l}^{s_h} f(n, a, \boldsymbol{x}) da\, dn \right) dV \qquad (2.1)$$

In this most general case, the joint probability distribution function may depend on position or possess spatial correlations. In this case, the probability of finding flaws within a given size range depends on the spatial location, the size of the search volume, and the other flaws in the neighborhood. There has been some work in these areas [33, 45]; however, that is not the focus of this work. We assume that the number of flaws, the flaw size, and location are independent quantities, and as a result the joint probability distribution function can be written as the product of the individual

probability functions $g(s)$ and $h(n)$ ($f(n,s) = h(n)g(s)$). With these assumptions, equation (2.1) becomes:

$$P_{n,a}(n_l < n < n_h, s_l < a < s_h) = \iiint_\Omega dV \int_{n_l}^{n_h} h(n)dn \int_{s_l}^{s_h} g(s)ds. \tag{2.2}$$

Since we assume that flaws are independent of position and each other, the number of flaws within a local volume $V_0 = \iiint_\Omega dV$ is reasonably described using a Poisson distribution. A Poisson distribution describes the number of independent events that occur during a finite interval. A commonly used example is the number of buses arriving at a bus stop in a given period of time (for example one hour). In this one dimensional case, the parameter for the distribution is the average rate that the busses arrive at the bus stop multiplied by the duration of the time interval. The extension to three dimensional volumes is trivial. For arbitrary volumes, the parameter for this Poisson distribution is given by the average flaw density η (the effective rate) multiplied by the volume V_0 (the observation interval):

$$\iiint_\Omega dV \int_{n_l}^{n_h} h(n)dn = \int_{n_l}^{n_h} \text{Pois}[\eta V_0](n)dn. \tag{2.3}$$

The flaw size probability distribution function, $g(s)$, is related to the probability P that a given flaw has size a between flaw sizes s_l and s_h:

$$P(s_l \leq a < s_h) = \int_{s_l}^{s_h} g(s)ds. \tag{2.4}$$

It is convenient to introduce the cumulative distribution function (CDF) for flaw size

$$G(s) = \int_0^s g(a)da. \tag{2.5}$$

Rewriting equation (2.4) using the CDF results in the simpler notation:

$$P(s_l \leq a < s_h) = G(s_h) - G(s_l). \tag{2.6}$$

In this work, the flaw size distribution $g(s)$ and the flaw density η are characteristics of the material. They will depend on the processing path, the precursor materials, the machining practices, and any screening processes that are put in place to reject unacceptable specimens.

With the statistical description of the flaw distribution defined, we now describe our approach to simulating a specific realization of the flaw distribution. This is used to define the initial conditions in an initial boundary value problem. As a part of the computational solution technique, we discretize the computational domain into a collection of non-overlapping particle domains (section 3.1). Each of these particles has an initial volume V_{0i}. In general, each particle could have a different volume; however, for notational simplicity, we do not carry the subscript denoting the volume of particle i and use V_0 as the particle volume, with the understanding that these calculations are local to a particle and therefore particles could have different volumes without modifying the approach.

Within each discretization volume V_0, we capture the effect of microcracks using a homogenized damage model. One scalar damage definition is the sum, over all N_f cracks, of the cubed crack sizes (s_i) in the discretization volume (V_0) divided by V_0

[46]:

$$D = \frac{1}{V_0} \sum_{i=1}^{N_f} s_i^3. \tag{2.7}$$

When there is a large number of flaws, computing this quantity directly becomes unrealistic. To reduce the computational cost of the damage parameter, we group similar sized flaws into N_{bins} flaw families (or "bins"). Each of the N_{bins} represents the N_k flaws between flaw sizes s_k^l and s_k^h in the volume V_0 using the representative flaw size s_k and the flaw family density $\omega_k = \frac{N_k}{V_0}$. Using this binning approach, the damage parameter in equation (2.7) can be approximated using:

$$D = \sum_{k=1}^{N_{\text{bins}}} \omega_k s_k^3. \tag{2.8}$$

Each flaw size within the family is a statistical quantity described by a probability function $g_k(a)$, which is related to the parent flaw distribution $g(s)$ through

$$g_k(a) = \frac{1}{G(s_k^h) - G(s_k^l)} \begin{cases} g(a) & s_k^l \leq a < s_k^h \\ 0 & \text{otherwise} \end{cases}. \tag{2.9}$$

Choosing $s_k^3 = \frac{1}{N_k} \sum_{i=1}^{N_k} a_i^3$ (3-norm) results in the most accurate approximation of the damage parameter, but it will skew the representative flaw size for a family towards larger flaw sizes. Optimizing the selection of s_k to capture other quantities, such as the total increase in crack area within a family, will lead to other relationships between the sampled flaws within a bin and the representative flaw size for the bin. Recognizing the multiple possible choices for s_k, we define s_k as the sample mean (1-norm) of the flaw family. This is defined for a collection of N_k flaws with sizes a_i

in the flaw family as:

$$s_k = \frac{1}{N_k} \sum_{i=1}^{N_k} a_i. \tag{2.10}$$

We discuss the consequences of using the 1-norm instead of the 3-norm during the discussion of the convergence of our sampling approach. This is discussed after we complete our discussion of the sampling method.

In general, the finite size of V_0 introduces variability in the number of flaws that reside in any specific volume. In the following discussion, we denote statistical quantities with a tilde over the variable name. The expected value of a quantity is denoted with an overbar. For statistical quantities the plain variable represents a specific realization of the value drawn from its corresponding distribution. The expected value of $\tilde{\omega}_k$ is equal to the parent flaw density multiplied by the probability that a specific flaw falls in the range covered by the flaw family. Using equation (2.6) we write $\bar{\omega}_k$ as a function of the parent flaw CDF ($G(s)$) and the flaw density:

$$\bar{\omega}_k = \eta \left(G(s_k^h) - G(s_k^l) \right). \tag{2.11}$$

When all of the flaw families are considered, they cover the entire range of the flaw distribution. By definition, we must have

$$\sum_{k=1}^{N_{\text{bins}}} \bar{\omega}_k = \eta. \tag{2.12}$$

If V_0 is sufficiently large that the effects of material heterogeneity can be ignored, ω_k approaches its expected value $\bar{\omega}_k$.

As a first approximation, we model the spatial distribution of flaws using a Poisson process. This process is consistent with the assumption that the location of flaws are independent. From the assumption of a Poisson process, the number of flaws in each family becomes a Poisson distributed random variable defined by

$$\tilde{N}_k = \text{Pois}(V_0 \bar{\omega}_k). \tag{2.13}$$

Since the particle volume is deterministic, the family flaw density $\tilde{\omega}_k$ has a distribution that depends only on the distribution of $\tilde{N}_k$.

When there is only a single flaw in the family, $\tilde{s}_k$ must have a distribution identical to $g_k(a)$. However, for large values of N_k, the central limit theorem states that the distribution of $\tilde{s}_k$ becomes Gaussian where the mean is given by the first moment of g_k:

$$\bar{s}_k = \int_{-\infty}^{\infty} a g_k(a) da, \tag{2.14}$$

and the variance is given by the variance of g_k divided by N_k:

$$\sigma_{s_k}^2 = \frac{\int_{-\infty}^{\infty} a^2 g_k(a) da - \bar{s}_k^2}{N_k}. \tag{2.15}$$

For a small number of flaws within a flaw family it is reasonable to explicitly simulate all of the flaws within the family and calculate the sample mean, however when there are many flaws within the family this becomes unrealistic and sampling the Gaussian distribution is necessary.

Figure 2.3 provides a graphical representation of the relationship between the flaw size distribution ($g(s)$), the flaw density (η), the expected value of the flaw

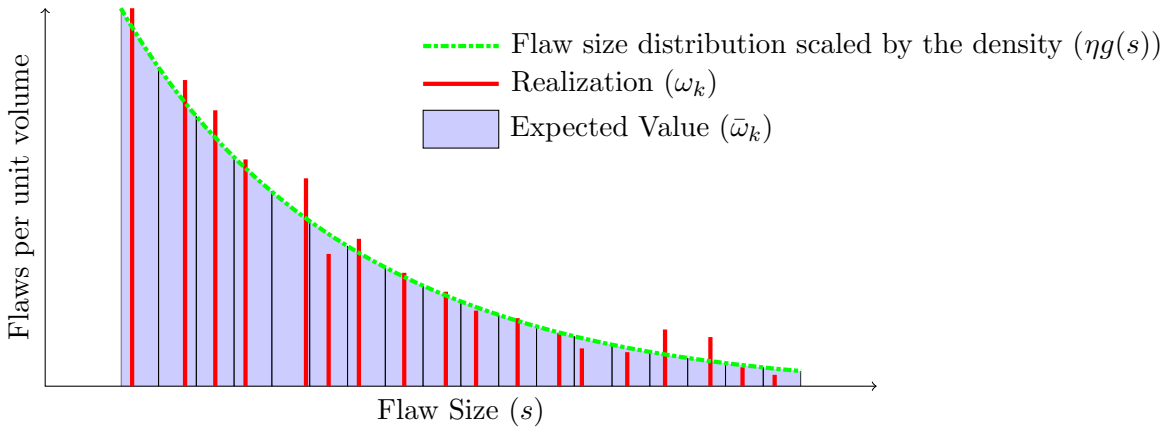

Figure 2.3: The flaw distribution is divided into bins of similar sized flaws. The area under the parent flaw distribution is the total number of flaws per unit volume for large sample volume. Dividing the flaw size range into bins and integrating the area under the flaw distribution within each bin multiplied by the flaw density (η) gives an expected value of the flaw density for each bin ($\bar{\omega}_k$). In finite particle volumes we generate a realization of the flaw density for each bin (ω_k), shown using the height of the red lines, and a realization for the location of each bin center (s_k), shown using the location of the red lines.

family density ($\bar{\omega}_k$), and a realization of the flaw family density (ω_k). The flaw size distribution and flaw density are defined as a part of the material. The flaw size distribution is shown schematically in figure 2.3 using a green dashed and dotted line. The expected value of each family flaw density ($\bar{\omega}_k$) is the area under the parent flaw distribution multiplied by the parent flaw density. It is a deterministic quantity and is shown using the shaded areas in figure 2.3. To create a local realization of the microstructure, we assign a specific family flaw density (ω_k) and representative family flaw size (s_k) to each flaw family. These are realizations of statistical quantities. In every discretization volume a different set of family flaw densities and family flaw sizes could be chosen. This is illustrated by the red vertical lines in figure 2.3. The location of the line indicates a specific realization of s_k while the height of the line indicates a realization of the family flaw density.

We create a realization of the microstructure in a given physical problem by assigning s_k and ω_k for each family in every particle in the discretized problem. The algorithm that we use to generate these realizations is shown in figure 2.4. By simulating the flaw family density and representative flaw family size for every flaw family in each particle in the simulation, we generate a realization of the size and spatial distribution of flaws within the simulation volume $\hat{V}$.

To ensure reasonable computational cost of simulating $\tilde{N}_k$ and $\tilde{s}_k$ and to avoid numerical underflow associated with generating a realization from a Poisson distribution, we introduce a cutoff number of flaws N_{cutoff}. When the expected number

of flaws in family k ($V_0\bar{\omega}_k$) exceeds N_{cutoff}, we use a Gaussian approximation to the Poisson distribution to generate a realization of the number of flaws in the family N_k, otherwise we directly sample a Poisson distribution [47, p. 132]. If N_k exceeds N_{cutoff}, we create a realization s_k using a Gaussian distribution with a mean given by equation (2.14) and variance given by equation (2.15), otherwise we explicitly simulate N_k realizations from g_k and set s_k equal to the sample mean of these values. We select $N_{\text{cutoff}} = 20$ to provide a balance between accuracy, computational cost, and to avoid numerical underflow issues associated with large negative exponents. This choice is further discussed in section 2.2.1.

Introducing the cutoff N_{cutoff} limits the computational cost (CPU time) of assigning a family density and family flaw size to each flaw family, however there is still an incremental cost for each flaw family. The memory usage during the simulation, data transfer cost at each time step, and the data storage cost for all of the subscale information scales with the number of flaw families. The computational cost for each time step scales with the number of flaw families with a non-zero family flaw density. An efficient choice of the flaw family boundaries can reduce the amount of memory that is wasted tracking empty flaw families. For most flaw distributions of interest there is a small number of large flaws and a large number of small flaws [44]. If we bias the size of the flaw families so that they are larger for large flaws and smaller for small flaws (like adaptive mesh refinement), then for a given number of bins the biased flaw families should give us a better representation of the flaw distribution.

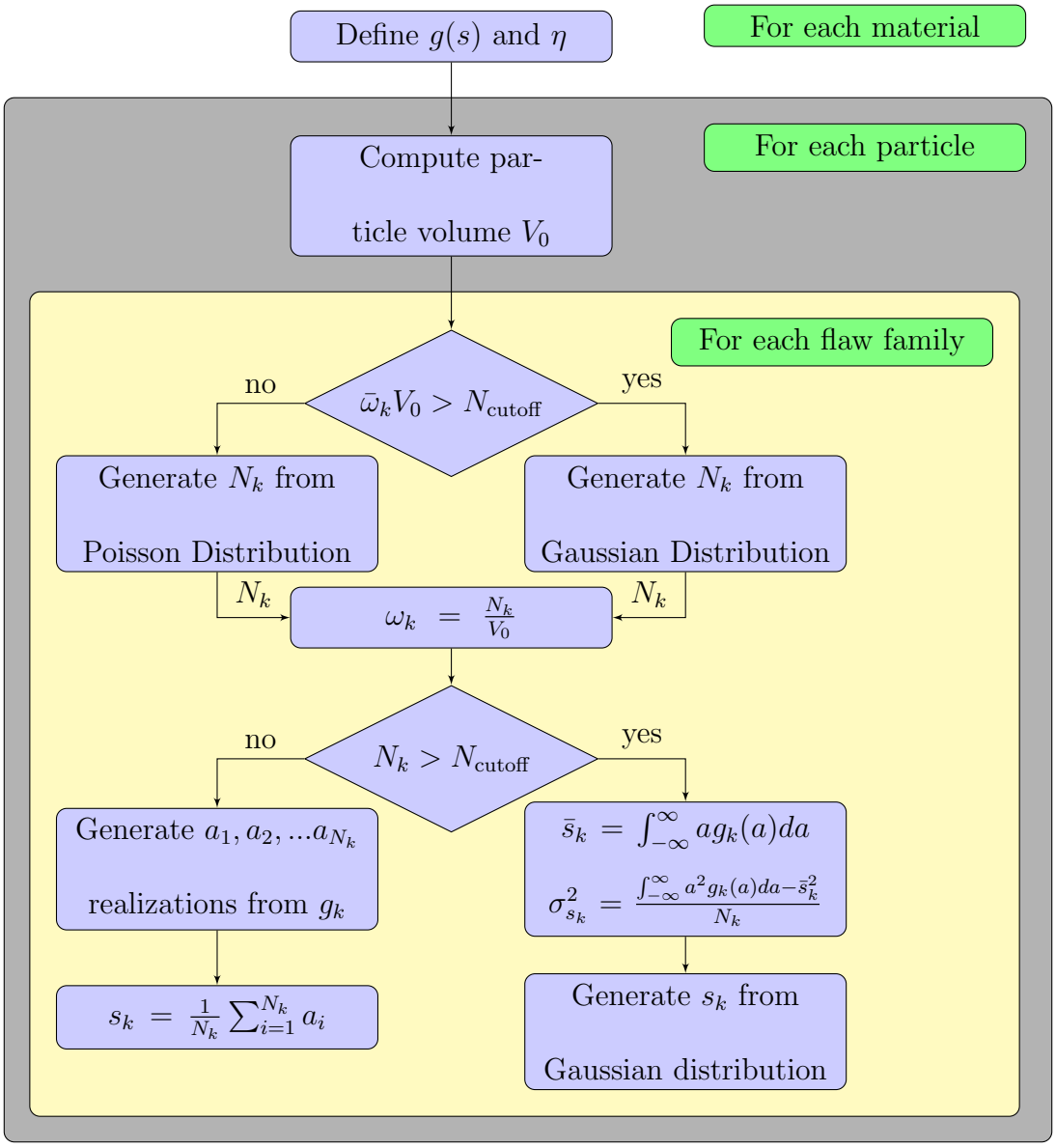

Figure 2.4: Algorithm for generating a simulated microstructural realization of flaws in a material. The material is defined by the parent flaw size distribution ($g(s)$) and the parent flaw density (η). The geometry is discretized into particles with volume V_0 for the Material Point Method. The microstructure is simulated by generating the local flaw distribution at every particle.

To create the bias we define a function $\zeta(s)$, which maps flaw sizes s in the range $s_{\min} \leq s \leq s_{\max}$ onto the interval from 1 to $\zeta_{\max}$. When the interval is divided into uniform increments, the flaw sizes are divided into biased increments. We use a rational function to do the mapping because the stress required to activate a flaw of size s scales as $1/\sqrt{s}$. The flaw binning scheme is given by:

$$\zeta(s) = \left(\frac{s_{\max}}{s}\right)^{1/a} \tag{2.16}$$

$$s(\zeta) = \zeta^{-1}(\zeta) = \frac{s_{\max}}{\zeta^a} \tag{2.17}$$

$$\zeta_{\max} = \left(\frac{s_{\max}}{s_{\min}}\right)^{\frac{1}{a}} \tag{2.18}$$

$$s_k^l = \zeta^{-1}\left(1 + \frac{k(\zeta_{\max} - 1)}{N_{\text{bins}}}\right) \tag{2.19}$$

$$s_k^h = \zeta^{-1}\left(1 + \frac{(k-1)(\zeta_{\max} - 1)}{N_{\text{bins}}}\right) \tag{2.20}$$

A selection of $a = 2$ results in each bin covering the same increment in stress for activation (e.g. for a particular choice of crack growth parameters and parent flaw distribution, one could choose the number of bins such that every 50 MPa of additional load will activate cracks in the next smaller bin size). This algorithm takes the computational discretization and the parent flaw distribution (including the parent flaw density) as an input and computes a specific realization of the distribution of flaws with the sample volume $\hat{V}$. Since each discretization volume V_0 is associated with a position $\boldsymbol{X}$, the local flaw distribution at specific locations within the sampled volume $\hat{V}$ is a function of position. However this function has zero correlation length, which is consistent with our initial assumption that flaws follow a Poisson process.

2.2.1 Verification of Microstructure Simulation Algorithm

The previous section presented a procedure for generating a realization of a flaw distribution to be used as initial conditions in the numerical solution of an initial boundary value problem. Although the procedure sounds reasonable, it is necessary to verify that the procedure correctly simulates the flaw distribution that is provided as an input. In this section, we show that the simulated distributions within a finite volume of material converge to the parent flaw size distribution and the parent flaw density. We use a bounded Pareto distribution for the flaw density where the PDF is given by:

$$g(s) = \frac{\alpha s_{\min}^{\alpha} s^{-(\alpha+1)}}{1 - \left(\frac{s_{\min}}{s_{\max}}\right)^{\alpha}} \quad \text{and the CDF is:} \quad G(s) = \frac{1 - \left(\frac{s}{s_{\min}}\right)^{-\alpha}}{1 - \left(\frac{s_{\max}}{s_{\min}}\right)^{-\alpha}} \tag{2.21}$$

For this comparison the power law slope (α) is 3.0; the minimum flaw size ($s_{\min}$) is 2 μm, and the maximum flaw size ($s_{\max}$) is 40 μm. For this verification exercise, we use a 50 mm cube simulation domain. This is sufficiently large that we expect negligible sampling errors due to a finite domain.

We define the empirical cumulative distribution function ($eCDF(s)$) in the same manner as Bishop and Strack [48]:

$$eCDF(s) = \frac{1}{N_{\text{tot}}} \sum_{i}^{N_{\text{tot}}} \mathcal{H}(a_i - s) \tag{2.22}$$

where N_{tot} is the total number of flaws, a_i is the size of each individual flaw, and $\mathcal{H}$

is the Heaviside step function. The $eCDF$ is a measure of the fraction of the total flaws that are less than the argument flaw size.

For a fixed spatial resolution, one expects that increasing the number of bins used to discretize the flaw distribution within a particle will lead to a better representation of the distribution both within the particle and within the simulation domain. As shown in figure 2.5, increasing the number of bins used in each particle results in a smoother representation of the simulated $eCDF$. The particle size should be set by the requirements of the initial boundary problem and not by the approach used to simulate the microstructure. However, for completeness, we investigated the behavior of the simulated $eCDF$ as the particle size changes for a fixed simulation volume and number of bins per particle. As shown in figure 2.6, increasing the number of particles used in the simulation (decreasing the particle size) slightly improves the representation of the total flaw distribution by smoothing out the steps in the $eCDF$.

The simulation algorithm introduces an arbitrary cutoff (N_{cutoff}) to switch from sampling a Poisson distribution to sampling from a Gaussian approximation to a Poisson distribution. Figure 2.7 demonstrates that switching from a cutoff of 20 to a cutoff of 100 has a minimal effect on the simulated flaw distribution. Increasing N_{cutoff} beyond 100 can result in numerical stability issues because the algorithm for generating a realization from a Poisson distribution computes $\exp(-V_0\bar{\omega}_k)$. When N_{cutoff} is large this exponential quantity rapidly approaches 0. This demonstrates that 20 is a reasonable cutoff value.

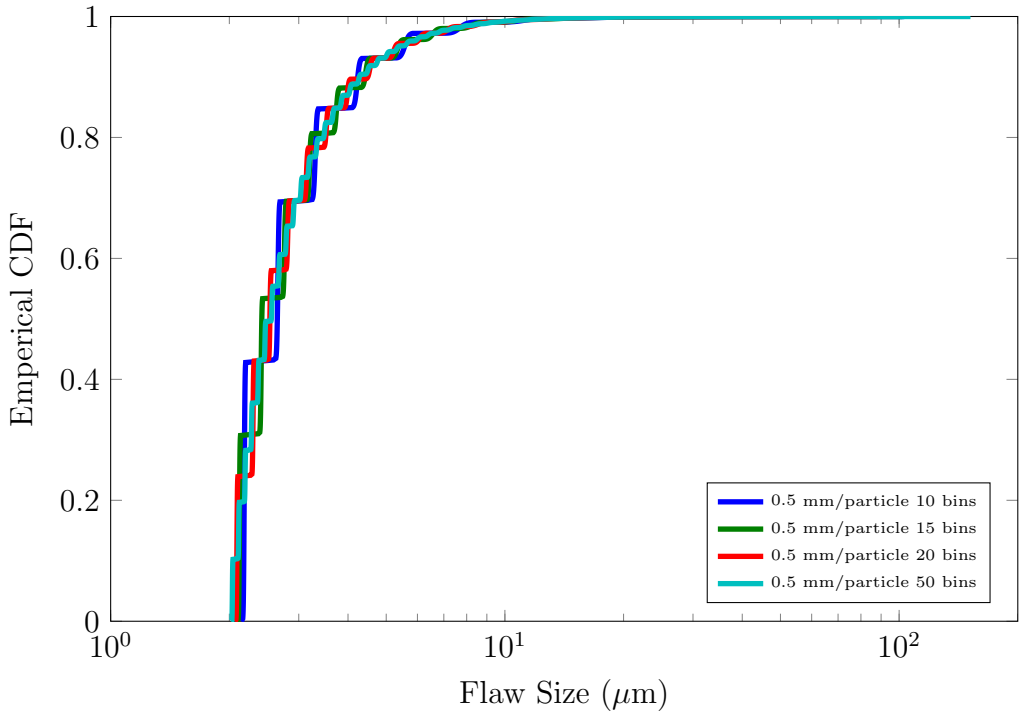

Figure 2.5: Effect of the number of bins on the simulated flaw CDF in a 50 mm cube of material using the sample mean to represent the flaw size within a flaw family. As more bins are used to represent the flaw distribution, the representation becomes more accurate.

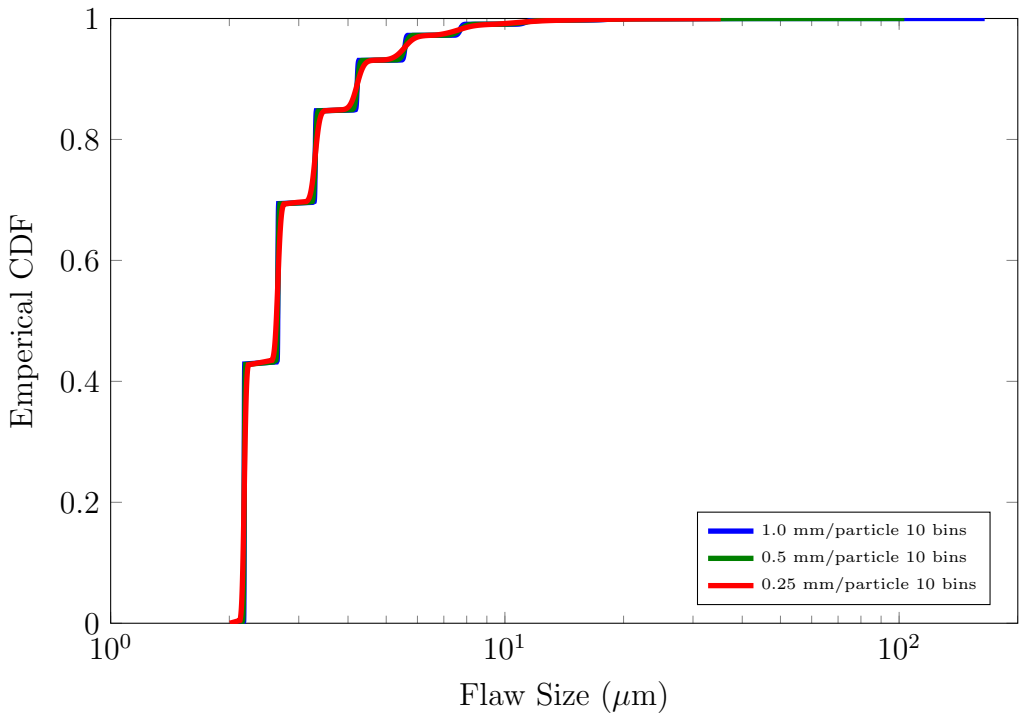

Figure 2.6: Effect of the particle size on the simulated flaw CDF in a 50 mm cube of material using the sample mean to represent the flaw size within a flaw family. As more particles are used to discretize the body the representation of the flaw distribution averaged over the entire body becomes more accurate.

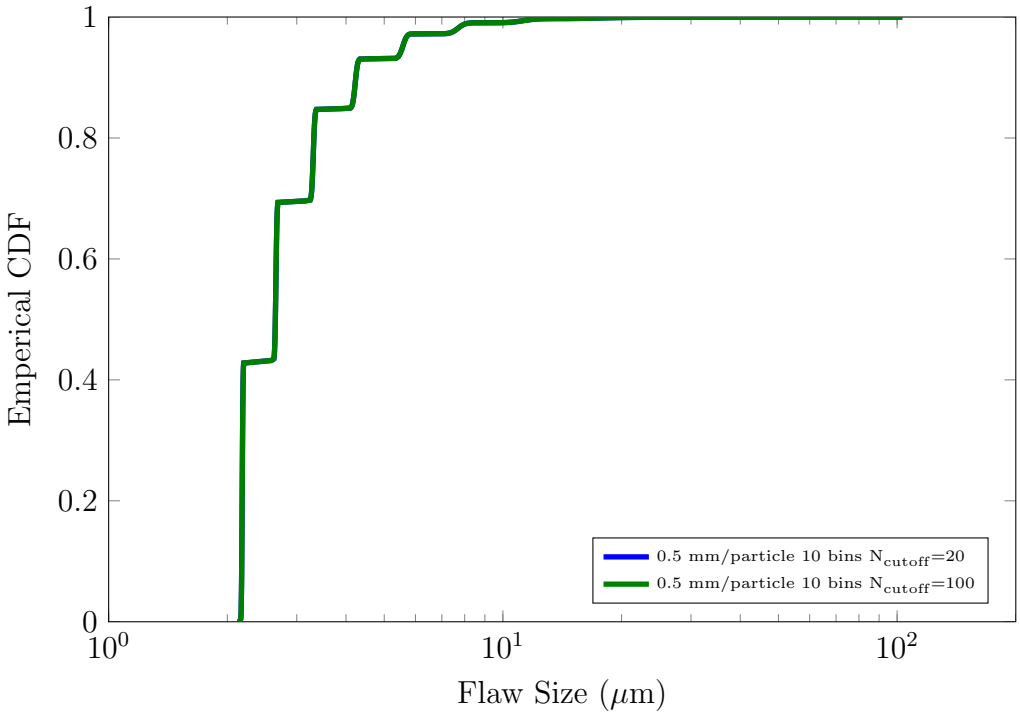

Figure 2.7: The simulated flaw size CDF for the 50 mm cube does not depend on the numerical cutoff used to switch from direct sampling of a Poisson distribution to a Gaussian approximation to a Poisson distribution.

2.2.1.1 Effect of the Definition of the Representative Flaw Size

As discussed earlier, there are a number of choices for the representative flaw size for a given flaw family. In this section we discuss the implications of choosing the 1-norm to represent the flaw family instead of the 3-norm of the flaw sizes. For clarity we label the representative flaw size computed using the sample mean using s_A and use the label s_B when the representative flaw size is computed using the cube root of the sample mean of the flaw sizes cubed. In the limit of a large number of flaws within a flaw family, the effects of variability become negligible and the representative flaw sizes are given by the corresponding expected values:

$$s_A = E[s] \tag{2.23}$$

$$s_B = \left(E[s^3]\right)^{\frac{1}{3}}. \tag{2.24}$$

There is a difference between the two quantities s_A and s_B; however, in the limit of a large number of flaw families, the width of an individual flaw family $(s_h - s_l)$ approaches zero and the difference between these quantities also goes to zero.

Since this work uses a bounded Pareto distribution as a representative flaw distribution, we compute the difference between these two representations for a specific distribution. We start by computing the required moments of a bounded Pareto

distribution. The first moment (mean) of the distribution is given by:

$$E(s) = \int_{s_l}^{s_h} sg(s)ds = \begin{cases} \left(\frac{\alpha s_l^{\alpha}}{1-\left(\frac{s_l}{s_h}\right)^{\alpha}}\right)\left(\frac{s_h^{-(\alpha-1)}-s_l^{-(\alpha-1)}}{1-\alpha}\right) & \alpha \neq 1 \\ \left(\frac{\alpha s_l^{\alpha}}{1-\left(\frac{s_l}{s_h}\right)^{\alpha}}\right)\ln\left(\frac{s_h}{s_l}\right) & \alpha = 1 \end{cases} . \tag{2.25}$$

The second moment is given by:

$$E(s^2) = \int_{s_l}^{s_h} s^2 g(s)ds = \begin{cases} \left(\frac{\alpha s_l^{\alpha}}{1-\left(\frac{s_l}{s_h}\right)^{\alpha}}\right)\left(\frac{s_h^{-(\alpha-2)}-s_l^{-(\alpha-2)}}{2-\alpha}\right) & \alpha \neq 2 \\ \left(\frac{\alpha s_l^{\alpha}}{1-\left(\frac{s_l}{s_h}\right)^{\alpha}}\right)\ln\left(\frac{s_h}{s_l}\right) & \alpha = 2 \end{cases} . \tag{2.26}$$

The third moment is given by:

$$E(s^3) = \int_{s_l}^{s_h} s^3 g(s)ds = \begin{cases} \left(\frac{\alpha s_l^{\alpha}}{1-\left(\frac{s_l}{s_h}\right)^{\alpha}}\right)\left(\frac{s_h^{-(\alpha-3)}-s_l^{-(\alpha-3)}}{3-\alpha}\right) & \alpha \neq 3 \\ \left(\frac{\alpha s_l^{\alpha}}{1-\left(\frac{s_l}{s_h}\right)^{\alpha}}\right)\ln\left(\frac{s_h}{s_l}\right) & \alpha = 3 \end{cases} . \tag{2.27}$$

The sixth moment (used to compute the variance of the quantity s_k^3) is given by:

$$E(s^6) = \int_{s_l}^{s_h} s^6 g(s)ds = \begin{cases} \left(\frac{\alpha s_l^{\alpha}}{1-\left(\frac{s_l}{s_h}\right)^{\alpha}}\right)\left(\frac{s_h^{-(\alpha-6)}-s_l^{-(\alpha-6)}}{6-\alpha}\right) & \alpha \neq 6 \\ \left(\frac{\alpha s_l^{\alpha}}{1-\left(\frac{s_l}{s_h}\right)^{\alpha}}\right)\ln\left(\frac{s_h}{s_l}\right) & \alpha = 6 \end{cases} . \tag{2.28}$$

An example discretization of a flaw distribution is shown in table 2.1. The distribution shown in this table extends from 2.0 μm to 40 μm with a power-law slope of 3. For all of the flaw families s_A is smaller than s_B as expected, because the higher order moment gives more weight to larger flaws within the bin. The result of this difference is that using s_B to set the representative bin size leads to earlier activation of a flaw family and ultimately would result in a weaker material. Even for the large flaw family span from 22 μm to 40 μm the relative error in the flaw size is less than 3 percent. Using s_B to compute the representative flaw size for a flaw family does result in a

s_l (μm)	s_h (μm)	$s_A = E(s)$ (μm)	$s_B = \left(E(s^3)\right)^{\frac{1}{3}}$ (μm)	Percent Error
22.039	40.000	27.647	28.433	2.765
13.932	22.039	16.788	17.075	1.682
9.596	13.932	11.237	11.366	1.127
7.009	9.596	8.036	8.102	0.806
5.343	7.009	6.027	6.064	0.605
4.208	5.343	4.686	4.708	0.470
3.399	4.208	3.746	3.760	0.376
2.803	3.399	3.063	3.072	0.308
2.351	2.803	2.551	2.557	0.256
2.000	2.351	2.157	2.161	0.217

Table 2.1: Discretization of $g(s)$ in to 10 flaw families showing the expected value for the representative bin size computed using two different methods. The non-uniform discretization of the flaw distribution uses smaller bin sizes for smaller flaw sizes. The difference between the two methods will become negligible for a large number of flaw families.

smoother $eCDF$ for a given number of bins per particle as shown in figures 2.8 and 2.9. Figure 2.8 demonstrates that the discrete steps in the $eCDF$ rapidly decrease so that even with only 15 bins per particle they are difficult to see in the figure. In figure 2.5 the steps in the $eCDF$ are easily visible in the 15 and 20 bins per particle curves. Using s_B instead of s_A as the representative flaw size for a bin results in a larger variation in the representative flaws for each bin. With a negative power-law slope, higher moments will weight the larger flaw sizes in the distribution more heavily than the smaller flaw sizes. The shallower slope of the steps in the green line in figure 2.9 results from greater variability in the representative flaw sizes.

2.2.1.2 Convergence to the Input Flaw Distribution

In order to quantitatively demonstrate that our algorithm for generating a flaw distribution converges, we define an error measure based on the L_2 distance between

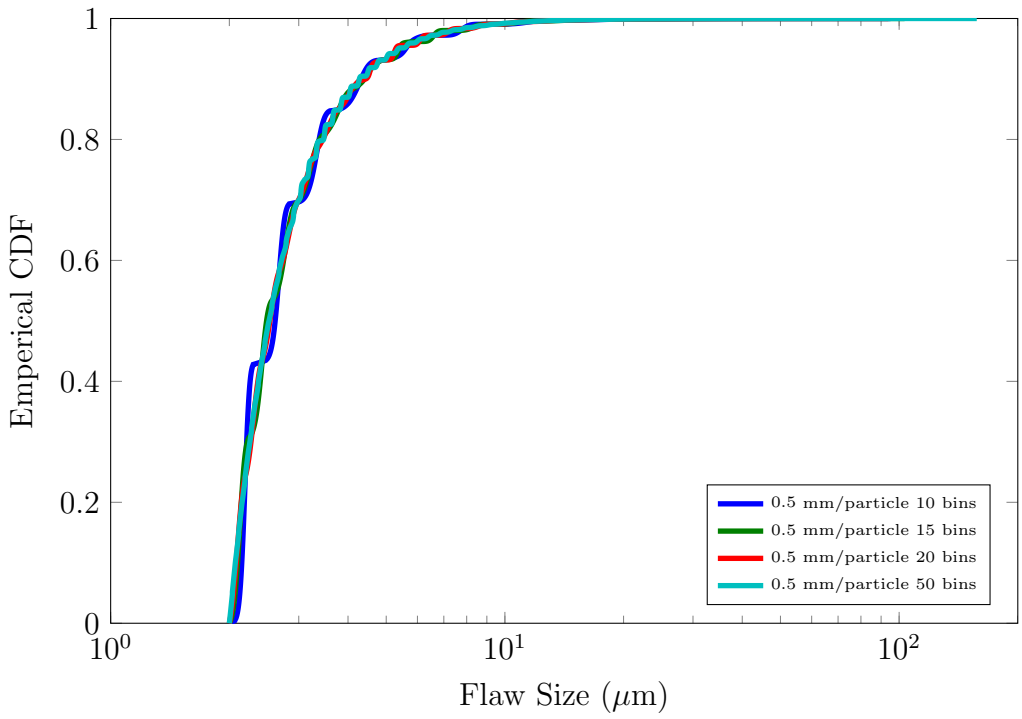

Figure 2.8: Effect of the number of bins on the simulated flaw CDF in a 50 mm cube of material using the cubed root of the mean of the flaw sizes cubed to represent the flaw size within a flaw family. The CDF is smoother than the case shown in figure 2.5 for a similar number of bins.

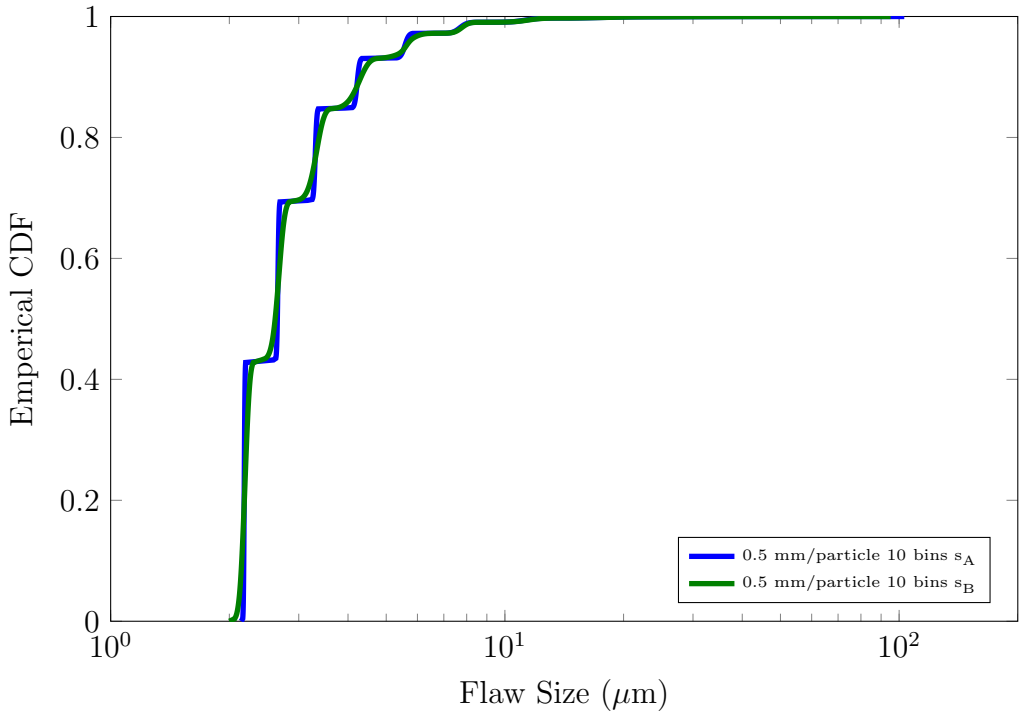

Figure 2.9: Direct comparison between the simulated flaw CDF within a 50 mm cube of material when representing the flaw family size using a the mean size with the bin or the cube root of the mean of the flaw sizes cubed. The second method results in a smoother CDF.

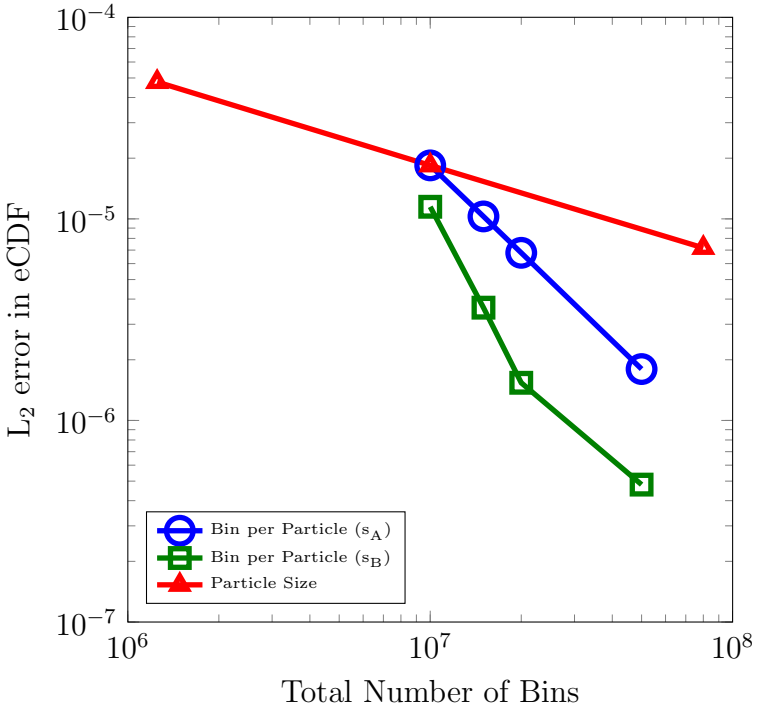

Figure 2.10: Decrease in the distance between the simulated flaw size distribution and the input flaw size distribution. Changing flaw size decreases the error slowest, while increasing the number of bins per particle, where the representative flaw size is computed using the s_B method results in the fastest convergence.

the $eCDF$ and the parent flaw distribution:

$$\mathcal{E} = \frac{1}{N_f^{\text{tot}}} \sqrt{\sum_i^{N_f^{\text{tot}}} (eCDF(a_i) - G(a_i))^2}. \tag{2.29}$$

Here $G(s)$ is the CDF for the parent flaw distribution defined by equation (2.5) and N_f^{tot} is the total number of flaw families in the simulated sample. Figure 2.10 shows the decrease in the error measure ($\mathcal{E}$) with N_f^{tot}, which is a measure of the computational cost. All of the curves show a downward slope, which indicates that as more

bins are added to the system (either through additional particles or more particles per bin), the simulated $eCDF$ approaches the input flaw size distribution. Figure 2.10 also quantitatively demonstrates that using s_B to approximate the representative flaw size within a bin converges to the parent flaw distribution faster than using s_A. The improved convergence behavior of s_B over s_A could be important when there is a very large number of flaws in each flaw family and the loading exercises the entire flaw distribution. This situation is likely encountered in large structures made from concrete or geologic materials subjected to impact loading. Under these conditions, the large size of the structure will require a relatively coarse mesh, while the high loading rate will exercise the large range of flaw sizes in the distribution.

2.3 Summary

In this chapter we discussed the issues associated with simulating flaws in materials over a wide range of length scales. This general discussion addressed the case of both explicit flaws that are large enough that the computational discretization is able to capture their effects directly and subscale, or implicit, flaws that are homogenized into an effective material behavior. Additionally we identified a *resolution dependent* range of flaw sizes that are too small to resolve explicitly yet too sparse to homogenize and presented an argument that these flaws can usually be ignored (with caution). We then limit the scope of this work to problems that contain only subscale flaws. In the

second section, we discussed an approach and algorithm for simulating a realization of a flaw distribution within a simulation volume by creating realizations of the flaw distribution for all of the subvolumes created through the discretization process. This method was shown to converge to the input flaw distribution in a sufficiently large sampled volume. In the next chapter we briefly review the computational approach that is used to simulate boundary value problems in this work.

Chapter 3

Review of the Material Point Method

3.1 The Material Point Method

Complicated loading geometries coupled with dynamic loading and complex constitutive response require numerical approaches to solve the governing equations. In this work we use computational approaches that were developed from the Material Point Method [49]. A background grid is used to compute gradients and solve the equations of motion. During a simulation time-step the local velocity gradient is computed at each material point using the nodal velocity on the grid. This velocity gradient is used to update the deformation gradient and compute an updated particle stress. The gradient of the stress is then calculated at the nodes of the grid

along with an interpolated effective mass at the node. The stress gradient and nodal mass are used to compute an updated grid velocity, which is mapped back to the material points to compute an updated position. The positions of the grid nodes are not updated and as a result mesh entanglement issues are avoided. Love and Sulsky [2] discuss stability of some implementations of the Material Point Method and in particular provide a useful analogy, in which the MPM is compared to the Finite Element Method where the material points serve the role of integration points and the grid nodes are similar to the finite element nodes. This connection becomes clear as we present the equations used in the method, following [50].

For clarity and completeness we present the CPDI1 formulation [51] and note where departures would be made to recover either the original Material Point Method (MPM) or the Generalized Interpolation Material Point Method (GIMP). The equations of motion are solved on a background grid. On this background grid a continuous field $G(\boldsymbol{x})$ is represented as:

$$G(\boldsymbol{x}) = \sum_i S_i(\boldsymbol{x}) G_i \tag{3.1}$$

The basis functions S_i are chosen to form a partition of unity and represent a C^0 continuous function. This representation is common between FEM and MPM. The starting point for this discussion is the discretized weak form of the balance of linear momentum on the grid. At each node (i):

$$m_i \boldsymbol{a}_i = \boldsymbol{f}_i^{\text{int}} + \boldsymbol{f}_i^{\text{ext}} \tag{3.2}$$

In the Finite Element Method (FEM), there are a number of ways to compute the lumped mass matrix from the consistent mass matrix (which involves computing the exact integral of the density field in the material). In FEM, integrals are evaluated by introducing Gauss integration points with locations derived from the nodal positions. In MPM integrals are performed by adding up contributions from particle domains. We define a particle characteristic function χ_p such that it is unity inside the particle domain Ω_p and zero everywhere else:

$$\chi_p(\boldsymbol{x}) = \begin{cases} 1 & \boldsymbol{x} \in \Omega_p \\ 0 & \text{otherwise} \end{cases} \tag{3.3}$$

The particle domains (Ω_p) are non-overlapping domains that span the body. Since χ_p is a top-hat function and the particle domains cover the entire body, but do not overlap, the particle characteristic functions also form a partition of unity.

As discussed in [50], minimizing the square error in the nodal representation of the mass and momentum fields results in nodal masses and velocities defined by:

$$m_i = \sum_p \overline{S_{ip}} m_p \quad \text{and} \quad v_i = \frac{\sum_p \overline{S_{ip}} m_p v_p}{m_i}. \tag{3.4}$$

The quantity $\overline{S_{ip}}$ is the volume averaged product of the particle indicator function χ_p and the nodal basis function S_i defined as:

$$\overline{S_{ip}} = \frac{\int_{\Omega_p} \chi_p(\boldsymbol{x}) S_i(\boldsymbol{x}) d\Omega}{V_p}, \quad \text{where} \quad V_p = \int_{\Omega_p} \chi_p(\boldsymbol{x}) d\Omega \tag{3.5}$$

In FEM the nodal velocity is one of the solution variables and is updated directly from the solution of the equations of motion. Since MPM uses Lagrangian particles to

carry all of the material state information, the nodal velocity field must be computed from the particle velocity field. The external nodal forces ($\boldsymbol{f}_i^{\text{ext}}$) and the internal forces ($\boldsymbol{f}_i^{\text{int}}$) are computed as:

$$\boldsymbol{f}_i^{\text{ext}} = \int_\omega S_i \boldsymbol{b} \rho d\Omega + \int_\Gamma S_i \boldsymbol{n} \cdot \boldsymbol{\sigma} d\Gamma \quad \text{and} \quad \boldsymbol{f}_i^{\text{int}} = -\int_\Omega \nabla S_i \cdot \boldsymbol{\sigma} d\Omega \tag{3.6}$$

In a FEM formulation, these integrals are computed by summing over the integration points to arrive at the FEM approximation. In [50] these integrals are computed by a summation over the particles:

$$\boldsymbol{f}_i^{\text{ext}} = \sum_p \int_{\omega_p} S_i \boldsymbol{b} \rho d\Omega + \int_\Gamma S_i \boldsymbol{n} \cdot \boldsymbol{\sigma} d\Gamma \quad \text{and} \quad \boldsymbol{f}_i^{\text{int}} = -\sum_p \int_{\Omega_p} \nabla S_{ip} \cdot \boldsymbol{\sigma} d\Omega. \tag{3.7}$$

By assuming that the stress is approximately constant over a particle domain the integrals can be rewritten as summations:

$$\boldsymbol{f}_i^{\text{ext}} = \sum_p \overline{S_{ip}} \boldsymbol{b} m_p \quad \text{and} \quad \boldsymbol{f}_i^{\text{int}} = -\sum_p \overline{\nabla S_{ip}} \cdot \boldsymbol{\sigma}_p V_p. \tag{3.8}$$

The volume averaged product of the grid basis function and the particle indicator function $\overline{S_{ip}}$ and the volume averaged gradient of the same quantity are given by:

$$\overline{S_{ip}} = \frac{\int_{\Omega_p} \chi_p(\boldsymbol{x}) S_i^*(\boldsymbol{x}) d\Omega}{V_p} \quad \text{and} \quad \overline{\nabla S_{ip}} = \frac{\int_{\Omega_p} \chi_p(\boldsymbol{x}) \nabla S_i^*(\boldsymbol{x}) d\Omega}{V_p} \tag{3.9}$$

In these integrals the particle indicator function $\chi_p(\boldsymbol{x})$ is replaced with an approximate indicator function $\chi_p^*(\boldsymbol{x})$ and the particle domain (Ω_p) is replaced with an approximate particle domain (Ω_p^*) to arrive at the final approximation:

$$\overline{S_{ip}} \approx \frac{\int_{\Omega_p^*} \chi_p^*(\boldsymbol{x}) S_i(\boldsymbol{x}) d\Omega}{V_p^*} \quad \text{and} \quad \overline{\nabla S_{ip}} \approx \frac{\int_{\Omega_p^*} \chi_p^*(\boldsymbol{x}) \nabla S_i^*(\boldsymbol{x}) d\Omega}{V_p^*} \tag{3.10}$$

In the original formulation of MPM the approximate indicator function (χ_p^*) was a Dirac delta function, and the grid basis functions (S_i) were FEM tent functions. In GIMP the approximate indicator function is a top hat function defined over a grid aligned box (or cube in three dimensions). The two GIMP variations uGIMP and cpGIMP differ in that cpGIMP stretches the box based on the diagonal components of the deformation gradient tensor. In CPDI1 the approximate indicator function is a parallelogram, which is then modified by the deformation gradient of the particle. Additionally, CPDI1 and CPDI2 modify the grid basis functions so that they are linear within a particle domain but still satisfy the partition of unity. This modification simplifies evaluating the integrals over the particle domain and eliminates the tensile instability when particles are separated by at least one grid cell [51].

After computing the internal and external forces, the nodal acceleration is trivially computed using:

$$\boldsymbol{a}_i = \frac{\boldsymbol{f}_i^{\text{int}} + \boldsymbol{f}_i^{\text{ext}}}{m_i}. \tag{3.11}$$

Based on the grid acceleration we compute an updated grid velocity using:

$$\boldsymbol{v}_i^{n+1} = \boldsymbol{v}_i^n + \boldsymbol{a}_i \Delta t. \tag{3.12}$$

Particle velocities are updated by mapping the grid accelerations back to the particles using:

$$\boldsymbol{v}_p^{n+1} = \boldsymbol{v}_p^n + \sum_i \overline{S_{ip}^*} \boldsymbol{a}_i \Delta t \tag{3.13}$$

Similarly the particle positions are updated by mapping the nodal velocities to the

particles:

$$\boldsymbol{x}_p^{n+1} = \boldsymbol{x}_p^n + \sum_i \overline{S_{ip}^*} \boldsymbol{v}_i \Delta t \tag{3.14}$$

The spatial velocity gradient $\boldsymbol{L}$ is computed from the updated nodal velocities using:

$$\boldsymbol{L}_p^{n+1} = \sum_i \boldsymbol{v}_i^{n+1} \otimes \overline{\nabla S_{ip}}. \tag{3.15}$$

The deformation gradient is updated using a second order accurate update based on the velocity gradient:

$$\boldsymbol{F}_p^{n+1} = \left(\boldsymbol{I} + \boldsymbol{L}_p^{n+1} \Delta t + \boldsymbol{L}_p^{n+1} \boldsymbol{L}_p^{n+1} \frac{(\Delta t)^2}{2} \right) \boldsymbol{F}_p^n \tag{3.16}$$

The second order accurate deformation gradient ensures that under large superimposed rotations, the deformation gradient is updated correctly. This verification test is discussed in section 4.4.3. The MPM implementation used in this work is the one contained in the Uintah [52] computational framework. The massively parallel capabilities and the open source nature of this code enabled running the large parallel simulations discussed in the following chapters.

As noted in [50], this calculation for the velocity gradient is accurate when all of the particles influenced by a node i have similar stiffnesses. When this condition is not satisfied the velocity gradient calculation is enriched in CPDI2; however, in this work we do not use CPDI2. Instead, we use only one particle per background cell. This approach ensures that in the presence of damage the stiffness within a computational cell is constant. The disadvantage of this approach is the use of only one particle per

cell, which can degrade the solution accuracy when there are large deformations and leads to a less accurate representation of non-rectangular geometries.

3.2 Energy Dissipation in the Material Point Method

The focus of this work is primarily a discussion of the interaction of flaw sampling with a micromechanics based damage model and the effect of this model and flaw interactions on the impact response of brittle materials. This work does not strive to correct or improve the family of numerical techniques related to the material point method. This work could have been completed using a different numerical technique (such as finite elements), but the large deformations involved in impact problems and the availability of the Open Source massively parallel Uintah implementation of the material point method lead us to use Uintah for this work.

Love and Sulsky [2] demonstrated that, when using the material point method with a leap frog type explicit time integrator and a lumped mass matrix, the momentum mapping from the particles to the grid and back to the particles dissipates kinetic energy. Since we are adopting the Uintah implementation of CPDI1 [51] from the perspective of a user, we must check the method and see if it exhibits the same dissipative nature as was observed for lumped mass matrices in [2]. To investigate this dissipation we set up the same problem that was used in [2]. In this simula-

tion we simulate a compressible rubber like material bouncing around in a box. To simplify the problem we constrain it to two dimensions by enforcing plane strain conditions. The material response is defined by a compressible Neo-Hookean strain energy function of the form:

$$W(\boldsymbol{C}) = W_{\text{iso}}(\bar{I}_e) + U(J) \tag{3.17}$$

$$\boldsymbol{C} = \boldsymbol{F}^T\boldsymbol{F} \tag{3.18}$$

$$J^2 = \det(\boldsymbol{C}) \tag{3.19}$$

$$\bar{I}_e = J^{-\frac{2}{3}}\text{tr}(\boldsymbol{C}) \tag{3.20}$$

$$W_{\text{iso}} = \frac{1}{2}G\left(\bar{I}_e - 3\right) \tag{3.21}$$

$$U(J) = \frac{1}{2}\kappa\left(\frac{1}{2}\left(J^2 - 1\right) - \ln(J)\right) \tag{3.22}$$

Here G is the linearized shear modulus and κ is the linearized bulk modulus. From this strain energy function, the Kirchhoff stress can be written in terms of isochoric part of the left Cauchy-Green deformation tensor $\bar{\boldsymbol{b}} = J^{-\frac{2}{3}}\boldsymbol{F}^T\boldsymbol{F}^T$ and the Jacobian of the deformation gradient J as:

$$\boldsymbol{\tau} = G\left(\bar{\boldsymbol{b}} - \frac{1}{3}\bar{I}_e\boldsymbol{I}\right) + J\kappa\left(J - \frac{1}{J}\right)\boldsymbol{I} \tag{3.23}$$

The Cauchy stress is given by:

$$\boldsymbol{\sigma} = \frac{1}{J}\boldsymbol{\tau} = \frac{G}{J}\left(\bar{\boldsymbol{b}} - \frac{1}{3}\bar{I}_e\boldsymbol{I}\right) + \kappa\left(J - \frac{1}{J}\right)\boldsymbol{I}. \tag{3.24}$$

For this test problem we choose $G = 30$ Pa, $\kappa = 170$ Pa, and $\rho_0 = 4$ kg/m^3. This choice is consistent with the material parameters in [2] although they did not provide

units in their paper. In the majority of this work the system of units is the standard SI system of kg, m, Pa, J. This choice of material properties could represent a very low density foam, but the point is to illustrate the energetic properties of the computational method.

We consider a cylinder that has an initial radius of 1.5 m located at (2.5 m, 2.5 m) in a 15 m by 5 m box with its lower left corner located at the origin. The cylinder starts with an initial velocity of (0.5, 0) m/s. The boundaries of the box are roller boundary conditions so there is no motion normal to the boundary but motion parallel to the boundary is allowed with no external resistance. We simulate the cylinder bouncing for 100 s, which is long enough for 3 bounces. In these simulations, the background mesh is 0.5 m/cell in all directions. We perform simulations with both 2 particles per cell in each direction and 1 particle per cell in each direction.

During a simulation we track the total strain energy, total kinetic energy and the total thermal energy in the system. The results from the three simulations are shown in figure 3.1. In the unified compressible Neo-Hookean (UCNH) model there is no mechanism to convert the excess work done on a particle into thermal energy and as a result there is no temperature rise in the simulation (figure 3.1a). The model developed in this work (referred to at the Tonge-Ramesh model) defaults to the compressible Neo-Hookean material model when all of the additional dissipation mechanisms are disabled. This implementation of the compressible Neo-Hookean model gives nearly identical results to the UCNH model implementation (figure 3.1b).

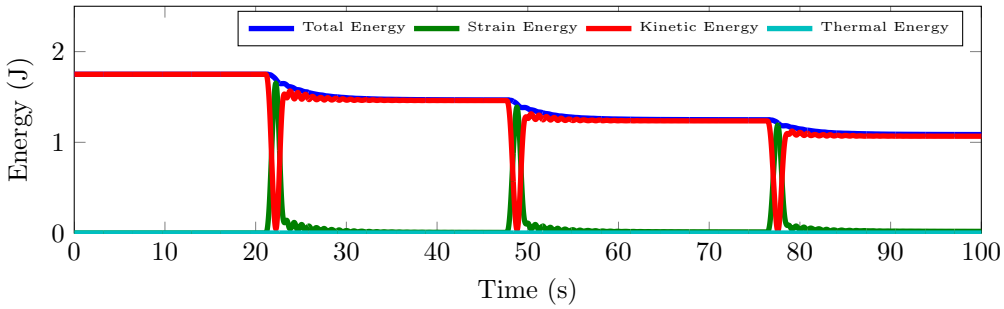

(a) Unified Compressible Neo-Hookean (UCNH) implementation, 2 ppc

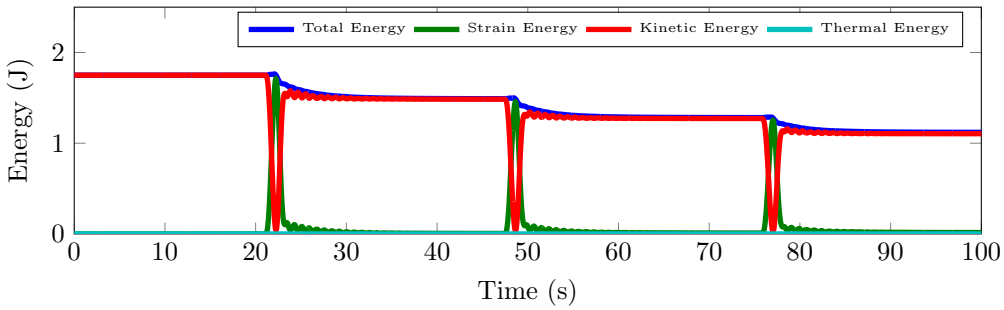

(b) Tonge-Ramesh implementation, 2 ppc

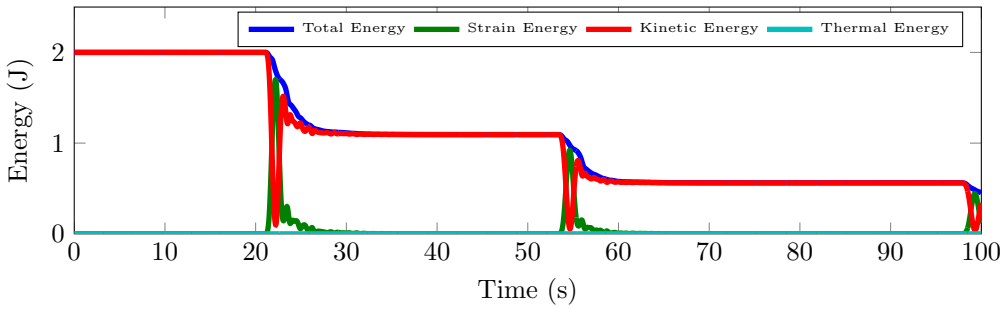

(c) Tonge-Ramesh implementation, 1 ppc

Figure 3.1: A hyper-elastic cylinder bouncing in a box loses energy consistent with observations of [2] for a lumped mass matrix. These results are included to document the host code capabilities and we recognize these limitations and will interpret our results accordingly.

The Tonge-Ramesh model implementation does show a slight increase in total energy at the beginning of each collision event. This increase is very small and is a very small difference from the UCNH implementation. This slight difference does not change the conclusions in this section, which demonstrates that MPM with a lumped mass matrix tends to dissipate total energy. Switching from 2 ppc to 1 ppc results in a coarser discretization of the cylinder and more total energy lost during the impact events (figure 3.1c). It is common to use at least 2 ppc in MPM simulations so that the geometry is better represented and fractional particles in a cell are avoided; however, as discussed in the previous section the elastic damage process and localized granular flow that result when using the Tonge-Ramesh material can cause artificial numerical strengthening when more than 1 ppc is used. The numerical strengthening results from averaging un-damaged material with failed material and not distributing the incremental deformation between the two subvolumes of material appropriately. These results are provided to demonstrate the limitations of the host code (Uintah MPM). We recognize these limitations and are aware of them when interpreting our results.

3.3 Plasticity Algorithm Used in This Work

Within the TR model we provide for granular flow of the highly damaged material. The numerical algorithm used to evolve the material configuration as a result of the

plasticity is based on the algorithm presented in [53, ch. 9]. In this section we discuss the volume preserving plasticity algorithm, but a straight forward extension of the algorithm to address no-volume preserving plasticity is used to model the granular flow in chapter 4. For volume preserving plasticity, the plasticity update takes the increment in the deformation gradient ($\boldsymbol{f}_{n+1}$ such that $\boldsymbol{F}_{n+1} = \boldsymbol{f}_{n+1}\boldsymbol{F}_n$), and the measure of elastic deformation at the end of the previous time step ($\bar{\boldsymbol{b}}^e_n$) as input and computes the stress and measure of elastic deformation at the end of the time step:

1. Compute the volume preserving part of the increment in deformation:

$$\bar{\boldsymbol{f}}_{n+1} = \det(\boldsymbol{f}_{n+1})^{-\frac{1}{3}}\boldsymbol{f}_{n+1} \tag{3.25}$$

2. Assume the increment is elastic to compute the trial state:

$$\bar{\boldsymbol{b}}^e_{tr} = \bar{\boldsymbol{f}}_{n+1}\bar{\boldsymbol{b}}^e_n\bar{\boldsymbol{f}}^T_{n+1} \tag{3.26}$$

3. Compute the trial stress $\boldsymbol{\tau}^{tr}_{dev}$ using the constitutive law:

$$\bar{I}^{tr}_e = \mathrm{tr}(\bar{\boldsymbol{b}}^e_{tr}) \tag{3.27}$$

$$\boldsymbol{\tau}^{tr}_{dev} = G\left(\bar{\boldsymbol{b}}^e_{tr} - \frac{1}{3}\bar{I}^{tr}_e\boldsymbol{I}\right) \tag{3.28}$$

4. Compute the stress at the end of the time step ($\boldsymbol{\tau}^{n+1}_{dev}$) a standard stress projection algorithm. In the case of non-hardening or linear hardening pressure independent plasticity this can be done analytically by scaling the magnitude of the deviatoric stress.

5. Using the updated stress compute the updated elastic measure of the deformation using:

$$\bar{\boldsymbol{b}}^e_{n+1} = \frac{\boldsymbol{\tau}^{n+1}_{dev}}{G} + \frac{1}{3}\bar{I}^{tr}_e \boldsymbol{I} \tag{3.29}$$

6. One can also update the plastic strain increment based on information from the stress projection.

In this algorithm the update equation for $\bar{I}_e$ is $\bar{I}^{n+1}_e = \bar{I}^{tr}_e$ whether or not there is plastic flow ([53, box 9.1]). This update, while internally consistent, does not correctly update the elastic strain energy because if there is plastic deformation during a time step then the strain energy at the end of the step ($W^{n+1}_{\text{iso}} = W_{\text{iso}}(\bar{I}^{n+1}_e)$) must be less than the strain energy in the trial state ($W^{tr}_{\text{iso}} = W_{\text{iso}}(\bar{I}^{tr}_e)$), which assumed all deformation was elastic (the condition $W^{tr}_{\text{iso}} > W^{n+1}_{\text{iso}}$ must hold during plastic loading). Since W_{iso} is a monotonically increasing function of $\bar{I}_e$, we have the condition: $\bar{I}^{n+1}_e \leq \bar{I}^{tr}_e$ where the equality holds *only* during elastic deformation, for plastic deformation the inequality holds. Due to the non-linear kinematics it is more efficient to compute $\bar{I}^{n+1}_e$ using an energy based argument than directly from the increment in deformation. We define a surrogate strain energy $\tilde{W}_{\text{iso}} = \frac{1}{2G}\boldsymbol{\tau}_{\text{dev}} : \boldsymbol{\tau}_{\text{dev}}$ and require that the ratio between the surrogate strain energy in the trial state and the final state is the same as the ratio of the actual strain energies in these two states:

$$\frac{W^{n+1}_{\text{iso}}}{W^{tr}_{\text{iso}}} = \frac{\tilde{W}^{n+1}_{\text{iso}}}{\tilde{W}^{tr}_{\text{iso}}}. \tag{3.30}$$

This leads to an update for $\bar{I}_e^{n+1}$ that depends only on the known quantities $\bar{I}_e^{tr}$, $\boldsymbol{\tau}_{dev}^{tr}$, and $\boldsymbol{\tau}_{dev}^{n+1}$:

$$\bar{I}_e^{n+1} = 3\left(1 + \frac{1}{3}\left(\bar{I}_e^{tr} - 3\right)\frac{\boldsymbol{\tau}_{dev}^{n+1} : \boldsymbol{\tau}_{dev}^{n+1}}{\boldsymbol{\tau}_{dev}^{tr} : \boldsymbol{\tau}_{dev}^{tr}}\right). \tag{3.31}$$

To illustrate this we consider an elastic-plastic material subjected to simple shear deformation defined by:

$$\boldsymbol{F}(t) = \begin{bmatrix} 1 & (1\times 10^{-3})\,\frac{t}{\mu\text{s}} & 0 \\ 0 & 1 & 0 \\ 0 & 0 & 1 \end{bmatrix}. \tag{3.32}$$

We choose material parameters similar to the high strength steel discussed in chapter 4, but set the hardening to 0 to make the illustration clearer. The bulk and shear moduli are 173.33 GPa and 80 GPa with a density of 7830 kg/m^3 and a yield strength of 2 GPa. Since the material is non-hardening during loading, we expect an elastic portion, where the strain energy rises, followed by a plastic portion at constant strain energy. As shown in figure 3.2a both the original algorithm (UCNH) and the updated algorithm (TR) correctly reproduce the expected stress time behavior with a linear rise in the stress followed by a constant stress during plastic loading. The strain energy as a function of time (shown in figure 3.2b) illustrates the necessity of using the strain energy correction in equation (3.31). The UCNH algorithm (without the correction) continues accumulating strain energy during the plastic loading (which is not correct) while the TR algorithm correctly shows a constant strain energy (reflecting the constant elastic deformation) after the onset of plasticity.

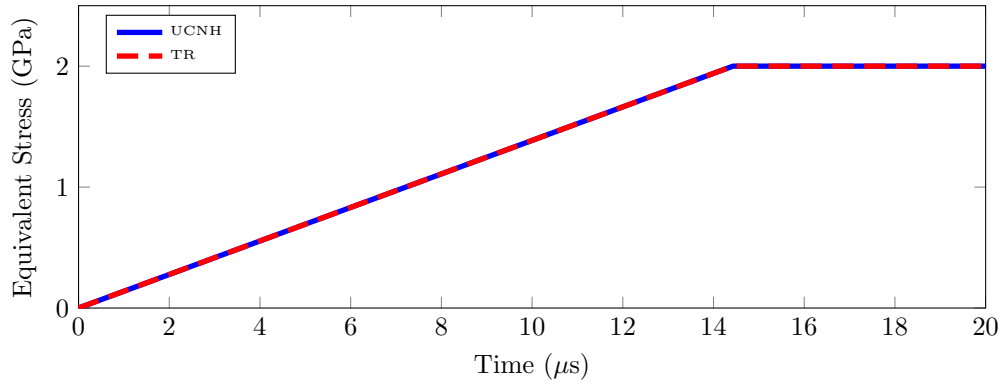

(a) Evolution of equivalent stress with time for simple shear deformation

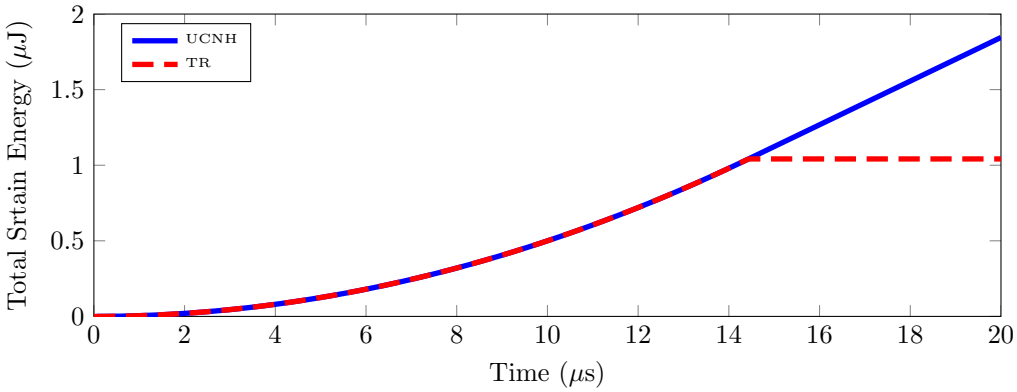

(b) Evolution of strain energy with time for simple shear deformation

Figure 3.2: Simple shear deformation of an elastic-plastic material using the UCNH model and the TR model. Both models correctly evolve the stress; however, a correction to $\bar{I}_e^{n+1}$ is required (and included in the TR model) to get the correct strain energy.

3.4 Summary

In this chapter we have presented a review of the material point method followed by an example of one of the limitations of the method. Finally we discussed a commonly used algorithm for finite deformation plasticity that has the benefit of being solved completely in the spatial configuration while maintaining objectivity. In discussing this algorithm we noted the necessity of using a correction factor to update the strain energy after an increment in plastic work that was not included in the original description of the algorithm. In the following chapter we use an adapted version of this algorithm to solve the pressure dependent plasticity problem for granular flow.

Chapter 4

Multi-Scale Defect Interactions in High Rate Brittle Material Failure

4.1 Introduction

Failure processes in brittle materials are fundamentally linked to the nature and distribution of defects within the materials. In many brittle materials, the controlling defects are crack-like flaws. By understanding the interactions of a population of crack-like defects, researchers have developed models for the evolution of damage parameters (e.g. [17]), which capture the history dependence of the strength and failure of brittle materials.

The more specific problem of the failure of brittle materials subjected to impact loading is an important problem in geology and geophysics, planetary science, and

defense. In order to address these types of problems, the failure mechanisms that occur during an impact event must be captured. Capturing these failure mechanisms requires mechanism-based models.

Most of the micromechanics models for failure under compressive loading [10–12, 14–16, 18, 19] provide for the growth of a population of cracks based on some measure of the crack tip driving force and a crack kinetics law. The models differ in how crack interactions are handled. This is typically done either through the use of a crack array (e.g. [20]) or through an effective medium approach (e.g. [46]). The distribution of cracks is important for capturing the correct scaling response of strength with strain rate[21].

As the microcracks continue to grow they will eventually intersect creating numerous fragments and the material is then reasonably described as a granular material [22]. The behavior of granular materials has been extensively studied [23]. Recent work has focused on developing models for granular materials based on explicit modeling of grain interactions using the discrete element method [24]. The granular flow contributes two key aspects to an impact event. First, as the granular material is sheared, it "bulks" and increases the pressure on the surrounding material [54]. Second it provides a mechanism for dissipating additional energy [25].

Some of the largest microcracks grow and become unstable macro-scale cracks. A number of methods have been developed to explicitly track crack fronts and crack paths, including the cohesive element method [8], and the extended finite element

method [37]. These methods are very effective for tracking a few dynamically interacting cracks; however, they become computationally expensive when many dynamically interacting cracks are considered, and some have poor scaling performance in parallel environments [38]. Techniques such as element deletion [39] can provide successful representations of regions that look like, and behave similar to, explicit cracks at lower computational cost. Alternatively, one could model cracks as damage zones where the material behavior is described by the behavior of the highly damaged material as in the Kayenta model [22] and the brittle material models by Johnson and coworkers [40–42].

In this work we develop a model for brittle material failure during impact events, such as the Edge On Impact experiments of Strassburger [55] conducted on AlON [56]. In these events the structural dimensions are typically much larger than any of the microscale features. This separation of scales necessitates the used of a homogenized damage approach because we cannot afford the computational cost of resolving the cohesive zone for the microcracks while still capturing the macroscopic loading.

Figure 4.1 shows the important physical processes that we capture with the material model presented in this work. Over the years a number of models have been developed that incorporate internal variables that are directly related to microstructural features (e.g. [10, 18, 19, 27, 29]). In all of these models, the key microstructural feature is a distribution of cracks. Although these models acknowledge the statistical nature of brittle materials, they do not explicitly incorporate the variability within

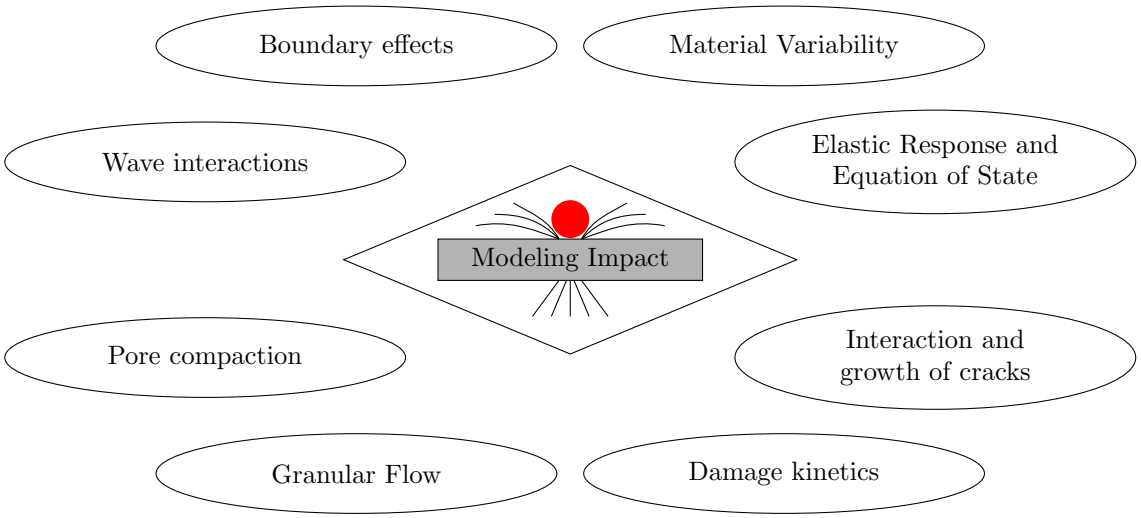

Figure 4.1: Physical processes captured in the material model

the materials from point to point [35, 36].

Variability is a key feature of brittle materials. Introducing this variability has the added benefit of stabilizing the damage problem and providing natural initiation sites for damage [34–36, 57]. Micromechanics-based damage models have the potential to introduce physically based variability into the constitutive response. Initial work has linked the physical variability observed in brittle materials to the process of sampling flaws in a material and the interactions of these flaws [33]. In this work, we present a mechanism based material model that incorporates macroscopic variability for use in high rate simulations and look at the implications of the variability for structural problems.

This chapter is organized as follows. We first discuss flaw distributions and an approach to generating realizations of flaw distributions in the context of numerical

simulations. This discussion is followed by a detailed development of the new material model. After developing the material model, we discuss the verification procedures that were used to ensure that the implementation of the model is correct. We then look at some results from the model, in two parts. We first discuss results for simple uniaxial compression simulations and determine the influence of variability and specimen size on the rate dependent strength. Finally we use the model to look at an edge on impact experiment, providing validation, and then discuss the interaction of multiple mechanisms. Finally, we consider the implications of our results.

4.2 Incorporating Flaw Distributions Into Simulations

Material variability is particularly important for simulations of brittle materials. In such materials, the defects that constitute the defect/flaw distribution include: pores, micro-cracks, and inclusions. These flaws may have both size and orientation distributions; for this work, we focus on the size distribution. Since the computational discretization is determined by the geometry and macroscopic loading conditions, it is important to consider the effects of sampling the defect population. We assume that microstructural features such as grain boundaries and grain orientations are homogenized into effective properties, which include the stiffness, fracture toughness, and crack growth laws. These effective properties are uniform through out the material.

For each material (defined by specific composition and processing, e.g. PAD Boron Carbide), there is an associated parent flaw size probability distribution $g(s)$ (defined below) and parent flaw density η; these characterize the material.

The parent flaw size probability density function ($g(s)$, where s is the flaw size) determines the probability (P) of finding a flaw of size between a lower limit s_l and an upper limit s_h through the relation:

$$P = \int_{s_l}^{s_h} g(s)ds. \tag{4.1}$$

The cumulative distribution function (CDF) for flaw size is defined as $G(s) = \int_0^s g(a)da$. Using the CDF we can rewrite the probability that a given flaw has size between flaw sizes s_l and s_h as $P(s_l \leq s < s_h) = G(s_h) - G(s_l)$. Knowing the CDF simplifies computing the fraction of a flaw distribution that lies between two limiting flaw sizes.

The parent flaw density (η) describes the expected number of flaws per unit reference volume. In a finite volume ($\hat{V}$) of material we can define a local flaw density $\hat{\eta}$ as follows. If the number of flaws in $\hat{V}$ is N_f, then we define the local flaw density $\hat{\eta} = \frac{N_f}{\hat{V}}$. In general, the local flaw density is not equal to the parent flaw density ($\hat{\eta} \neq \eta$). By creating a normalized histogram of the flaw sizes in the local flaw population, we can also calculate the local flaw distribution $\hat{g}(s)$. For sufficiently large volumes (or numbers of flaws), $\hat{\eta}$ and $\hat{g}(s)$ converge to the parent flaw density and the parent flaw distribution function.

Consider a computational discretization of the sampled volume $\hat{V}$. This discretization introduces another volume associated with the size of each discretization. We

give this discretization volume the label V_0. In general, the finite size of V_0 introduces variability in the number of flaws as discussed above.

Within each discretization volume V_0, we capture the effect of microcracks using a homogenized damage model. Our scalar damage definition is the sum, of the cubed crack sizes (s_i) over all N_f cracks in V_0 divided by V_0:

$$D = \frac{1}{V_0} \sum_{i=1}^{N_f} s_i^3. \tag{4.2}$$

When there is a large number of flaws, computing this quantity directly becomes unrealistic. To reduce the computational cost of the damage parameter, we group similar sized flaws in N_{bins} flaw families (or "bins"). Each of the N_{bins} represents the N_k flaws with sizes between s_k^l and s_k^h in the volume V_0 using the representative flaw size s_k and the family flaw density $\omega_k = \frac{N_k}{V_0}$. Using this binning approach, the damage parameter in equation (4.2) can be approximated using:

$$D = \sum_{k=1}^{N_{\text{bins}}} \omega_k s_k^3. \tag{4.3}$$

Each discretization volume within the simulation has its own local flaw distribution determined by the collection of flaw families at that location. Different discretization volumes will in general have different values for the family densities in that discretization volume.

We treat both the flaw family density and the representative flaw size for a family as statistical quantities. To simplify the discussion we introduce the notation where an over tilde ($\tilde{s}_k$) denotes a statistical quantity; an overbar ($\bar{s}_k$) denotes the

expected value of the quantity, and the quantity alone (s_k) denotes a realization of that quantity.

As an approximation for the spatial heterogeneity of the flaw distribution, we assume that the locations of flaws are independent of each other and of the flaw size, and model the spatial distribution of flaws using a Poisson process. The expected value of the family flaw density $\bar{\omega}_k$ is the parent flaw density (η) multiplied by the probability that a given flaw size is between s_k^h and s_k^l ($\bar{\omega}_k = \eta\left(G(s_k^h) - G(s_k^l)\right)$). From the assumption of a Poisson process, the statistical number of flaws in each family in V_0 becomes a Poisson distributed random variable defined by:

$$\tilde{N}_k = \text{Pois}\left[V_0 \bar{\omega_k}\right]. \tag{4.4}$$

Since the particle volume is fixed, the family flaw density $\tilde{\omega}_k$ has a distribution that depends on only the distribution of $\tilde{N}_k$.

We define s_k as the sample mean of the flaw sizes within the family resulting in $s_k = \frac{1}{N_k}\sum_{i=1}^{N_k} a_i$, where a_i are the sizes in the family (for an extended discussion of this choice see section 2.2.1.1). Each flaw size a_i within the family is a statistical quantity described by a probability function $g_k(a)$, which is related to the parent flaw distribution $g(s)$ through:

$$g_k(a) = \frac{1}{G(s_k^h) - G(s_k^l)} \begin{cases} g(a) & s_k^l \leq a < s_k^h \\ 0 & \text{otherwise} \end{cases}. \tag{4.5}$$

For large values of N_k the distribution of $\tilde{s}_k$ becomes Gaussian with the mean given

by the first moment of g_k:

$$\bar{s}_k = \int_{-\infty}^{\infty} a g_k(a) da, \tag{4.6}$$

and the variance is given by the variance of g_k divided by N_k:

$$\sigma_{s_k}^2 = \frac{\int_{-\infty}^{\infty} a^2 g_k(a) da - \bar{s}_k^2}{N_k}. \tag{4.7}$$

After discretizing the physical problem of interest, we create a realization of the flaw distribution by assigning s_k and ω_k for each family in every particle. The algorithm that we use to generate these realizations is shown in figure 4.2. By simulating the flaw family density and representative flaw family size for each family in each particle in the simulation, we generate a realization of the size and spatial distribution of flaws within the simulation volume $\hat{V}$.

To ensure a reasonable computational cost of simulating $\tilde{N}_k$ and $\tilde{s}_k$ and to avoid numerical underflow associated with generating a realization from a Poisson distribution, we introduce a cutoff number of flaws N_{cutoff}. When the expected number of flaws in family k exceeds N_{cutoff}, we use a Gaussian approximation to the Poisson distribution to generate a realization of the number of flaws in the family N_k; otherwise we directly sample a Poisson distribution using the procedure by Knuth [47, p. 132]. If N_k exceeds N_{cutoff}, we create a realization s_k using a Gaussian distribution with a mean given by equation (4.6) and variance given by equation (4.7); otherwise we explicitly simulate N_k realizations from the flaw size distribution for the k flaw family ($g_k(a)$) and set s_k equal to the sample mean of these values. Using $N_{\text{cutoff}} = 20$ provides a balance between accuracy and computational cost. In section 2.2.1, we

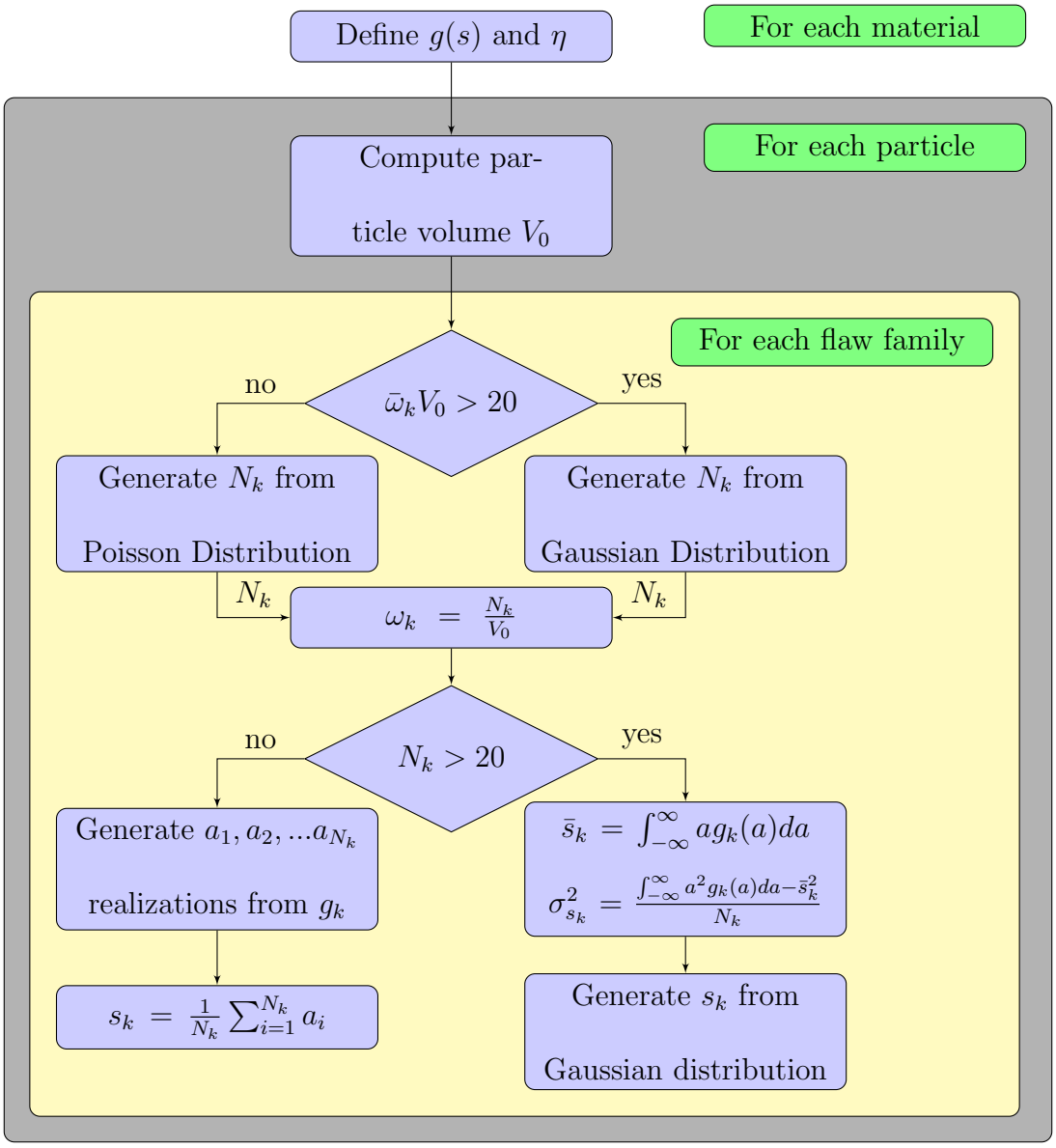

Figure 4.2: Algorithm for generating a simulated microstructural realization of flaws in a material. The material is defined by the parent flaw size distribution ($g(s)$) and parent flaw density (η) and the geometry is discretized into particles with volume V_0 for the Material Point Method. The microstructure is simulated by generating the local flaw distribution at every particle.

showed that changing N_{cutoff} does not noticeably change the simulated flaw distribution. Additionally, very large values of N_{cutoff} can cause numerical underflow issues in the algorithm for creating a realization from a Poisson distribution.

Introducing N_{cutoff} limits the computational cost (CPU time) of assigning a family density and family flaw size to each flaw family; however, there is still an incremental cost for each flaw family. The computational cost for each time step scales with the number of flaw families with a non-zero family flaw density. For most flaw distributions of interest, there is a small number of large flaws and a large number of small flaws. We bias the size of the flaw families so that they are larger for large flaws and smaller for small flaws so that for a given number of bins, the biased flaw families should give us a better representation of the flaw distribution (for a discussion of this approach see 2.2.1.1).

This algorithm (figure 4.2) takes the computational discretization and the parent flaw distribution as inputs and computes a specific realization of the distribution of flaws within the sample volume $\hat{V}$. Since each discretization volume V_0 is associated with a position $\boldsymbol{X}$, the local flaw distribution at specific locations within the sampled volume $\hat{V}$ is a function of position.

We next discuss a constitutive model accounting for the initial flaw distribution.

4.3 A Constitutive Model That Includes Flaw Distributions

We develop a model that incorporates finite deformation kinematics, thermodynamic effects through an equation of state, micromechanics based damage growth, and granular flow of the highly damaged material.

4.3.1 Kinematics

Impact events produce large deformations in the material. We choose to use the framework outlined by Simo and Ortiz [58]. We use the multiplicative split of the deformation gradient into an elastic part $\boldsymbol{F}^e$ and a plastic part $\boldsymbol{F}^{vp}$ such that $\boldsymbol{F} = \boldsymbol{F}^e\boldsymbol{F}^{vp}$, where $\boldsymbol{F}^{vp}$ represents the granular viscoplastic flow of the highly damaged material. We introduce the plastic deformation tensor $\boldsymbol{C}^{vp} = \boldsymbol{F}^{vp^T}\boldsymbol{F}^{vp}$, which is a material measure of the plastic deformation. The elastic finger tensor ($\boldsymbol{b}^{e^{-1}}$) is a spatial measure of the elastic deformation, it follows that we can write $\boldsymbol{b}^e$ in terms of material tensors as $\boldsymbol{b}^e = \boldsymbol{F}\boldsymbol{C}^{vp^{-1}}\boldsymbol{F}^T$. This identity is important when we define an objective integration procedure for the evolution of $\boldsymbol{b}^e$ with time following Simo and Ortiz [58] and discussed in chapter 3.

We also introduce a multiplicative split of the volumetric and volume preserving deformation. The volume change ratio is the Jacobian of the deformation gradient

$J = \det(\boldsymbol{F}) = \frac{\rho_0}{\rho}$. We similarly define the volume change ratio due to granular flow $J_{GP} = \det(\boldsymbol{F}^{vp})$ and the elastic volume change ratio $J^e = \det(\boldsymbol{F}^e)$. The volume preserving deformation measures ($\bar{\boldsymbol{F}}$, $\bar{\boldsymbol{F}}^e$, and $\bar{\boldsymbol{F}}^{vp}$) are obtained by dividing by the cube root of the associated Jacobian ($\bar{\boldsymbol{F}} = J^{-1/3}\boldsymbol{F}$, $\bar{\boldsymbol{F}}^e = J_e^{-1/3}\boldsymbol{F}^e$, $\bar{\boldsymbol{F}}^{vp} = J_{GP}^{-1/3}\boldsymbol{F}^{vp}$). We can then define the corresponding symmetric deformation measures $\bar{\boldsymbol{C}}$, $\bar{\boldsymbol{C}}^{vp}$, and $\bar{\boldsymbol{b}}^e$ as $\bar{\boldsymbol{C}} = J^{-2/3}\boldsymbol{F}^T\boldsymbol{F}$, $\bar{\boldsymbol{C}}^{vp} = J_{GP}^{-2/3}\boldsymbol{F}_{vp}^T\boldsymbol{F}_{vp}$, and $\bar{\boldsymbol{b}}^e = J_e^{-2/3}\boldsymbol{F}_e\boldsymbol{F}_e^T$. The total rate of deformation tensor $\boldsymbol{d}$ is the symmetric part of the spatial velocity gradient $\boldsymbol{l} = \frac{\partial \boldsymbol{v}}{\partial \boldsymbol{x}}$. We define the rate of deformation associated with the viscoplastic granular flow as $\boldsymbol{d}^{vp} = \frac{1}{2}\boldsymbol{F}^e\left[\left(\dot{\boldsymbol{F}}^{vp}\boldsymbol{F}^{vp-1}\right)^T + \dot{\boldsymbol{F}}^{vp}\boldsymbol{F}^{vp-1}\right]\boldsymbol{F}^{eT}$, and the elastic rate of deformation is then given by $\boldsymbol{d}^e = \boldsymbol{d} - \boldsymbol{d}^{vp}$. These kinematic definitions are similar to those in [58], except that our material model is not plastically incompressible so we account for the volume change associated with the plastic flow.

4.3.2 Deviatoric Elastic Response

Experimental observations suggest that materials support much larger elastic deformations resulting in a compressive volume change than elastic deformations resulting in a shape change. This difference in response leads us to adopt a similar decomposition in our constitutive relation. We divide the Kirchhoff stress ($\boldsymbol{\tau}$) into a hydrostatic portion ($-p_s J^e$) and a deviatoric portion ($\boldsymbol{\tau}_{dev}$)

$$\boldsymbol{\tau} = \boldsymbol{\tau}_{dev} - p_s J_e \boldsymbol{I}. \tag{4.8}$$

The Kirchhoff stress is related to the Cauchy stress ($\boldsymbol{\sigma}$) through the determinant of the deformation gradient $\boldsymbol{\tau} = J\boldsymbol{\sigma}$. Computing the pressure as $-\frac{1}{3}\mathrm{tr}(\boldsymbol{\sigma}) = p$ results in $p = p_s/J_{GP}$. Note that in this material model the granular flow may have some dilatation associated with it, and therefore J_{GP} is in general not equal to 1 and J_e is in general not equal to J. The volume change associated with granular plasticity J_{GP} is identical to the distension (usually given the label α) discussed by Carroll and Holt [59]. The subscript in p_s represents the pressure in the solid material if it was subjected to the volume change described by J_e.

Since there is limited information regarding the deviatoric elastic response of ceramic materials subjected to large elastic deformations, we assume a simple linear form that uses a finite deformation strain measure. This form is motivated by a generalized Neo-Hookean model where the volumetric and isochoric deformations are decoupled and reduces to the infinitesimal strain linear elastic response in the limit of infinitesimal deformation [58]. The deviatoric part of the Kirchhoff stress tensor is assumed to be a linear function of the shear modulus G and the isochoric measure of elastic deformation $\bar{\boldsymbol{b}}^e$ given by

$$\boldsymbol{\tau}_{dev} = G\left(\bar{\boldsymbol{b}}_e - \frac{1}{3}\mathrm{tr}(\bar{\boldsymbol{b}}_e)\boldsymbol{I}\right). \tag{4.9}$$

The coupling with damage is discussed after defining the volumetric response.

4.3.3 Mie-Grüneisen Equation of State

In sufficiently high velocity impact problems, the amount of energy deposited over a very short time interval is sufficient to cause the formation of shock waves in the material. Within a shock a significant amount of mechanical energy is converted into heat. In order to capture this energy dissipation pathway, we need a pressure volume relationship that is thermodynamically consistent, couples the effect of temperature and pressure, and has an increasing bulk stiffness as a function of density.

We start by assuming that the internal energy (e) associated with volume changes ($J = \frac{\rho}{\rho_0}$) can be separated into a thermal contribution e_θ and a "cold" contribution e_c, which is only a function of the volumetric deformation J:

$$e(J, \theta) = e_c(J) + e_\theta(J, \theta). \tag{4.10}$$

Following the arguments in[60, sec. 4.2] we arrive at the Grüneisen equation which relates the total pressure p to the "cold" reference pressure p_c and the temperature θ through the use of the Gruneisen parameter Γ and the specific heat at constant entropy c_η:

$$p = p_c + \rho_0 \frac{\Gamma}{J} c_\eta \theta \tag{4.11}$$

This equation could also be written in terms of the internal energy and the cold internal energy:

$$p = p_c + \rho_0 \frac{\Gamma}{J} (e - e_c) \tag{4.12}$$

A suitable reference curve is the Principal Hugoniot, which is the locus of points

that are achievable through a single shock process from ambiant conditions (room temperature and pressure). The balance of mass, momentum, and energy across the shock front relate the initial pressure (p_0), initial density (ρ_0), and initial internal energy per unit mass (e_0) to the shock speed (U_s), particle velocity (U_p), density (ρ), pressure (p), and internal energy per unit mass (e) behind the shock. These equation are referred to as the Rankine–Hugoniot shock jump conditions [60, sec. 3.4]:

$$\rho_0 U_s = \rho \left(U_s - U_p\right) \tag{4.13}$$

$$p - p_0 = \rho_0 U_s U_p \tag{4.14}$$

$$pU_p = \frac{1}{2}\rho_0 U_s U_p^2 + \rho_0 U_s (e - e_0) \tag{4.15}$$

Equation (4.13) and equation (4.14) can be combined with the volumetric deformation (J) to write the pressure on the Hugoniot as a function of J and the empirical relationship between the shock speed (U_s) and the volumetric deformation (J):

$$p_H(J) = \rho_0 \left(U_s(J)\right)^2 (1 - J) \tag{4.16}$$

These equations ((4.13), (4.14), and (4.15)) can be rearranged to write the internal energy as a function of the pressure ($p_H(J)$) and the volumetric deformation:

$$e_H(J) = \frac{p_H(J)}{2\rho_0}(1 - J) + e_0 \tag{4.17}$$

Here e_0 is the internal energy at ambiant conditions. We now apply equation (4.12) to compute the equilibrium pressure (p_+) at the Hugoniot state:

$$p_+ = p_c(J) + \rho_0 \frac{\Gamma}{J}(e_H - e_0 - e_c(J) + e_0) = p_H \tag{4.18}$$

Solving for the cold pressure (p_c) and using equation (4.17) results in:

$$p_c(J) = p_H(J)\left[1 - \frac{\Gamma}{2J}(1-J)\right] + \rho\Gamma(e_c(J) - e_0). \tag{4.19}$$

Using equation (4.19) to evaluate equation (4.12) completes the transition from a reference curve as the cold curve to a reference to the principal Hugoniot.

$$p(J,\theta) = p_H(J)\left(1 - \frac{\Gamma(J)}{2J}(1-J)\right) + \rho_0\frac{\Gamma(J)}{J}(e(J,\theta) - e_0). \tag{4.20}$$

As we stated at the beginning of this discussion, the specific internal energy (e) is composed of both a thermal energy e_θ and a cold energy e_c. Using equation (4.10) the specific heat at constant entropy c_η we rewrite the internal energy using the temperature, the cold energy, and the specific heat:

$$e(J,\theta) = e_c(J) + c_\eta(\eta)\theta. \tag{4.21}$$

We define the cold energy such that ($e_c(1) = 0$). Therefore, the reference energy e_0 is given by:

$$e_0 = c_\eta\theta_0 \tag{4.22}$$

Using equation (4.21) and (4.22) we rewrite the pressure $p(J,\theta)$ using the temperature and cold energy:

$$p(J,\theta) = p_H(J)\left(1 - \frac{\Gamma(J)}{2J}(1-J)\right) + \rho_0\frac{\Gamma(J)}{J}(e_c(J) + c_\eta(\theta - \theta_0)) \tag{4.23}$$

The cold energy, by definition, is related to the cold pressure:

$$-\rho_0\frac{de_c}{dJ} = p_c. \tag{4.24}$$

Using this equation and equation (4.19) we have a first order linear ordinary differential equation for the cold energy:

$$\frac{de_c}{dJ} + \frac{\Gamma}{J}(e_c - e_0) = \frac{-p_H}{\rho_0}\left(1 - \frac{\Gamma}{2J}(1 - J)\right) \tag{4.25}$$

This equation can be integrated once the reference pressure $p_H(J)$ and the Grüneisen parameter $\Gamma(J)$ are specified.

We note that the specific heat is only a function of the entropy ($c_\eta(\eta)$) and the Grüneisen parameter is only a function of the density ($\Gamma(\rho)$). The specific heat is a measure of the coupling between energy and temperature. The Grüneisen parameter quantifies the coupling between thermal energy (atomic vibrations) and pressure. The cold energy is the potential energy stored by the atomic bonds in the absence of atomic vibrations. This is the same measure as the strain energy except strain energy is referenced per unit volume not unit mass. Additionally at finite temperature, we normalize e_c such that $e_c(1) = 0$ which results in $e_c < 0$ when the volumetric compression is less than the thermal expansion. This shift just represents a constant factor shift, but does make it possible for there to be total strain energies in the system that are less than 0.

In order to finish specifying the equation of state, we select functional dependences for $\Gamma(J)$ and $c_\eta(\eta)$:

$$\Gamma(J) = J\Gamma_0 \tag{4.26}$$

$$c_\eta(\eta) = c_\eta = c_v \tag{4.27}$$

Here Γ_0 and c_v are empirical material constants. The choice of $\Gamma(J) = J\Gamma_0$ implies that $\Gamma\rho = \Gamma_0\rho_0$ is a constant. This choice of Γ allow us to simplify equation (4.23) to:

$$p = p_H(J)\left(1 - \frac{\Gamma_0}{2}(1-J)\right) + \rho_0\Gamma_0\left(e_c + c_\eta(\theta - \theta_0)\right). \tag{4.28}$$

Many materials are accurately represented with a linear relationship between the shock speed U_s and the particle velocity U_p. By assuming a linear relationship between the shock speed and the particle velocity, the shock speed can be written as:

$$U_s = C_0 + SU_p \tag{4.29}$$

$$U_s(J) = \frac{C_0}{1 - S(1-J)} \tag{4.30}$$

In most materials shocks do not form under hydrostatic tension ($J > 1.0$). Therefore, we assume a constant wave speed ($U_s = C_0$) in this regime. This specification of $U_s(J)$ results in a reference pressure curve given by:

$$p_H(J) = \begin{cases} \frac{\rho_0 C_0^2(1-J)}{(1-S(1-J))^2} & J < 1.0 \\ \rho_0 C_0^2(1-J) & \text{otherwise} \end{cases}. \tag{4.31}$$

Using equation (4.26), the differential equation for the cold energy (equation (4.25)) becomes:

$$\frac{de_c}{dJ} + \Gamma_0(e_c - e_0) = \frac{-p_H(J)}{\rho_0}\left(1 - \frac{\Gamma_0}{2}(1-J)\right) \tag{4.32}$$

This equation can be solved by the method of integrating factors:

$$e_c(J) = \exp(\Gamma_0(1-J))\left(c_v\left(\theta_H(J) - \theta_0\right)\right) + c_v\theta_0. \tag{4.33}$$

Rearranging this equation into a more convenient form:

$$e_c(J) = \exp(\Gamma_0(1-J))c_v\theta_H(J) + c_v\theta_0\left(1-\exp(\Gamma_0(1-J))\right) \tag{4.34}$$

We have introduced the term $\theta_H(J)$, which is an effective temperature given by:

$$c_v\theta_H(J) = \left(-\int_1^J \frac{p_H(J)}{\rho_0}\left(1-\frac{\Gamma_0}{2}(1-J)\right)\exp(-\Gamma_0(1-J))dJ\right). \tag{4.35}$$

By introducing the compressive volume strain $\epsilon_c = 1-J$ with $dJ' = -d\epsilon_c'$ we write this equation in the more compact form:

$$c_v\theta_H(J) = \int_0^{\epsilon_c} \exp\left(-\Gamma_0\epsilon_c'\right)\left[\frac{p_H}{\rho_0}\left(1-\frac{1}{2}\Gamma_0\epsilon_c'\right)\right]d\epsilon_c' \tag{4.36}$$

Under compression this integral must be evaluated numerically, but under tension ($\epsilon_c < 0$) the cold energy (e_c) is:

$$e_c(\epsilon_c \leq 0) = C_0^2\epsilon_c^2 + c_v\theta_0(1-\exp(\Gamma_0\epsilon_c)) \tag{4.37}$$

Once the cold energy is known the pressure at a given temperature and volumetric compression is given by equation (4.28) and equation (4.21):

$$p(J,\theta) = p_H(J)\left[1-\frac{\Gamma_0}{2}(1-J)\right] + \rho_0\Gamma_0\left[e_c(J) + c_\eta(\theta-\theta_0)\right] \tag{4.38}$$

In the computational scheme that we use, we do not track the discontinuity that is caused by shock waves and explicitly solve the Rankine-Hugoniot relations across the shock front. Instead, we treat all elastic deformations as isentropic processes. Since pressure and temperature are coupled through the Grüneisen parameter, isentropic changes in volume result in a change in temperature. In coupled thermo-mechanical

problems, it is common to split the solution procedure into an isentropic mechanical step followed by a heat conduction step under fixed mechanical conditions [61]. Since we are interested in short time evolutions, we assume adiabatic conditions and skip the heat transfer calculation. The heating rate ($\dot{\theta}_{ent}$) associated with the adiabatic and isentropic elastic rate of deformation is:

$$\dot{\theta}_{ent} = \frac{-\theta \Gamma_0 \rho_0}{\rho} \mathrm{tr}(\boldsymbol{d}^e). \tag{4.39}$$

The temperature reached through a shock process is not the same as the temperature reached through an isentropic and adiabatic compression. The shock process is a dissipative non-equilibrium process. Although we do not track shock fronts in the computational scheme we can capture the dissipative nature of shocks by introducing an "artificial" bulk viscosity. We implement this viscosity by introducing an additional viscous pressure p_{visc} that is activated under volumetric compression and provides an additional dissipation mechanism. We a use common form for the artificial viscosity based on the form proposed by VonNeumann and Richtmyer [62]:

$$p_{visc} = \begin{cases} (A_1 C_0 |\mathrm{tr}(\boldsymbol{d}_e)| dx + A_2 \mathrm{tr}(\boldsymbol{d}_e)^2 dx^2)\, \rho & \mathrm{tr}(\boldsymbol{d}_e) \leq 0 \\ 0 & \text{otherwise} \end{cases}. \tag{4.40}$$

Here dx is the average edge length for the cell, and the parameters $A_1 = 0.4$ and $A_2 = 4.0$ were chosen to smooth the shock front over several cells and eliminate oscillations behind the shock. These viscosity parameters smooth the shock over about 9 computational cells. We assume that all of the energy dissipated by the artificial viscosity is converted into heat. The temperature rise associated with the

viscous heating is

$$\dot{\theta}_{visc} = \frac{-Jp_{visc}\mathrm{tr}(\boldsymbol{d})}{\rho_0 c_v} \tag{4.41}$$

The coupling between the elastic behavior and damage are discussed in the next section as part of the micromechanics model discussion.

4.3.4 Micromechanics of Dynamic Fracture

We begin by extending the work of Grechka and Kachanov [63] to account for a flaw orientation distribution function and the effect of interacting microcracks. We then discuss the model for dynamic damage growth, which takes into account crack dynamics.

The elastic response discussed in the previous section assumes an isotropic material behavior. However, at the micromechanics scale we must address the induced anisotropy associated with the cooperative growth of microcracks. Schematically, this is shown in figure 4.3. The macroscale potato is treated as an isotropic medium while the microscale calculation utilizes the local stress state to define the orientation of the micromechanics calculation. The computational discretization occurs at the macroscale in a three dimensional continuum. At each material point, we compute the damage evolution using a micromechanics based damage model. This damage model computes the effective interaction of the surrounding cracks using an ellipse imbedded within an effective matrix. In three dimensions the crack would be embedded in an ellipsoid instead of an ellipse. However, we only have an analytic

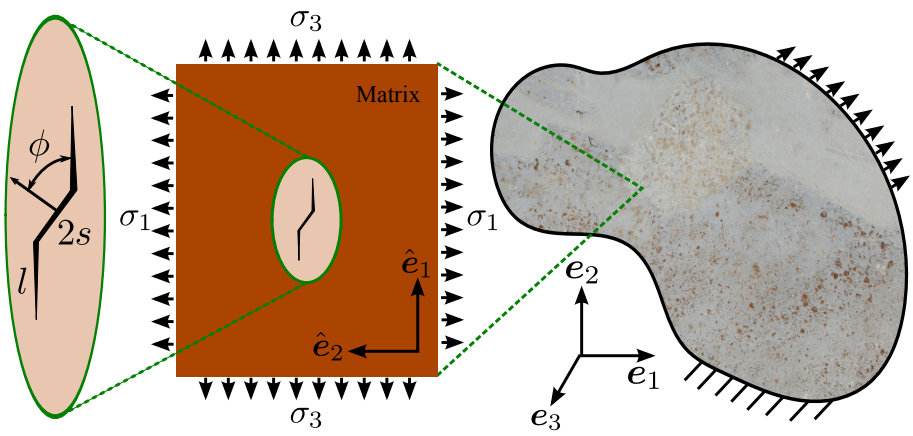

Figure 4.3: Multi-Scale approach including the wing crack geometry for the self consistent calculation. The boundary loads (σ_1 and σ_3) bridge from the macroscale to the microscale. The crack length l bridges back to the macroscale through the damage parameter D. The IBV problem is discretized at the macroscale. At this scale we assume an isotropic response and apply the granular flow and pore compaction models. The effective medium at the microscale is treated as an anisotropic material to develop tension along $\hat{\boldsymbol{e}}_2$ in response to tension along $\hat{\boldsymbol{e}}_1$

solution for the two dimensional micromechanics problem, and so we do not address the complicated three dimensional wing cracking process. For the micromechanics calculation we assume plane strain conditions and pick the two extreme (maximum and minimum) principal stresses as boundary conditions, thus providing a local two dimensional approximation.

The presence of cracks increases the elastic compliance of the system by introducing an additional strain, which is proportional to the applied stress. Grechka and Kachanov demonstrate that the strain energy density associated with a population of cracks within a representative volume V_0 can be written as:

$$f = \frac{1}{2}\boldsymbol{\tau} : \mathbb{S}_0 : \boldsymbol{\tau} + \boldsymbol{\tau} : \frac{1}{2V_0} \sum_{i}^{N_{cracks}} (\boldsymbol{n} \otimes \boldsymbol{Z} \otimes \boldsymbol{n} A)^{(i)} : \boldsymbol{\tau}. \tag{4.42}$$

Here $\mathbb{S}_0$ is the fourth order compliance tensor of the undamaged material, and $\boldsymbol{n}_i$, $\boldsymbol{Z}_i$, and A_i are the unit normal, crack compliance and area of each individual crack. For penny shaped cracks the radial and transverse directions are the same, so the crack compliance can be written in terms of the crack normal and the identity tensor $\boldsymbol{I}$ as:

$$\boldsymbol{Z} = \frac{a}{\pi} \left(Z_r \boldsymbol{I} - (Z_r - Z_n) \boldsymbol{n} \otimes \boldsymbol{n} \right). \tag{4.43}$$

Here Z_r and Z_n are the compliances in the normal and radial directions normalized by $\frac{a}{\pi}$[63]:

$$Z_r = \frac{16(1-\nu_0^2)}{3E_0(1-\frac{\nu_0}{2})} \qquad\qquad Z_n = \frac{16(1-\nu_0^2)}{3E_0}. \tag{4.44}$$

When this strain energy (eq. (4.42)) is used to derive the compliance of the effective medium surrounding the ellipse, a transverse compression results from an applied axial

compression. Under such conditions the driving force on the crack tip decreases with increasing crack length. However, experiments [64] show that as the level of damage grows, interactions between the cracks lead to an acceleration of the damage rate. In addition to an accelerated damage growth rate, brittle materials exhibit a bulking behavior when loaded in compression. We account for both effects by introducing an additional term into the strain energy density function of equation (4.42):

$$f = \frac{1}{2}\boldsymbol{\tau} : \mathbb{S}_0 : \boldsymbol{\tau} + \boldsymbol{\tau} : \frac{1}{2V_0} \sum_{i}^{N_{cracks}} (\boldsymbol{n} \otimes \boldsymbol{Z} \otimes \boldsymbol{n}A)^{(i)} : \boldsymbol{\tau} + \\ \boldsymbol{\tau} : \frac{1}{2V_0} \sum_{i}^{N_{cracks}} \frac{Z_c a_i A_i}{\pi} (\boldsymbol{n} \otimes \boldsymbol{n} \otimes \boldsymbol{I} + \boldsymbol{I} \otimes \boldsymbol{n} \otimes \boldsymbol{n} - 2\boldsymbol{n} \otimes \boldsymbol{n} \otimes \boldsymbol{n} \otimes \boldsymbol{n})^{(i)} : \boldsymbol{\tau}. \quad (4.45)$$

The form for this term is based on the representation for a transversely isotropic fourth order tensor[65]. This additional fourth order tensor provides a way to introduce a Poisson-like effect. The parameter Z_c controls the strength of this coupling between loading normal to the crack face and transverse to it.

Remembering the scalar damage parameter D, we note that $D = 0.125$ when the flaws have grown so that on average a is equal to half of the average spacing between flaws for a delta distribution of flaw sizes. When the cracks have grown so that a is equal to the average spacing between flaws, $D = 1$. In this model, all positive values of D are mathematically permitted, however at some value of D between 0.125 and 1.0 the cracks will strongly interact resulting in fragmentation of the material and a transition to granular flow. We choose $D = 0.125$ as the critical condition for the onset of granular flow, and when damage equals 1.0 we stop computing additional

damage growth. Physically this choice means that we allow continued fracture within the grains in the granular plasticity model for damage values between 0.125 and 1.0. However when damage reaches 1.0 we assume that there is no further cracking of the grains (and thus no further softening of the elastic moduli). The details of the granular flow model are discussed in the next section.

In general, there is a distribution of flaw orientations that can be characterized by the flaw orientation distribution function $\rho(\boldsymbol{n})$. Using the damage and the orientation distribution function we can rewrite the strain energy density as an integral over all possible flaw orientations ($\boldsymbol{n}$) as:

$$\begin{aligned} f = \frac{1}{2}\boldsymbol{\tau} : \mathbb{S}_0 : \boldsymbol{\tau} + \frac{D}{2}\frac{1}{4\pi}\iint_{\omega} \rho(\boldsymbol{n}) \Big(& Z_r \boldsymbol{\tau}\cdot\boldsymbol{\tau} : \boldsymbol{n}\otimes\boldsymbol{n} \\ & - (Z_r - Z_n)\boldsymbol{\tau} : \boldsymbol{n}\otimes\boldsymbol{n}\otimes\boldsymbol{n}\otimes\boldsymbol{n} : \boldsymbol{\tau} \\ & + Z_c \boldsymbol{\tau} : (\boldsymbol{n}\otimes\boldsymbol{n}\otimes\boldsymbol{I} + \boldsymbol{I}\otimes\boldsymbol{n}\otimes\boldsymbol{n} - 2\boldsymbol{n}\otimes\boldsymbol{n}\otimes\boldsymbol{n}\otimes\boldsymbol{n}) : \boldsymbol{\tau} \Big) d\omega \end{aligned} \tag{4.46}$$

This integral places all of the orientation information in the orientation distribution function ($\rho(\boldsymbol{n})$), and all of the flaw size and density information in D. We now define an equivalent isotropic strain energy function f_{iso} by evaluating equation (4.46) with $\rho(\boldsymbol{n}) = \rho_{iso}(\boldsymbol{n}) = 1$. The details of the integration are presented in A.1 with the final result:

$$\begin{aligned} f_{iso} = & \left(\frac{1+\nu_0}{2E_0} + \frac{D}{30}\left(3Z_r + 2Z_n - 4Z_c\right) \right) \boldsymbol{\tau} : \boldsymbol{\tau} \\ & - \left(\frac{\nu_0}{2E_0} + \frac{D}{30}\left(Z_r - Z_n - 8Z_c\right) \right) \left(\mathrm{tr}(\boldsymbol{\tau})\right)^2 . \end{aligned} \tag{4.47}$$

This equivalent strain energy density function is now used at the discretization scale.

Although we need to use the anisotropic effective medium in order to compute the crack growth in the micromechanics model, the only information that we use at the discretization scale is the resulting scalar damage parameter. Thus the elastic response at the discretization scale only needs to be isotropic and we use f_{iso} at this scale.

In this framework, therefore, the compliance at the micromechanics scale and at the computational discretization scale are derived from the same form of the strain energy function, but make different assumptions about the effective local distribution of flaw orientations. Using these two different assumptions can introduce errors when the elastic anisotropy of the problem is important, but is an acceptable approximation in other cases. The loading conditions where the elastic anisotropy may be important are conditions where:

- there are many aligned families of cracks (gas and oil exploration),
- there is a single or only a few dominant cracks that grow through cleavage,
- or cases where the highly damaged but not fully damaged state under proportional loading is of interest (e.g. interrupted quasistatic compression tests).

Under conditions more applicable to impact problems where the failure process occurs rapidly, and the principal stresses will tend to rotate (complex loading histories) we expect a very wide distribution of crack orientations and therefore the approximation of an isotropic distribution of flaws at the computational discretization scale may be

reasonable. Accepting the limitations introduced by this approximation, we leave the issue of handling the fully anisotropic problem to future work.

From this isotropic strain energy density function (equation (4.47)) we compute an effective bulk modulus $K(D)$:

$$K(D) = \left(K_0^{-1} + D\left(Z_n + 4Z_c\right)\right)^{-1} \tag{4.48}$$

and an effective shear modulus $G(D)$:

$$G(D) = \left(G_0^{-1} + \frac{2D}{15}\left(3Z_r + 2Z_n - 4Z_c\right)\right)^{-1}. \tag{4.49}$$

Since we are using a Mie-Grüneisen equation of state for the hydrostatic response of the material, we scale the pressure computed using equation (4.12) by the ratio of the damaged bulk modulus ($K(D)$) to the undamaged bulk modulus (K_0). This gives us a pressure in the solid material defined by:

$$p_s(J^e, \theta, D) = \frac{K(D)}{K_0}\left(p_H(J^e)\left[1 - \frac{\Gamma_0}{2}\left(1 - J^e\right)\right]\right.$$
$$\left. + \rho_0\Gamma_0\left[e_c(J^e) + c_\eta(\theta - \theta_0)\right]\right) \tag{4.50}$$

A sufficient condition to insure that damage growth $\dot{D}$ causes non-negative energy dissipation, is that the rate of change of the shear and bulk moduli with damage are less than or equal to zero ($\frac{\partial K}{\partial D} \leq 0$ and $\frac{\partial G}{\partial D} \leq 0$). Applying this condition results in the following constraint on the coefficient of the interaction term in equation (4.46):

$$-Z_n \leq 4Z_c \leq 3Z_r + 2Z_n \tag{4.51}$$

For $Z_c < 0$ the interactions between flaws cause a transverse tension as a result of an applied axial compressive stress. This transverse tension accelerates the damage growth rate and is consistent with experimental observations[64]. However, at the limit where the tensile interactions are maximized ($Z_c = -\frac{Z_n}{4}$), the bulk modulus is independent of damage. In tension, it does not make physical sense for the bulk modulus of a damaged material to be independent of damage; therefore, we choose an interaction term that gives the expected interactions, while maintaining some softening of the bulk modulus:

$$Z_c = \frac{-Z_n}{8} \tag{4.52}$$

This choice of Z_c results in an effective Poisson's ratio that decreases only slightly with damage.

At the microscale, we are solving a self consistent problem using an effective medium approach as shown in figure 4.3. We select the local coordinate system such that the most compressive principal stress is aligned with $\hat{\boldsymbol{e}}_1$ and the most tensile principal stress is aligned with $\hat{\boldsymbol{e}}_2$. For wing crack growth, the crack face normals are given by $\boldsymbol{n} = \hat{\boldsymbol{e}}_2$. The equivalent orientation density function is a delta function centered at $\boldsymbol{n} = \hat{\boldsymbol{e}}_2$ multiplied by 4π. The resulting strain energy density function in the effective medium (f_{aniso}) is given by:

$$\begin{aligned} f_{aniso} = \frac{1}{2}\boldsymbol{\tau} : \mathbb{S}_0 : \boldsymbol{\tau} + \frac{D}{2}\left(Z_r \boldsymbol{\tau}\cdot\boldsymbol{\tau} : \hat{\boldsymbol{e}}_2 \otimes \hat{\boldsymbol{e}}_2 - (Z_r - Z_n)\boldsymbol{\tau} : \hat{\boldsymbol{e}}_2 \otimes \hat{\boldsymbol{e}}_2 \otimes \hat{\boldsymbol{e}}_2 \otimes \hat{\boldsymbol{e}}_2 : \boldsymbol{\tau}\right) \\ + \frac{DZ_c}{2}\boldsymbol{\tau} : (\hat{\boldsymbol{e}}_2 \otimes \hat{\boldsymbol{e}}_2 \otimes \boldsymbol{I} + \boldsymbol{I} \otimes \hat{\boldsymbol{e}}_2 \otimes \hat{\boldsymbol{e}}_2 - 2\hat{\boldsymbol{e}}_2 \otimes \hat{\boldsymbol{e}}_2 \otimes \hat{\boldsymbol{e}}_2 \otimes \hat{\boldsymbol{e}}_2) : \boldsymbol{\tau} \end{aligned} \tag{4.53}$$

The anisotropic compliance matrix associated with the strain energy function f_{aniso} is given by:

$$\mathbb{S}_{aniso} = \mathbb{S}_0 + \Delta\mathbb{S}^{NIA}(D) + \Delta\mathbb{S}^{INT}(D) \tag{4.54}$$

Here the first term is the isotropic compliance of the base material, $\Delta\mathbb{S}^{NIA}$ is the additional compliance computed from the non-interacting assumption in Grechka and Kachanov [63], and $\Delta\mathbb{S}^{INT}$ is the additional compliance term associated with the crack interactions. The isotropic compliance tensor written in terms of the Poisson's ratio and the Young's modulus is $\mathbb{S}_0 = \frac{1+\nu_0}{E_0}\mathbb{I}_s - \frac{\nu_0}{E_0}\boldsymbol{I}\otimes\boldsymbol{I}$. From Grechka and Kachanov [63] the additional compliance associated with the non-interacting assumption is:

$$\Delta\mathbb{S}^{NIA}_{ijlm} = \frac{8(1-\nu_0^2)}{3E_0(2-\nu_0)}\left(\alpha^p_{il}\delta_{jm} + \alpha^p_{im}\delta_{jl} + \alpha^p_{jl}\delta_{im} + \alpha^p_{jm}\delta_{il} + 4\beta^p_{ijml}\right). \tag{4.55}$$

Here the second order tensor $\boldsymbol{\alpha}^p$ and the fourth order tensor $\boldsymbol{\beta}^p$ are given by $\boldsymbol{\alpha}^p = D\hat{\boldsymbol{e}}_2\otimes\hat{\boldsymbol{e}}_2$ and $\boldsymbol{\beta}^p = -\frac{\nu_0}{2}D\hat{\boldsymbol{e}}_2\otimes\hat{\boldsymbol{e}}_2\otimes\hat{\boldsymbol{e}}_2\otimes\hat{\boldsymbol{e}}_2$. The interaction term is:

$$\Delta\mathbb{S}^{INT} = \frac{-2(1-\nu_0^2)}{3E_0}D\left(\hat{\boldsymbol{e}}_2\otimes\hat{\boldsymbol{e}}_2\otimes\boldsymbol{I} + \boldsymbol{I}\otimes\hat{\boldsymbol{e}}_2\otimes\hat{\boldsymbol{e}}_2 - 2\hat{\boldsymbol{e}}_2\otimes\hat{\boldsymbol{e}}_2\otimes\hat{\boldsymbol{e}}_2\otimes\hat{\boldsymbol{e}}_2\right). \tag{4.56}$$

We use a revision due to Liu et al. [1] of the Paliwal and Ramesh [10] damage model to compute the evolution of the damage variable D. The corresponding corrected self consistent method solution is presented by Liu et al. in an erratum to [10]. For completeness we summarize the important features of the micromechanics growth model next.

The self consistent problem can be solved analytically, as discussed in the erratum to Paliwal and Ramesh [10] and provided for reference in A.2, for the stress inside the

ellipse $\boldsymbol{\sigma}^e$. This effective stress provides the local loading environment for potential crack activation and growth. The local stress is resolved into tractions normal and tangent to crack faces. Since the frictional contact forces can only resist a finite shear traction across the crack faces, the excess traction is converted into a wedging force (F_w). This wedging force depends on the initial crack length (s), the angle (ϕ) between the crack face normal and the compression direction $\hat{\boldsymbol{e}}_1$, and the crack face coefficient of friction (μ). As discussed by Paliwal and Ramesh [10], the wedging force is given by:

$$F_w = 2s\left[\mu\left(\sigma_{11}^e\cos^2(\phi) + \sigma_{22}^e\sin^2(\phi) + \sigma_{12}^e\sin(2\phi)\right) - \left(\frac{1}{2}\left(\sigma_{11}^e - \sigma_{22}^e\right)\sin(2\phi) - \sigma_{12}^e\cos(2\phi)\right)\right] \quad (4.57)$$

The combination of the wedging force and the direct contribution from σ_{22}^e results in an effective stress intensity factor at the wing crack tip given by

$$K_I = \frac{F_w}{\sqrt{\pi(l+0.27s)}} + \sigma_{22}^e\sqrt{\pi(l+\sin(\phi)s)}. \quad (4.58)$$

When the local stress intensity factor (K_I) exceeds the microscale fracture toughness (K_{IC}), crack growth begins. Since we are particularly interested in capturing the competition between a low density of large flaws and a high density of small flaws, we require a crack growth law that captures the dynamic effects related to a moving crack tip. A suitable crack growth law was developed by Freund [66]. In this model, the crack tip velocity ($\dot{l}$) asymptotically approaches the maximum crack growth velocity, which is an experimentally determined fraction of the Rayleigh wave speed ($\frac{C_r}{\alpha_c}$), as

the stress intensity factor increases. An additional empirical fitting parameter γ_c is added to control the rate that the crack growth velocity approaches its maximum value. The crack growth law is:

$$\dot{l} = \frac{C_r}{\alpha_c} \left(\frac{K_I - K_{IC}}{K_I - 0.5 K_{IC}} \right)^{\gamma_c}. \tag{4.59}$$

The dimensionless constants α_c and γ_c can be determined experimentally by measuring the crack velocity as a function of the applied stress intensity factor. By adopting this crack growth law we are applying a macroscopic crack growth relationship in a micromechanics model. This application assumes that the microscale environment around the cracks can be treated as a continuum and that the Rayleigh wave speed and fracture toughness are well defined at this scale. These are reasonable assumptions; however, additional experimental measurements of the microscale fracture toughness of materials could help improve this model. We assume that the microscale fracture toughness is similar to the macroscale fracture toughness and discard microstructural details such as the variation in fracture toughness between cleavage planes and grain boundaries.

In addition to a three dimensional stress state, we address the case where crack faces separate and resulting in tensile crack growth by requiring a non-negative wedging force ($F_w \geq 0$). As a result of this limitation we recover $K_I = \sigma_{22}^e \sqrt{\pi(l + \sin(\phi)s)}$ under appropriate conditions, which is consistent with the stress intensity factor for a crack in a large plate under tension.

From Paliwal et al. [67], we identify the fracture toughness, quasistatic and dy-

namic strength of AlON, the material used in the Edge-On-Impact experiments by Strassburger et al. that we simulate later in the paper. We select a fracture toughness of 2.9 MPa $m^{1/2}$ [67]. We assume that the crack face friction coefficient is similar to contact friction in well rounded granular materials which have a friction angle of close to 30°. This translates into a coefficient of friction of 0.57 which has a most damaging crack orientation of $\phi = 60°$.

We assume that the flaw distribution ($g(s)$) is a bounded Pareto distribution which has the form:

$$g(s) = \frac{\alpha s_{\min}^{\alpha} s^{-(\alpha+1)}}{1 - \left(\frac{s_{\min}}{s_{\max}}\right)^{\alpha}}. \tag{4.60}$$

An exponent of $\alpha = 3$ gives self-similar flaw scaling where, in three dimensions, the average distance between flaws longer than a specified size (a) scales linearly with a. Since we are looking at dynamic failure, we calibrated our material model using a dynamic strength under uniaxial compression of 3.5 GPa at a strain rate of 10^3 s^{-1}. A flaw size range from $s_{\min} = 2\mu$m to $s_{\max} = 40\mu$m with a flaw density of $4 \times 10^{12} m^{-3}$ fits the dynamic compressive strength of AlON. This flaw distribution is equivalent to an average spacing of 63 μm between flaws that are at least 2 μm in size.

Paliwal et al. [64] observed some carbonaceous defects on the surfaces of fragments *post mortem*. It is likely that in typical AlON samples there are a small number of large flaws, which could also fit the compressive strength data. However, in our model the flaw density introduces a lower bound on the mesh size that is reasonable given our homogenization approach. A reasonable lower bound is the mesh size that

corresponds to an average of 8 flaws per discretization volume. For this flaw density that lower bound is close to 125 μm. The structural problems that we are interested in solving have a minimum spatial dimension of 10 mm. It is reasonable to expect that meshes in the sub-millimeter size range are required to capture the dynamics in the problem. Considering these constraints, we recognize that these parameters represent an AlON-like material and probably do not reflect the behavior of commercial AlON, where many other deformation and failure mechanisms are likely active.

4.3.5 Granular Plasticity

A number of researchers have investigated the dynamic strength of fragmented and granular materials under high confining pressure and dynamic loading [3, 68–72]. In these experiments a linear relationship between pressure and shear strength was observed up to pressures in excess of 1 GPa. Deviations from linearity are often attributed to the activation of additional deformation mechanisms (e.g. plasticity within the grains). In this work, we are not driving the material into the extreme compression regime and therefore assume that the deviatoric strength of the granular material is linearly dependent on the hydrostatic pressure. We assume the existence of a yield surface defined by $f(\boldsymbol{\tau}) = 0$, which defines the onset of plastic flow. We use the common Drucker-Prager yield surface where the deviatoric strength increases

linearly with pressure resulting in a yield function defined by:

$$f(\boldsymbol{\tau}) = \sqrt{\boldsymbol{\tau}_{dev} : \boldsymbol{\tau}_{dev}} - Y + A\left(\frac{\mathrm{tr}(\boldsymbol{\tau})}{\sqrt{3}} - B\right). \tag{4.61}$$

Here the parameter B represents the cohesive forces between grains and provides a hydrostatic tensile limit, the parameter A represents the magnitude of the coupling between the hydrostatic and deviatoric components, and the deviatoric yield stress Y represents the deviatoric strength when the hydrostatic term is equal to 0. We use the parameters $A = 0.6$, $B = 0.1$ MPa, and $Y = 0$ based on confined dynamic compression experiments on dry sand [72].

Granular flow involves the rearrangement of a collection of grains within a representative material volume. Since this rearrangement generally takes some amount of time, we model the granular flow as a viscoplastic process. We decompose the tensorial viscoplastic rate of deformation ($\boldsymbol{d}^{vp}$) into a scalar viscoplastic flow rate ($\dot{\lambda}$) and a flow direction ($\boldsymbol{m}$):

$$\boldsymbol{d}^{vp} = \dot{\lambda}\boldsymbol{m} \tag{4.62}$$

Assuming that the granular flow is associative to the yield surface $f = 0$ results in a granular flow direction given by $\boldsymbol{m} = \frac{\partial f}{\partial \boldsymbol{\tau}}$. Evaluating the derivative $\frac{\partial f(\boldsymbol{\tau})}{\partial \boldsymbol{\tau}}$ gives:

$$\frac{\partial f(\boldsymbol{\tau})}{\partial \boldsymbol{\tau}} = \frac{\boldsymbol{\tau}_{dev}}{\sqrt{\boldsymbol{\tau}_{dev} : \boldsymbol{\tau}_{dev}}} + \frac{A}{\sqrt{3}}\boldsymbol{I}. \tag{4.63}$$

Introducing the deviatoric unit tensor $\boldsymbol{n} = \frac{\boldsymbol{\tau}_{dev}}{\|\boldsymbol{\tau}_{dev}\|}$, and the hydrostatic unit tensor $\hat{\boldsymbol{I}} = \frac{1}{\sqrt{3}}\boldsymbol{I}$, the direction of plastic flow can be written as

$$\boldsymbol{m} = \boldsymbol{n} + A\hat{\boldsymbol{I}}. \tag{4.64}$$

The ratio of the bulking deformation to the shear deformation is A, consistent with our assumption of associative flow. For computational simplicity and to ensure that we always have positive plastic dissipation in the presence of non-linear effective moduli we define an effective strain direction $\boldsymbol{m}_{eff}$ using:

$$\boldsymbol{m}_{\text{eff}} = \begin{cases} \boldsymbol{n} + \zeta A\hat{\boldsymbol{I}} & \text{tr}\left(\boldsymbol{\tau}\right) < 0 \\ \boldsymbol{n} + A\hat{\boldsymbol{I}} & \text{otherwise} \end{cases} . \tag{4.65}$$

The original return direction $\boldsymbol{m}$ is used for all of the projections and to compute the effective strain rate discussed below. The parameter ζ starts as 1.0 and is iteratively reduced by multiplication with 0.9 if the computed plastic dissipation is less than zero. The plastic dissipation is computed by subtracting the strain energy in the final state (i.e. $\bar{b}^e n+1$, J^{GP}_{n+1}, J_{n+1}) from the strain energy in the trial state (i.e. $\bar{b}^e tr$, J^{GP}_{n}, J_{n+1}) plus the thermal energy required to move along an isentropic path from J^{GP}_{n} to J^{GP}_{n+1} at constant J. This thermal term is only non-zero when using an equation of state like the Mie-Grüneisen that couples the mechanical deformation to the temperature. We require this extra step in the solution procedure to ensure non-negative plastic work because most algorithms for pressure dependent plasticity assume an additive decomposition of the strain rate and assume that the stiffness is constant during a time step. Since our problem may violate either of these assumptions, we use the return algorithm for Drucker-Prager plasticity discussed in [73] to provide an initial estimate of the return state then use the iterative procedure described above to ensure that there is non-negative plastic dissipation. This numerical adjustment will reduce

effective pressure durring granular flow, which could result in more deviatoric granular flow and less bulking than if the actual return direction was used. However, this approach is still more consistent than the approach used in [42] where they use the pressure from the previous time step to set the deviatoric strength in the current time step. Future work will include updating to a fully non-linear solver for the stress projection that can account for the non-linear material behavior during a time step.

The influence of the rate of deformation on granular flow can be examined in a variety of ways. One appealing concept is based on the argument that the arrangement of particles within a granular medium requires some time to reach the lowest energy configuration corresponding to a particular deformation. A representative volume of the granular material will then require a specific stress $\hat{\boldsymbol{\tau}}$ to be deformed at an extremely low "quasistatic" rate of deformation so that the particles are able to achieve the lowest energy configuration. However, when the same original representative volume element is taken to the same deformation state at a higher rate of deformation, the particles are unable to reach their lowest energy configuration in the time available, and so the stress $\boldsymbol{\tau}$ required to achieve that deformation state is higher. The difference between the stress required at high strain rates and that for quasistatic deformations is defined as the overstress $\bar{\boldsymbol{\tau}} = \boldsymbol{\tau} - \hat{\boldsymbol{\tau}}$.

We expect that the rate of viscoplastic flow $\dot{\lambda}$ should be a scalar function of the overstress $\bar{\boldsymbol{\tau}}$ and a material timescale τ_{GP}. Since the overstress contains both a deviatoric and hydrostatic component, the three standard invariants of $\bar{\boldsymbol{\tau}}$ are not good

scalar measures of the energetic driving force for rearranging the particles. Instead, we define a strain-like scalar quantity $\bar{\mu}$, which measures the magnitude of the elastic strain associated with $\bar{\boldsymbol{\tau}}$ along the direction $\boldsymbol{m}$

$$\bar{\mu}\boldsymbol{m} = \mathbb{C}^{-1} : \bar{\boldsymbol{\tau}}. \tag{4.66}$$

We now write the flow rate using the material timescale τ_{GP} and $\bar{\mu}$ as:

$$\dot{\lambda} = \frac{\bar{\mu}}{\tau_{GP}}. \tag{4.67}$$

The timescale τ_{GP} is essentially a material characteristic timescale defining the time needed for the particles in the RVE of the granular material to relax from the configuration developed at the high rate of loading to the ground state configuration corresponding to quasistatic deformations. Such a material timescale has been defined in the past for granular materials within dynamic loading by Curran et al. [74], who defined this time from a microscale viewpoint in terms of the average particle size, the packing density, and the shear wave speed (i.e., the timescale arises because of the time needed to communicate across a particle or block within the granular medium). Based on the flaw distribution that we selected the average flaw spacing ($\eta^{-\frac{1}{3}}$) is 63 μm. A shear wave traverses this distance in just over 10 ns while a longitudinal wave takes just over 6 ns. In our simulations, we use a timescale for granular flow that is 7 ns ($\tau_{GP} = 7$ ns).

From the definition of the overstress $\bar{\boldsymbol{\tau}}$ it follows that $\hat{\boldsymbol{\tau}} = \boldsymbol{\tau} - \bar{\boldsymbol{\tau}}$. Further, at yield, we must have $f(\hat{\boldsymbol{\tau}}) = 0$. From this condition and equation (4.66), it follows

that the overstress $\bar{\boldsymbol{\tau}}$ must satisfy the relation $f(\boldsymbol{\tau} - \bar{\boldsymbol{\tau}}) = 0$. We note that the magnitude of the viscoplastic flow rate $\dot{\lambda}$ can now be computed from the condition that $f(\boldsymbol{\tau} - \bar{\boldsymbol{\tau}}) = f(\boldsymbol{\tau} - \mathbb{C} : (\bar{\mu}\boldsymbol{m})) = 0$ once the characteristic timescale τ_{GP} has been defined. For simplicity we treat this characteristic timescale as a constant which is related to the initial flaw density in the material and the shear wave speed, but it is a straight forward extension of the model to make τ_{GP} a function of the dilatation and total equivalent granular plastic strain.

4.3.6 Pore Collapse Model

Our granular plasticity formulation introduces dilatation through the interaction of grains as a result of shear deformation. However, under high confining pressures, we expect a reduction in the porosity. Experimentally, the relationship between the distension J^{GP} and the applied pressure ($P = -\frac{1}{3}\text{tr}(\boldsymbol{\sigma})$) is expressed through the crush curve for a given material. For simplicity we choose a primitive crush curve defined by $J^{GP} = 1 + (J_0^{GP} - 1)J^2 \left(\frac{P_c - P}{P_c - P_0}\right)^2$. The material parameter P_0 represents the pressure when inelastic compaction of the porous medium begins for an initial distension of J_0^{GP}, and P_c represents the pressure required for full densification. We select a reference crush pressure (P_0) of 1GPa with a reference distension (J_0^{GP}) of 2.0 and assume that full densification (P_c) occurs at a pressure of 10 GPa. Although these numbers are not based on experimental data, they are reasonable because typical porosities of ceramics prior to sintering are about 50 percent and typical manufactur-

ing pressures (up to a couple hundred MPa) do not significantly reduce this porosity (R. Haber personal communication).

Since our material model can develop a distension greater than J_0^{GP} prior to loading in compression, we require that the crush curve is defined for all values of distension. We extend the crush curve beyond the inelastic compaction limit by assuming an exponential relationship between the distension and the crush pressure ($P_\alpha = P_0 \exp\left(-\kappa(J^{GP} - J_0^{GP})\right)$). The crush pressure should be a smooth function of the distension requiring $\kappa = \frac{P_c - P_0}{2P_0(J_0^{GP}-1)}$. Writing the crush curve as a yield surface results in:

$$f_\phi(P, J^{GP}, J) = \begin{cases} \frac{P}{P_c - P_0} - \frac{P_0}{P_c - P_0} \exp\left(-\frac{P_c - P_0}{2P_0(J_0^{GP}-1)}(J^{GP} - J_0^{GP})\right) & P < P_0 \\ (J^{GP} - 1) - (J_0^{GP} - 1)J^2 \left(\frac{P_c - P}{P_c - P_0}\right)^2 & P_0 \leq P < P_c \\ J^{GP} - 1 & P > P_c \end{cases} . \tag{4.68}$$

This yield surface represents the quasistatic crush curve. Since we are incorporating dynamic effects into the granular flow portion of the model, we also incorporate dynamic effects into the pore collapse portion of the model. We do this following the same procedure as in section 4.3.5. The equilibrium distension (J_{eq}^{GP}) satisfies $f_\phi(J_{eq}^{GP}, J) = 0$. We define a strain like measure of excess distension as $\Delta J^{GP} = J^{GP} - J_{eq}^{GP}$. We assume the same simple model as equation (4.67) for the rate dependence for the rate of change of the distension: $\dot{J}_{pore}^{GP} = \frac{-\Delta J^{GP}}{\tau_{GP}}$ when $\Delta J^{GP} > 0$ and $\dot{J}_{pore}^{GP} = 0$ otherwise.

The total rate of change of the distension is the sum of the distension change due to granular flow and the distension change due to pore compaction:

$$\dot{J}^{GP} = J^{GP}\mathrm{tr}(\boldsymbol{d}^{vp}) + \dot{J}^{GP}_{pore} \tag{4.69}$$

This pore collapse model, combined with the granular flow model that allows dilatation, produces a steady state porosity (after large shear deformations) that is pressure and rate dependent. The equilibrium porosity may be important for the excavation flow in impact cratering problems and in the flow of the comminuted material during penetration events.

Both the pore compaction process and the granular flow process are dissipative processes that can generate a significant amount of heat. Granular flow is primarily a frictional process so we assume that all of the energy dissipated through these processes is converted into heat resulting in a temperature change given by:

$$\dot{\theta}_{GP} = \frac{\mathcal{H}(-\mathrm{tr}(\boldsymbol{\tau}))\boldsymbol{d}^{vp} : \boldsymbol{\tau} + \dot{J}^{GP}_{pore} J^{e}(-p_s)}{\rho_0 c_v}. \tag{4.70}$$

Here $\mathcal{H}$ is the Heaviside step function that only allows heating due to granular flow if the mean stress is compressive in nature. If it is tensile, then the subscale fragments are being disassembled and the only resistance to deformation is their momentum and the requirement that one piece must move before the other pieces can move. One can think of this process as transferring the macroscale energy into the kinetic energy of the fragments. Since we do not track this form of energy, we allow it to be dissipated. The rate of plastic work due to granular flow ($\boldsymbol{\tau} : \boldsymbol{d}^{vp}$) is computed

Thermal Parameters	Density (ρ)	3595 kg/m^3
	Specific Heat Capacity (C_v)	800 J/(kg °K)
	Thermal Conductivity (α_θ)	9 W/(m °K)
Equation of State Parameters	C_0	7670 m/s
	S	1.3
	Γ_0	1.6
Elastic Parameters	Shear Modulus (G)	125 GPa
	Bulk Modulus (κ)	211 GPa
Flaw Distribution	Minimum Flaw size ($s_{\min}$)	2 μm
	Maximum Flaw size ($s_{\max}$)	40 μm
	Distribution Exponent (α)	3.0
	Flaw Density (η)	4 $\times 10^{12}$ m^{-3}
Micromechanics Parameters	Fracture Toughness (K_{IC})	2.9 MPa$\sqrt{\text{m}}$
	Maximum Crack Velocity(V_m)	0.2 C_r
	Crack Growth Exponent (γ_c)	1.0
	Crack Face Coefficient of Friction (μ)	0.57
	Crack orientation (ϕ)	60°
Granular Flow Parameters	A	0.6
	Y	0 MPa
	Damage Cohesive Strength (B)	0.1 MPa
	Relaxation time (τ_{GP})	7$\times 10^{-9}$s
	Damage for Granular flow (D_c)	0.125
	Maximum Damage ($D_{\max}$)	1.0
Pore Compaction	Reference crush pressure (P_0)	1 GPa
	Reference distension (J_0^{GP})	2.0
	Consolidation pressure (P_c)	10 GPa
	Bulking ratio for localization (J_{loc}^{GP})	2.0

Table 4.1: Material model parameters for AlON

using the difference between the strain energy in the trial (reached through elastic deformation) state and the state at the end of the time step. We have found that this is more accurate than computing the work rate from the plastic strain rate. The total rate of temperature change is the sum of the contributions from granular flow, isentropic heating, and viscous heating ($\dot{\theta} = \dot{\theta}_{ent} + \dot{\theta}_{av} + \dot{\theta}_{GP}$).

Pore compaction is the final piece of the material model description. To summarize, the model also incorporates a Mie-Grüneisen equation of state, micromechanics based damage growth with a dynamically interacting distribution of flaws, degrada-

tion of the elastic behavior of the material with damage, and granular flow once a sufficient level of damage is reached. All of the material parameters are summarized in table 4.1.

4.4 Verification of Model Pieces

Numerical implementations of complex constitutive models require verification that the numerical approximation of the mathematical description of the material model is consistent and accurately solves the expected problem. Since exact analytic solutions, which exercise the full complexity of the material model, are not available, we approach the verification problem by looking at the pieces of the material model independently. The implementation of the Mie-Grüneisen equation of state was verified by comparison to the analytic solution for a planar shock. We verify the micromechanics damage growth model by comparing the output for a single material point subjected to uniaxial stress loading to a MATLAB calculation that solves the micromechanics damage growth model under the same loading conditions. Objectivity is demonstrated through a stretch and rotate problem. After verifying objectivity, we simulate hydrostatic expansion followed by hydrostatic compression to exercise the pore compaction model and demonstrate that the computed pressure-porosity relationship is the same as the input relationship. The final single element test takes a material point through a path in strain space that exercises the three main compo-

nents of the model (compressive damage growth, granular flow, and pore compaction). Following the single element tests, we address the total energy balance in the system using the symmetric impact of two spheres and a plate impact simulation.

4.4.1 Equation of State Verification Through Symmetric Hypervelocity Impact

Our development of the Mie-Grüneisen equation of state uses the Principal Hugoniot as a reference curve. This decision makes the obvious verification problem a shock propagating in a plate. To ensure that the simulated material uses the same assumptions as the analytic solution we simulate symmetric impact in a Mie-Gruneisen solid with a negligible shear modulus.

We consider a plate initially moving with a velocity of 2.5 km/s striking a rigid wall. Experimentally these initial conditions correspond to a symmetric impact at 5 km/s. The plate has large dimensions transverse to the direction of motion resulting in uniaxial strain conditions for the duration of the test. The material constants for this test correspond to AlON, but the shear modulus has been reduced to nearly 0 (125 Pa) so that only the EOS is tested. The material properties are summarized in table 4.2. The analytic solution to this initial boundary value problem is a shock wave propagating from the wall through the specimen. The particle velocity behind the shock is 0 km/s and the velocity in front of the shock is 2.5 km/s. The shock

Density (ρ)	3595 kg/m^3
Specific Heat Capacity (C_v)	800 J/(kg °K)
Thermal Conductivity (α_θ)	9 W/(m °K)
C_0	7670 m/s
S	1.3
Γ_0	1.6
Shear Modulus (G)	125 Pa

Table 4.2: Material model parameters for EOS verification based on AlON

speed is given by equation (4.29) as:

$$U_s = 7670\frac{\text{m}}{\text{s}} + 1.3 \times 2500\frac{\text{m}}{\text{s}} = 10920\frac{\text{m}}{\text{s}}. \tag{4.71}$$

The change in volume, pressure, and internal energy across the shock front are described by the Rankine-Hugoniot jump conditions (equations (4.13), (4.14), and (4.15)):

$$J = \frac{\rho_0}{\rho} = \frac{U_s - U_p}{U_s} = \frac{10920\frac{\text{m}}{\text{s}} - 2500\frac{\text{m}}{\text{s}}}{10920\frac{\text{m}}{\text{s}}} \approx 0.771 \tag{4.72}$$

$$p = \rho_0 U_s U_p + p_0 = 3595\frac{\text{kg}}{\text{m}^3}\left(10920\frac{\text{m}}{\text{s}}\right)\left(2500\frac{\text{m}}{\text{s}}\right) \approx 98.1GPa \tag{4.73}$$

To compute the temperature behind the shock front we first compute the total internal energy change resulting from the shock using equation (4.15):

$$e - e_0 = \frac{pU_p - \frac{1}{2}\rho_0 U_s U_p^2}{\rho_0 U_s} \tag{4.74}$$

$$= \frac{(98.1 \times 10^9\text{Pa})\left(2500\frac{\text{m}}{\text{s}}\right) - \frac{1}{2}\left(3595\frac{\text{kg}}{\text{m}^3}\right)\left(10920\frac{\text{m}}{\text{s}}\right)\left(2500\frac{\text{m}}{\text{s}}\right)^2}{\left(3595\frac{\text{kg}}{\text{m}^3}\right)\left(10920\frac{\text{m}}{\text{s}}\right)} \tag{4.75}$$

$$\approx 3.12\frac{\text{J}}{\text{kg}} \tag{4.76}$$

To compute the temperature behind the shock front we start by computing the cold energy associated with the compression to the same volume ratio (J_+) using equation

(4.34), which requires numerical integration of equation (4.36). Plugging this cold energy into the Mie-Grüneisen equation of state gives the pressure at 0K for a volumetric compression ratio of J_+; we refer to this pressure as the cold pressure (p_{c+}). The difference between the Hugoniot pressure and the cold pressure is due to thermal energy. Dividing this pressure difference by $\rho_0 \Gamma_0 c_v$ gives the temperature behind the shock front. Performing these calculations results in a temperature of $\theta_+ \approx 1,335$ K behind the shock front.

From the perspective of a Lagrangian tracer particle in the material at a position x measured from the rigid wall the analytic solution for the temperature, volumetric compression $\epsilon_c = 1 - J$, velocity, and pressure are functions of time given by:

$$v_{\text{analytic}}(t) = U_p \mathcal{H}\left(t - U_s x\right) \tag{4.77}$$

$$p_{\text{analytic}}(t) = p_+ \mathcal{H}\left(t - U_s x\right) \tag{4.78}$$

$$\epsilon_{c\text{analytic}}(t) = \left(1 - J_+\right) \mathcal{H}\left(t - U_s x\right) \tag{4.79}$$

$$\theta_{\text{analytic}}(t) = \theta_0 + \theta_+ \mathcal{H}\left(t - U_s x\right) \tag{4.80}$$

We verify our implementation of the Mie-Grüneisen equation of state by simulating the impact conditions described above using a range of computational meshes from 12.5 μm to 1.5625 μm per cell and 1 particle per cell. We enforce the uniaxial strain conditions in the full three dimensional computational framework by using only one computational cell and prescribing roller boundary conditions in the two transverse directions (y and z). These simulations used an artificial viscosity as discussed in

section 4.3.3 to capture the dissipation associated with the shock process and to spread the shock over several computational cells.

In all of the simulations, the arrival time of the shock wave is captured to within the rise time of the shock at the four tracer particle locations. Figure 4.4 shows the analytic and simulated evolution of pressure, temperature, volumetric strain, and particle velocity with time at the four tracer particle locations for the resolution of 12.5 μm per cell. In this figure the black dashed lines are the analytic solutions.

To access the convergence rate of these simulations, and provide a quantitative verification of our implementation, we define the error measure for a field quantity A as:

$$\mathcal{E}_A = \sqrt{\frac{\int_0^{1\mu\text{s}} \left(\frac{A_{\text{analytic}}(t) - A_{\text{sim}}(t)}{A_+}\right)^2 dt}{1\mu\text{s}}}. \tag{4.81}$$

Discretizing this integral using midpoint integration and taking advantage of the uniform time interval between output times we rewrite equation (4.81) as a summation over all N_{steps} time steps:

$$\mathcal{E}_A = \sqrt{\frac{\sum_i^{N_{\text{steps}}} \left(\frac{A_{\text{analytic}}(t_i) - A_{\text{sim}}(t_i)}{A_+}\right)^2}{N_{\text{steps}}}} \tag{4.82}$$

The maximum error norm among the four tracer particles converges at a rate that is better than linear, but less than quadratic for the finest two resolutions, as shown in figure 4.5. This behavior is reasonable because we are using a first order accurate update procedure for the nodal velocities (which are then mapped to particles). Grid refinement reduces the stable time step (improving temporal resolution) and increases

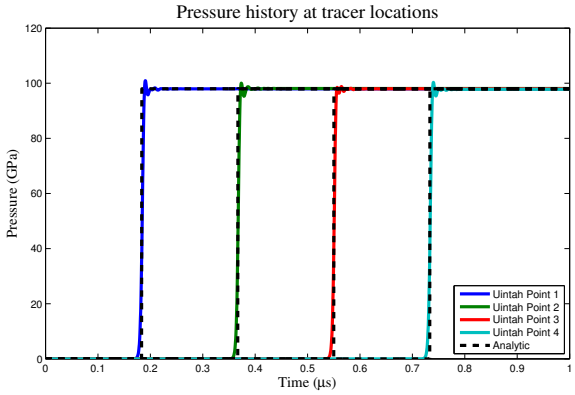

(a) Pressure at tracer locations

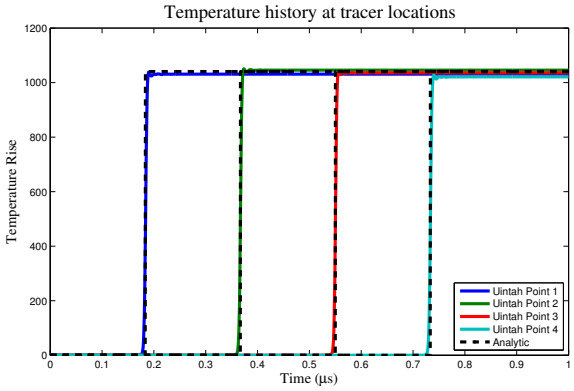

(b) Temperature rise at tracer locations

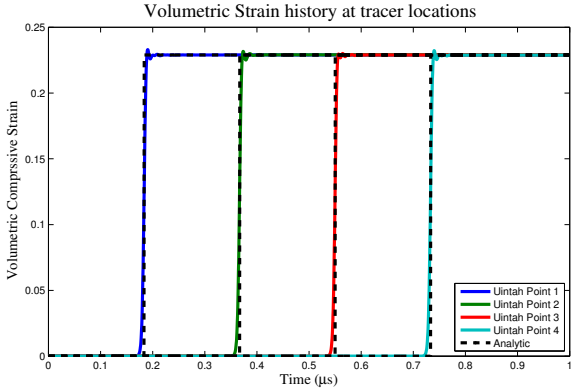

(c) Volumetric strain $(1 - J)$

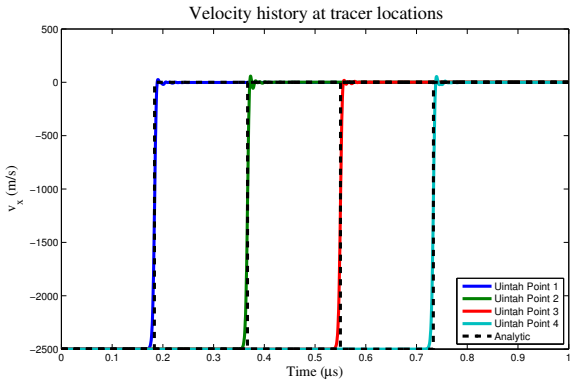

(d) Particle velocity at tracer locations

Figure 4.4: Pressure, velocity, density and temperature histories at Lagrangian tracer locations in 2.5 km/s planar shock simulation. Analytic results are plotted in a dotted line. The wave speed matches and the final values after the shock are in good agreement with the analytical predictions.

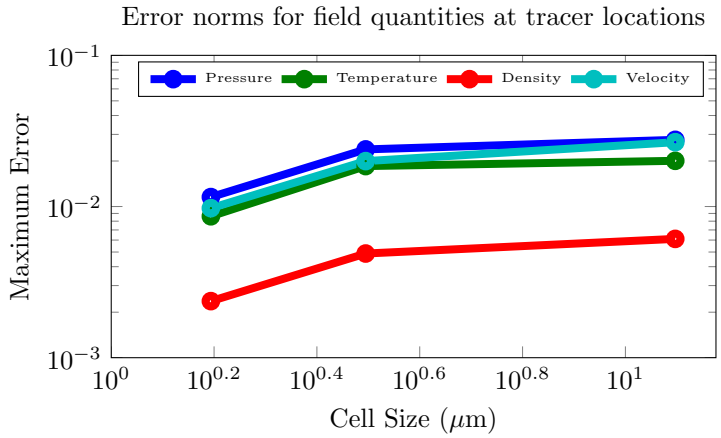

Figure 4.5: Convergence of temperature, velocity, pressure, and density in a simulated plate impact configuration to the analytic solution for a planar shock.

the spatial resolution in the simulation. The net result is convergence that is better than linear but less than quadratic.

4.4.2 Micromechanics Verification Through Comparison to a MATLAB Implementation

Ideally, verification of complicated constitutive models, such as the one described in chapter 3, is demonstrated through comparison to highly accurate or analytic solutions produced by a tool such as Mathematica or the variable precision ODE solvers in MATLAB. For this model, we have not completed a general solution of the model using one of the highly accurate ODE solvers; instead, we implemented the model in a MATLAB code using simple backward Euler time integration for

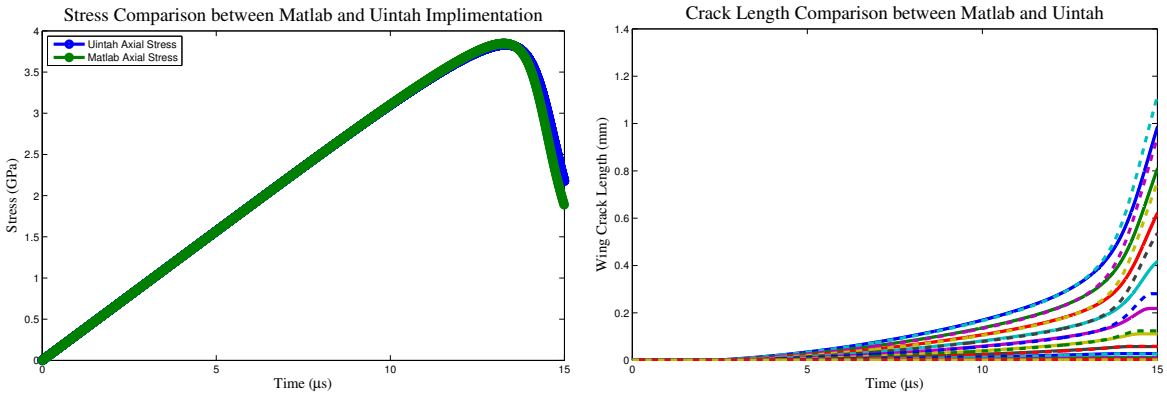

(a) Stress verses time

(b) Wing-crack length verses time

Figure 4.6: The predicted stress and wing crack length histories match between the Matlab (green and dashed lines) and Uintah (blue and solid lines) implementations of the damage model. This provides confidence in the Uintah implementation.

pure uniaxial compression loading. We compare the output of this calculation to the output from running the full model in Uintah for a single material point subjected to uniaxial stress loading. For a test problem, we use a uniaxial stress loading at a constant strain rate of 10^3 1/s. Figures 4.6a and 4.6b show the stress and crack length histories for the two numerical implementations. The two implementations give very similar results. The differences in the results are a result of slightly different initial crack distributions. This level of agreement suggests that we are solving the damage evolution equations correctly.

4.4.3 Verification of Objective Integration

In impact events, the excavation of material can cause large deformations including large rotations. Since these conditions will be experienced during a simulation, it is important to demonstrate that our computational implementation of the material model is properly behaved under conditions of both large distortion and large rotation. To verify the performance of our integration scheme under superimposed large rotations, we apply a simple shear deformation defined by:

$$\boldsymbol{F}(t) = \begin{bmatrix} 1 & (1 \times 10^{-3})\,\frac{t}{\mu\text{s}} & 0 \\ 0 & 1 & 0 \\ 0 & 0 & 1.0 \end{bmatrix}. \tag{4.83}$$

This deformation causes failure in the material followed by granular flow. We give the stress history resulting from this simple shear deformation the label $\boldsymbol{\sigma}_1(t)$. We define a second loading path by applying the deformation $\boldsymbol{F}(t)$ with a rotation $\mathcal{R}(t)$ superimposed. We define the rotation such that the material rotates through a full rotation about the x-axis in a period of 40 μs:

$$\mathcal{R}(t) = \begin{bmatrix} \cos(\frac{2\pi t}{40\,\mu\text{s}}) & -\sin(\frac{2\pi t}{40\,\mu\text{s}}) & 0 \\ \sin(\frac{2\pi t}{40\,\mu\text{s}}) & \cos(\frac{2\pi t}{40\,\mu\text{s}}) & 0 \\ 0 & 0 & 1 \end{bmatrix}. \tag{4.84}$$

The stress history resulting from this loading history is given the label $\boldsymbol{\sigma}_2(t)$. The six components of the stress tensors $\boldsymbol{\sigma}_1$ and $\boldsymbol{\sigma}_2$ are plotted as a function of time in figure 4.7a. In this figure both stress tensors are referenced to the same non-rotating

coordinate frame. The dashed lines that represent the components of $\boldsymbol{\sigma}_2$ show the effect of the rotation by deviating from the solid lines representing the non-rotating case. In figure 4.7b we have removed the rotations from $\boldsymbol{\sigma}_2$ using the inverse of the applied rotation tensor. This figure shows qualitatively that the existence of the large rotation did not change the material response, or equivalently, the constitutive model integration scheme is objective. We quantify the error introduced by the time integration scheme using:

$$\mathcal{E}_\sigma(t) = \frac{\|\mathcal{R}^{-1}(t)\boldsymbol{\sigma}_2(t)\mathcal{R}^{-T} - \boldsymbol{\sigma}_1(t)\|}{\|\boldsymbol{\sigma}_1(t)\|}. \tag{4.85}$$

The maximum value of $\mathcal{E}_\sigma$ as the rotation angle was taken from 0 to 2π was less than 5×10^{-4}. This agreement indicates that the constitutive model integration procedure is appropriate for problems that involve large rotations.

4.4.4 Testing Pore Compaction Through Hydrostatic Deformation

To illustrate the pore compaction behavior in the material model we prescribe a deformation history consisting of hydrostatic expansion at a constant rate to a volume ratio of 1.953 in 4 μs followed by a 5 μs rest followed by hydrostatic compression to a volume ratio of 0.973 in 10 μs. The resulting relationship between pressure and distension is shown in figure 4.8c. The initial tension produces the initial distension. During the compaction phase, the pressure first increases at constant distension until

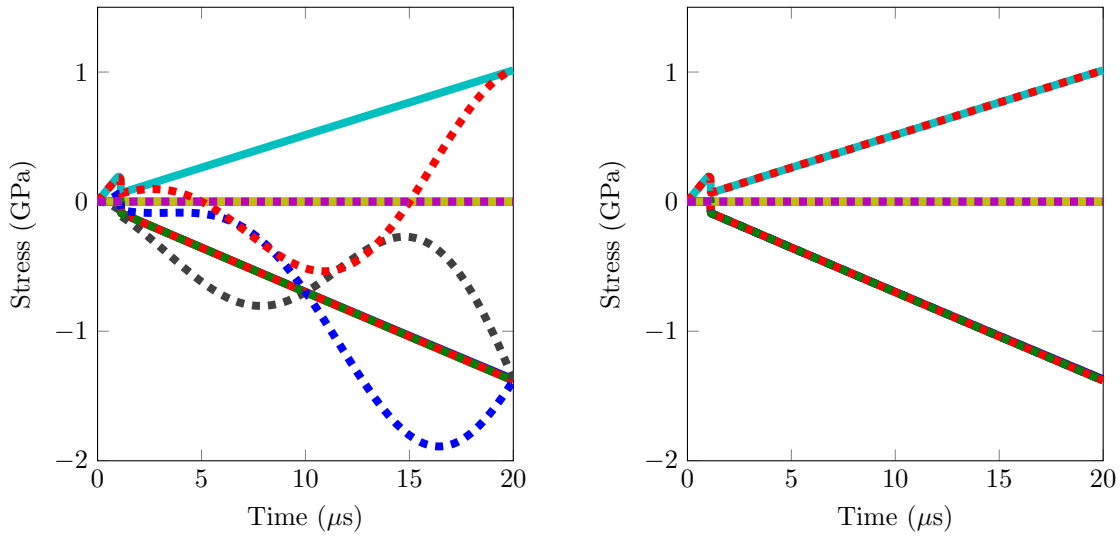

(a) Stress versus time

(b) Unrotated stresses versus time

Figure 4.7: All 6 components of stress as a function of time for simple shear at a shear rate of 10^3 s^{-1} with (dashed lines) and without (solid lines) a 360 degree rotation super imposed on the shear deformation. In figure 4.7b the stresses have been transformed to remove the rotation. This indicates that the model is capable of handling large rotations.

the pressure reaches the green curve, which indicates the input pressure distension relationship, after crossing the green curve the pressure is sufficient to crush out the porosity. The simulated pressure porosity relationship then follows the prescribed input curve indicating that the numerical implementation of the compaction process is correctly solving the equations. The distension as a function of time is shown in figure 4.8a. We see that the initial tensile deformation introduces the distension that is then compressed out. As shown in figure 4.8b, there is a significant temperature rise that results from the work done during the compression process.

4.4.5 Complex Stress Path That Checks All Regimes of Granular Flow

This final loading path is more complicated and illustrates the key features of the granular flow model. We first apply a uniaxial strain which increases the pressure and the deviatoric stress. There is some slow damage growth during the uniaxial strain compression. After holding the uniaxial strain for 5 μs, the material is sheared at a rate of $1 \times 10^5 \mathrm{s}^{-1}$ for the next 90 μs. This shear deformation increases the deviatoric stress and causes damage to occur. The damage causes material softening that relaxes both the hydrostatic and deviatoric stresses. This is manifested as a spike in the deviatoric stress, a dip in the hydrostatic stress, and a large increase in the damage. Once damage reaches 0.125, granular flow continues to relax the deviatoric

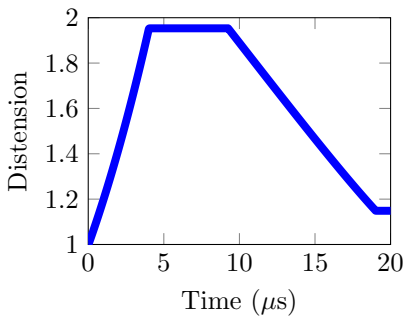

(a) Distension

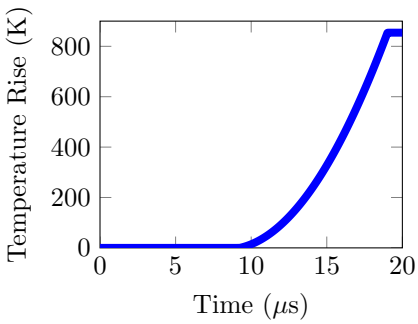

(b) Temperature Rise

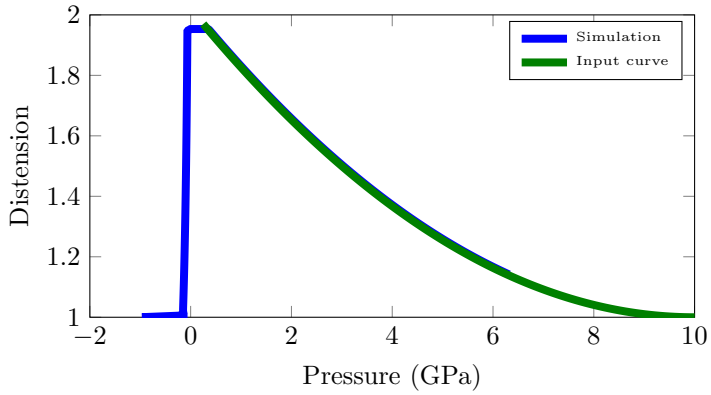

(c) Pressure-Distension

Figure 4.8: Figures a and b show the distension (figure 4.8a) and temperature rise (figure 4.8b) as function of time for hydrostatic tension followed by compaction. The expansion does not cause a temperature rise (a modeling assumption) but the compaction phase causes a large temperature rise because there is a large amount of work done during compaction. Figure 4.8c shows the simulated (blue) and the input (green) pressure distension relationships. The agreement between the two curves (with the blue slightly above the green) indicates that we are correctly solving the pore compaction portion of the material model.

stress while increasing the pressure. This increased pressure causes an increase in the deviatoric strength until the pressure reaches a pressure that is sufficient to cause pore collapse. Once the pore collapse mechanism is activated, the material continues to flow without increasing the dilation or pressure. The next loading step from 100 μs to 150 μs is a uniaxial extension. In the final loading step the pure shear is reversed to end with the material point returned to its original shape, but there is a residual stress and dilatation. Figure 4.9 shows the time history of the stress, damage, and components of granular flow.

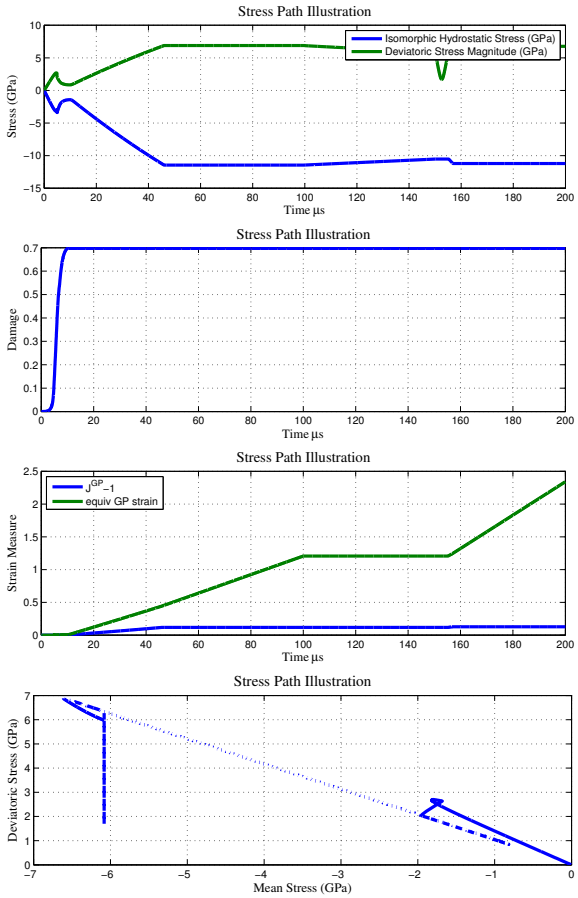

Figure 4.9: Material model output for a path through stress space.

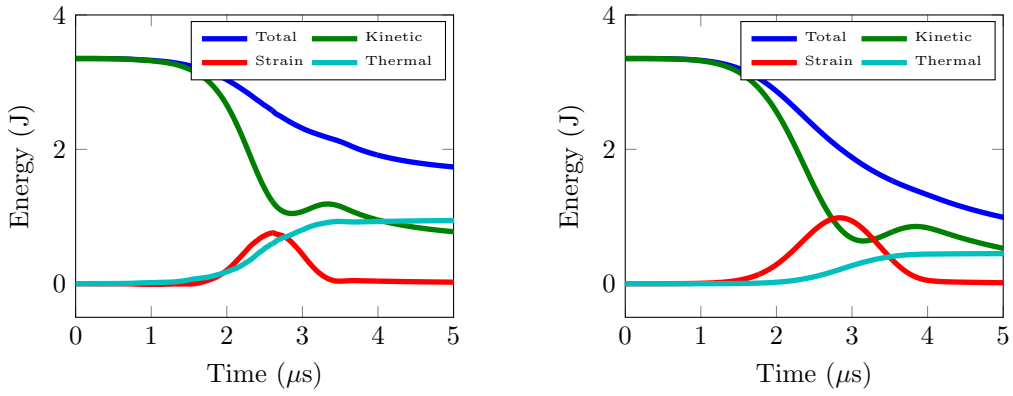

(a) Full boron carbide model

(b) Granular flow only

Figure 4.10: Symmetric impact of two spheres for the full material model including damage and the Mie-Grüneisen equation of state (a) and for only the granular flow portion of the model (b). In both cases the total energy decreases because we do not allow frictional heating when the hydrostatic stress is tensile.

After looking at the behavior of a single element, we now move on to two boundary value problems that illustrate the behavior of the total energy in the system.

4.4.6 Energy Balance in Plate Impact and Ball on Ball Impact

The final two sets of verification tests, which proved the most informative, are the symmetric impact of two spheres and a simulated plate impact problem. In both of these problems, it is a closed system with no external forcing from the boundary. As a

result we expect the total energy in the system to be conserved. If there is numerical dissipation then the total energy will decrease. Increases in energy suggest that there may be issues with the energy accounting in the system. The kinetic energy should not increase beyond the initial kinetic energy in any of these tests.

The symmetric ball impact tests shown in figure 4.10 primarily test the granular flow portion of the material model. In figure 4.10a the full model is exercised including the Mie-Grüneisen equation of state, damage growth, and granular flow. In the early stages of the impact event, the strain energy decreases (becomes less than 0) because this early portion of the contact is dominated by the volumetric response and at finite temperature, our assertion that $e_c(1) = 0$ results in small negative cold energy contributions (if the volumetric compression is less than the thermal expansion from 0K to 294K). At later times the deviatoric contribution to the strain energy becomes important and the strain energy rises rapidly. The increase in temperature results from isentropic heating from the equation of state, and frictional heating in the granular flow model. The total energy drops partially because we are not accounting for the energy dissipated in microcracking, but also because the implementation of MPM in Uintah uses a lumped mass matrix, which can dissipate energy during collisions due to the particle to grid and grid to particle mapping (section 3.2). The most important feature in figure 4.10a is that for the full model with the ball impact case the total energy does not increase. Figure 4.10b shows the results of the same simulation except only the granular flow model is active and a compressible Neo-Hookean

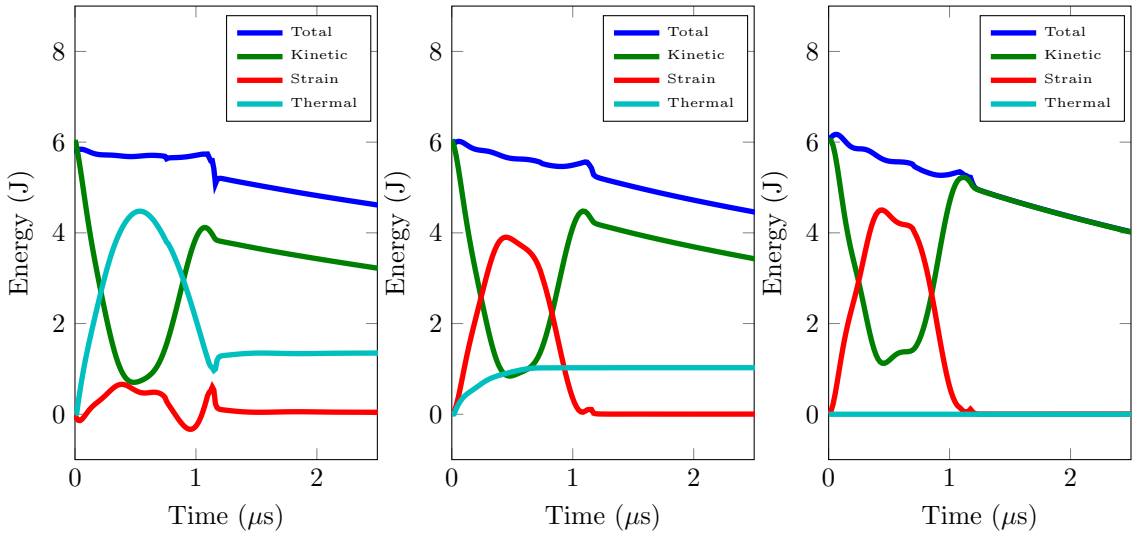

(a) Mie-Grüneisen EOS (b) Neo-Hookean EOS (c) No artificial viscosity

Figure 4.11: Plate impact verification tests

equation of state is used. In this simulation all of the heating is due to granular flow. Again the total energy is a strictly decreasing function of time. These symmetric ball impact simulations were performed for a variety of combinations of material parameters and the model produced physically reasonable results in all cases except extreme cases when $A \approx 0$ and $B = 3$ Pa. In this extreme case numerical issues allowed for the apparent production of energy (and negative plastic work) because of the poorly conditioned nature of the problem (the cohesive strength was almost 11 orders of magnitude smaller than the bulk modulus). Since this was an extreme case designed to test the model limits, we recognize the necessity of choosing reasonable values for both the effective friction coefficient and the cohesive strength relative to the expected loads in the problem of interest.

The second set of test problems is a simulated plate impact problem where the flyer plate is half of the thickness of the target plate. After the impact event a compressive wave is generated and the kinetic energy is converted into strain energy. When the reflected unloading waves interact they cause a tensile spall zone where damage quickly develops followed by granular flow. The results of these tests are shown in figure 4.11. Figure 4.11a shows the energy results for the full material model including the Mie-Grüneisen equation of state. The large increase then decrease in the thermal energy is due to isentropic coupling of temperature to the volumetric deformation. This heating allows for the calculation of negative strain energies due to the shifted strain energy reference. The sudden drop in the total energy is the result of damage growth (decreasing thermal energy indicates isentropic expansion). It is quickly followed by an increase in thermal energy resulting from granular flow. As the spall region expands the non-zero cohesive strength of the material and viscosity in the granular flow model reduce the kinetic energy in the system. Since we do not allow frictional heating when there is a tensile mean stress, the total energy in the system decreases with the kinetic energy. Figure 4.11b shows the same problem run with an equation of state that does not have any temperature coupling (compressible Neo-Hookean). All of the heating in this simulation results from the artificial viscosity (which is converted into heat). This conclusion is supported by figure 4.11c, which has the artificial viscosity turned off and produces no change in temperature. Although there are fluctuations (both increases and decreases) in the total energy in all of the

plate impact simulations, we do not see any large increases in total energy. Future algorithmic development could focus on improving the energy accounting capabilities in both the constitutive model and the host code. These results are acceptable for the purposes of this work because the focus is on the interactions of material variability with the different mechanisms that are active during dynamic failure events. If this model were to be used in a predictive environment for high consequence decision making, then greater understanding of the fluctuations in total energy would be required.

4.5 Flaw Sampling and the Coupling Between Specimen Size and Strength

Coupling the flaw sampling discussion in section 4.2 with the material model discussed in section 4.3 results in one of the major motivations for retaining local information about the flaw distribution. When testing ceramic materials, significant variability in the strength is observed from one specimen to the next. This variability depends on the specimen size, type of loading, and loading rate. Weibull type arguments are often applied in these cases. For ceramic materials, this argument implies the largest flaw controls the strength. This may be the case in quasistatic tensile tests, but it is not the case for dynamic compressive failure. One example is provided by the experiments of Paliwal et al. [64] who observe multiple bright spots prior to

failure indicating the activation of multiple flaws. Our approach is naturally able to capture such behavior.

Graham-Brady [33] investigated the statistical variation of specimen strength with specimen size for different spatial distributions of flaws using a similar micromechanics model and a Gaussian flaw size distribution. She concluded that a standard two parameter Weibull distribution provides a poor fit to the distribution of strengths in dynamic compression. We reach the same conclusion using a bounded Pareto distribution of flaws instead of a Gaussian distribution (details in A.3). In this section we perform a similar study using our material model and sampling procedure to illustrate the coupling between flaw sampling, strain rate sensitivity, and the distribution of compressive strengths.

Since we expect the strength of a specimen to depend on both size and loading rate, we simulate the uniaxial compression problem using a variety of specimen sizes from 4.0 mm on a side to 0.125 mm on a side and a strain rate of 10^3 1/s. To ensure a homogeneous stress state, these simulations were performed using a single particle with free boundaries in the $\boldsymbol{e}_1$ and $\boldsymbol{e}_2$, a constant velocity on the positive $\boldsymbol{e}_3$ surface and zero displacement on the negative $\boldsymbol{e}_3$ surface. The results are summarized in the box plots shown in figure 4.12. In general, large specimen sizes have lower median strengths, as indicated by the red horizontal bar, and a narrower distribution of strengths, as indicated by the box and whisker sizes. Larger specimens are expected to be weaker because larger specimens have a higher probability of containing a large

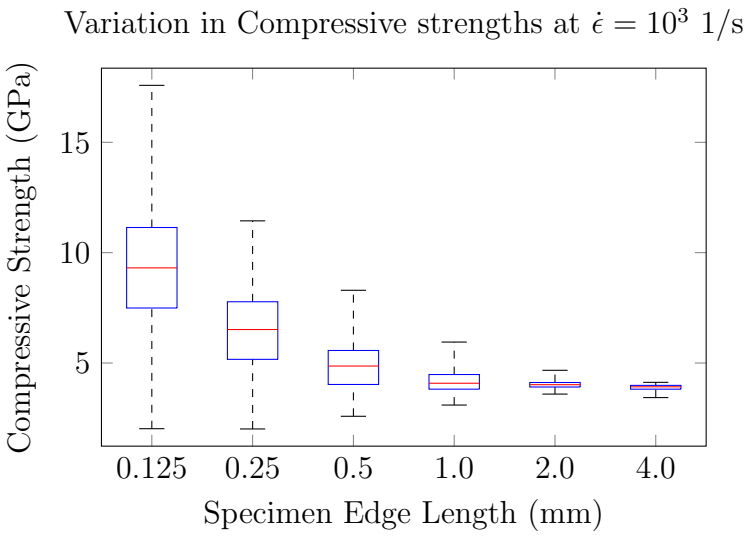

Figure 4.12: A box plot showing the change in the distribution of uniaxial compressive strengths as the simulated specimen edge length is decreased from 4 mm to 0.125 mm. The median strength and the variability in the strength increases as the specimen size decreases.

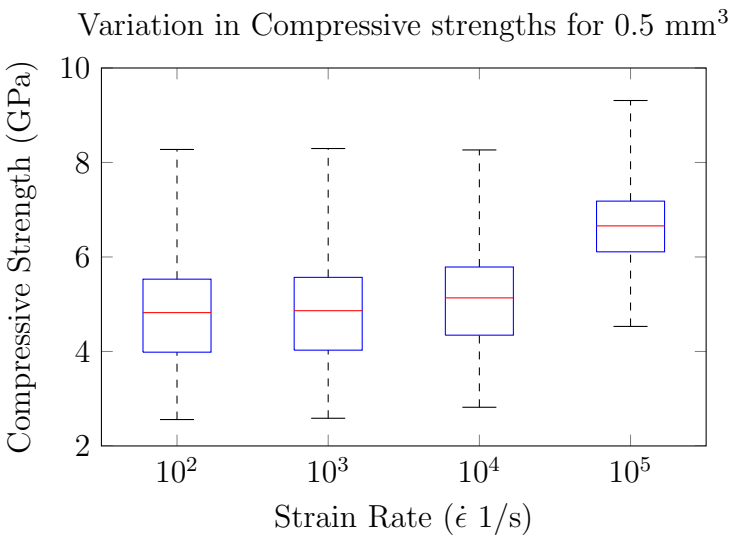

Figure 4.13: Box plot of the compressive strength variation with strain rate for a sample size of 0.5 mm per side. The median strength increases with strain rate while the spread in the strength distribution as indicated by the whisker length decreases with strain rate.

flaw. However, one also expects larger specimens to have less variability than smaller specimens since the large specimens should contain more of the flaw distribution and the sampling effect of the flaw distribution becomes less important.

In general, for a fixed specimen size, as the strain rate increases the strength increases and the spread in the strength distribution decreases. This trend is shown in figure 4.13 for a specimen size of 0.5 mm per side. Note that the nature of the rate sensitivity depends on the local flaw distribution, because it is a competition between the stress required to drive the activated cracks faster and the activation of the next set of available flaws by the cracks. This complex interplay between local sampling,

strain rate sensitivity, and the specimen size is one of the reasons that we elect to retain the local flaw distribution data despite the associated additional computational cost.

The combined influence of specimen size and strain rate on the strength distributions is shown in figure 4.14, which presents the empirical CDFs of the peak strength for two specimen sizes (0.5 mm/cell and 0.125 mm/cell) and three loading rates from $\dot{\epsilon} = 10^3$ 1/s to $\dot{\epsilon} = 10^5$ 1/s. In this plot the blue lines correspond to 0.5 mm specimens and the red lines correspond to the 0.125 mm specimens. The different strain rates are denoted by the line patterns (solid lines correspond to strain rates of 10^3 s^{-1}, dashed lines to rates of 10^4 s^{-1}, and dash-dotted lines to rates of 10^5 s^{-1}).

For all specimen sizes, the strength increases when the strain rate is increased. This effect is a result of the micromechanics damage model, and specifically the flaw distribution and limiting crack growth velocity. For all of the strain rates, as the specimen size decreases, the median strength increases and the variability in the strength also increases. The physical reason for these trends relates directly to the flaw sampling process discussed in section 4.2. As the specimen size increases, the local flaw distribution approaches the parent flaw distribution. Since the local flaw distributions in larger specimens are in general closer to the parent flaw distribution, they are in general also closer to each other. This explains the trend towards greater variability in smaller specimens. The mean strength increases with decreasing specimen size because smaller specimens are less likely to have large flaws, which results in an increase

in strength. Even though a large portion of the flaw distribution participates in the damage growth process, the initial damage growth is determined by the largest flaw.

The final observation relating to these strength distributions is that the rate sensitivity (strength increase between a strain rate of 10^3 s^{-1} and 10^5 s^{-1}) decreases as the sample size decreases. This is caused by both the sampling and the micromechanics damage model as previously noted. The high rates require more active flaws to relax the stresses, and the additional flaws that are available are smaller and require high stresses for activation. When the specimen size is reduced, most of the realizations will be missing the large flaws in the flaw distribution. Since the large flaws are missing, higher stresses are required to initiate damage growth, resulting in an increased strength. The flaw sampling procedure discussed in section 4.2 enforces integer numbers of flaws within each discretization volume, which results in a quantization of the flaw densities. In smaller specimens adding or removing a single flaw has a large effect on the local flaw density. This results in a reduced strain rate sensitivity because the strengths at lower strain rates are increased more than the strengths at higher strain rates.

Although the mechanisms behind these size and rate effects are general, the degree of rate sensitivity and size effect depend on the specific defect distribution. We expect that the trends would be qualitatively similar but quantitatively different if a different flaw size distribution was used. The power of this approach is that the rate and size effects are natural outcomes of the input distribution, and do not need to be specified

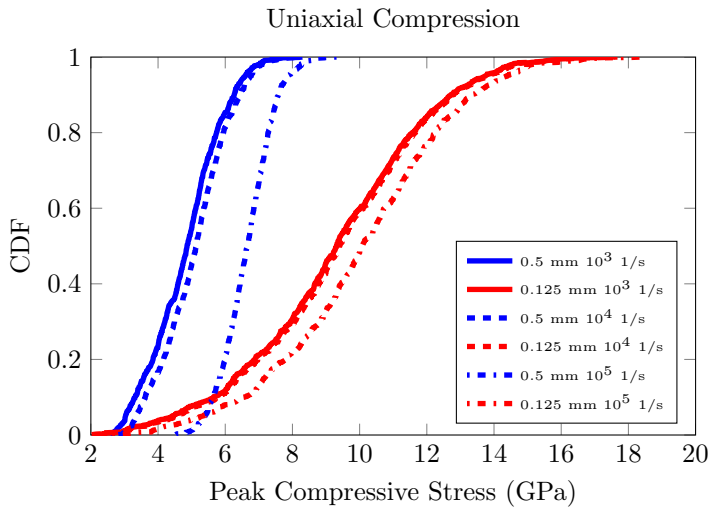

Figure 4.14: The distribution of material point strengths is a function of both material point size and the loading rate. As the specimen size decreases from 0.5 mm/cell (blue) to 0.125 mm/cell (red) the median strength and the variability in the strength increases (figure 4.12). The strain rate sensitivity, shown by the difference between the solid and dash-dotted lines, decreases with smaller specimen sizes. These changes are a result of the flaw distribution sampling and are a key benefit of using the micromechanics based damage model.

a priori.

In the following section we use this framework and model to perform simulations of Edge on Impact (EOI) experiments by Strassburger et al. [56] conducted on AlON tiles.

Bulk Modulus	173 GPa
Shear Modulus	80 GPa
Yield stress	2000 MPa
Hardening Modulus	750 MPa
Density	7.83 $\times 10^3$ kg/m^3

Table 4.3: Material properties for projectile

4.6 Simulations of Edge on Impact Experiments

The EOI experiment is interesting because it provides real time information about the dynamic propagation of damage as a result of an impact event. In the experiment (figure 4.15), a projectile strikes the edge of an armor ceramic tile. As a result of the impact, stress waves travel through the target and cause the formation of a network of cracks. Since the tile is thin, and in the case of AlON transparent, the development and propagation of the crack network can be recorded using high speed cameras.

In the particular experiment that we simulate (labeled experiment number 14897 in [43]), a 10 mm thick, 100 mm square AlON tile is impacted at a velocity of 381 m/s by a 23 mm long steel cylinder with a diameter of 30 mm. We model the steel projectile as a simple elastic plastic material with linear strain hardening, with the properties summarized in table 4.3. The impactor strikes the edge of the tile causing a damage front to develop and propagate through the tile. The impact event and subsequent damage front propagation were imaged using high speed photography (Strassburger et al. [56]). Images were captured every 0.5 to 1.0 microseconds [43].

Using these images Strassburger computed the velocity of the damage front resulting from the impact event. The authors also computed the velocity of discrete cracks that nucleated in front of the primary damage front. Since this material model is not designed to track the evolution of individual cracks, we compare our simulation results to the reported damage front location.

4.6.1 Simulation Setup

These simulations were performed using convected particle domain interpolation (CPDI) [51] and explicit time integration [75] implemented in the Uintah [52] computational framework. CPDI is based on the Material Point Method[49] in which the constitutive description of the material is carried in a set of Lagrangian material points. A background Eulerian grid is used to compute gradients and solve the equations of motion. Love and Sulsky [2] discuss stability of some implementations of the Material Point Method. This computational method was discussed in detail in chapter 3. In these simulations we use 1 particle per cell in the grid. This choice focuses the computational effort on resolving high stress gradients while sacrificing the ability to resolve sub grid variations in the constitutive response.

We compare our simulations to experimental shadowgraphs that show the damage pattern at discrete instants in time. Examples of the experimental images are the bottom two images in figure 4.15, taken 3.0 μs and 6.0 μs after impact. These figures show light and dark regions. In the light regions, the light is fully transmitted, and

we interpret this as a state of no damage. In the dark regions, the light is blocked by a large amount of damaged material through the thickness of the tile. We interpret the gray regions in the experimental images as regions where there is some cracking or damage in some location through the thickness of the tile, but the damage is less extensive than in the fully black regions. In the simulation results we present an isometric view of the damage pattern where a quarter of the specimen is removed. This view allows us to see damage on both the surface and on the mid plane of the tile. At both 3.0 and 6.0 μs, the computed damage extent is larger at the mid-plane of the tile than at the surface. The damaged region is concentrated in a zone downrange of the projectile. The material is fully damaged near the projectile. As one moves further from the projectile and closer to the surface the damage zone becomes more heterogeneous. This is especially evident in the 6.0 μs image. Although the simulations do not show well developed fingers of damaged regions as seen in the experiments, they do show a heterogeneous damage pattern near the leading edge of the damage front.

It is always important to understand the effect of mesh resolution on the results and ensure that the mesh has sufficient resolution. We conducted a mesh refinement study (figure 4.16) using four different meshes (1.0 mm/cell to 0.125 mm/cell) and examining the time history of the damage extent at the specimen surface and the center plane of the specimen measured along the impact direction (figure 4.15). The location history of the damage extent at the mid plane of the tile agrees (figure 4.16a)

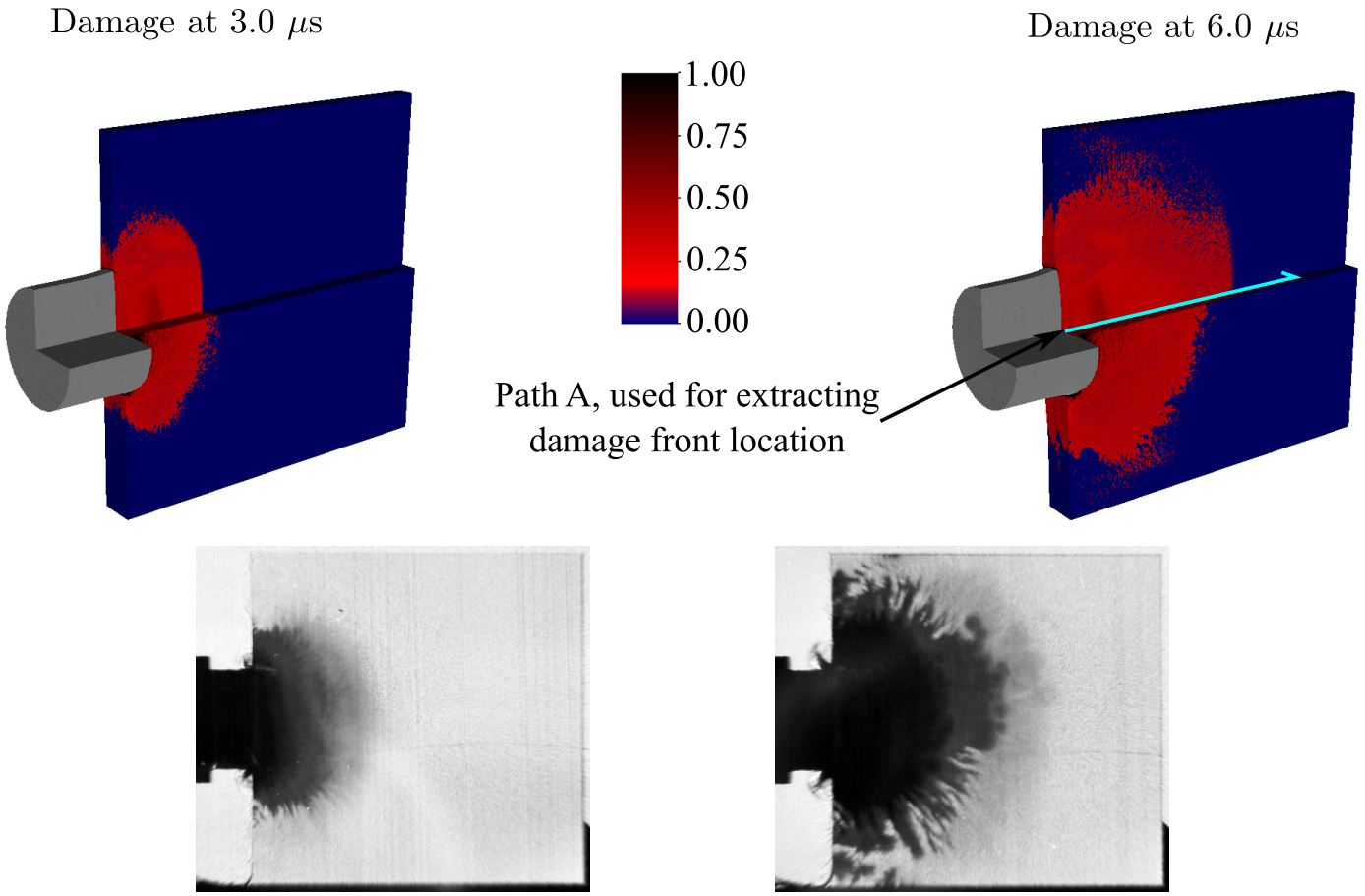

Figure 4.15: Comparison of experimental results with simulation results for 3 and 6 μs after impact with a resolution of 0.25 mm/cell. The cutaway shows the difference between the damage location in the interior of the plate and on the surface. Non-homogeneous damage patterns develop at later times.

for all times for resolutions higher than 0.5 mm/cell. The damage extent at the top surface is more sensitive to the cell size (figure 4.16b), but the 0.25 mm/cell and the 0.125 mm/cell results are similar. Damage growth on the surface of the tile is sensitive to interactions through the thickness of the tile, which are discussed in section 4.6.3. Since the thickness of the tile is one tenth of the length in the other two directions, we note that the velocity of the damage front on the surface is similar between the 0.25 mm/cell and 0.125 mm/cell simulations although the arrival times are different. To balance computational effort and our ability to look at multiple sets of material parameters, we use the 0.25 mm/cell resolution for all subsequent results.

Strassburger et al. [43] computed the distance from the impact site to the boundary between the light and dark regions in the experimental images as a function of time. In figure 4.17 we plot their results (in black) along with the computed damage extent measured at the center plane and on the surface of the target. The experimentally observed damage front velocity was 8,381 m/s [55], which is 89 percent of the 9,367 m/s longitudinal wave speed. In the simulations the longitudinal wave speed (based on the material properties listed in table 4.1) is 10,256 m/s and the computed damage velocity in the center of the tile is 9,900 m/s, which is 97 precent of the longitudinal wave speed. These high damage velocities suggest that the damage nucleation and growth is driven by the longitudinal wave. The computed surface damage lags behind the damage at the center of the plate suggesting that the arrival of damage at the surface depends on the behavior of the damaged material and on how the

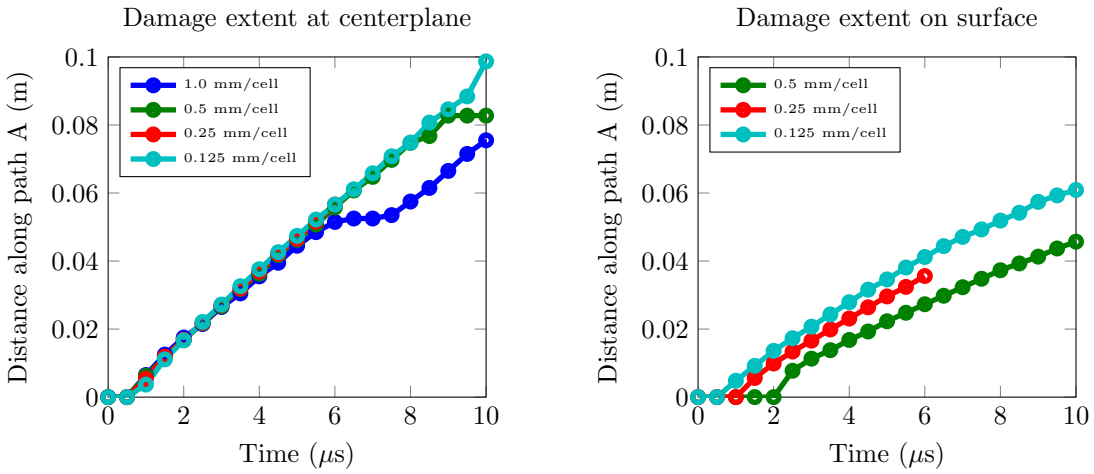

(a) Damage extent at the center plane of the tile along the impact direction.

(b) Damage extent at the top surface of the tile along the impact direction

Figure 4.16: Mesh refinement study results. The damage extent at the center plane of the target shows good agreement at all resolutions. Damage reaches the top surface of the target at earlier times with a finer resolutions, but the change in the arrival times is decreasing with increased resolution.

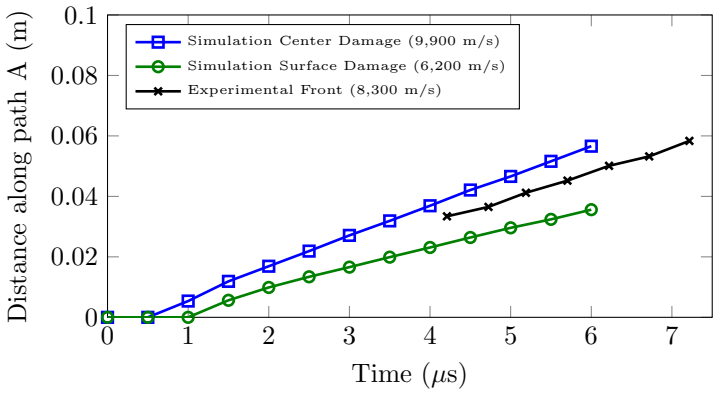

Figure 4.17: Comparison between simulated and experimental observations of the damage front propagation history. The damage front velocity, based on a linear best fit, is reported in parenthesis in the legend. The experimentally observed damage front velocity is between the simulated damage growth velocity measured at the top surface and in the center of the plate.

damage in the center of the tile interacts with the free surface boundary condition. The general agreement with experiments provides confidence that our material model and simulation approach capture the important physical processes within this loading regime. Similar comparisons have been made by Leavy et al. [76]. They were able to capture the fingering of the damage patterns and dependence of the damage front velocity on impact speed using the Kayenta material model.

4.6.2 The Consequences of Variability and the Damage Kinetics

Strassburger et al. also observed the development and growth of a number of finger like localized damage zones during the experiments. This transition from a relatively homogeneous damage zone to the propagation of discrete localized features is common in experimental observations of the failure of brittle materials. Our simulations also show heterogeneity, but not the localization into fingers.

In our material model we illustrate the importance of local fluctuations in the material strength in figure 4.18 by disabling the sampling procedure discussed in section 4.2. As shown in figure 4.18, the heterogeneous damage pattern disappears when the variability is removed. Without variability, the damage pattern is purely the result of the stress interactions, and since this system is highly symmetric, that symmetry is carried into the damage pattern and it does not have any localized features. While the variability has a strong effect on the heterogeneous nature of the damage, it seems to have little effect on the general kinetics and extent of the damage zone. From this observation we conclude that the damage growth rate and general damage shape are controlled primarily by the macroscopic loading, boundary conditions, and average material behavior. This is a reasonable result, because one expects to see generally the same pattern of damage for two similar tiles; however one does not expect the detailed local damage pattern to be identical for two different

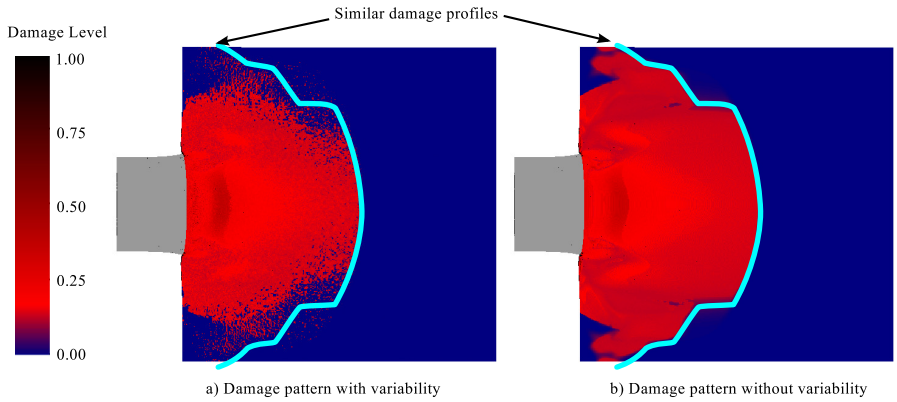

Figure 4.18: Damage pattern at the center of the plate 6 μs after impact demonstrating the effect of variability. Macroscopic variability promotes the development of a heterogeneous damage pattern, which is observed in the experimental results. The development of heterogeneous damage patterns is a prerequisite for developing physically reasonable fragment distributions.

tests. This comparison provides another example of when the symmetry breaking effect of local variability is important for obtaining physically realistic results from simulations of high rate brittle failure.

In addition to investigating the effect of flaw sampling, we are able to look at the effect of changing parameters that define the material behavior. During the discussion of the material model in section 4.3 we identified sources for many of the model parameters. However there is still uncertainty about the effective friction coefficient in the granular flow relationship as well as the crack growth speed for the microcracks in the micromechanics based damage model. We investigated the effect of changing the pressure sensitivity of the granular flow and changing the rate sensitivity of the

material by reducing the maximum crack velocity. The pressure sensitivity of the granular material has little effect on the damage front location in the center plane of the tile. This is illustrated by comparing figure 4.18a and the center simulation in figure 4.19. Both of these simulations use a maximum crack velocity (v_m) of 20 percent of the Rayleigh wave speed, but use different effective coefficients of friction in the granular flow rule. Similar results were observed with friction coefficients of 0.2 and 1.2. This reinforces the conclusion that the damage front location in the center of the plate is dominated by interactions resulting from the longitudinal wave, which are discussed in more detail in section 4.6.3.

The damage kinetics have a moderate effect on the location of the damage front in the center plane of the tile, but have a large effect on the damage pattern behind the damage front. In figure 4.19 we demonstrate this effect by showing the damage pattern on the center plane 6 μs after impact for three simulations where the maximum allowable crack velocity increases from 1 percent of the Rayleigh wave speed, on the left, to 20 percent in the center, and 100 percent on the right. All of these simulations use a coefficient of friction of 0.8 instead of the 0.6 used in the baseline simulations. From these images, we see that as the damage kinetics become faster, we see larger damage gradients behind the damage front. Additionally, the shape of the damage front changes from a smooth, almost circular front with $v_m = 0.01C_r$ to an angular almost trapezoidal front with $v_m = C_r$. The rate sensitivity in the damage model has a regularizing effect and resists the formation of sharp damage gradients (a

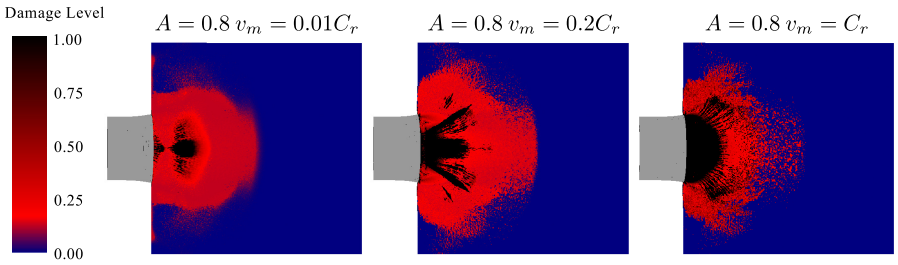

Figure 4.19: Damage distribution at the center of the plate after 6 μs for different damage growth rates. As the maximum crack velocity increases from 1 percent of the Rayleigh wave speed to the Rayleigh wave speed the damage pattern behind the damage front becomes more heterogeneous. The location of the damage front is the same for 100 percent and 20 percent of the Rayleigh wave speed.

longer time to failure provides more time for neighboring material points to develop similar damage). Decreasing the maximum allowable crack velocity increases the rate sensitivity of the damage resulting in a more uniform damage pattern. Conversely, increasing the limiting crack growth velocity decreases the rate sensitivity of damage and promotes localization and the formation of sharp damage gradients.

While the damage extent at the center plane is relatively insensitive to the granular flow parameters, the damage extent on the surface is sensitive to the granular flow parameters. The location of the damage extent on the surface of the tile changes when the pressure dependence of granular flow is altered. Comparing the computed arrival time of the damage front (figure 4.20) to that seen in the experiments, we find that $A \leq 0.8$ and use $A = 0.6$ in all subsequent calculations.

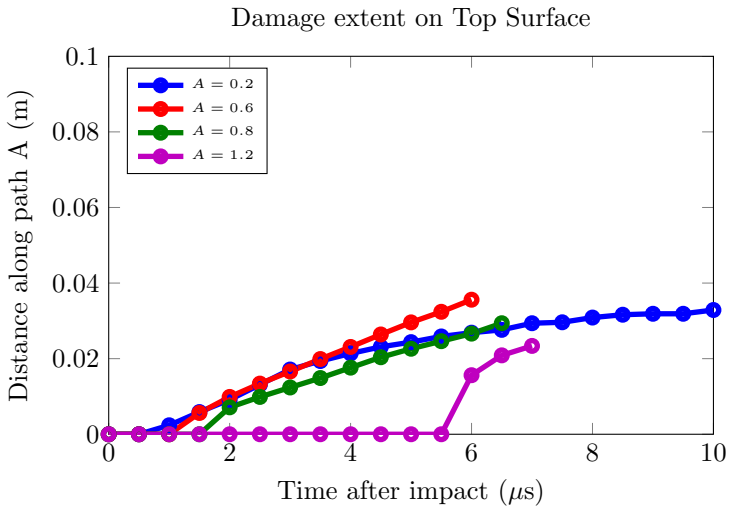

Figure 4.20: The damage front location on the surface of the plate suggusts that a granular flow coefficient of 1.2 is too high. Although the granular flow coefficients of 0.2 and 0.8 produce different damage front location histories, there is not sufficient experimental data to favor one of these two over the other.

4.6.3 Center Plane Damage Driven by the Longitudinal Wave

The experimental images in [43] present a 2 dimensional view of the damage propagation within the target plate; however, the development of damage is a three dimensional process. As discussed in the previous section, the location of the damage front at the center plane of the tile is in front of the damage front observed on the top surface of the tile. In this section we investigate the stress wave interactions that favor damage growth on the interior of the tile.

Both the experimental measures of the damage velocity and the simulations indicate that the damage front moves at around 90 percent of the longitudinal wave speed (figure 4.17). To explain the reasons for this behavior, we investigate the stress and damage pattern on a cross section through the target plate 6 μs after the impact event in figure 4.21. The schematic at the top of figure 4.21 shows the orientation of the cross section with respect to the tile and the impactor. Looking at the pressure (top cross section image) and the equivalent stress (second cross section image) reveals that the longitudinal wave (shown in the dashed green line) reflects from the free surfaces and causes a region of tension when the reflected longitudinal waves from the two boundaries interact. The domains of the reflected longitudinal and shear waves are shown in the equivalent stress plot using black and red lines respectively. Comparing the damage pattern (third image down) with the pressure and equivalent

stress indicates that the damage begins to grow first in the high shear region just under the surface of the tile. As the damage develops and granular flow is activated, the local stresses are relieved. The cross section views of the deviatoric (fourth image down) and volumetric (bottom image) components of granular flow indicate that, for a fixed distance from the impact site, there is more granular flow away from the center of the tile than at the center. This occurs because of the effective inertial confinement at the center of the plate. The dilation associated with granular flow requires that the material on the surface of the plate moves away from the centerline to accommodate the additional porosity. Accelerating the material away from the center plane of the plate provides a confining stress that resists granular flow.

4.7 Summary and Future Work

We present a micromechanics based material model that incorporates flaw sampling statistics, damage growth from a distribution of interacting microcracks, a Mie-Grüneisen equation of state, and granular flow of the fully damaged material. A major feature of the model is the explicit incorporation of flaw sampling statistics by considering a Poisson process acting at each material point subvolume. This sampling process results in a distribution of effective material point strengths, which depends on both size and loading rate. We simulate an Edge on Impact experiment [43] to validate the model. We then use the model to understand why damage grows pref-

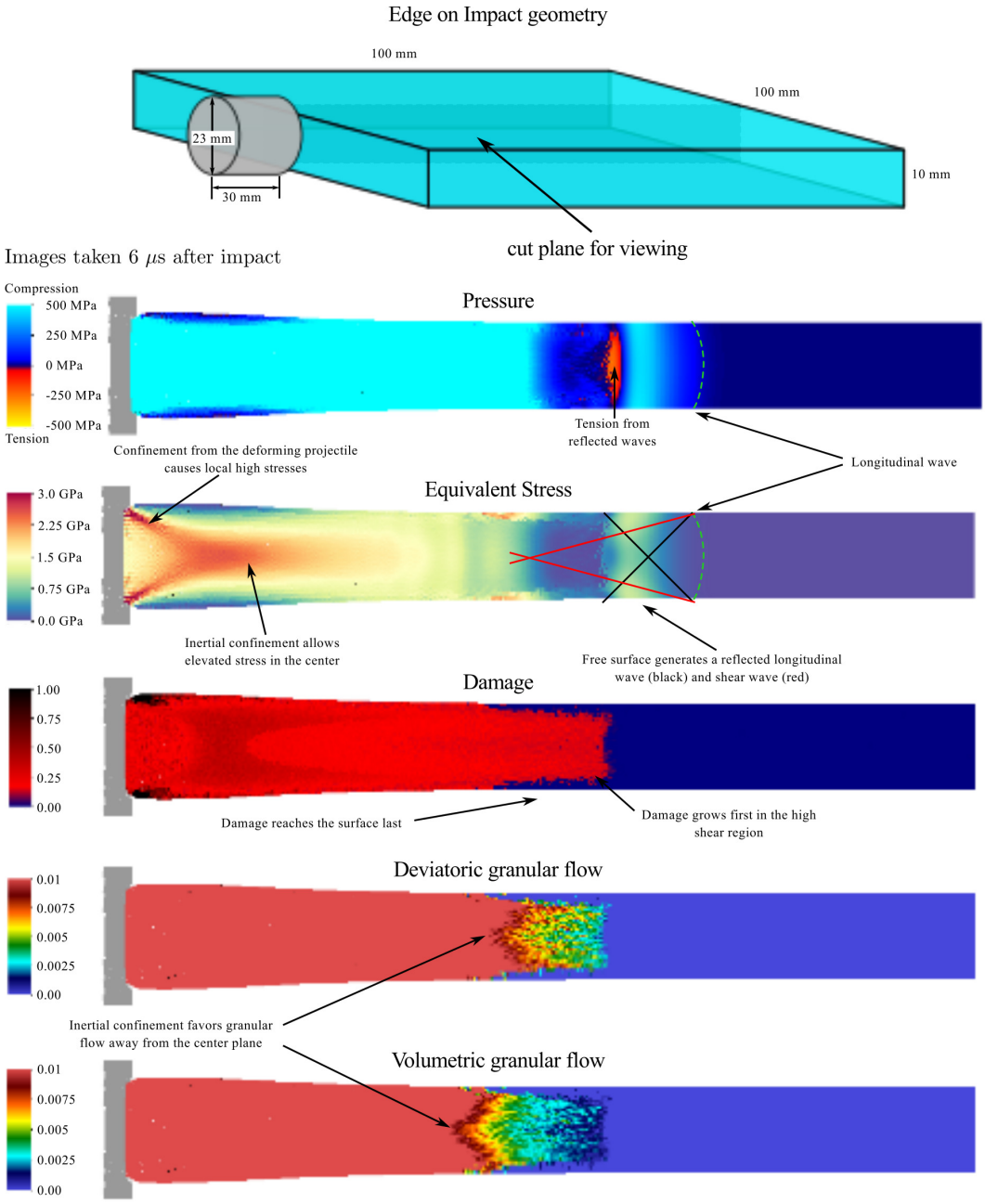

Figure 4.21: Cross sections from the simulation after 6 μs illustrate nonuniform behavior in the through thickness direction due to wave interactions and inertial confinement. Release waves from the longitudinal loading wave interact to initiate damage below the surface of the tile.

erentially in the interior of the plate rather than on the surface in that experiment, and discuss the coupling of propagation of the damage zone with crack kinetics and the parameters for the granular flow model.

The combination of this material model with a numerical technique allows us to perform detailed simulations of impact events where the failure process is linked to microstructural variables. The microstructural link is important for material design. In future work, it will be possible to use experimentally obtained microstructures to provide a flaw distribution, leading to the possibility of predictive material models. Similarly, since the microstructure is accounted for, we could perform a study using different flaw distributions to suggest promising investigation paths towards improved material performance.

Chapter 5

Simulations of Boron Carbide Under Uniaxial Compression and Simplified Ballistic Loading Using the Tonge-Ramesh Material Model

5.1 Introduction

Computational models of failure during impact events are important for a variety of impact applications including personnel and vehicle protection. In order to design new materials for improved protective systems, it is important to capture the competing mechanisms that control the performance of a given material under impact

loading conditions. Our interest here is the design of improved armor ceramic materials. Micromechanics based models (e.g that presented in section 4.3) that provide a connection between the material microstructure and the input parameters for application scale models can enable targeted material development and accelerate the design cycle. As these models are developed, one must ensure that they accurately reproduce the observed behaviors of the materials in the application environment. In this work, we perform simulations of two experimental loading geometries to test the model presented in section 4.3 for an advanced ceramic under a ballistically relevant range of impact conditions. First we discuss the important physical processes that occur during a high velocity impact event, and provide a brief review of the material model.

5.1.1 Energy Pathways in Impact Events

During high velocity impact events, there is a large amount of energy deposited in a short amount of time. Since the energy cannot travel through the material faster than the fastest wave speed in the material, the rapid nature of impact events leads to very high local energy densities. These high local energy densities activate a number of energy dissipation pathways. It is the nature of these pathways, the timescales over which they operate, and their effect on the structural integrity of the material that determine how a given material performs in a particular impact scenario. In this work, we focus on impact events on brittle materials where the energy dissipation

pathways are:

- shock heating,
- microcracking, and
- granular flow of the highly damaged material.

In addition to these energy dissipation pathways, brittle materials exhibit a distribution of strengths, which is important for controlling the onset and degree of localization leading to fragmentation.

When modeling impact events, the goal is typically to predict the outcome of a given impact scenario for a particular material (although quantitative measures of the outcome are often poorly defined). As industry moves towards leveraging computational power to reduce the number of costly design-build-test iterations required to bring a new product to market, there is increased reliance on the ability of computer models to predict the outcome of an impact scenario. For robust predictions of impact outcome, one first needs to capture the dissipation processes that occur during an impact event and the timescales associated with those processes.

In the previous chapter, we presented a mechanism based material model that captures these dissipation processes and captures the effect of material variability. In this work, we use that material model to simulate simplified ballistic experiments in which a tungsten carbide cobalt sphere impacts a boron carbide cylinder at velocities between 100 to 400 m/s. We begin by reviewing key features of the Tonge-Ramesh

material model. In the next section we simulate dynamic uniaxial compression loading to understand the effects of the model input parameters before continuing on to more complex loading conditions. In section 5.4 we simulate simplified ballistic experiments similar to the ones conducted by Lasalvia et al. [77] to validate the material model and to suggust future areas of research both to improve the performance of the material and to improve the predictive capabilities of the material model.

5.2 Brief Review of the Tonge-Ramesh Material Model

The material model developed by in chapter 4 is a mechanism based material model suitable for looking at the interaction of failure mechanisms in impact events for brittle materials. This micromechanics based damage model captures the important physical processes (figure 5.1) during impact events. It is useful to think of these processes in terms of both time and length scales. Starting from the green quadrant (upper right) in figure 5.1 and moving clockwise through the bubbles, the key physical processes are listed in generally increasing length and time scale after an impact event occurs. In the green quadrant labeled thermodynamic response we have the elastic response (specifically the shear modulus) and the equation of state. In the Tonge-Ramesh model this is a Mie-Grüneisen equation of state, but at higher impact velocities one may need a more complex equation of state. The orange box contains

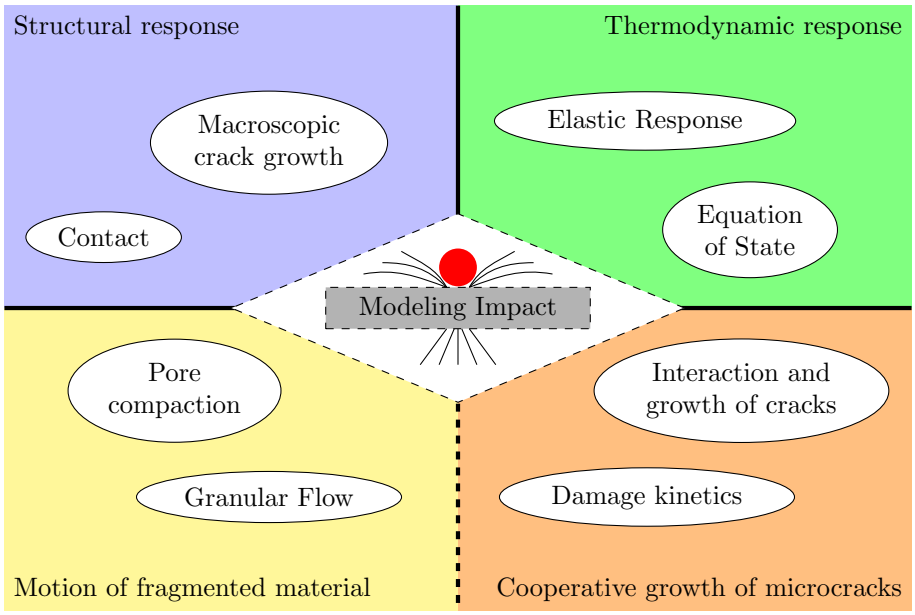

Figure 5.1: Important physical processes in impact events

processes associated with dynamic crack growth. Specifically, the interaction and growth of microcracks leads to rate effects [21] that limit the rate at which a material point with a given distribution of defects can fail through microcrack growth. These rate effects [21] are a direct result of the subscale flaw distribution and the existence of a limiting crack growth speed. Moving from the orange region in figure 5.1 across the dotted line to the yellow region, one moves to slightly larger length scales and later times. This region describes processes that occur within the fully damaged material as it continues to deform. The granular flow produces dilatation (and thus effective porosity) through an associative flow model. We include a pore compaction model to account for evolution of that porosity. The upper left corner of the figure lists physical processes that must be resolved by the computational mechanics framework

(they are changes to the boundary problem rather than subscale processes occurring within a representative material volume).

5.2.1 Key Equations in the Tonge-Ramesh Material Model

5.2.1.1 Elastic Response

The model assumes a decoupled representation of the Kirchoff stress tensor:

$$\boldsymbol{\tau} = \boldsymbol{\tau}_{dev} - p_s J_e \boldsymbol{I}. \tag{5.1}$$

The hydrostatic term ($p_s J_e \boldsymbol{I}$) correctly reproduces the P-α [59] model behavior when p_s is the pressure in the matrix material and the total volume change ratio (J) is divided into an elastic portion J_e and a distension that results from the granular flow J_{GP} ($J = J_e J_{GP}$). The deviatoric stress $\boldsymbol{\tau}_{dev}$ is a linear function of the deviatoric part of the volume preserving elastic deformation as measured by $\bar{\boldsymbol{b}}_e = J_e^{-2/3} \boldsymbol{F}_e \boldsymbol{F}_e^T$:

$$\boldsymbol{\tau}_{dev} = G \left(\bar{\boldsymbol{b}}_e - \frac{1}{3} \mathrm{tr}(\bar{\boldsymbol{b}}_e) \boldsymbol{I} \right). \tag{5.2}$$

Here G is the damaged shear modulus defined as:

$$G(D) = \left(G_0^{-1} + \frac{2D}{15} \left(3Z_r + 2Z_n - 4Z_c \right) \right)^{-1} \tag{5.3}$$

where the scalar damage parameter D is evolved using a micromechanics based damage model described in the next section. The parameters Z_n, Z_r, and Z_c are functions

(see section 4.3.4) of the elastic moduli and relate to the compliance of an individual crack. Similarly, the damaged bulk modulus is defined as:

$$K(D) = \left(K_0^{-1} + D\left(Z_n + 4Z_c\right)\right)^{-1}. \tag{5.4}$$

Since we use an equation of state that has a non-linear pressure-volume change ratio relationship, we account for the effect of the damage on the volumetric response by scaling the computed pressure for the undamaged material by the ratio of the damaged bulk modulus to the undamaged bulk modulus.

The volumetric response is determined by a Mie-Grüneisen equation of state which relates the elastic part of the volume change ratio (J_e) and the current temperature of the material (θ) to the pressure (p_s):

$$p_s(J_e, \theta) = \frac{K(D)}{K_0} p_H(J_e)\left[1 - \frac{\Gamma_0}{2}\left(1 - J_e\right)\right] + \rho_0 \Gamma_0 \left[e_c(J_e) + c_\eta(\theta - \theta_0)\right]. \tag{5.5}$$

Here p_H is the pressure on the principal Hugoniot, which depends on only the volume change ratio J_e and material parameters including the bulk wave speed (C_0) at room temperature and pressure, the density (ρ_0) at room temperature and pressure, and the slope (S) of the shock speed-particle velocity relationship:

$$p_H(J^e) = \begin{cases} \frac{\rho_0 C_0^2 (1 - J^e)}{(1 - S(1 - J^e))^2} & J^e < 1.0 \\ \rho_0 C_0^2 (1 - J^e) & \text{otherwise} \end{cases}. \tag{5.6}$$

5.2.1.2 Micromechanics of Damage

The micromechanics based damage model tracks a subscale distribution of flaw sizes that grow through a wing cracking mechanism when loaded in compression and

a tensile crack growth mode when loaded in tension. Within this model, the scalar damage parameter D is defined as:

$$D = \sum_{k=1}^{N_{\text{bins}}} \omega_k \left(s_k + l_k\right)^3 . \tag{5.7}$$

In the summation the bin number k loops over the N_{bins} that are used to discretize the local flaw size distribution, ω_k is the number density of flaws per unit volume that are represented by the flaw family k, and the initial flaw size is s_k, which has grown an additional length l_k due to the applied loading history.

We use a self consistent approach to compute the effective stress intensity factor due to both the applied load and the crack environment for the representative flaw size s_k. In addition to the stress computed from the self consistent solution, the stress intensity factor depends on the angle (ϕ) between the most compressive principal stress and the crack face normal as well as on the coefficient of friction between the two crack faces. From that stress intensity factor (K_I) we compute the crack growth rate using:

$$\dot{l} = \frac{C_r}{\alpha_c} \left(\frac{K_I - K_{IC}}{K_I - 0.5 K_{IC}} \right)^{\gamma_c} . \tag{5.8}$$

The increased crack length is used to update the damage parameter.

5.2.1.3 Granular Plasticity and Pore Compaction

When the damage parameter D reaches a critical damage level defined by D_c, granular flow is activated. The yield surface for granular flow is defined by:

$$f(\boldsymbol{\tau}) = \boldsymbol{\tau}_{dev} : \boldsymbol{\tau}_{dev} + A\left(\frac{\mathrm{tr}(\boldsymbol{\tau})}{\sqrt{3}} - B\right). \tag{5.9}$$

The visco-plastic granular flow model is a linear viscosity model (with a timescale τ_{GP}) that assumes associative flow (which, for this yield surface, leads to the production of effective porosity). The porosity evolution is accounted for by assuming that the maximum equilibrium porosity lies on a hydrostatic yield surface defined by:

$$f_\phi(P, J^{GP}, J) = \begin{cases} \frac{P}{P_c - P_0} - \frac{P_0}{P_c - P_0} \exp\left(-\frac{P_c - P_0}{2P_0(J_0^{GP} - 1)}(J^{GP} - J_0^{GP})\right) & P < P_0 \\ (J^{GP} - 1) - (J_0^{GP} - 1)J^2\left(\frac{P_c - P}{P_c - P_0}\right)^2 & P_0 \leq P < P_c \\ J^{GP} - 1 & P > P_c \end{cases} . \tag{5.10}$$

This is a simple porosity model with a quadratic crush behavior for pressures beyond P_0 and an exponential compaction behavior for lower pressures.

5.2.2 Model Parameter Selection

The parameters for the micromechanics based damage model describe the behavior of an individual microcrack and the distribution of microcracks in the system. Based on [4] we assume that the fracture toughness of boron carbide is 2.5 MPa $\sqrt{\mathrm{m}}$. As in chapter 4, we assume a bounded Pareto distribution with a maximum flaw size

$s_{\max} = 25\mu$m, a minimum flaw size $s_{\min} = 1.0\mu$m, and an inverse power law slope $\alpha = 2.6$ for the flaw size distribution. This flaw size distribution with a flaw density of $\eta = 22 \times 10^{12}$ flaws/m^3 gives a dynamic uniaxial compressive strength that is consistent with experiments [4]. Measurements of crack growth speed in boron carbide during dynamic compression in Kolsky bar testing have suggested crack growth velocities of 480 m/s [4] (6 percent of the Rayleigh wave speed). The observed speed of a surface crack in an opaque material represents a lower bound on the actual crack growth speed because one cannot guarantee that the crack growth direction is parallel to the surface and that the crack front is perpendicular to the surface. Recognizing these limitations, we assume a maximum crack growth velocity v_m of 20 percent of the Rayleigh wave speed. Given the lack of experimental data, we assume an exponent of $\gamma_c = 1$ in the crack growth law (equation 5.8). Consistent with chapter 4, we assume that granular flow begins when damage reaches 0.125 (D_c) and that continued microcrack growth stops when damage reaches 1.0 ($D_{\max}$). The micromechanics parameters for boron carbide that we use are summarized in table 5.1.

Chocron et al. [3] measured the residual strength of boron carbide fragments in a triaxial compression configuration. In this work they prepared the fractured boron carbide by thermal cycling the material. The specimens were then compressed in a triaxial compression configuration. They reported both the stress required to cause an initial load drop in the pre-damaged specimens and the residual strength of the specimens after the initial load drop. These results are summarized in figure

Minimum Flaw size ($s_{\min}$)	1.0 μm	
Maximum Flaw size ($s_{\max}$)	25 μm	
Distribution Exponent (α)	2.6	
Flaw Density (η)	22 $\times 10^{12}$ m^{-3}	Dynamic strength
Fracture Toughness (K_{IC})	2.5 MPa$\sqrt{\text{m}}$	Paliwal and Ramesh [4]
Maximum Crack Velocity(V_m)	0.2 C_r	Experiments
Crack Growth Exponent (γ_c)	1.0	
Coefficient of Friction (μ)	0.8	Chocron et al. [3]
Crack orientation (ϕ)	60°	
Granular Flow Activation Damage (D_c)	0.125	
Maximum Damage ($D_{\max}$)	1.0	

Table 5.1: Baseline flaw size distribution and micromechanics damage model parameters for boron carbide

5.2. In addition to the experimental results, figure 5.2 shows the uniaxial stress compression path (dashed line) and the best fit granular flow function used in this work ($A = 0.8$ and $B = 3$ MPa). Based on a flaw density of 22×10^{12} flaws/m^3, the average flaw spacing is 35 μm, which corresponds to flaw communication times of 2.7 ns (longitudinal wave) and 4 ns (shear wave). As discussed in section 4.3.5 and [74], the granular flow timescale should depend on the fragment size in the granular material. We select a granular flow timescale of 7 ns, which corresponds to most cracks linking up to form fragments (we investigate the effect of choosing different granular flow parameters in section 5.3.1.1). We choose $P_0 = 100$ MPa, $P_c = 10$ GPa, and $J_0^{GP} = 2.0$ as the parameters for the pore compaction model. These parameters are poorly constrained and additional experimental work on the compaction behavior of boron carbide at high pressures would improve the model. The granular flow and pore compaction parameters are summarized in table 5.2.

Effective friction coefficient A_0	0.8	Chocron et al. [3]
Cohesive Strength (B_0)	3 MPa	Chocron et al. [3]
Relaxation time (τ_{GP})	7×10^{-9} s	
Reference crush pressure (P_0)	100 MPa	
Reference distension (J_0^{GP})	2.0	
Consolidation pressure (P_c)	10 GPa	

Table 5.2: Baseline boron carbide granular flow and pore compaction parameters

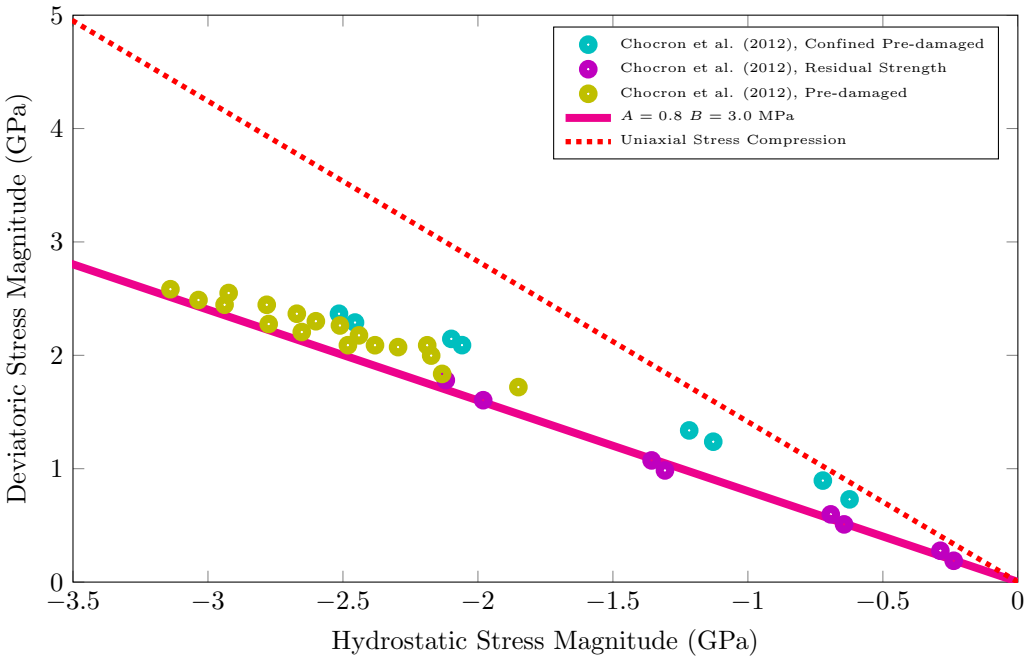

Figure 5.2: Experimental measurements of the strength of damaged boron carbide under confinement using triaxial compression experiments[3]. Experimental data is shown with open circles and the flow surface for different selections of granular flow parameters are shown in solid lines. The dashed line is the uniaxial compression path.

Density (ρ)	2520 kg/m^3	Theoretical density [81]
Specific Heat Capacity (C_v)	962 J/(kg K)	Dandekar [80]
Bulk sound speed (C_0)	9.6 $\times 10^3$ m/s	Calculated
$U_s - U_p$ Slope (S)	0.914	Dandekar [80]
Grüneisen Parameter Γ_0	1.28	Dandekar [80]
Shear Modulus (G)	197 GPa	Paliwal and Ramesh [4]
Bulk Modulus (K_0)	232 GPa	Dandekar [80]

Table 5.3: Equation of state parameters for boron carbide

A number of authors have conducted plate impact experiments on boron carbide [78–80]. There is no consensus on a single equation of state for this material, and it has been suggested that this is because each of the experimental investigations use a slightly different version of the material. In light of this disagreement, we use the material parameters contained in [80] because this reference used the Cercom PAD Boron Carbide that was used in the experiments that we discuss in subsequent sections. We modify the bulk wave speed reported in [80] to be consistent with the theoretical density ($\rho_0 = 2520$ kg/m^3) and bulk modulus ($K_0 = 232$ GPa). The baseline equation of state parameters used are summarized in table 5.3.

5.2.3 Implementation of Material Variability

Micromechanics based damage models that explicitly track the subscale flaw distribution provide a natural mechanism for incorporating physically based variability into the material response. The variability of ceramic materials is a well established experimental observation. As discussed in section 4.5, the specific distribution of strengths is a function of both loading rate and specimen size. In general, this distri-

bution is non-Weibull. There are a variety of ways that one could specify the local flaw distribution. In chapter 4 we used a Poisson process at each material point to determine the local flaw distribution.

When the local flaw distribution is defined using a Poisson process, as discussed in section 2.2, there are two consequences that have implications for convergence. First, the length scale of the fluctuations in the local flaw distribution changes with mesh size, and therefore any length scale that depends on the local flaw distribution also changes with mesh size and cannot provide a length scale for numerical convergence. Secondly, each successively finer mesh is a new realization of the flaw distribution within the specimen. Effectively, each simulation creates a new specimen, so we expect some scatter in the results, just as we expect scatter in the experimentally measured dynamic strength. This variability, while physical, complicates the assessment of convergence and may require an approach such as the one described by Bishop and Strack [48]. Since assessing convergence in distribution is computationally expensive, we choose to separate the description of the local flaw density from the computational discretization and *define* the fluctuations in local flaw density as a model input like the problem geometry.

Physically, we consider a single specimen where the spatial distribution of flaws follows a Poisson process. We then compute the local flaw density using a moving window averaging approach with a window size λ_w. This process results in a smooth flaw density field with a minimum length scale λ_w. By defining the flaw density field

as a continuous function that is independent of the discretization length scale and ensuring that the same function is used for all resolutions, the convergence question is no longer statistical, and a traditional mesh refinement study can be used. We have performed a number of mesh refinement studies using this approach for specifying the local flaw density and the simulation geometry shown in figure 5.3. For some sets of material parameters and loading rates, the material model seems to converge with mesh resolution while for other choices of material parameters it does not seem to converge. This emphasizes the need for caution when interpreting the results from simulations with softening material models. The physics in the model does put a lower limit on the computational mesh size, because the computational subvolumes (MPM particles in this work) should be large enough that almost all of the particles in a simulation will contain at least one flaw. A particle without a flaw will have infinite strength because microcracking is the only failure mechanism considered. Future revisions to the model will remove this restriction and possibly incorporate dislocation based plasticity or a mechanism for crack nucleation and propagation from one material point into another. Adding these additional physical mechanisms may improve the convergence behavior of the model, but those studies are left to future work.

We define the local flaw density $\hat{\eta}$ as the mean flaw density η plus a local fluctuation that is the superposition of sine functions with predefined wave vectors ($\boldsymbol{k}_i$) and a

random phase (ϕ):

$$\hat{\eta}(\boldsymbol{x}) = \eta + \sum_{i=1}^{N_k} \beta_i \sin(\boldsymbol{k}_i \cdot \boldsymbol{x} + \phi_i). \tag{5.11}$$

Here $\boldsymbol{x}$ is the position vector and β_i is the amplitude of the fluctuations. Since the Poisson process is a white noise process, we choose a constant amplitude such that the standard deviation of the fluctuations is equal to the standard deviation of a Poisson process at the averaging scale (λ_w):

$$\beta_i = \beta = \frac{1}{\sqrt{2}} \sqrt{\frac{\eta}{\lambda_w^3}}. \tag{5.12}$$

The wave vector $\boldsymbol{k}_i$ is composed of both a magnitude and a direction. For the direction we take motivation from the vertex spacing in a regular dodecahedron, which provides the location of 20 equally spaced points on the unit sphere. Since positive and negative directions with respect to each wave vector are treated the same, we discard the 10 points in the southern hemisphere of the sphere due to symmetry. The magnitude of the wave vector is given by 2π divided by the wave length. For these simulations we used wave lengths of $\lambda_w = 0.5$ mm, $2\lambda_w$, $4\lambda_w$, and $8\lambda_w$. Using 10 orientations for each wave length results in a total of 40 different wave vectors. In addition, we apply a random rotation to each set of 10 wave vectors to prevent them from lining up exactly. One can view this Fourier-like process as a method of creating a realization of the fluctuations in flaw density based on a fixed averaging length.

In this work, we use this Fourier-like approach when we need a consistent and predictable variation in the local flaw distribution. We use the Fourier-like approach

in section 5.3.1. We use a Poisson process when comparing to experiments or interpreting experimental results because the Poisson process captures the variability more accurately. When a Poisson process is used, we follow the procedure presented in section 2.2 with the modification that the representative flaw size within a bin is given by the 3-norm of the flaw sizes within a bin instead of the sample mean that was used in section 4.2. As suggested in section 2.2.1.1 this leads to a more rapid convergence of the simulated flaw distribution to the input flaw size distribution.

5.3 Dynamic Uniaxial Compression

Chapter 4 discussed the behavior of this material model with respect to homogeneous uniaxial compression and Edge on Impact. However, experiments [4] demonstrate heterogeneous damage growth even under uniaxial compression. Simulations of dynamic uniaxial compression loading like that encountered in Kolsky bar loading [4] are thus also useful for evaluating this material model, because this is a loading condition that is nominally homogeneous except for the symmetry breaking effect of the fluctuations in initial damage.

To insure a stress state that is minimally affected by the numerical contact algorithm, we design a simulation geometry that consists of a rigid loading platen acting on a section of material that is constrained to be elastic, which then transfers the load to the test section. The dimensions of the simulation geometry are shown in

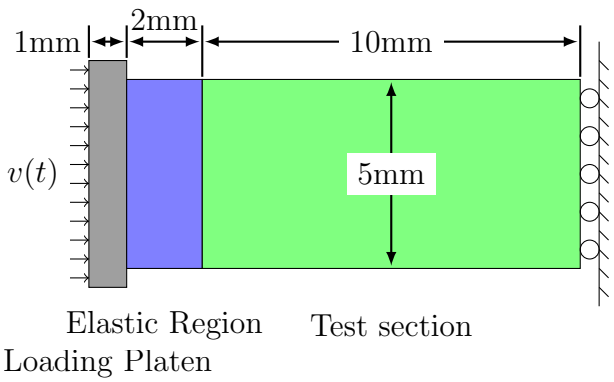

Figure 5.3: The uniaxial compression geometry is composed of a rigid loading platten, an elastic buffer region and a test section. The elastic properties of the buffer region and the test section are the same to eliminate stress concentrations. We assume perfect no-slip contact for all interfaces.

figure 5.3. The loading platen is 1 mm thick followed by the 2 mm elastic region with the same elastic properties as the 10 mm test section and finally a roller boundary condition at the far surface (this geometry does not correspond to typical experimental geometries). The specified platen velocity is rigidly enforced and the reaction force is recorded as an output. The elastic region serves to smooth out any stress fluctuations or elastic mismatch resulting from the rigidly applied velocity history on the loading platen. Since the elastic buffer region and the test section are treated as perfectly bonded (infinite friction) and are initially elastically matched, there is no stress concentration as a result of the load application prior to material failure.

The uniaxial compression configuration shown in figure 5.3 provides a convenient mechanism to interrogate the effect of the model parameters in a simplified loading

environment. While the boundary conditions in the experiments and simulations are different, we seek to understand which components of the material model affect the peak stress and the stress collapse rate in the simulations, and hope to gain additional information about the failure process in ceramics from these simulations.

5.3.1 Influence of Model Parameters

For the baseline material parameters, we use the values discussed in the previous section (shown in tables 5.1, 5.2, and 5.3). Figure 5.4 provides the computed platen reaction force normalized by the initial specimen area (interpreted as the applied boundary stress) as a function of time for a dynamic uniaxial compression simulation using a nominal strain rate of 500 1/s and the baseline material properties. While the computational simulations provide the damage and granular flow at all points within the simulation domain, for this section we focus on the peak stress and the time it takes for the stresses in the material to collapse (labeled in figure 5.4).

5.3.1.1 Effect of the Granular Plasticity Model

The slope of the flow surface in the granular flow model is determined by the parameter A. When this value is increased the effective behavior of the granular material is more sensitive to changes in the hydrostatic pressure. One expects this type of behavior for more angular fragments. From the baseline simulation we increase the granular slope and set $A = 1.2$ while still allowing the competition between damage

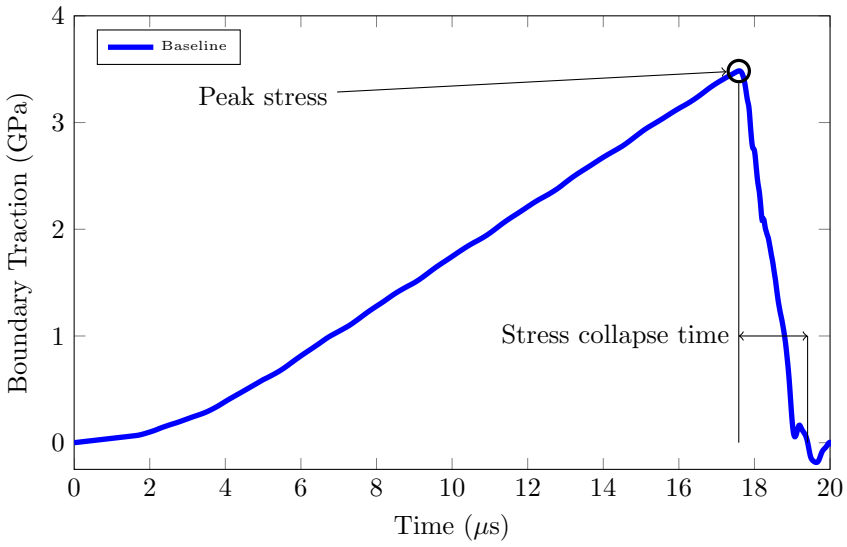

Figure 5.4: Boundary stress as a function of time for the baseline dynamic uniaxial compression simulation using the Fourier like process to assign the local flaw density. The peak stress and time it takes the stresses to collapse are indicated in the figure.

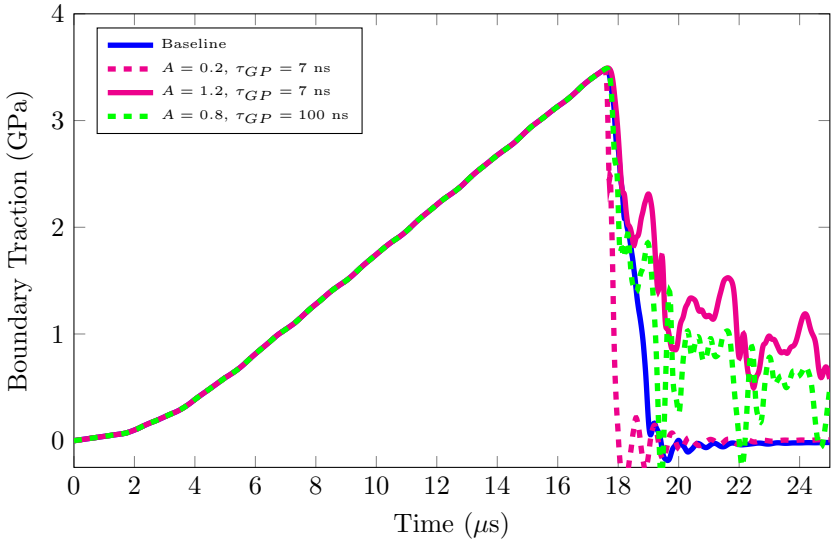

Figure 5.5: Boundary stress as a function of time as the granular flow parameters are changed. The magenta lines represent changes in the granular slope, and the dashed green line represents changing the granular flow timescale.

and granular flow ($D_{\max} = 1.0$). The boundary stresses collapse more slowly than in the baseline simulation, as shown by the solid magenta line in figure 5.5. We note that section 4.6.2 demonstrated that a slope of 1.2 was inconsistent with the surface damage propagation in edge on impact experiments, but we include the high granular slope for completeness. The boundary stresses collapse more slowly because the increased pressure sensitivity of the granular material results in a larger dilatation as granular flow occurs and that provides an inertial confining stress that slows damage growth, and slows the granular flow, resulting in a reduced stress collapse rate. Additionally, the collapse of the stresses is no longer smooth. This could be caused by stress waves interacting with the lateral boundaries of the specimen and reflecting as compressive waves. The time between a local minimum and a local maximum is about 0.5 μs, which is consistent with the time it takes a stress wave to travel from the center of the specimen to the boundary and back (the longitudinal and transverse wave speeds are 13 mm/μs and 8.8 mm/μs respectively). The added compression would increase the confinement in the specimen leading to an increase in the strength and a spike in the stress during the stress collapse process.

Decreasing the granular slope in the granular flow model should cause the opposite effect of increasing the friction angle. Decreasing A to 0.2 should accelerate the collapse of the stresses, since the stresses are easily reduced through granular flow. This is the observed response as shown in the dashed magenta line in figure 5.5. The stresses collapse rapidly due to the low bulking and low strength of the damaged

material.

The baseline simulations use a granular flow timescale of 7 ns based on the wave transit time between flaws. If fewer flaws are activated or more than one wave transit cycle is required for motion of the granular material, then the time scale for granular flow increase. The dashed green line shows in Figure 5.5 shows the boundary traction that results from using a granular flow timescale of 100 ns instead of 7 ns. The peak stress remains the same as in the baseline case, but the stresses collapse slower after the peak load is reached. In this case we also see the non-smooth collapse behavior and attribute it to the same wave propagation effect as in the case for $A = 1.2$.

5.3.1.2 Effect of the Damage Model

Some micromechanics based damage growth models only account for elastic softening due to damage growth (e.g. [10]) and do not include a transition to granular flow. We simulate this type of behavior in our material model by setting the maximum allowable damage ($D_{\max}$) to a large number (in this case 15) and setting the cohesive strength for granular flow to a large value ($A = 0.8$ and $B = 100$ GPa) to ensure that the stress stays inside of the granular flow surface at all times for these loading conditions. This has the effect of disabling granular flow and allowing large amounts of elastic softening due to damage. As shown in the olive line in figure 5.6, the model with granular flow suppressed has about the same peak strength as the baseline model, but the stresses collapse faster than the baseline case. This acceler-

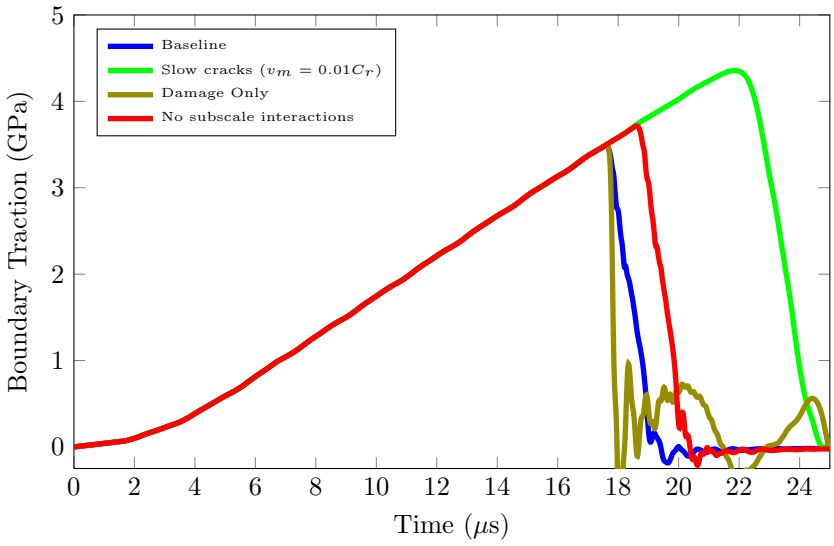

Figure 5.6: Boundary stress as a function of time as different aspects of the damage model are changed. The light blue curve represents the case where granular flow is suppressed. The orange corresponds to decreasing the maximum crack growth speed by a factor of 20. The red curve results from suppressing crack interactions.

ated stress collapse is a result of the crack interaction model. In section 4.3.4, the effective crack interaction term (Z_c) was chosen so that as the damage level increases, an applied uniaxial compressive stress causes increasing transverse tension, which accelerates damage growth (consistent with experiments [64]). The accelerated damage growth rate leads to accelerated material softening and a shorter time between the peak stress and the collapse of all of the stresses in the material.

The baseline simulation assumes that the maximum crack growth velocity is 20 percent of the Rayleigh wave speed; however as mentioned in section 5.2.2, this quantity is difficult to measure experimentally. To test the effect of this material param-

eter, we reduce the maximum crack growth velocity by a factor of 20 to 1 percent of the Rayleigh wave speed and plot the resulting boundary traction as a function of time in the green curve in figure 5.6. As expected, the peak stress attained in the specimen is higher than the reference simulation (blue line); however, the profile of the applied load as a function of time curve is similar to the baseline simulation suggesting that the damage kinetics are not the only factor that control the rate of collapse of the stresses in the material.

In this model we use a self consistent approach, where the crack interactions are addressed through their effect on the compliance of the effective medium surrounding a representative crack. This leads to the development of tensile stresses transverse to an applied compressive stress. This tensile stress accelerates the crack growth eventually leading to unstable crack growth. Other damage models handle the crack interactions differently. One extreme case is a model that assumes no crack interaction. To demonstrate the effect of this interaction term we perform a simulation with the subscale crack interaction term disabled. While we have disabled subscale crack interactions in this simulation, we are still solving an initial boundary value problem and the local regions can explicitly communicate with each other through the resolved changes in the stress field. The results from this simulation are plotted in the red curve in figure 5.6. The peak stress increases slightly relative to the baseline configuration, but the stress collapse behavior remains unchanged. This behavior is expected because the reduced crack interactions result in a reduced damage rate,

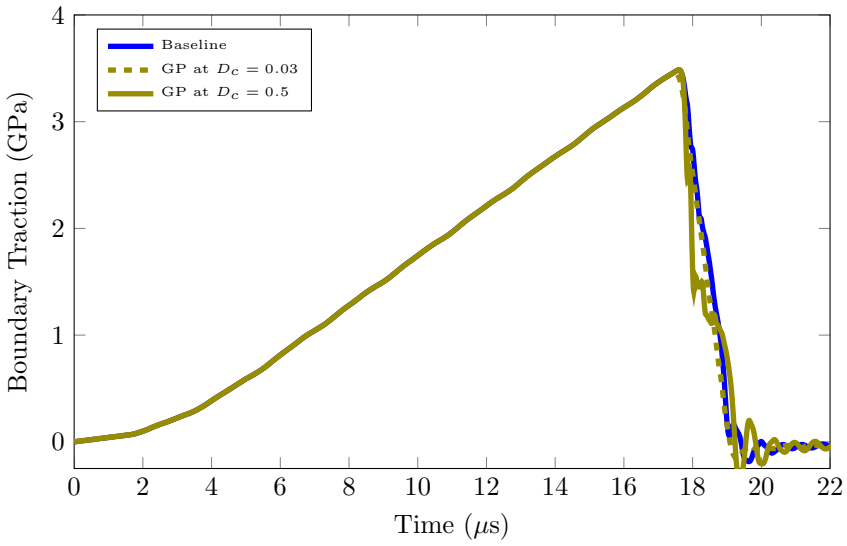

Figure 5.7: Boundary stress as a function of time for looking at the effect of the damage value (D_c) used to enable granular flow. The boundary stress response is not very sensitive to this parameter.

which will increase the peak stress; however, as discussed in the previous paragraph, the collapse behavior is a consequence of both the damage kinetics and the granular flow.

A final piece of the model, is the damage level required to activate granular flow. In the baseline case this critical damage level (D_c) is 0.125; however, other values could be justified. To ensure that the results are not excessively sensitive to this choice we preformed one simulations where this parameter was reduced to 0.03 and another where the parameter was increased to 0.5. As shown in figure 5.7, the choice of this parameter has very little effect on the boundary stresses in this dynamic uniaxial compression simulation.

In this section we have demonstrated that the model parameters affecting the damage evolution calculation do not control the rate of collapse of the stresses under uniaxial compressive loading. The rate of collapse is sensitive to some of the granular flow parameters, but physical arguments (and the results from chapter 4) preclude the use of extreme values of either A or τ_{GP}.

5.3.1.3 Effects of Flaw Size and Flaw Density

The previous simulations assumed that the flaw distribution was a bounded Pareto distribution which extended from 1.0 μm to 25 μm with a power law slope of 2.6. Having a distribution of flaw sizes affects the rate sensitivity of the material strength [21]. For an observed strength, at a single strain rate, there are many choices of flaw density and flaw size that could fit the data using only a delta distribution of flaw sizes. To understand the coupling between the flaw density, flaw size, and the macroscopic behavior, we look at two delta distributions of flaw sizes. We define a large flaw distribution where the flaw size is 20 μm and the flaw density is 18×10^9 $1/\text{m}^3$ and a small flaw distribution were the flaw size is 8.75 μm and the flaw density is 4×10^{12} $1/\text{m}^3$. Under homogeneous loading conditions (using a single material point), both of these distributions fit the experimentally observed strength. Like all of the other simulations in this section, these simulations were performed using a mesh resolution of 62.5 μm/cell. At this fine mesh resolution there is on average one flaw per material point with the small flaw distribution and one flaw for every

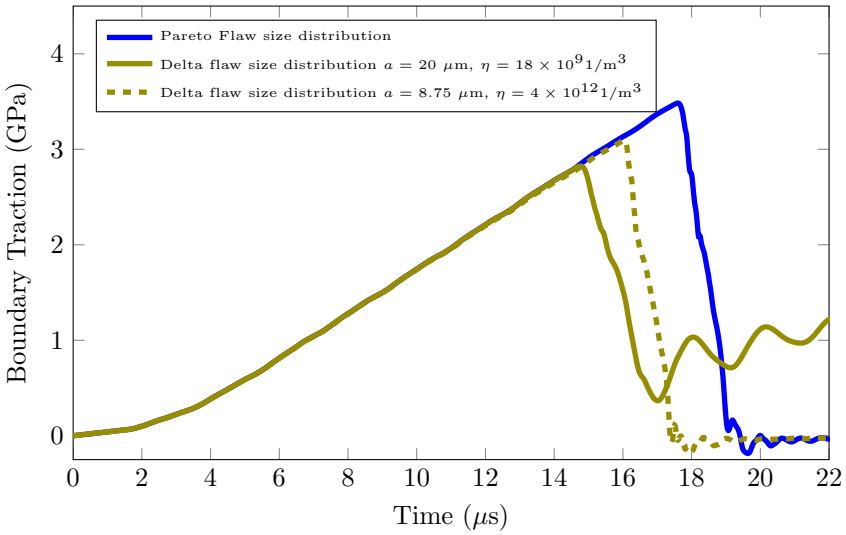

Figure 5.8: Boundary stress as a function of time for a delta distribution of crack sizes. The blue line is the baseline simulation. The dashed olive colored line corresponds to a high density of small flaws, while the solid olive colored line corresponds to a lower density of large flaws. Both combinations of flaw size and flaw density match the dynamic strength for homogeneous loading conditions.

250 material points with the large flaw distribution. This inconsistency between the physical spacing between the flaws and the mesh resolution is another motivation for the more physical Poisson based flaw distribution assignment process. However, we use these two flaw distributions to illustrate a feature in the model. The amplitude of the fluctuations in the Fourier like spatial distributions were updated to reflect the changed flaw densities using equation (5.12). Since the flaw density for the large flaw case is so low, the 0.5 mm wave length fluctuations were suppressed to avoid regions of zero flaw density.

The simulation involving the large flaws has the lowest strength and the slowest collapse rate. In figure 5.8, the solid olive curve represents the boundary stress for the large flaw case while the dashed olive line represents the boundary stress for the simulation with a greater density of smaller flaws. The low strength and slow collapse rate for the large flaw simulation is likely because the large flaws initiate damage early but grow slowly (because of the lower density) leading to a more gradual collapse of the stresses. This indicates the importance of both the flaw size and the flaw density.

5.3.1.4 Influence of Method of Assigning Microstructure

The previous sections described the effect of the material model parameters on the boundary stress as a function of time for dynamic uniaxial compression simulations. In all of these simulations, we assigned the local flaw density using a Fourier like process and did not change the representative flaw size for each bin within a simulation. In the more realistic approach based on a Poisson process described in chapter 2.2, both the local flaw density and the local flaw size distribution vary throughout a specimen. To investigate the effect of the procedure used to assign the local flaw distribution, we compare dynamic simulations where the initial microstructure is assigned using a Poisson like process and one using the Fourier like process.

Variations in the representative flaw size for each bin through out the specimen result in local regions that initiate damage earlier than the surrounding material. This effect is similar to the regions with higher local flaw densities produced through the

Fourier approach; however, since they may have both larger flaws and a higher local density, they can be activated sooner than the regions that just have a higher local flaw density. The consequence of having more weaker regions is that the simulated strength is lower than the simulation using a Fourier like approach, as shown in figure 5.9. There is also a clear difference in the damage pattern for these two simulations. When the Fourier like approach is used, the localized damage initiation sites quickly grow and granular flow is activated in the majority of the body. The Poisson process, on the other hand, favors the development of thin damage regions that form a network around regions with very low damage. These connected regions where the damage is below the threshold for granular flow can be interpreted as fragments. The development of moderately large fragments during dynamic compression is consistent with the experimental images shown in [4].

5.3.1.5 Effect of Granular Flow Timescale When Using a Poisson Process to Assign the Local Flaw Distribution

When the granular flow timescale decreases to 7 ns from 100 ns the peak stress and the stress collapse time decreases. Previous authors that have used linear viscosity models for granular flow have used timescales ranging from 1 μs [74] to 10^{-13} μs [27] depending on the type of problem and the resolution of the simulation. The selection of this timescale likely will depend on the loading rates in the problem because in

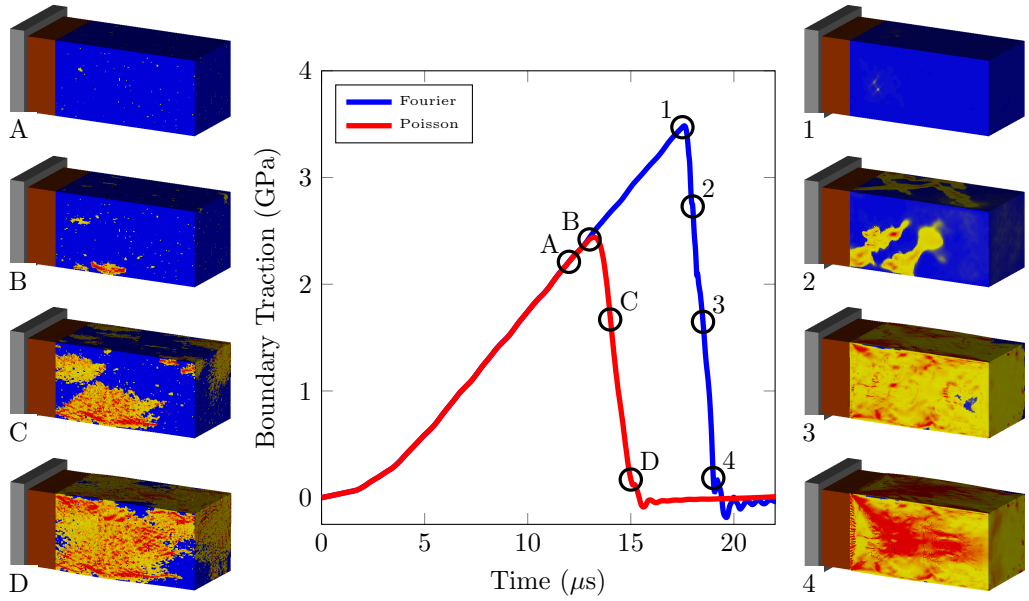

Figure 5.9: Consequence of using a Poisson process (left) instead of a Fourier like process (right) to assign the local flaw size distribution and flaw density. The images on the left show snapshots of the damage pattern for the Poisson process while the images on the right show the damage distribution when flaw densities are assigned using a Fourier like process. The Fourier like process seems to promote inclined damaged regions while the Poisson process produces damaged regions aligned with the compression axis.

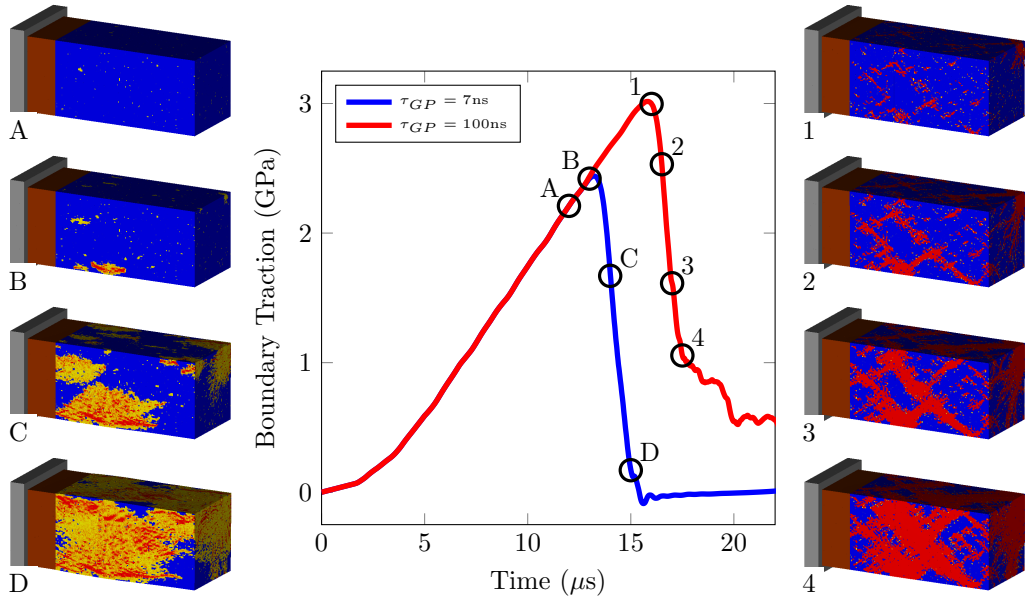

Figure 5.10: Changing the granular flow timescale has a large effect on the failure pattern and a shorter granular flow timescale promotes a more axial orientation for the damage features, while the longer timescale promotes a shear faulting damage mode and higher lamage levels. Flaw distributions are assigned using a Poisson process for both simulations

general higher loading rates will produce smaller fragments which should use a smaller timescale. Since this granular flow timescale plays an important role in the behavior of the material, we also discuss the effect of this timescale in the context of the simplified ballistic simulations (section 5.4.2.4).

When the granular flow timescale decreases from 100 ns to 7 ns, we see two changes in the response shown in figure 5.10. First, more of the material has a damage value near 0.125 (the yellow color) instead of a value of 1.0 (shown in red).

This indicates that the granular flow time scale is fast enough for the granular flow to releve the stresses and prevent further damage growth. Since there are some regions of red in the image, we conclude that these granular flow parameters do not completely suppress further damage growth. It is physically reasonable to have similar timescales for granular flow and continued damage growth because it is possible that the grains continue to fracture during granular flow. Secondly, the zones with the highest damage levels (red zones with $D = 1.0$) align with the compression axis for the run with a 7 ns granular flow timescale. This is likely because the fast granular flow promotes more localization. When granular flow occurs and relaxes the shear stresses in a region, the material bulks increasing the pressure in the failed material. This increased pressure must be balanced by either inertial confinement or the stresses in the surrounding material. When the stresses in the surrounding material are used this will tend to drive localized regions of damage.

5.3.2 Comparing Simulations of Dynamic Compression and Kolsky Bar Experiments

5.3.2.1 Dynamic Uniaxial Compression Experiments

Kolsky bar testing is an experimental technique for subjecting specimens to homogeneous deformation at high strain rates. In this technique, as in quasistatic testing, the experiment is designed such that the entire specimen is loaded uniformly at the

desired strain rate. During a Kolsky bar test, energy is delivered to the system when a projectile impacts an incident bar causing an elastic wave to form in the incident bar. The incident bar acts as a wave guide that transmits the stress pulse to the specimen. The shape of the stress pulse can be controlled by changing the length and velocity of the projectile as well as through the use of "pulse shapers" [82] placed between the striker bar and the incident bar. Once the stress pulse reaches the specimen, a portion of the stress pulse is transmitted through the specimen and into a third bar called the transmitted bar. By measuring the incident, reflected, and transmitted stress pulses, one can reconstruct the stress history at the interface between the bars and the specimen, provided that the bars remain elastic through out the test.

When using the Kolsky bar technique, one must take extra precautions to ensure that the recorded response of the specimen represents homogeneous loading at the desired constant strain rate [83]. In particular "pulse shapers" are used to convert the square pulse loading from the impact event into a triangular pulse that has a constant stress rate [4, 82], since ceramic materials remain mostly elastic prior to failure, the stress rate is proportional to the strain rate.

In the boron carbide experiments conducted by [4], the authors used cylindrical specimens with a diameter and length of about 3 mm. In these experiments, the authors observed a dynamic strength of 3.8 GPa at a strain rate of about 500 1/s. During these tests high speed imaging revealed a failure process as follows:

- Cracks are first visible on the specimen surface about 4 μs prior to the peak

load

- Over the next few microseconds these cracks that are visible on the surface grow in an apparent (only the intersection of the crack with the surface is visible) axial direction

- at the peak stress many axial cracks are visible, but the axial pieces that look like columns are well aligned and intact

- after the peak stress, the material continues to fragment into pieces. The largest of these pieces are several hundred microns in size. From the stress-time plot, the time for the stresses to collapse in these experiments was 8 μs.

As discussed in [83], a stress collapse the occurs in less than 6.4 μs can be severely affected by dispersion in 12.5 mm diameter steel bars. Additionally, the effective strain rate increases as the specimen fails, as shown with SiC-N in [82]. Both the dispersion in the bars and the increasing strain rate during failure can lead to an increase in the observed time it takes for the stresses to collapse in the experiment. Because of these complications, many experiments on brittle materials focus on the dynamic strength of the material and not on the failure process. However, during a penetration event, the projectile is interacting with the fragmented material directly and with the intact ceramic only through the damaged material [25] for this reason, and because it provides a stronger test of the material model, we compare our simulations of dynamic compression of boron carbide with these experiments.

5.3.2.2 Simulation Results

There are a few important differences between the boundary conditions in the simulations and the experiments. First the specimens in the experiments were 3mm long cylinders while the gauge section in the simulations is 10mm long with a 5mm square cross section. Secondly, the platens in the experiments are lubricated to reduce the coefficient of friction between the specimen and the platen, while the simulation assumes perfectly bonded contact an incorporates a buffer region that is constrained to remain elastic between the platen and the gauge section. The elastic buffer region successfully isolates the gauge section from the contact at the platen boundary, so that 6 μs into the simulation (prior to damage growth and during constant strain rate loading) the average of the transverse stress magnitudes is less than 2.5 percent of the magnitude of the axial stress ($\frac{|\sigma_{22}|+|\sigma_{33}|}{2|\sigma_{11}|} < 0.025$). Regions further from the elastic buffer region are even closer to a uniaxial stress state. The larger specimen size in the simulations was chosen because this material model was designed to homogenize the behavior of several subscale cracks into an constitutive behavior. This places a limit on the minimum mesh size that can be used in the simulations (chapter 4). To obtain a high resolution of the failure process, we increase the specimen length to 10 mm. We maintain the 5mm cross-section so that we have a larger region of the gauge section that is far from the elastic buffer region.

The 2:1 aspect ratio in the simulations introduces two communication timescales into the problem. The time that it takes a longitudinal wave to travel between the

two transverse boundaries is 0.4 μs, while it will take just under 1 μs for a wave to travel from the loading platen to the roller boundary condition on the opposite end of the specimen. In the experiments the communication time is 0.25 μs due to its smaller size. In the simulations, the displacement boundary conditions are applied rigidly at the platen and the roller boundary (resulting in a constant strain rate during material failure), while in the experiment, the specimen boundary condition in the loading direction is a mixed boundary condition. A direct consequence of this boundary condition is that as the specimen fails, the strain rate in the specimen increases [82].

Figure 5.11 shows a comparison of one experimental result (reproduced from [4]) and the simulation results. In the simulations the stress rises linearly with time from 4 μs to 13 μs after an initial period while the stresses in the specimen homogenize (0 to 4 μs). Once the peak stress is reached at point B, the stresses collapse in 2 μs. The experiments reach a higher stress level and the stresses collapse more slowly than in the simulations. The higher experimentally observed strength may be due to the smaller volume of the experimental specimen; however, it is more likely that the calibrated flaw distribution produces an effective material response that is too weak. The flaw distribution was calibrated to the experimental results without accounting for the effect of variability or a non-homogenous stress state, and both of these (when present in the simulation) will reduce the simulated strength. One could recalibrate the flaw distribution to match the Kolsky bar results, but since the

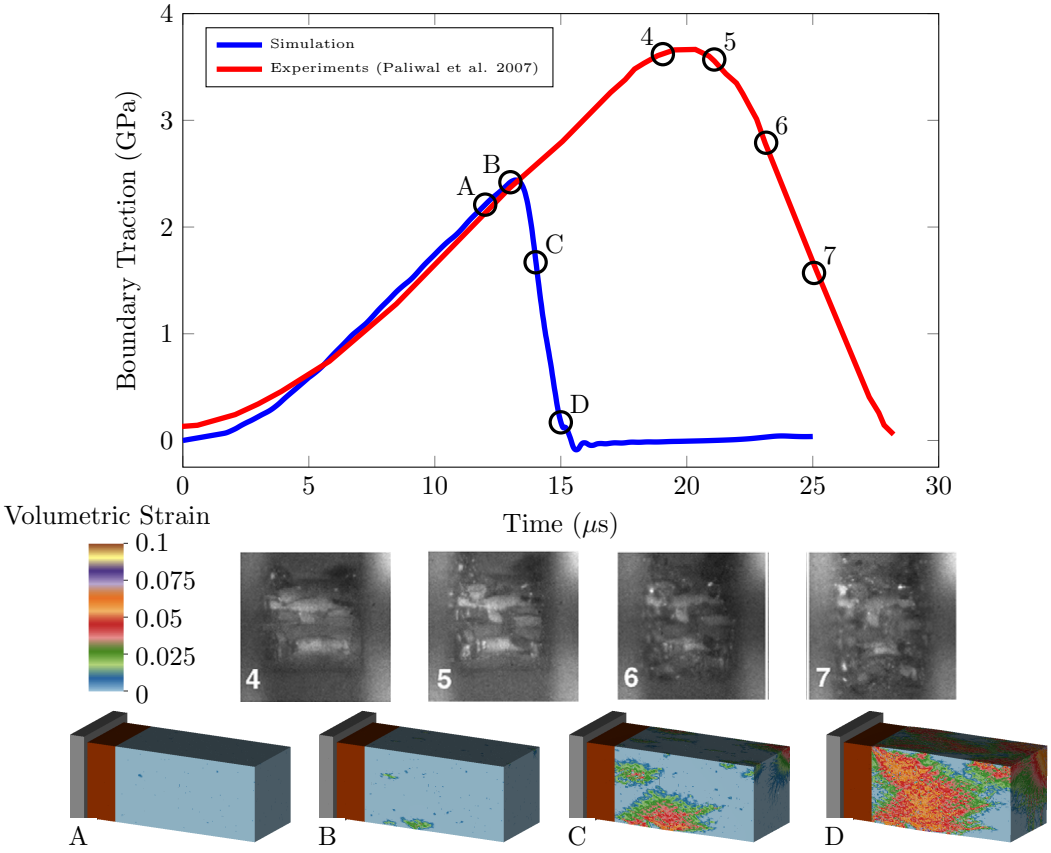

Figure 5.11: Comparison between dynamic compression simulations and Kolsky bar experiments on boron carbide. The experimental images and results are reproduced from [4]. The simulation images (labeled with letters) show the volume change ratio due to granular flow. Both the simulations and the experiments show the formation of high aspect ratio fragments at late times and a small amount of damage on the surface at the time of the peak stress.

purpose of this paper is to discuss the general behavior of the model, we recognize these limitations in the calibrated material parameters during our comparison with experiments. Additionally, the effective strain rate during specimen failure increases in the experiments but does not in the simulations.

In the simulation images, we begin to see granular flow (distension that indicates the insertion of porosity) on the specimen surface just before the peak stress at time A. At the peak stress there are some isolated regions of granular flow on the specimen surface. These regions are aligned in the axial direction, which is consistent with the experimental results (images 4 and 5). As failure progresses to images C and D, the regions of granular flow extend towards the right. In image D the localized region of granular flow near the end with symmetry boundary conditions should be interpreted as a crack propagating towards the boundary and forming a fragment in the bottom right corner (light blue regions are intact material). The wedge shaped region of low granular flow near the elastic buffer region in simulation image D is a result of the simulation boundary conditions. Since the buffer region (shown in brown) remains elastic and is perfectly bonded to the gauge section, it provides a confining stress as the specimen fails and granular flow causes dilatation and radial expansion. This confining stress in turn suppresses further granular flow. The effect of the buffer region decreases with increasing distance from the interface, resulting in the wedge shaped region. Near the roller boundary condition (where the specimen is free to expand laterally, the granular flow regions are preferentially aligned in the

axial direction and there appear to be a number of intact fragments developing.

The simulations show reasonable agreement with the behaviors seen in dynamic compression experiments; however additional work (specifically on the contact conditions) is needed to make detailed quantitative comparisons between the simulations and the experiments. The best approach to performing a quantitative comparison between simulations and experiments would be to first incorporate a capability for applying the mixed displacement/traction boundary conditions that exist in the experiments in the simulation framework. Secondly, one needs to calibrate the flaw distribution to the Kolsky bar results (using a 3mm cube sample size) while accounting for the effect of variability. Thirdly a validation experiment should be conducted using the largest reasonable specimen size (10 mm cubed would be good, but 8 mm cubed is likely the limit of the bars at JHU). Finally simulations using the experimental input pulse could be directly compared to the experimental images, output pulse, and fragment size.

5.4 Simplified Ballistic Impact

While dynamic uniaxial compression provides useful insights into competing mechanisms, the stress state during an impact event varies rapidly in space and time. For this reason, it is important to test the model performance relative to a realistic impact event. We begin our discussion of the simplified ballistic tests with a comparison to

experiments to establish the validity of our modeling approach. This is followed by additional discussion of internal variables in the model that may suggest additional areas of research based on these experiments.

5.4.1 Experimental Setup

The simplified geometry for these experiments consists of a sphere impacting a cylinder. The spherical projectile is composed of tungsten carbide with a cobalt binder in order to provide a high kinetic energy and momentum at lower impact velocities. For an impact velocity of 400 m/s the peak pressure for planar impact, based on impedance matching, is expected to be 7.5 GPa. The experimental configuration is a 6.34 mm tungsten carbide cobalt sphere impacting a ceramic cylinder that is 38.1 mm in diameter and 31.75 mm tall. These are planned experiments. Similar experiments were using smaller (25.4 mm diameter cylinders) conducted on a variety of armor ceramics including boron carbide in [77]. To help contain the fragments in the higher impact velocity tests, the cylindrical targets are encased in 6.35mm thick Bakelite plastic. This thin coating of plastic should not provide significant additional confinement and therefore is not modeled in our simulations.

Density (ρ)	14,300 kg/m^3	Frutschy and Clifton [84]
Specific Heat Capacity (C_v)	200 J/(kg °K)	Frutschy and Clifton [84]
Thermal Conductivity (α_θ)	100 W/(m °K)	Frutschy and Clifton [84]
Thermal Expansion Coefficient	3.0 $\times 10^{-6}$ °K	Frutschy and Clifton [84]
Shear Modulus (G)	232 GPa	Frutschy and Clifton [84]
Young's Modulus (E)	579 GPa	Frutschy and Clifton [84]
Poisson's Ratio (ν)	0.25	Frutschy and Clifton [84]
Bulk Modulus (K_0)	383 GPa	Calculated
Bulk wave speed (C_0)	5.18$\times 10^3$ m/s	Calculated
S	1.309	Dandekar and Grady [85]
Grüneisen Parameter (Γ_0)	1.2	Calculated
Initial Yield Stress (σ_y)	3.62 GPa	Frutschy and Clifton [84]
Hardening modulus	100 MPa	For stability

Table 5.4: Material properties for Tungsten Carbide Cobalt projectile

5.4.2 Material Model for the Impactor

The experiments use a sphere 6.34 mm in diameter made from tungsten carbide with 6 percent cobalt binder as the projectile. Frutschy and Clifton [84] provide basic mechanical properties for both pure tungsten carbide and tungsten carbide with 12 percent cobalt. We use a simple elastic plastic constitutive model with linear strain hardening for the deviatoric response. For the volumetric response, we use a Mie-Grüneisen equation of state. In pure tungsten carbide the shock speed is given by $U_s = 4.93\text{km/s} + 1.309U_p$ [85]. Since the tungsten carbide cobalt is mostly tungsten carbide, we assume that the slope of the $U_s - U_p$ curve for tungsten carbide cobalt is the same as for pure tungsten carbide. We compute the Grüneisen parameter based on the bulk modulus, coefficient of thermal expansion, initial density, and specific heat ($\Gamma_0 = \frac{3\alpha K_0}{\rho_0 c_v}$) [86, eq. 5.16]. The material parameters along with a reference are provided in table 5.4.

EOS	Density (ρ)	2520 kg/m^3	Theoretical density [81]
	Specific Heat Capacity (C_v)	962 J/(kg °K)	Dandekar [80]
	Bulk sound speed (C_0)	9.6 $\times 10^3$ m/s	calculated
	$U_s - U_p$ Slope (S)	0.914	Dandekar [80]
	Grüneisen Parameter Γ_0	1.28	Dandekar [80]
	Shear Modulus (G_0)	197 GPa	Paliwal and Ramesh [4]
	Bulk Modulus (K_0)	232 GPa	Dandekar [80]
Flaw Distribution	Minimum Flaw size ($s_{\min}$)	1.0 μm	
	Maximum Flaw size ($s_{\max}$)	25 μm	
	Distribution Exponent (α)	2.6	
	Flaw Density (η)	22 $\times 10^{12}$ m^{-3}	Dynamic strength
Micromechanics	Fracture Toughness (K_{IC})	2.5 MPa$\sqrt{\text{m}}$	Paliwal and Ramesh [4]
	Maximum Crack Velocity(V_m)	0.2 C_r	Experiments
	Crack Growth Exponent (γ_c)	1.0	
	Coefficient of Friction (μ)	0.8	
	Crack orientation (ϕ)	60°	Most damaging
Granular Flow	A_0	0.8	
	Y_0	0 MPa	
	Cohesive Strength (B_0)	3 MPa	
	Relaxation time (τ_{GP})	7$\times 10^{-9}$s	
	Activation Damage (D_c)	0.125	
	Maximum Damage ($D_{\max}$)	1.0	
	Reference crush pressure (P_0)	100 MPa	
	Reference distension (J_0^{GP})	2.0	
	Consolidation pressure (P_c)	10 GPa	

Table 5.5: Summary of material model parameters for boron carbide

5.4.2.1 Comparing Simulations and Experiments

In experiments and simulations involving brittle materials there is significant experimental variability so it is important to identify the key robust features in the experiments. These features should be sensitive to changes in the experimental conditions but not critically sensitive to the random distribution of flaws in the material. In impact experiments some of the robust features are radial cracks, and cone cracks [77]. Radial cracks can be identified by looking for damage zones that extend out from the central damage region. By looking at a slice through the specimen, we can identify cone cracks. Typically the cone cracks are connected through a number of bridging cracks at sufficiently high impact velocities. As the velocity is increased, the number of radial cracks increases along with the number of cone cracks [77]. The cone cracking angle decreases and cracks that bridge between adjacent cone cracks appear. The trend of an increasing number of radial and cracks with increasing impact velocity can be explained using an obscuration zone hypothesis (see [87] and references therein) additionally, the number of radial cracks at a given impact velocity has been used to determine the variability of the material strength by fitting the number of radial cracks using the Weibul modulus [88].

At an impact velocity of 103 m/s, the simulation shows 5 well developed radial damage features on the top surface of the target cylinder (figure 5.12). These radial features can be interpreted as radial cracks because they form a continuous damaged region. Within this region granular flow is active and as a result the region cannot

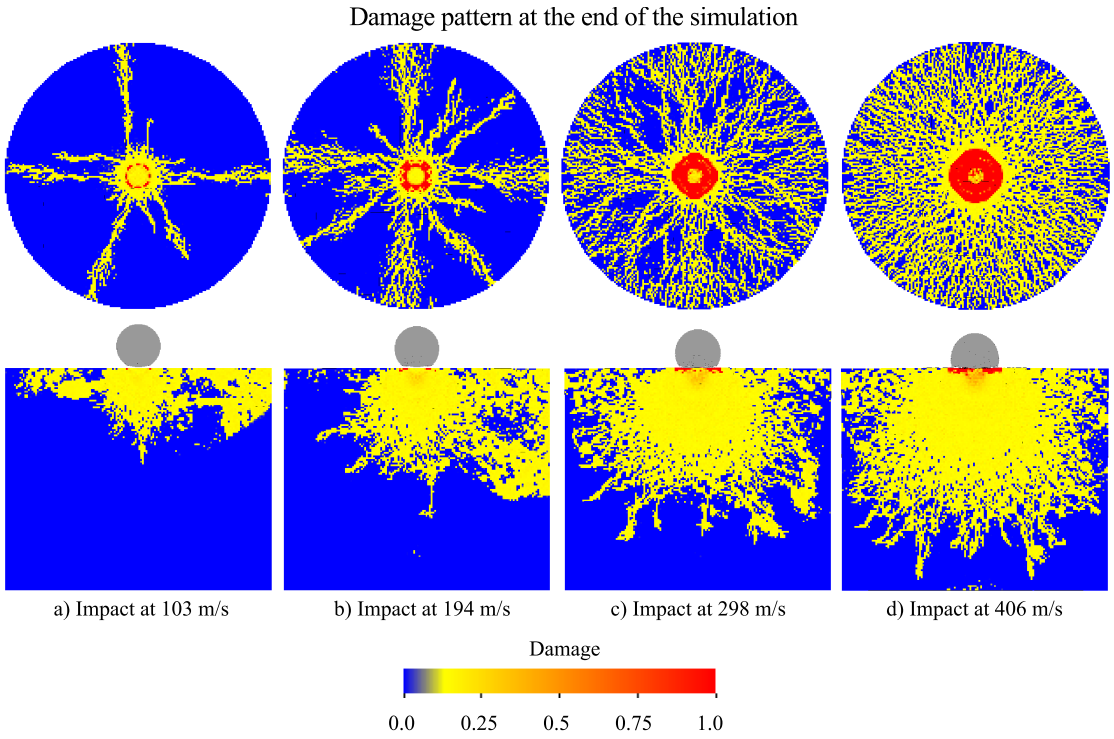

Figure 5.12: Top views and center cut views for sphere on cylinder impact simulations showing the damage pattern 10 μs after the impact event. All simulations were performed using a resolution of 0.25 mm/cell. The top row of images is a view looking down on the cylindrical target to reveal the radial cracks. The second row shows a slice through the center of the specimen this choice of material parameters does not show well defined cone cracks although the damage region does localize into thin regions at its outer boundary. Impact velocity increases from left to right.

sustain tensile stresses and the shear resistance is proportional to the applied pressure (or force normal to the effective crack faces). Moving right across the top row in figure 5.12, the increasing impact velocity results in longer radial cracks as well as a greater number of radial cracks. This is consistent with the experimental observations in smaller samples [77] and we expect the larger specimens to behave similarly.

The second row in figure 5.12 provides cross sections of the target pieces at the end of the simulation. In these cross sections, we see an increase in the extent of the damaged zone, but there do not appear to be well defined cone cracks in these simulation results. At the 298 and 406 m/s impact velocities the damage regions are starting to show some localization near the edges of the damage zone however these are not as well defined as the radial cracks on the top surface. One possible reason that we do not see the cone cracks that are observed in experiments is that the granular flow model that we have chosen is very sensitive to the confining pressure. As the material shears, it quickly increases the pressure in the neighboring region and prevents further deformation. Simulations of impacts on alumina sandwich panels conducted by Gamble et al. [89] suggest that allowing softening in the granular flow model as a result of accumulated granular flow can result in additional localization and may improve the agreement with experiments.

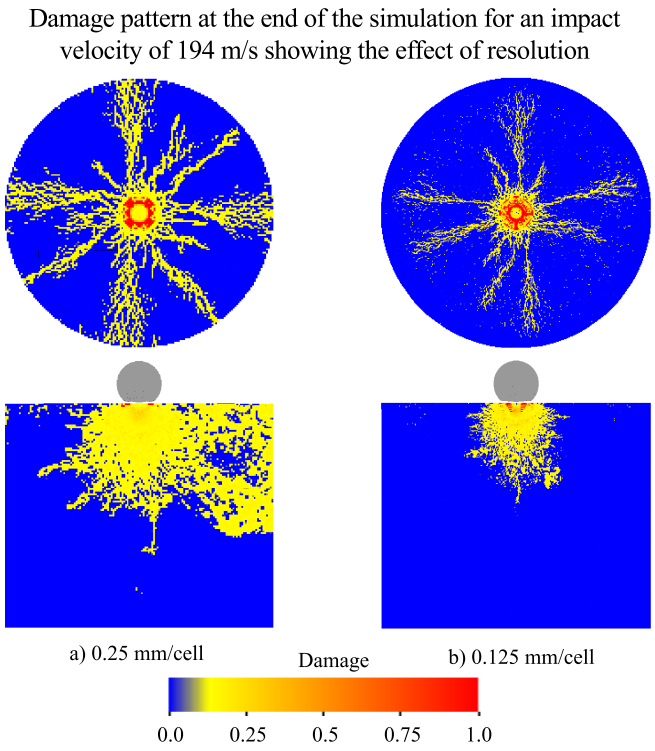

Figure 5.13: Top and center cut views for sphere on cylinder impact simulations showing the damage pattern for an impact velocity of 194 m/s for two different resolutions. Both simulations show a similar number of radial cracks. The higher resolution simulation shows a smaller damage extent in the cross-section and in the top view. Additionally the short radial cracks are better defined in the higher resolution simulation.

5.4.2.2 Effect of Numerical Resolution

When performing numerical simulations, it is important to understand the effect of resolution on the computational results. Figure 5.13 provides a comparison of the damage patterns for the 194 m/s impact velocity between a simulation run using 0.25 mm/cell and one using 0.125 mm/cell. The higher resolution simulation provides better defined damage zones and a slightly smaller damage extent in the cross section view. The higher computational resolution provides a greater opportunity for damage to localize, and provides better resolution of the stress gradients.

5.4.2.3 Global Energy Pathways

During an impact event the kinetic energy in the projectile is transfered from the projectile into the target. This energy is first converted into strain energy. In the small contact region, the stresses rapidly rise and activate the failure mechanisms in the system. These failure mechanisms convert the strain energy into thermal energy as the subscale processes drive the energy to lower scales. For the 194 m/s impact velocity, the global energy in the system as a function of time is displayed in figure 5.14. All of the energy initially starts as kinetic energy (shown in blue). This is converted into strain energy (green), which causes failure in the material and granular flow. The granular flow converts the energy into thermal energy (shown in red) as described in section 4.3.5. The total energy in the system is shown in black. In this closed system one expects the total energy to remain constant (if all of the

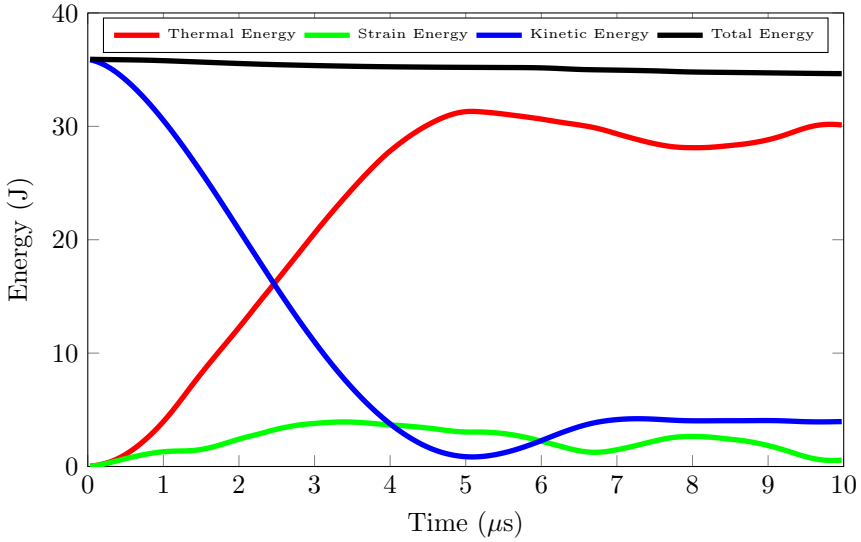

Figure 5.14: Thermal, strain, kinetic and total energy in the system as a function of time. The initial energy in the projectile is initially converted into strain energy, which is quickly converted into thermal energy through granular flow in the boron carbide and plasticity in the projectile.

energy is accounted for) or to decrease (if there is an energy dissipation mechanism that is not included in the energy total). In this system we do not explicitly track the energy dissipated by microcracking, so we expect the total energy to decrease with time.

5.4.2.4 Effect of Granular Flow Parameters

The choice of granular flow parameters has a large effect on the observed cracking pattern as shown in figure 5.15. Figure 5.15a shows the magnitude of the shear

component of the granular flow 10 μs after the 298 m/s impact when the best fit granular flow parameters are used. The impact results in the development of well defined radial cracks (top row) that also show significant shear (and volumetric) granular flow. In the cut view (bottom row) we see that there is some granular flow near the impact site, but it is not as extensive as the damage (figure 5.12c). When $A = 0.8$ the granular flow is highly pressure sensitive and produces a large amount of dilatation as a result of shear motion. This will limit the total granular flow in confined areas. The interior of the target is a highly constrained environment while the surface (where the radial cracks occur) has much lower effective confinement. Reducing the coefficient of friction (μ) on the crack faces from 0.8 to 0.6 has little effect on the granular flow pattern (comparing figure 5.15a and figure 5.15b), but it can have a moderate effect on the strength of a single material point loaded in uniaxial stress compression (observed during parameter fitting). This may suggest that for this impact problem the granular flow behavior is more important than the details of the micromechanics model.

Reducing the pressure sensitivity of the granular flow (A) from 0.8 to 0.6 results in more granular flow throughout the target (comparing figures 5.15a and 5.15c). The reduced pressure sensitivity produces more granular flow and cracking on the top surface of the target and produces large and well defined cone type cracks. This lower granular slope could represent less angular fragments. The difference in the granular flow pattern between these two simulations suggest that understanding the

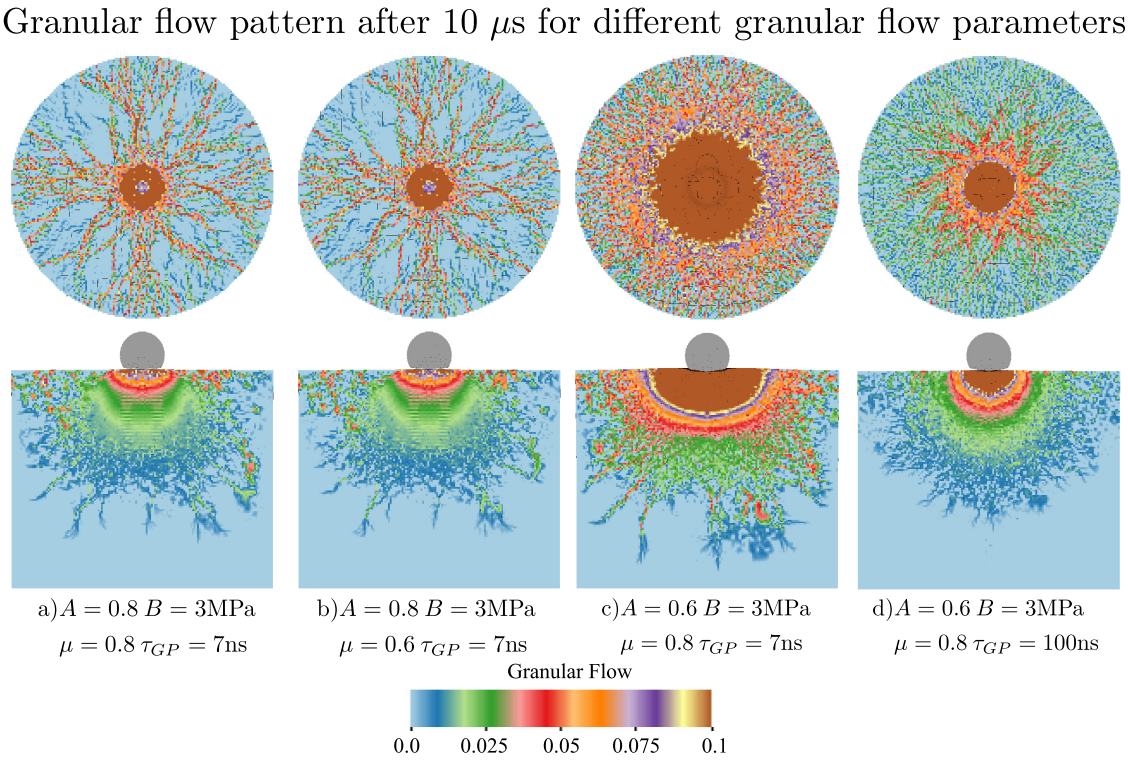

Figure 5.15: Effect of the granular flow model on the observed granular flow pattern 10 μs after impact at 298 m/s. Figure a is the reference figure with properties corresponding to all other simulations in this section. Reducing the crack face coefficient of friction (μ) has little effect on the granular flow pattern (b). Reducing the effective coefficient of friction for granular flow from $A = 0.8$ to $A = 0.6$ produces much more damage and granular flow and promotes the formation of features that look more like cone cracks (c). Increasing the granular flow timescale τ_{GP} reduces the total amount of granular flow (d) and results in less penetration of the ball into the cylinder, but the difference is not as large as the effect of the friction coefficient.

behavior of the failed material is important for correctly modeling impact events in brittle materials. The larger damage region in figure 5.15c relative to figure 5.15a suggests that maintaining a high granular slope during the failure process is beneficial for performance (if the goal is to reduce the size of the granular flow region). One may be able to maintain a high granular slope by developing high aspect ratio grains and promoting intragranular fracture. If the highly angular grains fracture along the grain boundaries and the fragment distribution mimics the initial high aspect ratio grain structure, then the granular slope may be higher and the damaged region may be more contained.

The timescale for granular flow can be related to the fragment size in the material [74]. If the material forms larger fragments, then the timescale associated with granular flow may be longer. To illustrate the effect of a longer granular flow timescale we compare results of the 298 m/s impact when the granular flow parameters are $A = 0.6$ and $\tau_{GP} = 100$ ns (figure 5.15d) to the results with a 7 ns timescale discussed in the previous paragraph (figure 5.15c). The longer granular flow timescale reduces the total amount of granular flow. This result suggests that a large granular flow timescale can also increase the apparent strength of the material. One may be able to increase the granular flow timescale through the formation of large fragments. To develop large fragments one could make a material with very large grains and weak grain boundaries, but the interior of the grains needs to be strong and have very few defects so that the grains do not fracture after becoming fragments. Although it is

not apparent in figure 5.15c, simulations using a previous iteration of the material model implementation showed a preference for failure along a 45 degree line with respect to the mesh orientation. Some of the damage patterns in figure 5.12 may show preferential orientation with the mesh so we discuss how one could test for mesh bias and what this model does to mitigate its effects.

5.4.2.5 Testing for Mesh Bias

At the 298 m/s impact velocity, there also seems to be a preference for radial cracking along a 45 degree line in figure 5.15. Since we are using a structured mesh in these simulations, we test for mesh bias by performing the same simulation with different random seeds. If there is no mesh bias, using a different random seed should produce a damage pattern with a similar radial pattern, but with a superimposed rotation. It is highly unlikely that the radial cracks will form in exactly the same location if there is zero mesh bias. As shown in figure 5.16, the 298 m/s impact velocity has a similar orientation after changing the random seed. This indicates that at the impact velocity of 298 m/s with the 0.125 mm/cell mesh, the orientation of the cross like pattern is likely partially due to the computational discretization. This mesh bias has been discussed by Strack et al. [90] and shown to be partially mitigated through the incorporation of aleatory uncertainty in the material response. However, this material model also includes explicit crack sampling that accounts for the aleatory uncertainty. We believe that this apparent mesh bias results from the discretization

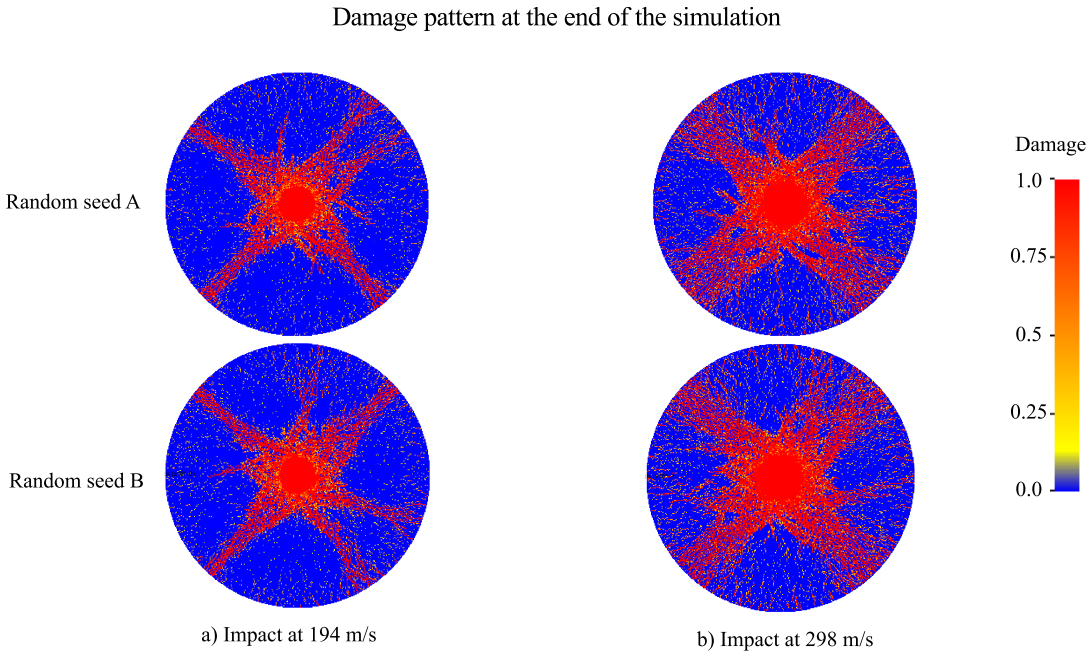

Figure 5.16: Top views of the damage pattern 20 μs after impact for the 194 m/s and the 298 m/s impacts for simulations with $\mu = 0.6$, $A = 0.6$, $B = 0.1$ MPa, and $\tau_{GP} = 100$ ns. The top and bottom rows use different random seeds. The similar orientations of the damage patterns for the 298 m/s impact indicate that there is some preference for failure along a 45 degree mesh bias.

of the spherical projectile. In the current CPDI formulation we discretize the sphere using a stair-stepped boundary which will distort the stress field in the contact region and break the axisymmetric loading before it can be broken by the aleatory uncertainty in the damage model. This possible mesh bias is an area that we are continuing to work on and future developments both in MPM representations of curved contact surfaces and the implementation of this model into other computational frameworks will provide additional information regarding the nature of this mesh sensitivity.

5.4.3 Summary and Future Research Directions

In this work we applied the micromechanics based damage model developed in chapter 4 to boron carbide in two different experimental configurations. In simulations of dynamic uniaxial compression we studied the influence of crack interactions, damage kinetics, and the granular flow parameters on the simulated failure behavior. We showed that:

- the damage model controls the strength in uniaxial compression, but
- the granular flow model influences the behavior of specimen after the peak stress is reached.
- Using a Poisson process to assign the local flaw distribution results in a more realistic failure pattern than when the Fourier like process is used.

By simulating 4 simplified ballistic experiments we provided additional validation of the material model under loading conditions that are relavent for simulating impact events. We demonstrated that we can decrease the size of the region that experience granular flow (a possible performance metric) by:

- increasing the slope of the granular flow surface (more angular fragments) or
- increasing the granular flow timescale (larger fragment).

We also identified a number of areas for future work. To perform more detailed validation tests using the Kolsky bar technique for this model, the simulation bound-

ary conditions need to be modified to account for the mixed boundary conditions in the experiments new experiments should be conducted that test larger specimens. In the impact simulations, the granular flow model plays an essential role in determining the failure pattern. This suggests that a more sophisticated granular flow model, which accounts for the fragments size in the granular material and the evolving shape of the fragments is justified. Additionally these simulations illustrated that further research to eliminate any mesh bias during high velocity impact events in the material point method is needed. Some possible areas for improvement include more faithful representations of the simulation geometry (the sphere had a stair stepped boundary) and improved contact algorithms.

Chapter 6

A Model for Impact-Induced Lineament Formation and Porosity on Eros

6.1 Introduction

The internal structure of asteroids is important both in terms of the asteroid's origin and subsequent evolution and when considering possible asteroid mitigation strategies. For example, estimates of the momentum coupling parameter depend on the internal strength of an asteroid and on how effectively waves travel through the body. Unfortunately, little is known about the internal structure of asteroids besides what can be learned from observed lineaments[91] and the measured bulk

density. Fortunately, impact events interrogate the interior of asteroids through the production of stress waves that travel through the body. Since a coherent body will transmit waves more efficiently than a rubble pile, the extent of the area of influence of an impact event can be used to assess the nature of the target body [92].

6.1.1 Eros as a Model NEO (Ordinary Chondrite)

One of the best studied Near Earth Objects (NEOs) is the asteroid Eros (433), shown in figure 6.1. The Near Earth Asteroid Rendezvous (NEAR) mission obtained detailed measurements of the surface of Eros and its bulk density. From spectral data, collected during the rendezvous mission, Eros is classified as an S type ordinary chondrite. Most ordinary chondrites in our meteorite collection that closely resemble Eros possess a density near 3400 kg/m^3 while the bulk density of Eros is 2670 kg/m^3 [93]. Gravity measurements obtained by NEAR do not obviously indicate that Eros is heterogeneous. The low measured density of Eros thus suggests that it must possess a porosity between 21 and 33 percent [93]. Such a porosity is small compared to the typical porosity of a loose sand or gravel, which is around 40 percent, and suggests that Eros is not a simple rubble pile. The hypothesis that Eros is a heavily interlocked body capable of transmitting seismic waves over significant distances is supported by the abundance of global lineament structures associated with individual impact events[91].

Figure 6.1: Image of Eros returned from NEAR just before begininning to orbit the asteroid (NEAR image 20000214f).

6.1.2 Impact History of Eros From NEAR Data

The craters on Eros provide a record of the order of impact events. There are three major craters on the surface of Eros: Himeros, Psyche, and Shoemaker (this latter crater is named Charlois Regio by the IAU; however, to be consistent with previous literature, we will use the name Shoemaker in this work). The distribution of the largest blocks on Eros correlates with the expected location of ejecta from Shoemaker crater, suggesting that the youngest of these three craters is Shoemaker. There is some debate about whether Himeros or Psyche is younger; however, Himeros appears more degraded than Psyche and so, for the purposes of this paper, we assume that Himeros occurred first. Since the density of asteroids is much higher in the asteroid

belt, we assume that all of these impacts occurred prior to Eros leaving the asteroid belt. In this region, typical impact velocities are around 5 km/s.

We investigate the impact history of Eros using a new material model for the dynamic failure of geologic materials. Using this new material model we perform simulations of the impact events on Eros and look for the expressions of material failure on the surface of the body that can be compared to observations. We investigate the hypothesis that Eros originated as a fragment from an impact event on a larger parent body and subsequent impact processing has produced the current body. Additionally, we will investigate the evolution of bulk porosity in Eros as a result of the impact history to determine if it is possible to generate 20 percent porosity from a fully dense body as a result of impact processes. We review the Tonge-Ramesh material model (chapter 4) next.

6.2 The Tonge-Ramesh Model for Geomaterials

The material model developed in chapter 4 is a mechanism based material model designed for impact events involving brittle materials (such as rocks). The key features of the new material model are self consistent dynamically interacting crack distributions, pressure dependent granular flow of the highly damaged material, pore compaction through the use of a P-α porosity model, and a Mie-Grüneisen equation of

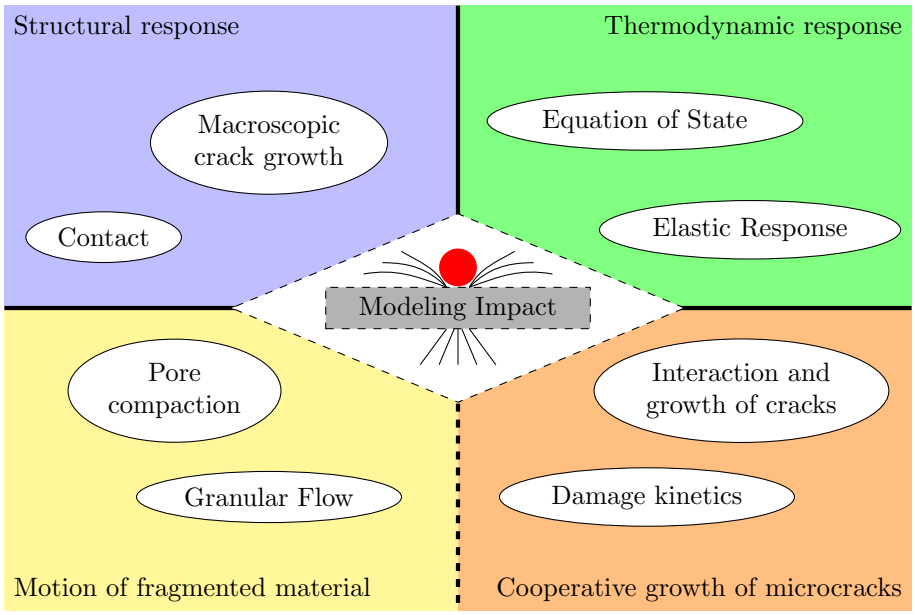

Figure 6.2: Important physical processes in impact events

state. This micromechanics based model captures the important physical processes (figure 6.2) during impact events. It is useful to think of these processes in terms of both time and length scales. Starting from the green quadrant in figure 6.2 and moving clockwise through the bubbles, the key physical processes are listed in generally increasing length and time scale after an impact event occurs. In the green quadrant labeled thermodynamic response we have the equation of state and the elastic response (specifically the shear modulus). In the Tonge-Ramesh model this is currently a Mie-Grüneisen equation of state, but at higher impact velocities one may introduce a more complex equation of state. The orange box contains processes associated with dynamic crack growth. Specifically, the interaction and growth of microcracks leads to rate effects [21] that limit the rate at which a material point with

a given distribution of defects can fail through microcrack growth. These rate effects [21] are a direct result of the subscale flaw distribution (flaws at a scale below the computational discretization threshold) and the existence of a limiting crack growth speed. Moving from the orange region in figure 6.2 across the dotted line to the yellow region, one moves to slightly larger length scales and later times. This region describes processes that occur within the fully damaged material as it continues to deform. The granular flow produces dilatation (and thus effective porosity) through an associative flow model. We include a pore compaction model to account for the evolution of that porosity. The upper left corner of the figure lists physical processes that must be resolved by the computational mechanics framework (they are changes to the initial boundary value problem rather than subscale processes occurring within a representative material volume).

6.2.1 Key Equations in the Tonge-Ramesh Material Model

The balance of linear momentum within a continuum body is often written using the Cauchy or true stress ($\boldsymbol{\sigma}$) as:

$$\nabla \cdot \boldsymbol{\sigma} + \boldsymbol{b}\rho = \rho \boldsymbol{a}. \tag{6.1}$$

Here $\boldsymbol{b}$ is the body force per unit mass, $\boldsymbol{a}$ is the acceleration, and ρ is the current density.

The stress can be split into a pressure ($p = -\frac{1}{3}\text{tr}(\boldsymbol{\sigma})$) and a deviatoric portion. Within this model we address porosity through the use of a P-α [59] porosity model such that the pressure is given by:

$$p(J, J_{gp}) = \frac{p_s(J_e)}{J_{gp}}. \tag{6.2}$$

Here we have introduced the total volume change ratio ($J = \frac{\rho_0}{\rho}$), the volume change ratio in the solid material ($J_e = \frac{\rho_0}{\rho_s}$), and the distension ($J_{GP} = \frac{\rho}{\rho_s}$). From these relationships we naturally have $J = J_e J_{gp}$. In developing the model, it is more convenient to define the alternative stress measure $\boldsymbol{\tau} = J\boldsymbol{\sigma}$, where $\boldsymbol{\tau}$ is called the Kirchhoff stress. We assume a decoupled representation of the Kirchhoff stress tensor:

$$\boldsymbol{\tau} = \boldsymbol{\tau}_{dev} - p_s J_e \boldsymbol{I}. \tag{6.3}$$

6.2.1.1 Elasticity and the Equation of State

The deviatoric stress $\boldsymbol{\tau}_{dev}$ is assumed to be a linear function of the deviatoric part of the volume preserving elastic deformation:

$$\boldsymbol{\tau}_{dev} = G\left(\bar{\boldsymbol{b}}_e - \frac{1}{3}\text{tr}(\bar{\boldsymbol{b}}_e)\boldsymbol{I}\right) \tag{6.4}$$

where $\bar{\boldsymbol{b}}_e = J_e^{-2/3}\boldsymbol{F}_e\boldsymbol{F}_e^T$ is obtained from the elastic part of the deformation gradient $\boldsymbol{F}$ (see section 4.3.1) with the decomposition $\boldsymbol{F} = \boldsymbol{F}_e\boldsymbol{F}_{GP}$. Here G is the damaged shear modulus defined as:

$$G(D) = \left(G_0^{-1} + \frac{2D}{15}\left(3Z_r + 2Z_n - 4Z_c\right)\right)^{-1}. \tag{6.5}$$

The parameters Z_n, Z_r, and Z_c are functions (section 4.3.4) of the elastic moduli and relate to the compliance of an individual crack while G_0 is the undamaged shear modulus. Similarly the damaged bulk modulus is defined as:

$$K(D) = \left(K_0^{-1} + D\left(Z_n + 4Z_c\right)\right)^{-1}. \tag{6.6}$$

The scalar damage parameter D is evolved using a micromechanics based damage model discussed in the next section.

The volumetric response is determined by a Mie-Grüneisen equation of state which relates the elastic part of the volume change ratio (J_e) and the current temperature of the material (θ) to the pressure (p_s):

$$p_s(J_e, \theta) = \frac{K(D)}{K_0} p_H(J_e)\left[1 - \frac{\Gamma_0}{2}\left(1 - J_e\right)\right] + \rho_0 \Gamma_0 \left[e_c(J_e) + c_\eta(\theta - \theta_0)\right]. \tag{6.7}$$

In this equation the Grüneisen constant determines the coupling between internal energy and the pressure, the energy stored in the deformation of atomic bonds is represented by the cold energy $e_c(J^e)$, and the thermal energy depends on the change in temperature $\theta - \theta_0$ and the specific heat at constant entropy c_η. The pressure is referenced to the pressure on the principal Hugoniot (p_H), which depends on only the volume change ratio J_e and material parameters including the bulk wave speed (C_0) at room temperature and pressure, the density (ρ_0) at room temperature and pressure, and the slope (S) of the shock speed-particle velocity relationship:

$$p_H(J^e) = \begin{cases} \frac{\rho_0 C_0^2 (1 - J^e)}{(1 - S(1 - J^e))^2} & J^e < 1.0 \\ \rho_0 C_0^2 (1 - J^e) & \text{otherwise} \end{cases}. \tag{6.8}$$

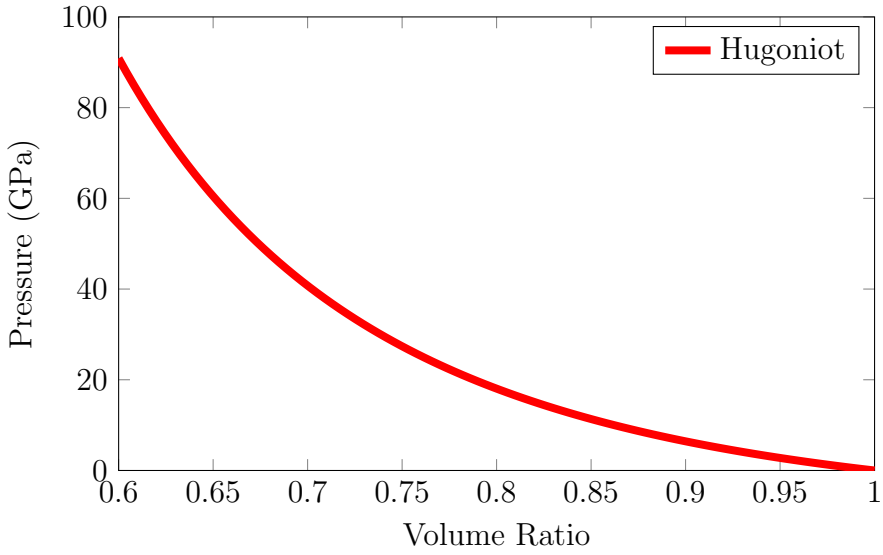

Figure 6.3: Mie-Grüneisen equation of state used in this work showing the Principal Hugoniot in pressure - volume change ratio space. Changes in temperature will move vertically from this reference curve.

This relationship between the pressure and the elastic volume change ratio (J^e) is shown graphically in figure 6.3. Damage is accounted for by scaling the computed pressure by the ratio of the damaged bulk modulus to the undamaged bulk modulus.

6.2.1.2 Micromechanics of Damage

Within this model, the scalar damage parameter D is defined as:

$$D = \sum_{k=1}^{N_{\text{bins}}} \omega_k \left(s_k + l_k\right)^3 \tag{6.9}$$

where ω_k is the number density of flaws per unit volume that are represented by the flaw family k, and the initial flaw size is s_k, which has grown an additional length l_k

due to the applied loading history. In the summation the bin number k loops over the N_{bins} that are used to discretize the local flaw size distribution

We use a self consistent approach [10] to compute the effective stress intensity factor due to both the applied load and the crack environment for the representative flaw size s_k. In addition to the stress computed from the self consistent solution, the stress intensity factor depends on the angle (ϕ) between the most compressive principal stress and the crack face normal and the coefficient of friction between the two crack faces. From that stress intensity factor (K_I) we compute the crack growth rate using [66]:

$$\dot{l} = \frac{C_r}{\alpha_c}\left(\frac{K_I - K_{IC}}{K_I - 0.5K_{IC}}\right)^{\gamma_c}. \tag{6.10}$$

Here C_r is the Rayleigh wave speed, K_{IC} is the critical stress intensity factor required for crack growth, α_c is a dimensionless parameter that determines the maximum crack velocity, and γ_c is an exponent that determines how fast cracks approach that limiting speed with increasing driving force (K_I). The increased crack length is used to update the damage parameter.

6.2.1.3 Granular Plasticity and Pore Compaction

When the damage parameter D reaches a critical damage level defined by D_c, granular flow is assumed to be activated. The yield surface for granular flow is defined by:

$$f(\boldsymbol{\tau}) = \boldsymbol{\tau}_{dev} : \boldsymbol{\tau}_{dev} + A\left(\frac{\text{tr}(\boldsymbol{\tau})}{\sqrt{3}} - B\right) \tag{6.11}$$

where A is the effective coefficient of friction for the granular material and B is the cohesive strength of the material. The visco-plastic granular flow model used is a linear viscosity model with a timescale τ_{GP} that assumes associative flow (which, for this yield surface, leads to the production of effective porosity). Based on dynamic compression experiments on sand [72] we select a slope of $A = 0.6$ for the relationship between the magnitude of the deviatoric stress and the magnitude of the hydrostatic stress at the onset of plastic flow. We account for self gravity only by setting the cohesive strength of the granular material to the gravitational overburden pressure at the center of Eros. Based on a simple spherical model, this pressure is 0.1 MPa ($B = 0.1$ MPa). This choice represents a simplification because the gravitational overburden pressure is a function of the depth, but we are not explicitly solving for the gravitational interactions and therefore accept this as an approximation.

The porosity evolution is accounted for by assuming that the maximum equilibrium porosity lies on a hydrostatic yield surface defined by:

$$f_\phi(P, J^{GP}, J) = \begin{cases} \frac{P}{P_c - P_0} - \frac{P_0}{P_c - P_0} \exp\left(-\frac{P_c - P_0}{2P_0(J_0^{GP} - 1)}(J^{GP} - J_0^{GP})\right) & P < P_0 \\ (J^{GP} - 1) - (J_0^{GP} - 1)J^2 \left(\frac{P_c - P}{P_c - P_0}\right)^2 & P_0 \leq P < P_c \\ J^{GP} - 1 & P > P_c \end{cases} . \tag{6.12}$$

This is a simple porosity model with a quadratic crush behavior for pressures larger than P_0 with full compaction occurring at a pressure of P_c and an exponential compaction behavior for lower pressures. The reference distension J_0^{GP} is the distension

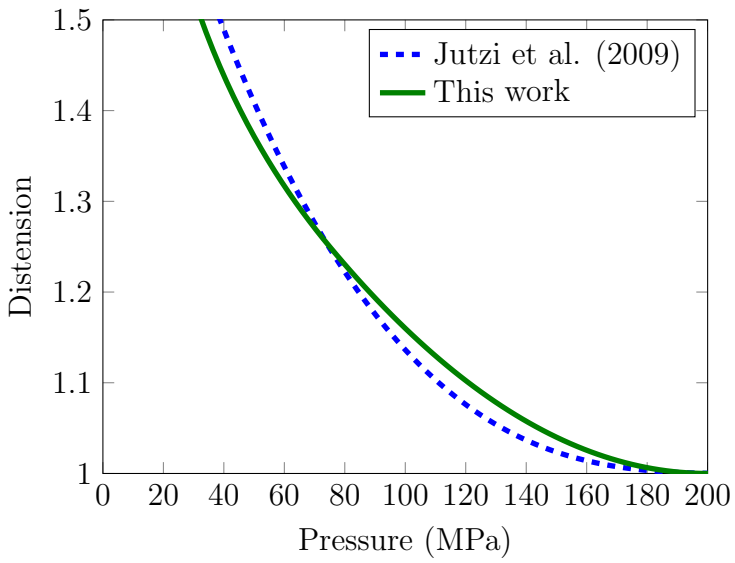

Figure 6.4: Pore crush model used in this work and the model used in [5].

corresponding to the transition pressure P_c. Based on pumice crush data [94], we use a transition pressure (P_0) of 75 MPa at a distension (J_0^{GP}) of 1.25, and a consolidation pressure of 200 MPa. The differences between the crush curve used by Jutzi et al. [5] and the model used in this work are shown in figure 6.4. In our model, porosity must be created through the shearing action of the granular material. Therefore it is difficult to produce large amounts of distension in a material and we focus the figure on the low distension range. In addition to using fewer parameters, our model incorporates the timescale associated with material movement during pore collapse using the same viscous timescale as the granular flow model.

6.3 Distribution of Flaws for Small Bodies

Observations of lineament structures on the surface of terrestrial bodies suggest that there are crack like features at all observed scales [95] from less than a millimeter up to several kilometers. When a computational discretization is imposed on the physical system, in order to simulate the evolution of the body after impact, there is a natural separation of these flaws into flaws much larger than the mesh size, and flaws much smaller than the mesh size. As discussed in section 2.1 flaws in the intermediate range near the mesh size are difficult to capture accurately. In this work we avoid this range of flaw sizes by assuming that the initial flaw distribution contains only subscale flaws. As damage regions coalesce they quickly grow to become large macroscale flaws.

Flaws much larger than the mesh size can be resolved explicitly as localized regions of deformation. These types of regions are well described by a zone of damaged material that behaves like a sand. They can sustain compressive loads, have a shearing resistance that is proportional to the applied compressive load, and cannot sustain tensile loads. For this work we assume that the initial body is free of these large macroscale flaws and contains only small flaws. This assumption is motivated by the observation that most linear features can be associated with a specific impact event [91] and our initial body is that before these events.

At the small end of the size scale, there are flaws that are much smaller than the computational discretization. These flaws are treated through the material model. Macro scale flaws grow through the activation and growth of subscale flaws near their tips. After sufficient growth of the subscale flaws, the material point reaches a critical damage level and granular flow is activated. At this point the material point behaves like a sand and becomes part of the macroscale flaw.

6.4 A Model of Young Eros

We begin with the assumption that Eros started as a monolithic piece with no initial porosity or fractures larger than the computational mesh size (80 m).

The major cratering events on Eros have removed and repositioned material during the impact process. As a first approximation to the shape of Eros, prior to the formation of the three major craters (Himeros, Psyche, and Shoemaker), we use a geometry sculpting tool to smooth and fill in the craters on the current shape model of Eros. We perform this task first by applying a smoothing algorithm to remove all of the small craters. We then add and remove material to eliminate the three large craters. Figure 6.5 shows a rendering of the current low resolution shape model for Eros and the model obtained through the smoothing process. This smoothed model is used as the basis for the simulations presented in this work.

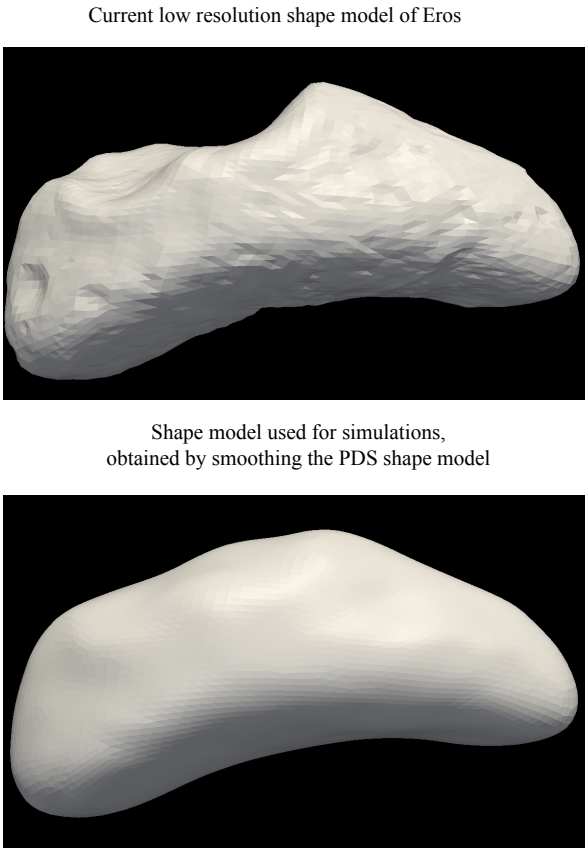

Figure 6.5: Rendered views showing one of the current low resolution shape model available at the NASA Planetary Data System (PDS) and the smoothed shape model used to represent a young version of Eros.

6.4.1 Basalt as a Model Material

Eros is classified as an S-type ordinary chondrite based on spectral observations. This class of asteroids typically has large amounts of olivine and orthopyroxene. These minerals are also present in terrestrial basalt. Since the basalt is a well studied geologic material, relative to chondrite material, we use basalt as a model material for the purposes of our simulations. The physical response of an ordinary chondrite and basalt are not expected to be that different especially at the impact velocities considered.

We obtained the Mie-Grüneisen equation of state parameters for basalt from the review article by Ahrens and Johnson [96]. The initial bulk density is 2,874 kg/m^3 with a bulk wave speed of 4,000 m/s, a shock speed - particle velocity slope of 1.35, and a Grüneisen parameter of 1.7. We use a shear modulus of 29 GPa.

Our damage model uses an internal distribution of flaws that provide a direct connection to the material microstructure. We assume that the flaw distribution in the material follows an inverse power-law characterized by a bounded Pareto distribution with a slope of 3.0. This slope gives self-similar scaling in the crack sizes and is consistent with many of the observations of Housen and Holsapple [95]. In many geologic materials, the distribution of linear crack like features follows a power-law over many orders of magnitude [95]. The fully fractured limit, where the average spacing between flaws is equal to the flaw size, is depicted with the dotted line in figure 6.6.

In earlier work, Tonge et al. [97] used a bounded Pareto distribution with a flaw range from 5 μm to 1.0 mm and a flaw number density of 2×10^{12} flaws per m^3 for laboratory scale impact studies of basalt. This flaw size distribution and flaw density were fit to the dynamic strength of basalt measured in Kolsky bar experiments. This flaw distribution, which is representative of laboratory scale Basalt samples is shown as the flaw distribution labeled strong in figure 6.6. One could also imagine that the coarser numerical resolution and larger body size used for asteroid simulations necessitates the inclusion of a larger portion of the flaw distribution. For this reason we define a second flaw distribution, which we label weak, in figure 6.6. This weaker flaw distribution extends from a maximum flaw size of 25 m to a minimum flaw size of 1 cm. The maximum flaw size of 25m is consistent with the homogenization process that we are using. As noted earlier we do not include flaws that are larger than the 80m discretization size. We cut off the flaw distribution at a lower limit of 1cm to maintain a balance between resolving the shape of the flaw size distribution and the available computational resources. For this weaker flaw size distribution, the flaw density is 250 flaws/m^3. In figure 6.6 both the weak and strong flaw distributions show a curvature towards the larger flaw end of the line. This is a result of using a bounded Pareto distribution where the density of flaws larger than $s_{\max}$ is 0. It is a consequence of the breakdown of power-law scaling as the limits are approached.

We use a fracture toughness of 1.9 MPa $m^{\frac{1}{2}}$ [98] and an internal coefficient of friction of 0.6, which is equivalent to a friction angle of about 30 degrees. The assumed

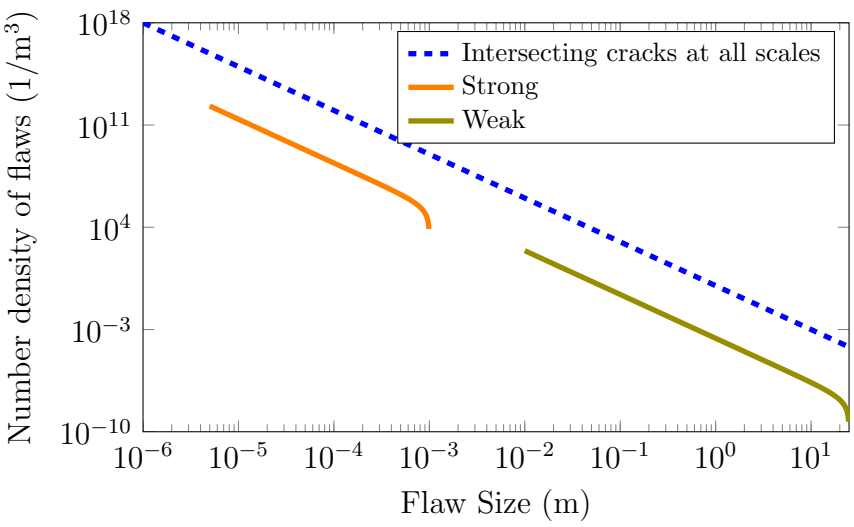

Figure 6.6: Plot showing the number density of flaws as a function of flaw size for the two flaw distributions designated weak and strong. The limiting density where on average all flaws are intersecting is shown using a dashed line.

maximum crack growth velocity of 20 percent of the Rayleigh wave speed is consistent with experimental observations of crack growth during dynamic compression[4]. Since there is little experimental evidence to suggest a different value for basalt, we leave the crack growth exponent (γ_c) as 1.0. In the granular flow model, we use the same coefficient of friction and associative flow. We assume a cohesive strength of 0.1 MPa based on the maximum overburden pressure due to gravity on Eros. Table 6.1 provides a summary of the material parameters used in these simulations.

Thermal	Density (ρ)	2874 kg/m^3	Ahrens and Johnson [96]
	Specific Heat Capacity (C_v)	850 J/(kg °K)	Robertson [99]
	Thermal Conductivity (α_θ)	1.75 W/(m °K)	Robertson [99]
EOS	C_0	4.09 $\times 10^3$ m/s	Ahrens and Johnson [96]
	S	1.35	Ahrens and Johnson [96]
	Γ_0	1.7	From S
Elastic	Shear Modulus (G)	29 GPa	
	Bulk Modulus (K_0)	49 GPa	
Weak Flaws	Minimum Flaw size ($s_{\min}$)	1.0 cm	
	Maximum Flaw size ($s_{\max}$)	25 m	
	Distribution Exponent (α)	3.0	Housen and Holsapple [95]
	Flaw Density (η)	250 m^{-3}	
Strong Flaws	Minimum Flaw size ($s_{\min}$)	5 μm	
	Maximum Flaw size ($s_{\max}$)	1 mm	
	Distribution Exponent (α)	3.0	Housen and Holsapple [95]
	Flaw Density (η)	2×10^{12} m^{-3}	
Micromechanics	Fracture Toughness (K_{IC})	1.6 MPa$\sqrt{\text{m}}$	Balme et al. [98]
	Maximum Crack Velocity(V_m)	0.2 C_r	Common in experiments
	Crack Growth Exponent (γ_c)	1.0	
	Coefficient of Friction (μ)	0.6	Martin et al. [72]
	Crack orientation (ϕ)	60°	Most damaging
Granular Flow	A	0.6	Martin et al. [72]
	Y	0 MPa	
	Damage Cohesive Strength (B)	0.1 MPa	
	Relaxation time (τ_{GP})	1×10^{-5}s	
	Damage for Granular flow (D_c)	0.125	
	Maximum Damage (D_{max})	0.2	
Pore Compaction	Reference crush pressure (P_0)	75 MPa	Fit to Jutzi et al. [94]
	Reference distension (J_0^{GP})	1.25	Fit to Jutzi et al. [94]
	Consolidation pressure (P_c)	200 MPa	Fit to Jutzi et al. [94]

Table 6.1: Material model parameters

6.5 Simulation Results

6.5.1 Computational Approach

To simulate these impact events, we use the Generalized Interpolated Material Point (GIMP) method[100], which has been implemented in the Uintah computational framework [52]. In this method, the solid body is discretized into a collection of material points, which track the constitutive response of the material in a Lagrangian frame. These material points interact through their representation on a grid, which is reset after each time step, simplifying the computation of gradients. In these computations we use GIMP instead of the more computationally expensive and accurate CPDI [51] because we are interested in the general implications of our model for these types of impact events not in the precise number of lineaments or the detailed stress evolution at a point. In all of the simulations that we present, we use a particle size of 80 m and a grid spacing corresponding to one particle per cell. Although this numerical resolution is not optimal for resolving the impactor in these impact events, we are simulating the response of the entire asteroid in three dimensions and therefore must compromise on the resolution to maintain computational tractability. A finer numerical resolution will likely affect the accuracy of the results during the initial shock wave propagation through the body and possibly change the peak pressure and may result in a finer lineament structure, but will not change [101] the global response of the system at later times.

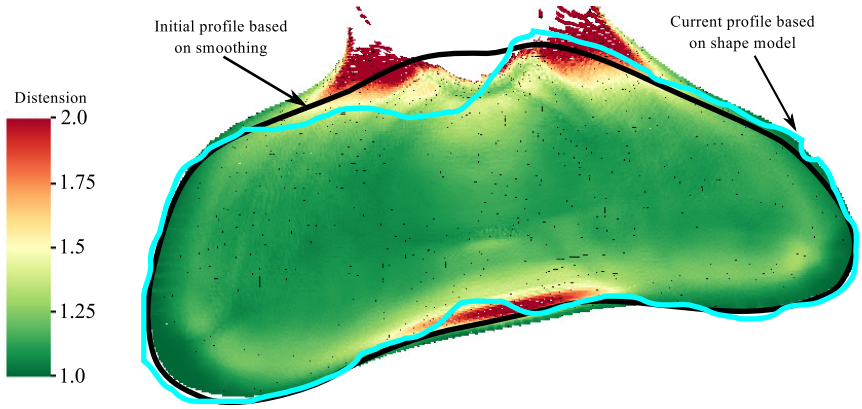

Figure 6.7: A cross-section of the simulation showing the distension 80s after the Himeros forming impact on the weak target. The outlines in the figure show the initial profile in black and the profile from the shape model shown in blue. The simulation shows reasonable agreement with the observed shape model. The region of high distension ($J_{gp} > 1.75$) are also regions that have a velocity greater than the escape velocity on the surface and therefor are likely to be excavated at later times.

6.5.2 Himeros Forming Impact

6.5.2.1 Simulation Setup

We begin by simulating the Himeros forming impact using the weak flaw distribution to represent the flaws within the initial body. Based on our prior lower resolution simulations, an impactor that is 800m in diameter produces a crater that is similar in size to the size of Himeros. Impactors with a diameter larger than 800m tended to disrupt the asteroid. The shape of Himeros is likely gravity dominated because it is so large compared to Eros. The purpose of this paper is not to determine the exact

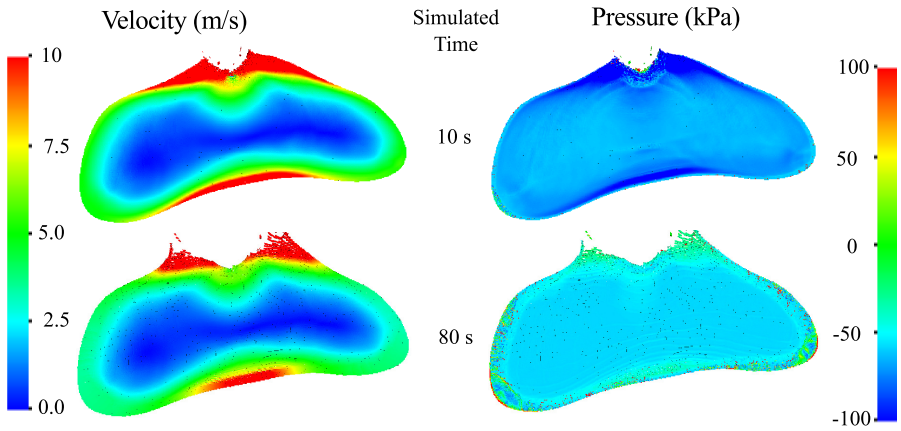

Figure 6.8: Pressure and velocity in a slice through Eros 10s and 80s after the Himeros impact for the weak target. On Eros the escape velocity at the surface is 10 m/s and the gravitational overburden stress at the center of the body is 100 kPa. After 10s most of the wave interactions have decayed, therefore in simulations of multiple impacts we stop the simulations after 10s and begin damping the material motion.

series of impacts that lead to the current shape of Eros but instead to investigate the effect of multiple impact events on bodies with different effective strengths. With this goal in mind we accept an 800 m diameter impactor for the Himeros forming event and compute the relative size of the impactors that formed Psyche and Shoemaker based on this size. Since we assume that all of the impact events occurred in the asteroid belt with a velocity of 5 km/s and are impacting the same target material, the material strength can be eliminated from the crater size scaling relationships [95]. We estimate the size of the Psyche forming impactor to be 400m in diameter and the Shoemaker forming impactor to be 600m in diameter. Figure 6.7 shows the initial, current, and simulated cross section of Eros 80 s after the simulated Himeros impact using a 800 m impactor. In this figure we see that the simulated crater profile is shallower and wider than the observed crater on Eros. The high distension regions near the impact site have a particle velocity greater than 10 m/s, which exceeds the escape velocity on the surface of the body, as shown in figure 6.8.

Running the simulation out to 80s is computationally very expensive and, since we are interested in both multiple impacts and the effect of the effective strength of the initial body, we seek to stop the simulation as early as possible, while still retaining the important features of the impact event. Figure 6.8 shows the velocity and pressure on a slice through the asteroid at 10s and 80s after the impact. The velocity scale saturates at 10 m/s, which is the escape velocity on the surface of the asteroid. In the time between 10s and 80s there is some material motion, but the wave

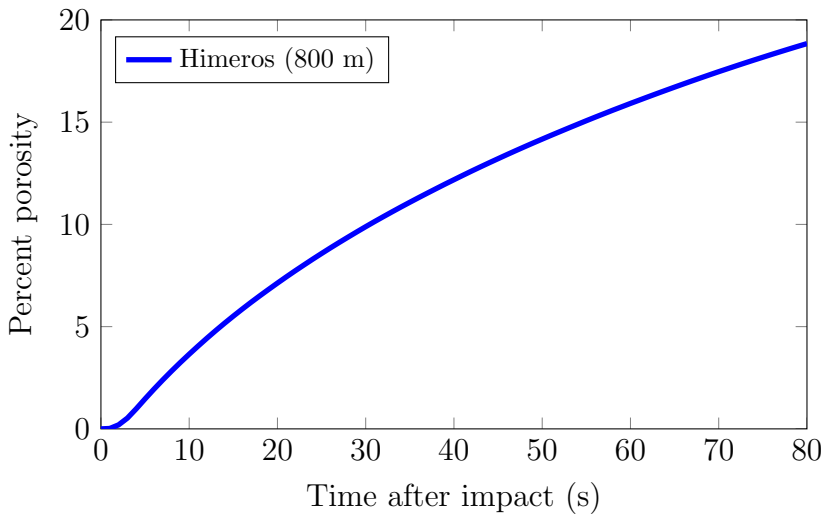

Figure 6.9: Bulk porosity evolution in Eros as a function of time after the Himeros forming impact event for the weak target.

interactions from the initial impact event have dissipated by the 10s time. Similarly the pressure plot, after 10s, shows there is only a small region of the asteroid that has a pressure above 100 kPa, which is the gravitational overburden pressure. This suggests that around 10s the problem is transitioning from a wave interaction and stress dominated problem to a problem dominated by gravity. In future simulations we stop after 10s and begin preparing for a subsequent impact event.

6.5.2.2 Bulk Porosity Evolution

The bulk porosity is one of the few observational quantities that relates to the internal structure of an asteroid. Figure 6.9 shows the computed bulk porosity evolution as a function of time for the Himeros forming impact using the weaker flaw

distribution. In this run, that was taken out to 80s, we see that initially the porosity grows rapidly and then the rate of growth of the porosity begins to slow after about 10s. At the end of the simulation, the porosity is just under 20 percent which is consistent with the current estimated porosity of Eros. Note that these simulation do not include the effects of gravity and therefore, one must be careful interpreting the long time data. These results demonstrate that it is possible to develop the observed porosity on Eros by starting from a solid initial shard. Note that we are using a simple-minded approximation for the effect of gravity by using a high (100 kPa) cohesive strength of the fully damaged granular material. If one were to perform these simulations without this extra cohesive strength but including the explicit gravity interactions, we believe that more porosity would be produced more quickly. In future work we plan to hand these calculations off to an N-body gravity code after the initial impact phase to comput the long time evolution of the body from both impacts and self gravity.

6.5.2.3 Damage and Granular Flow Evolution in the Body

One advantage of computer simulations is that they provide the time history during the impact event, so that we can look at the development of damage and granular flow with time. Figure 6.10a shows (for the special case of the weak distribution of flaws) the damage propagation and the development of granular flow at three times after the impact event. These views present a cross section of the body. The damage

propagates very quickly through the body, but the granular flow takes a longer time to develop. Although the damage boundary at 3.5s shows some signs of localization and fingering, this does not persist and the entire body is heavily damaged by the end of 10s. The granular flow pattern is smooth in these particular simulations. Heterogeneous surface features that indicate localized surface movement on scales larger than about 200m would not be consistent with this smooth granular flow pattern. However, these results would be consistent with a large number of smaller (several parallel faults with a spacing of less than 80 m) fault zones provided that they are relatively uniformly spaced and distributed over a wide area, because when these smaller faults are averaged over the 80m grid spacing the average strain would be smooth[102].

Switching to the stronger flaw distribution (figure 6.10b) changes the damage pattern that results from the Himeros forming impact substantially to a more heterogeneous damage pattern. Just as with the weaker flaw distribution, the development of granular flow occurs after the damage pattern is well developed. The granular flow is not alos strongly heterogeneous, with a network of internal failures that includes the beginnings of an antipodal spall zone. These localized regions of granular flow will behave like faults or cracks during subsequent impact events. Localized damage regions such as these are more consistent with the linear features observed by [91]. The corresponding surface features are discussed shortly.

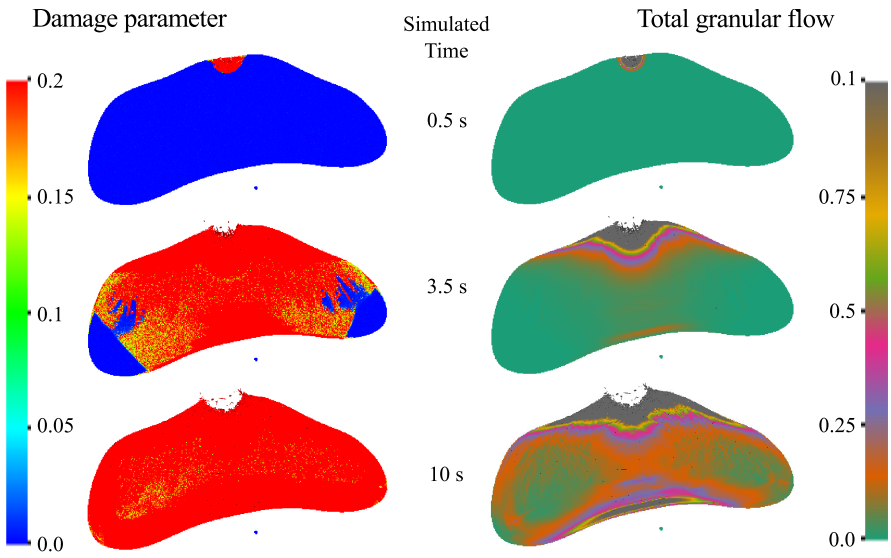

(a) Weak flaw distribution

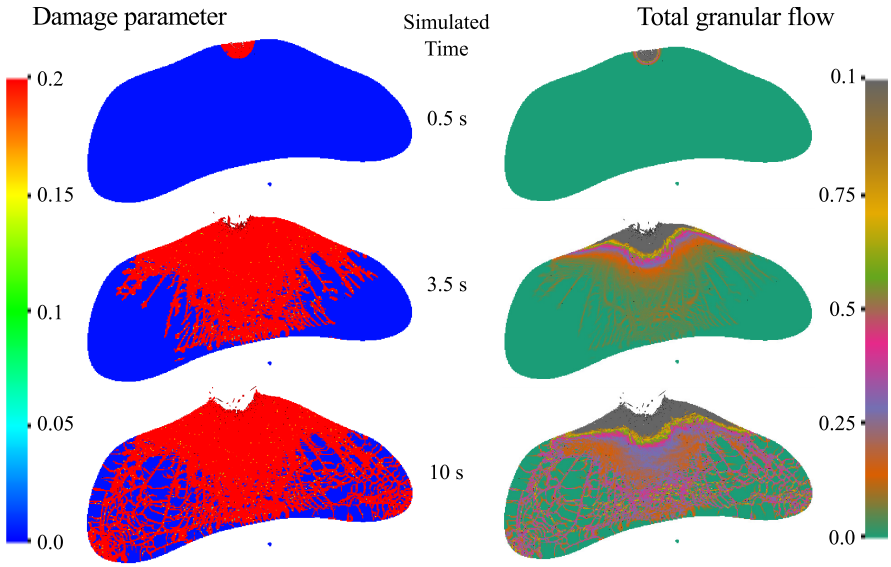

(b) Strong flaw distribution

Figure 6.10: Damage and granular flow evolution shown on a cross section for the weak (figure 6.10a) and strong (figure 6.10b) flaw distributions at three times after the Himeros forming impact event. Granular flow lags behind the damage growth. We see persistant localized features only for the strong flaw distribution case.

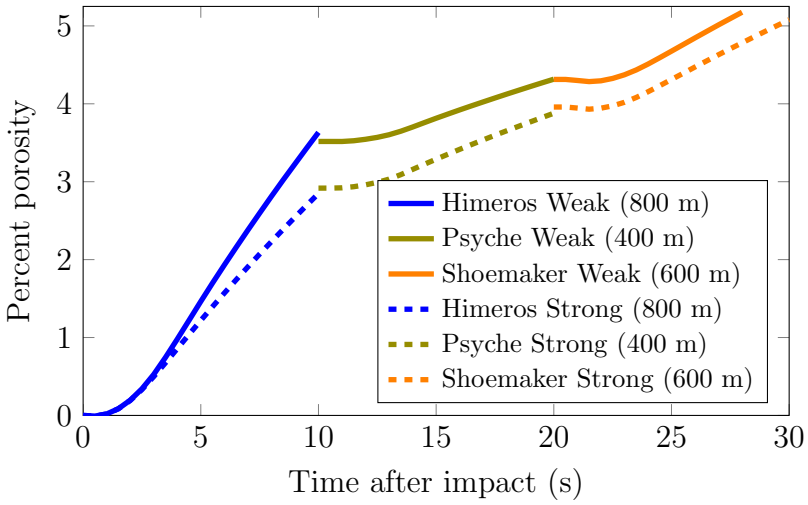

Figure 6.11: Bulk porosity (over 10 s each) evolution resulting from the interaction of multiple impact events

6.5.3 Multiple Impacts

6.5.3.1 Simulation Setup

We know that there have been multiple large impacts on Eros, and one expects the porosity in the body to evolve in response to these impact events. To simulate multiple impact events, we first simulate the Himeros forming impact event. After simulating 10s of time, we stop the simulation and use artificial viscous damping to stop all of the motion in the body. After allowing the damping to procede for an additional 10s we stop the simulation, and restart it with the damping turned off and give the next impactor its initial velocity.

Since our simulations do not include gravity and we are looking at the effect of the subscale flaw distribution on the observed impact response, we use strength scaling

[103] to compute the impactor size for the Psyche and Shoemaker events based on the size of the Himeros impactor. Since the target and impact velocities remain the same, the strength of the target can be removed from the scaling relationship and the resulting size for the Psyche forming impact was 400m in diameter and that for the Shoemaker forming impactor was 600m in diameter.

6.5.3.2 Bulk Porosity Evolution

After each impact, we compute the bulk porosity in the body as a function of time. These results are summarized in figure 6.11. Note that only 10 seconds are simulated after each impact event and so the total porosity is less than the porosity that was developed in the 80s long simulation. In the Himeros forming impact, the weak flaw distribution generated porosity faster than the strong flaw distribution. This is likely because the larger volume of material that is damaged for the weak flaw distribution produced porosity more readily than the smaller damaged volume in the simulation with the stronger flaw distribution. During the second impact, the weak distribution produced slightly less additional porosity than was produced in the strong distribution. This suggests that existing porosity inhibits the production of further porosity. This is consistent with rubble piles being difficult to disrupt because they absorb a large amount of energy through deformation at very low stresses[104]. The moderate porosity production rate for the Shoemaker event supports this idea because, while it is a more energetic event, it produces about the same rate of porosity

growth as the smaller Psyche forming event.

Based on these results, one should expect that at some critical porosity, a competition between pore compaction during the compression phase of the impact event and porosity development during the excavation phase will result in an equilibrium porosity in a body. If one considers an evolution from a solid body to a highly fragmented rubble pile, then it may be possible to define an additional measure of the maturity of an asteroid based on its porosity. Since the first impact on a solid body has the most influence over the crack network within the body, it appears to be appropriate to treat NEOs as rubble piles for the purposes of simulating asteroid mitigation strategies. Rubble piles will be more difficult to move than an intact shard and after the first large impact many bodies will be heavily fractured.

6.5.3.3 Lineament Structure Evolution

Just as the first impact event likely produced most of the porosity in Eros, it also sets up the fracture network for later impact events. As shown in figure 6.12, the structure of the linear features both in the interior of the body and on the surface is determined by the initial impact. Subsequent impact events add to the local deformation in the neighborhood immediately surrounding the impact site, but they do not add many linear features distant from the impact site. This implies that, regardless of the source of the background fabric on Eros, once it is formed, subsequent impact events of similar severity are unlikely to significantly reorient the features. This argu-

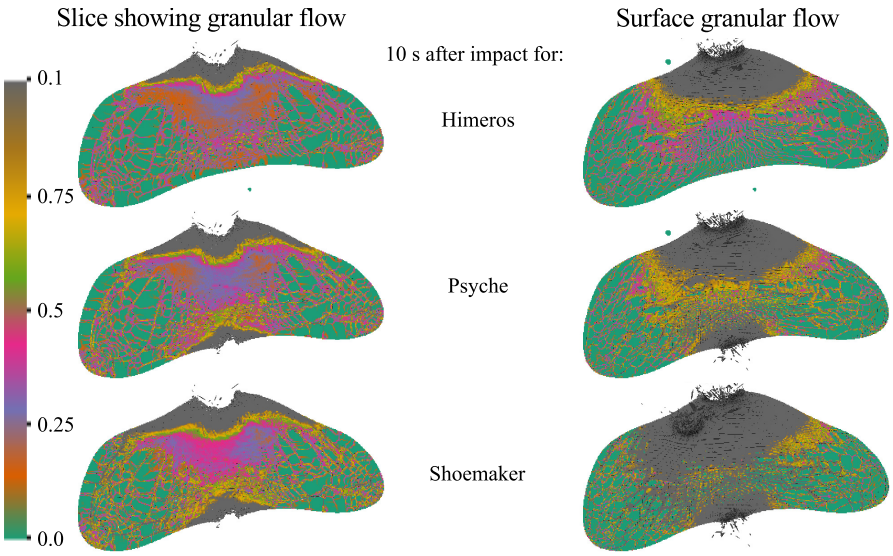

Figure 6.12: Internal and surface granular flow evolution resulting from multiple impacts for the strong flaw distribution. The color scale represents the total accumulated equivalent shear deformation due to granular flow at each particle. In this scale the limits of 0 (teal) and 0.1 (gray) were selected to highlight the linear features and the gray regions have saturated the scale. The initial impact event sets up the structure of the localizations then subsequent impacts only modify the localization pattern near the impact site.

ment applies to the strong flaw distribution case because we can see the development of lineament features in the simulations. It is possible that the same argument could apply to the weak flaw distribution case; however, we do not see explicit linear features in the weak flaw case, and so the simulations cannot tell us how they evolve with multiple impacts.

6.6 Summary

In this work we presented results for simulations of the impact history of Eros using a new material model based on subscale crack interactions. Using this material model we looked a the Himeros forming impact event in detail, then looked at the consequences of multiple impact events.

We demonstrated that the 20 percent observed bulk porosity of Eros is consistent with porosity developed in an initially solid body subjected to multiple impacts. The "stronger" flaw distribution that contained more small flaws develops linear features on the surface and in the interior of the body while the "weaker" distribution with larger flaws did not develop these features. Finally we observed that when the initial impact develops an internal structure consisting of many linear features, subsequent impacts only modify the structure locally and do not reorient the existing features.

Chapter 7

Summary and Future Work

7.1 Summary

In this work, we developed a material model for simulating the failure of brittle materials under impact loading. In the second chapter, we discussed an approach to incorporating a random distribution of flaws within a material into the computational discretization of an initial boundary value problem. In chapter 3, we briefly reviewed the material point method and propose an update to a popular and commonly used finite deformation plasticity algorithm. Chapter 4 provided a detailed discussion of the material model and uses that model to simulate dynamic failure of AlON subjected to Edge-On Impact loading. In chapter 5, we applied the material model to boron carbide in both uniaxial dynamic compression and simplified ballistic loading conditions. That chapter also discussed the importance of the granular flow

model and how that model works with the damage model to produce localized failure. Finally, in chapter 6, we applied the material model to a geologic material to simulate the evolution of the asteroid Eros under multiple impacts. The asteroid impact problem represents an application where models that bridge multiple scales based on the subscale physics provide a large advantage over traditional single scale material models. Even at these large scales, the statistical sampling of flaws is important to drive localization.

This work has presented a unified framework for incorporating microstructural information (particularly the flaw distribution) into a simulation of an impact event. This framework provides a mechanism to link microstructural information that can be modified through processing to application level performance metrics, which is an essential link for the materials by design process. In developing the material model we identified three key processes that informed the model:

- flaws in materials introduce statistical variability,
- in brittle materials, the controlling flaws are microcracks that grow and interact dynamically during the failure process
- flaw growth and interaction leads initially to elastic softening, but ultimately allows granular flow of the material

The specific problem of interest will determine which of these processes is most important for a particular application. This work presented a framework where these

components can be adjusted as needed.

7.2 Conclusions

In chapter 2 we discussed an approach to simulating a material microstructure by simulating the local flaw distribution within each computational subvolume (particle). We demonstrated that this approach converges to the input flaw distribution as additional flaw bins are used to simulate the flaw distribution and showed that using a 3-norm for the representative flaw size within a bin increases the rate that the simulated flaw distribution converges to the input flaw distribution.

In chapter 4 we developed a material model that incorporated the key physical processes that occur during the dynamic failure of brittle materials. This model captured the loading rate and specimen size dependent distribution of failure strengths that depends on the distribution of flaws within the material. Using this model we demonstrated that the failure front in Edge On Impact experiments propagates on the interior of the plate and is driven by the interaction of the longitudinal waves with the free (front and back) surfaces of the plate. Damage on the surface laggs behind the interior damage and a parametric study of slope for the granular flow behavior suggest that the slope must be less than 1.2 for AlON in these experiments. Additionally our results showed that both the damage kinetics and the granular flow behavior are important in this loading configuration.

With boron carbide we performed a more detailed parameter study of the material model using both uniaxial compression and simplified ballistic loading configurations. Based on experimental evidence we selected an slope of 0.8 for the granular flow surface; however, the simulations indicate that a lower slope (0.6) promotes more cone type cracking, which may suggest that the effective friction angle should be allowed to evolve as granular flow progresses. Increasing the time scale associated with granular flow decreased the total amount of granular flow for a given impact velocity, which could suggest improved performance (depending on the particular choice of a performance metric). This suggests that a material that produces large highly angular fragments is likely to produce a smaller total damage zone and less penetration in the sphere on cylinder loading geometry that we studied in chapter 5.

In expanding the application of our model to planetary science, we demonstrated that the 20 percent porosity found on Eros could have been developed from multiple impact events if Eros started as an intact shard of material. We showed that lineaments formed on the surface for a "stronger" distribution of flaws, while the "weaker" distribution of flaws did not produce any resolved lineaments. These lineaments were not substantially reoriented in subsequent impacts suggesting that the global lineament structure on an asteroid is a remnant of the largest early impacts on the body.

7.3 Future Work

Developing a modeling framework is the most difficult first step towards being able to solve many interesting problems, many of which we did not have space or time to fully address. In this section, we provide some thoughts on the future directions that this modeling framework opens up for exploration. These fall into three categories: computational methods, material modeling, and future application areas.

7.3.1 Computational Methods

In this work we identified four key areas that need further development to improve the ability of this model (and many others) to make predictions that can be used for decision making in an application environment:

- Representation of arbitrary geometries using conforming boundaries within an MPM like framework (B. Leavy and R. Brannon are working on this)
- An approach for treating both weak and strong discontinuities within the material point framework (this was done using enrichment in CPDI2 for weak discontinuities)
- Understanding the convergence behavior of this and other softening material models and developing improved tests for convergence in statistical material models

- Identifying methods to consistently allow for crack growth from the sub-scale into the macroscale within the material point method.

Constitutive models that can develop a highly heterogeneous response where the material stiffness varies rapidly from one subvolume to another require careful treatment when used with computational approaches that make assumptions about the continuity of the deformation field. For example, in this work, we always use 1 particle per cell when discretizing materials that use the Tonge-Ramesh material model. This was done because the local update for the velocity gradient assumed a smooth velocity field. There are two possible solutions to this limitation:

- one can either enforce smoothness in the effective material stiffness (by computing a "smoothed" damage value), or
- one can adapt the computational approach to remove the assumption of smoothness and allow piecewise constant stiffnesses.

The first approach may be less intrusive to the host computational framework, but the second approach is more general and preserves the local character of the constitutive model.

Accurately representing the development of material fragments in an efficient physically reasonable manner is an area of research that will continue to evolve because this is both a difficult problem and one that is difficult to test. Fragmentation and failure of brittle materials is a statistical process and we need well defined perfor-

mance metrics that can be used to compute convergence criteria. The combination of experiments that are difficult to analyze with large uncertainties has lead to judging models by how physical the results "look". Suitably large simulations of fragmentation should provide a method to test for mesh bias; however, one needs theoretical predictions to describe what the results should be in order to assess this mesh bias.

The community will clearly benefit from more quantitative measures that are reasonably inexpensive to compute. Once we define a metric for convergence, one can investigate why some approaches seem to converge and some do not. The model presented in this thesis seems to converge for some parameter choices but for other choices seems to not converge. Choosing the mesh resolution for investigating the failure of quasi-brittle materials under impact loading is unfortunately not as simple as performing a convergence study where the method has well established convergence properties. We have seen some results that suggest that for some parameter choices this material model converges nicely in the sense of a distribution; however another study with similar material properties did not show these properties. Assessing and establishing convergence in statistical material systems is an ongoing effort. An equally interesting question is why some models seem to converge and why some do not.

7.3.2 Material Modeling

Related to the convergence question is the question of whether the models capture all of the *relevant* physical processes for a particular initial boundary value problem. Different loading geometries will exercise different portions of the material model and inevitably there are some loading regimes where this model can benefit from improvements. A key consideration before adding additional processes to the material model is whether they are supported by experimental observations and whether the loading environment of interest is sensitive to those parameters.

For example, in this model some areas that could be improved include:

- tracking the evolving distribution of microcrack normals at the computational discretization scale,
- allowing for crack nucleation,
- allowing for the propagation of a crack into neighboring material volumes,
- incorporation of a more complex granular flow model,
- incorporation of a more complex equation of state that includes phase changes,
- accounting for dislocation (or twin boundary) mediated plasticity, or
- accounting for amorphization.

Tracking the distribution of crack normals would lead to an anisotropic stiffness, which may be important for proportional loading environments such as confined dynamic

compression experiments (this is similar to the work done by [26, 27, 29]). Tracking both the orientation distribution and size distribution of flaws introduces additional dimensionality into the flaw distribution discretization problem. For example we used 25 flaw size bins for the simulations in chapter 5. If we use 9 flaw orientation (the minimum suggested in [26, 27, 29]) then a total of 225 flaw bins will be required which represents a significant cost in memory, CPU time to solve the micromechanics, and the MPI communication time required to communicate the additional information. While non-uniform bin sizing was sufficient for simulating the flaw size distribution for a single flaw orientation (see section 2.2) some form of dynamic adaptive binning could be required if both the flaw orientation and size distributions are tracked.

The material model only accounts for the growth of pre-existing flaws, but does not allow for either crack nucleation or the growth of cracks into a neighboring material volume. This restriction ties the minimum mesh size to the flaw density of the material. When the discretization is on the order of the flaw spacing, there may be some subvolumes that contain no initial flaws resulting in a material point that cannot fail. An improved model will remove this possibility either by allowing crack nucleation or introducing an additional mechanism like lattice plasticity.

Similarly, this work used a very simple granular flow model. In future work we may update this model to compute the granular flow timescale based on the spacing between cracks that have exceeded an specific criteria. We showed that the granular flow model can influence a variety of boundary value problems from dynamic uniaxial

compression to edge on impact and the simplified ballistic tests. The challenge is to identify the simplest model that will work. One could also develop a granular flow model that includes an evolving coefficient of friction as a function of the amount of granular flow. Any of these modifications would need to be motivated by detailed experiments or meso-scale models.

At increased impact velocities it may be appropriate to use a different equation of state that includes phase changes. There are also model improvements that are specific to each material. For example boron carbide shows amorphization, which has been shown to influence the fragment size and ceramics such as Aluminum Nitride show a brittle to ductile transition and dislocation mediated plasticity. Any of these additional mechanisms could be incorporated into the model if there is sufficient experimental evidence to justify the inclusion and provide the necessary material parameters.

7.3.3 Applications of the Current Model

While there are always improvements that can be made to a model and a modeling framework, it is equally important to exercise the existing frameworks to extract the maximal amount of understanding and learn where their limitations may be.

7.3.3.1 Armor Ceramics

With regard to armor ceramic materials (either AlON or boron carbide), this model can be applied to the following problems without any modifications to the existing framework:

- simulate the fragmentation of an armor ceramic plate under biaxial tension,
- simulate the fragmentation of a cube of armor ceramic under triaxial tension,
- simulate the failure of a 10mm cube under dynamic uniaxial compression,
- simulate the dynamic failure of a 10mm cube with confinement in one direction followed by dynamic compression in the other direction,
- simulate additional simplified ballistic loading geometries (plate impact and perforation or long-rod penetration).

These five loading configurations are simulations that are basically ready to run. With the exception of the triaxial tension case, there are existing input files for similar geometries that were run using previous iterations of the model. The fragmentation problems may reveal some interesting coupling between the shape of the input flaw distribution (power law slope) and the observed flaw size (and possibly shape) distribution. It is equally possible that the test will highlight the existence or lack of mesh bias in the simulations. In either case, the ability to perform simulations of dynamic fragmentation using a massively parallel computational framework coupled with a

physics based material model that accounts for the statistical nature of brittle materials with make these fragmentation studies interesting. Even identifying discrete fragments in an arbitrary three dimensional space with large data sets is a difficult problem. Similar to tensile fragmentation, it will be interesting to use the model to simulate a Kolsky bar experiment on a larger (8 to 10mm cube) specimen and compare the predicted stress time behavior and the predicted fragment size distribution. With the existing model we expect the failure mode and failure pattern to be sensitive to additional planar confinement; however, we do not expect to capture the increase in dynamic strength with planar confinement because this model does not incorporate a distribution of flaw orientations. Still it is important to find the limits of a model before investing considerable effort in adding new features. This could also provide a useful test for models that do incorporate the orientation distribution of flaws. The potential to simulate additional simplified ballistic loading geometries exists and the possibile combinations of conditions are nearly endless. The important consideration in selecting problems for further study is what additional insight can be gained from these particular simulations. Long rod penetration will certainly test the granular flow model and could suggest improvements to that model.

Adding additional boundary conditions to the MPM component within the Uintah framework will allow more detailed comparisons to experiments. In particular, it would be useful to have the ability to apply a forced Robbin type boundary condition

where:

$$\boldsymbol{A}\boldsymbol{u} + \boldsymbol{B}(\boldsymbol{n} \cdot \nabla \boldsymbol{u}) = \boldsymbol{g}(t) \tag{7.1}$$

is applied on the boundary. This type of boundary condition could be used to enforce an infinite medium boundary, where waves propagate into the boundary and do not reflect from it, or to match the experimental boundary conditions in a Kolsky bar experiment. Using these boundary conditions, both the

- uniaxial dynamic compression, and the
- confined dynamic compression

simulations could be revisited and provide much better references for validation of the material model. Matching the boundary conditions in the experiments is essential for performing detailed validation simulations. Once these boundary conditions are implemented, Kolsky bar experiments become very powerful tools for testing the performance of this (or a similar) material model.

7.3.3.2 Planetary Science

Using the model presented in this work, there is great potential for applications in planetary science where the uncertainties that are inherent in the modeling of the impact events suggest the use of simple models because additional parameters only increase the number of unknowns in the system. Our work with Eros represents only the beginning of what can be done using this model. We have seen with previous

revisions of the model that the damage zone during an impact event seems to be relatively mesh insensitive when simulating asteroid sized bodies. Based on our previous work we suggest the following additional simulations that could be accomplished with little additional effort:

- study the lifetime of an initial macroscopic flaw distribution subjected to repeated impact events and
- use this model to simulate an initial impact event then hand the particle velocities and masses off to an N-body gravitational code (such as PkdGrav) and compute the trajectories of the particles after long times.

If someone is willing to invest the time to tightly couple this model to a gravity solver, then the model could be used to simulate an impact event by beginning with the explicit calculation of the impact event, then after the short wavelength stress waves have dissipated switch the calculation to an implicit computation with gravity to move to longer times, finally transitioning to using only an N-body gravity code to compute the distribution of the fragments formed during an impact event on the surface of the body. However, significant development would be needed to complete the explicit to implicit to N-body transition. The result of such an investment could position Uintah as the best available tool for modeling all stages of crater formation, from the initial impact event, to the gravitational slumping of the crater walls. In the short term we will look at performing the explicit simulation to N-body simulation

hand-off.

Using this modeling framework we have performed simulations of the possible impact evolution of the asteroid Eros. Chapter 6 presented a few key results from this study, but there is more information that could be gathered from the existing simulations. For example the total surface displacements could be compared to the displacement estimated from surface images. Similarly, we could use this model to create a very high resolution simulation of an impact event. We could then use tools for investigating large data-sets to derive further information from the large simulation.

Appendix A

Appendix From Chapter 4

A.1 Calculation of the Isotropic Strain Energy Density Function

In this section we derive the isotropic strain energy density function associated with the general strain energy density defined in equation (4.46). The isotropic strain energy density is defined by $\rho(\boldsymbol{n}) = 1$. Making this substitution and splitting the

integral into pieces results in:

$$\begin{aligned} f = & \frac{1}{2}\boldsymbol{\tau} : \mathbb{S}_0 : \boldsymbol{\tau} \\ & + \frac{D}{8\pi}\iint_\omega Z_r \boldsymbol{\tau}\cdot\boldsymbol{\tau} : \boldsymbol{n}\otimes\boldsymbol{n} d\omega \\ & - \frac{D}{8\pi}\iint_\omega (Z_r - Z_n)\boldsymbol{\tau} : \boldsymbol{n}\otimes\boldsymbol{n}\otimes\boldsymbol{n}\otimes\boldsymbol{n} : \boldsymbol{\tau} d\omega \\ & + \frac{D}{8\pi}\iint_\omega Z_c \boldsymbol{\tau} : \boldsymbol{n}\otimes\boldsymbol{n}\otimes\boldsymbol{I} : \boldsymbol{\tau} d\omega \\ & + \frac{D}{8\pi}\iint_\omega Z_c \boldsymbol{\tau} : \boldsymbol{I}\otimes\boldsymbol{n}\otimes\boldsymbol{n} : \boldsymbol{\tau} d\omega \\ & - \frac{D}{8\pi}\iint_\omega 2Z_c \boldsymbol{\tau} : \boldsymbol{n}\otimes\boldsymbol{n}\otimes\boldsymbol{n}\otimes\boldsymbol{n} : \boldsymbol{\tau} d\omega \end{aligned} \tag{A.1}$$

In these integrals the only dependence on orientation is in $\boldsymbol{n}$. By rearranging the integrals to move all of the orientation independent terms outside of the integral we have:

$$\begin{aligned} f = & \frac{1}{2}\boldsymbol{\tau} : \mathbb{S}_0 : \boldsymbol{\tau} \\ & + \frac{D}{8\pi} Z_r \boldsymbol{\tau}\cdot\boldsymbol{\tau} : \left(\iint_\omega \boldsymbol{n}\otimes\boldsymbol{n} d\omega\right) \\ & - \frac{D}{8\pi}(Z_r - Z_n)\boldsymbol{\tau} : \left(\iint_\omega \boldsymbol{n}\otimes\boldsymbol{n}\otimes\boldsymbol{n}\otimes\boldsymbol{n} d\omega\right) : \boldsymbol{\tau} \\ & + \frac{D}{8\pi} Z_c \boldsymbol{\tau} : \left(\iint_\omega \boldsymbol{n}\otimes\boldsymbol{n} d\omega\right)\otimes\boldsymbol{I} : \boldsymbol{\tau} \\ & + \frac{D}{8\pi} Z_c \boldsymbol{\tau} : \boldsymbol{I}\otimes\left(\iint_\omega \boldsymbol{n}\otimes\boldsymbol{n} d\omega\right) : \boldsymbol{\tau} \\ & - \frac{D}{8\pi} 2Z_c \boldsymbol{\tau} : \left(\iint_\omega \boldsymbol{n}\otimes\boldsymbol{n}\otimes\boldsymbol{n}\otimes\boldsymbol{n} d\omega\right) : \boldsymbol{\tau} \end{aligned} \tag{A.2}$$

There are two integrals that we need to evaluate. The approach for evaluating these intergals is due to conversations with R. Brannon. We start by evaluating:

$$\boldsymbol{B}_1 = \frac{1}{4\pi}\iint_\omega \boldsymbol{n}\otimes\boldsymbol{n} d\omega \tag{A.3}$$

We can interpret $\boldsymbol{n}$ as a position vector that extends from the origin to the boundary of the unit sphere:

$$\boldsymbol{B}_1 = \frac{1}{4\pi} \iint_{\partial\Omega} \boldsymbol{x} \otimes \boldsymbol{n} ds. \tag{A.4}$$

Here $\boldsymbol{x}$ is a position vector in the unit sphere (Ω) and $\boldsymbol{n}$ is a normal vector to the sphere surface. From the Gauss divergence theorem we convert the surface integral into a volume integral:

$$\boldsymbol{B}_1 = \frac{1}{4\pi} \iiint_{\Omega} \nabla_{\boldsymbol{x}} \boldsymbol{x} dV. \tag{A.5}$$

The gradient of a position vector is $\boldsymbol{I}$. The integral reduces to computing the volume of the sphere

$$\boldsymbol{B}_1 = \frac{1}{4\pi} \boldsymbol{I} V(r). \tag{A.6}$$

In this integral the volume is the unit sphere and therefore the total integral is given by:

$$\boldsymbol{B}_1 = \frac{1}{3} \boldsymbol{I}. \tag{A.7}$$

A similar procedure can be used to evaluate the other integral tensor:

$$\mathbb{B}_2 = \frac{1}{4\pi} \iint_{\omega} \boldsymbol{n} \otimes \boldsymbol{n} \otimes \boldsymbol{n} \otimes \boldsymbol{n} d\omega. \tag{A.8}$$

Writing this tensor in terms of its components:

$$(B_2)_{ijkl} = \frac{1}{4\pi} \iint_{\omega} n_i n_j n_k n_l d\omega. \tag{A.9}$$

We interpret the first three normal vectors as position vectors in the unit sphere Ω:

$$(B_2)_{ijkl} = \frac{1}{4\pi} \iint_{\partial\Omega} x_i x_j x_k n_l dS. \tag{A.10}$$

Applying the generalized divergence theorem:

$$(B_2)_{ijkl} = \frac{1}{4\pi} \iiint_\Omega \frac{\partial (x_i x_j x_k)}{\partial x_l} dV. \tag{A.11}$$

Expanding using the derivative:

$$(B_2)_{ijkl} = \frac{1}{4\pi} \iiint_\Omega x_{i,l} x_j x_k + x_{j,l} x_i x_k + x_{k,l} x_i x_j dV \tag{A.12}$$

We represent one of the position vectors in each of the terms in the sum as an orientation $\boldsymbol{n}$ multiplied by a radius r and write the volume integral as a surface integral and a radial integral:

$$(B_2)_{ijkl} = \frac{1}{4\pi} \int_0^1 \left(\iint_{\partial\Omega_r} \delta_{il} x_j n_k + \delta_{jl} x_i n_k + \delta_{kl} x_i n_j dS \right) r dr. \tag{A.13}$$

The evaluation of $\boldsymbol{B}_1$ indicates that the surface integral evaluates to:

$$\iint_{\partial\Omega_r} \delta_{il} x_j n_k dS = \frac{1}{3} \delta_{il} \delta_{jk} \frac{4\pi r^3}{3} \tag{A.14}$$

Comparing this result to equation (A.13) results in:

$$(B_2)_{ijkl} = \frac{1}{3} \left(\delta_{il}\delta_{jk} + \delta_{jl}\delta_{ik} + \delta_{kl}\delta_{ij} \right) \int_0^1 r^4 dr. \tag{A.15}$$

These three terms are the three isotropic fourth order tensors $(\mathbb{I}, \bar{\mathbb{I}}, \boldsymbol{I} \otimes \boldsymbol{I})$ and the integral evaluates to $\frac{1}{5}$:

$$(B_2)_{ijkl} = \frac{1}{15} \left(\mathbb{I} + \bar{\mathbb{I}} + \boldsymbol{I} \otimes \boldsymbol{I} \right) = \frac{1}{15} \boldsymbol{I} \otimes \boldsymbol{I} + \frac{2}{15} \mathbb{S} \tag{A.16}$$

A.2 Corrected Self Consistent Method Solution (Liu et al. [1])

The compliance of the matrix material is given by equation (4.54) however it is convenient to write out the non-zero components of the compliance tensor:

$$s_{1111} = \frac{1}{E_0} \tag{A.17}$$

$$s_{2222} = \frac{1}{E_0} + \frac{8(1-\nu_0^2)}{3E_0(2-\nu_0)}\left(D\left(4-2\nu_0\right)\right) \tag{A.18}$$

$$s_{3333} = \frac{1}{E_0} \tag{A.19}$$

$$s_{1122} = s_{2233} = \frac{-\nu_0}{E_0} - \frac{2(1-\nu_0^2)}{3E_0}D \tag{A.20}$$

$$s_{1212} = \frac{1+\nu_0}{2E_0} + \frac{8(1-\nu_0^2)}{3E_0(2-\nu_0)}D \tag{A.21}$$

$$s_{1133} = \frac{-\nu_0}{E_0} \tag{A.22}$$

$$s_{1313} = \frac{1+\nu_0}{2E_0} \tag{A.23}$$

$$s_{2323} = \frac{1+\nu_0}{2E_0} + \frac{8(1-\nu_0^2)}{3E_0(2-\nu_0)}D \tag{A.24}$$

To use plane strain instead of plane stress, we need to compute the stiffness tensor (c_{ijkl}) by inverting s_{ijkl}:

$$\begin{bmatrix} c_{1111} & c_{1122} & c_{1133} \\ c_{1122} & c_{2222} & c_{2233} \\ c_{1133} & c_{2233} & c_{3333} \end{bmatrix} = \begin{bmatrix} s_{1111} & s_{1122} & s_{1133} \\ s_{1122} & s_{2222} & s_{2233} \\ s_{1133} & s_{2233} & s_{3333} \end{bmatrix}^{-1} \tag{A.25}$$

From the stiffness tensor we can compute the reduced stiffness tensor. We then invert the reduced stiffness tensor to compute the reduced compliance tensor:

$$\begin{bmatrix} s_{11}^{11} & s_{22}^{11} \\ s_{22}^{11} & s_{22}^{22} \end{bmatrix} = \begin{bmatrix} c_{1111} & c_{1122} \\ c_{1122} & c_{2222} \end{bmatrix}^{-1} \tag{A.26}$$

The inversion of the 2x2 matrix can be done analytically which gives the planar compliance components in terms of the components of the stiffness tensor:

$$s_{11}^{11} = \frac{c_{2222}}{c_{1111}c_{2222} - c_{1122}^2} \tag{A.27}$$

$$s_{22}^{22} = \frac{c_{1111}}{c_{1111}c_{2222} - c_{1122}^2} \tag{A.28}$$

$$s_{22}^{11} = \frac{-c_{1122}}{c_{1111}c_{2222} - c_{1122}^2} \tag{A.29}$$

$$s_{12}^{12} = s_{1212} \tag{A.30}$$

For plane stress the reduction occurs for the compliance tensor not the stiffness tensor.

This self consistent solution is an application of the work in "Theoretical Elasticity" by Green and Zerna. The following solution was developed by Liu et al. as a correction to [10], it is provided here for completeness.

Starting from section 9.1 of Green and Zerna we define an Airy stress function $\phi(z)$ with the general form:

$$\phi = \Omega(z_1) + \bar{\Omega}(\bar{z}_1) + \omega(z_2) + \bar{\omega}(\bar{z}_2) \tag{A.31}$$

Here we have defined the complex variables z_k and $\bar{z}_k$ with $k = 1, 2$ as (equations

6.9.1 and 6.9.2):

$$0 = s_{22}^{22}\alpha^4 - 2\left(s_{22}^{11} + 2s_{12}^{12}\right)\alpha^2 + s_{11}^{11} \tag{A.32}$$

$$\alpha_1^2 = \frac{2\left(s_{22}^{11} + 2s_{12}^{12}\right) + \sqrt{4\left(s_{22}^{11} + 2s_{12}^{12}\right)^2 - 4s_{11}^{11}s_{22}^{22}}}{2s_{22}^{22}} \tag{A.33}$$

$$\alpha_2^2 = \frac{2\left(s_{22}^{11} + 2s_{12}^{12}\right) - \sqrt{4\left(s_{22}^{11} + 2s_{12}^{12}\right)^2 - 4s_{11}^{11}s_{22}^{22}}}{2s_{22}^{22}} \tag{A.34}$$

$$\alpha_k = \sqrt{\alpha_k^2} \tag{A.35}$$

$$\gamma_k = \frac{\alpha_k - 1}{\alpha_k + 1} \tag{A.36}$$

$$z_k = z + \gamma_k \bar{z} \tag{A.37}$$

$$\bar{z}_k = \bar{z} + \bar{\gamma}_k z \tag{A.38}$$

Here the material parameters s_{ij}^{kl} are the components of the planar compliance tensor (see section 5.12 for the relation to the common stiffness matrix in Voigt notation).

From Section 9.1 the displacements are given by (equation 9.1.4):

$$D = u + iv = \delta_1\Omega'(z_1) + \rho_1\bar{\Omega}'(\bar{z}_1) + \delta_2\omega'(z_2) + \rho_2\bar{\omega}'(\bar{z}_2) \tag{A.39}$$

Here (equations 6.9.4 and 6.9.5):

$$\beta_k = s_{22}^{11} - s_{22}^{22}\alpha_k^2 \tag{A.40}$$

$$\delta_1 = (1+\gamma_1)\beta_2 - (1-\gamma_1)\beta_1 \tag{A.41}$$

$$\delta_2 = (1+\gamma_2)\beta_1 - (1-\gamma_2)\beta_2 \tag{A.42}$$

$$\bar{\rho}_1 = (1+\gamma_1)\beta_2 + (1-\gamma_1)\beta_1 \tag{A.43}$$

$$\bar{\rho}_2 = (1+\gamma_2)\beta_1 + (1-\gamma_2)\beta_2 \tag{A.44}$$

And the tractions are (9.1.8):

$$P = X + iY = 2i\left(\gamma_1\Omega'(z_1) + \bar{\Omega}'(\bar{z}_1) + \gamma_2\omega'(z_2) + \bar{\omega}'(\bar{z}_2)\right) \tag{A.45}$$

To account for the elliptical geometry we define the mapping:

$$z = z(\zeta) = c\zeta + \frac{d}{\zeta} \tag{A.46}$$

$$c = \frac{a+b}{2} \tag{A.47}$$

$$d = \frac{a-b}{2} \tag{A.48}$$

$$z_k = (c + \gamma_k d)\zeta_k + \frac{(d + \gamma_k c)}{\zeta_k} \tag{A.49}$$

We now defined functions $f(\zeta_1)$ and $g(\zeta_2)$ such that:

$$\Omega'(z_1) = f(\zeta_1) \tag{A.50}$$

$$\omega'(z_2) = g(\zeta_2) \tag{A.51}$$

We try potentials of the form:

$$f(\zeta_1) = H_1\zeta_1 + \frac{G_1}{\zeta_1} \tag{A.52}$$

$$g(\zeta_2) = H_2\zeta_2 + \frac{G_2}{\zeta_2} \tag{A.53}$$

$$H_1 = (B + iC)(c + \gamma_1 d) \tag{A.54}$$

$$H_2 = (B' + iC')(c + \gamma_2 d) \tag{A.55}$$

Evaluating the stress at large ζ, and requiring bounded displacements leads to equations 9.1.16 and 9.1.17 in Green and Zerna, which can be used to solve for B, B', C,

and C': (Note $N_1 = \sigma_3$ and $N_2 = \sigma_1$)

$$N_1 + N_2 = 4\gamma_1(B + iC) + 4\bar{\gamma}_1(B - iC) + 4\gamma_2(B' + iC') + 4\bar{\gamma}_2(B' - iC' \tag{A.56}$$

$$N_1 - N_2 = -4\gamma_1^2(B + iC) - 4(B - iC) - 4\gamma_2^2(B' + iC') - 4(B' - iC') \tag{A.57}$$

Equation 9.1.18, which results from bounded displacements at infinity, is also required.

$$\begin{aligned} 0 = (1 - \gamma_1\bar{\gamma}_1)\,[(\gamma_1 - \gamma_2)(1 - \gamma_1\bar{\gamma}_2)(B + iC) - \\ (\bar{\gamma}_1 - \bar{\gamma}_2)(1 - \bar{\gamma}_1\gamma_2)(B - iC)] \\ - (1 - \gamma_2\bar{\gamma}_2)\,[(\gamma_1 - \gamma_2)(1 - \bar{\gamma}_1\gamma_2)(B' + iC') - (\bar{\gamma}_1 - \\ \bar{\gamma}_2)(1 - \gamma_1\bar{\gamma}_2)(B' - iC')] \end{aligned} \tag{A.58}$$

We can rearrange and group terms to set up the solution for B, B', C, and C':

$$N_1 + N_2 = 4(\gamma_1 + \bar{\gamma}_1)B + 4i(\gamma_1 - \bar{\gamma}_1)C + 4(\gamma_2 + \bar{\gamma}_2)B' + 4i(\gamma_2 - \bar{\gamma}_2)C' \tag{A.59}$$

$$N_1 - N_2 = -4(\gamma_1^2 - 1)B - 4i(\gamma_1^2 - 1)C - 4(\gamma_2^2 - 1)B - 4i(\gamma_2^2 - 1)C' \tag{A.60}$$

In the matrix at the boundary between the inclusion and the matrix we have $||\zeta|| = 1$ ($||z|| = 1 = ||\zeta||, \frac{1}{\zeta} = \bar{\zeta}$ and the displacements are given by:

$$D = \delta_1\Omega'(z_1) + \rho_1\bar{\Omega}'(\bar{z}_1) + \delta_2\omega'(z_2) + \rho_2\bar{\omega}'(\bar{z}_2) \tag{A.61}$$

$$D = \delta_1\left(H_1\zeta + G_1\bar{\zeta}\right) + \rho_1\left(\bar{H}_1\bar{\zeta} + \bar{G}_1\zeta\right) + \delta_2\left(H_2\zeta + G_2\bar{\zeta}\right) + \rho_2\left(\bar{H}_2\bar{\zeta} + \bar{G}\zeta\right) \tag{A.62}$$

$$D = (\delta_1 H_1 + \rho_1\bar{G}_1 + \delta_2 H_2 + \rho_2\bar{G}_2)\zeta + (\delta_1 G_1 + \rho_1\bar{H}_1 + \delta_2 G_2 + \rho_2\bar{H}_2)\bar{\zeta} \tag{A.63}$$

And the resulting force over an arc is given by:

$$P = 2i\left(\gamma_1\Omega'(z_1) + \bar{\Omega}'(\bar{z}_1) + \gamma_2\omega'(z_2) + \bar{\omega}'(\bar{z}_2)\right) \tag{A.64}$$

$$P = 2i\left(\gamma_1\left(H_1\zeta + G_1\bar{\zeta}\right) + \left(\bar{H}_1\bar{\zeta} + \bar{G}_1\zeta\right) + \gamma_2\left(H_2\zeta + G_2\bar{\zeta}\right) + \left(\bar{H}_2\bar{\zeta} + \bar{G}_2\zeta\right)\right) \tag{A.65}$$

$$P = 2i\left((\gamma_1 H_1 + \bar{G}_1 + \gamma_2 H_2 + \bar{G}_2)\zeta + (\gamma_1 G_1 + \bar{H}_1 + \gamma_2 G_2 + \bar{H}_2)\bar{\zeta}\right) \tag{A.66}$$

The inclusion is an isotropic material. If we assume that the complex potentials $\Omega_i(z)$ and $\bar{\omega}_i(\bar{z})$ describe the material the displacements and tractions are given by:

$$\mu D_i = k\Omega_i(z) - z\bar{\Omega}'_i(\bar{z}) - \bar{\omega}_i(\bar{z}) \tag{A.67}$$

$$P_i = 2i(z\bar{\Omega}'_i(\bar{z}) + \Omega_i(z) + \bar{\omega}_i(\bar{z})) \tag{A.68}$$

The material constant k is given by $k = (3-\nu)/(1+\nu)$ for plane stress and $k = 3-4\nu$ for plane strain. These calculations are done for plane stress conditions because for plane strain the planar compliance tensor must be recalculated (compute the 3D stiffness tensor, perform the planar reduction, then invert that matrix to compute the planar compliance tensor). We try potentials of the form $\Omega_i(z) = A_1 z$, $\Omega'_i(z) = A_1$, and $\bar{\omega}'_i(\bar{z}) = A_2\bar{z}$ and apply the same conformational mapping ($z = c\zeta + d/\zeta$). Now we can evaluate the traction and displacement at the boundary of the ellipse ($||z|| = 1 = ||\zeta||, \frac{1}{\zeta} = \bar{\zeta}$):

$$\mu D_i = \left((k-1)\,A_1 c - A_2 d\right)\zeta + \left((k-1)\,A_1 d - A_2 c\right)\bar{\zeta} \tag{A.69}$$

$$P_i = 2i\left(\left(2A_1 c + A_2 d\right)\zeta + \left(2A_1 d + A_2 c\right)\bar{\zeta}\right) \tag{A.70}$$

Displacements and tractions must be continuous across the ellipse boundary, and

along the boundary ζ and $\bar{\zeta}$ are independent so we have 4 complex equations:

$$\mu(\delta_1 H_1 + \rho_1 \bar{G}_1 + \delta_2 H_2 + \rho_2 \bar{G}_2) = ((k-1)\, A_1 c - A_2 d) \tag{A.71}$$

$$\mu(\delta_1 G_1 + \rho_1 \bar{H}_1 + \delta_2 G_2 + \rho_2 \bar{H}_2) = ((k-1)\, A_1 d - A_2 c) \tag{A.72}$$

$$(\gamma_1 H_1 + \bar{G}_1 + \gamma_2 H_2 + \bar{G}_2) = (2A_1 c + A_2 d) \tag{A.73}$$

$$(\gamma_1 G_1 + \bar{H}_1 + \gamma_2 G_2 + \bar{H}_2) = (2A_1 d + A_2 c) \tag{A.74}$$

We can separate the known (H_1 and H_2) quantities from the unknowns (G_1, G_2, A_1, and A_2):

$$(k-1)cA_1 - dA_2 - \mu\bar{\rho}_1 G_1 - \mu\bar{\rho}_2 G_2 = \mu\bar{\delta}_1 \bar{H}_1 + \mu\bar{\delta}_2 \bar{H}_2 \tag{A.75}$$

$$(k-1)dA_1 - cA_2 - \mu\delta_1 G_1 - \mu\delta_2 G_2 = \mu\rho_1 \bar{H}_1 + \mu\rho_2 \bar{H}_2 \tag{A.76}$$

$$2cA_1 + dA_2 - G_1 - G_2 = \bar{\gamma}_1 \bar{H}_1 + \bar{\gamma}_2 \bar{H}_2 \tag{A.77}$$

$$2dA_1 + cA_2 - \gamma_1 G_1 - \gamma_2 G_2 = \bar{H}_1 + \bar{H}_2 \tag{A.78}$$

These 4 complex equations can be solved for the necessary complex constants, then the stresses in the ellipse are given by equation 8.1.18 in Green and Zerna (evaluated inside the ellipse on the real axis $z = \bar{z}$):

$$\sigma_{rr} + \sigma_{\theta\theta} = 4\left(\Omega_i'(z) + \bar{\Omega}_i'(\bar{z})\right) \tag{A.79}$$

$$\sigma_{rr} - \sigma_{\theta\theta} + 2i\sigma_{r\theta} = -4\left(\bar{z}\bar{\Omega}_i''(\bar{z}) + \frac{\bar{z}}{z}\bar{\omega}_i''(\bar{z})\right) \tag{A.80}$$

Evaluating inside the ellipse these derivatives are:

$$\Omega_i' = A_1 \tag{A.81}$$

$$\Omega_i'' = 0 \tag{A.82}$$

$$\omega_i' = A_2 z \tag{A.83}$$

$$\omega_i'' = A_2 \tag{A.84}$$

$$\sigma_{rr} + \sigma_{\theta\theta} = 4\left(A_1 + \bar{A}_1)\right) \tag{A.85}$$

$$= 8\mathrm{Re}(A_1) \tag{A.86}$$

$$\sigma_{rr} - \sigma_{\theta\theta} + 2i\sigma_{r\theta} = -4\left(\bar{z}0 + \frac{\bar{z}}{z}\bar{A}_2\right) \tag{A.87}$$

$$= -4\mathrm{Re}(A_2) + 4i\mathrm{Im}(A_2) \tag{A.88}$$

With the coordinate system that we have set up $\sigma_{11} = \sigma_{rr}$, $\sigma_{22} = \sigma_{\theta\theta}$, and $\sigma_{12} = \sigma_{r\theta}$:

$$\sigma_{11} = 4\mathrm{Re}(A_1) - 2\mathrm{Re}(A_2) \tag{A.89}$$

$$\sigma_{22} = 4\mathrm{Re}(A_1) + 2\mathrm{Re}(A_2) \tag{A.90}$$

$$\sigma_{12} = -2\mathrm{Im}(A_2) \tag{A.91}$$

A.3 Non-Weibull Distribution of Compressive Strengths

Since the Weibull distribution is widely used for describing distributions of failure strengths, we compare the strength distribution predicted by our material model to a

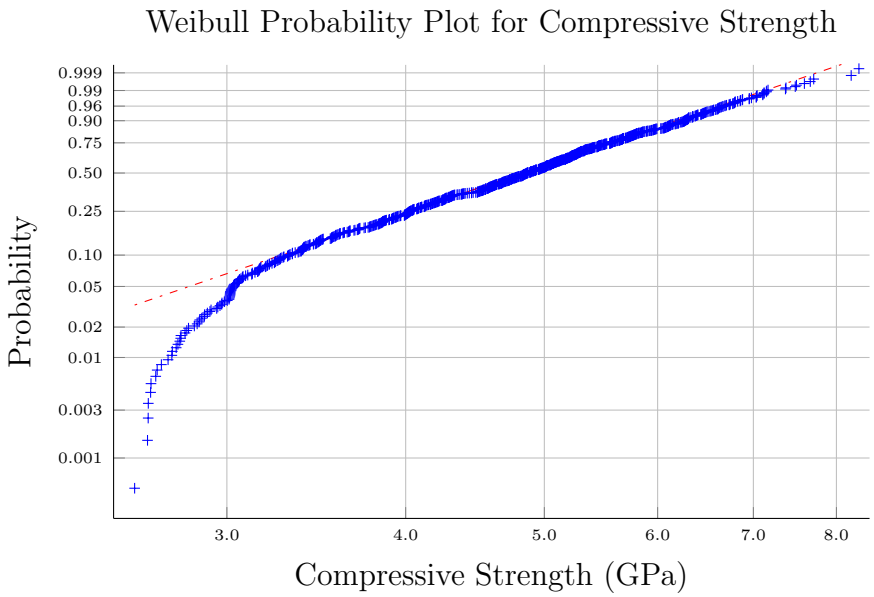

Figure A.1: Weibull plot of the computed compressive strength of a 0.5 mm cube at a strain rate of 10^3 1/s using 1000 samples. A Weibull distribution seems to fit the majority of the distribution, but provides a poor fit for the low strengths.

standard two parameter Weibull. For this study we enforce a homogeneous stress state by discretizing the specimen using a single material point. The 0.5 mm cube specimen is then loaded using a constant strain rate of $\dot{\epsilon} = 10^3$ 1/s under uniaxial stress conditions. We generate 1,000 independent samples by changing the random seed used to generate the flaw distribution for each simulation. After collecting all of the peak compressive stresses from the simulations, we construct the Weibull probability plot shown in figure A.1. The Weibull distribution is seen to provide a poor fit to the distribution of strengths, and over-predicts the probability of low compressive strengths.

Appendix B

User Manual for Tonge-Ramesh Material Model

B.1 Introduction

The Tonge-Ramesh material model is a micromechanics based constitutive model for the high rate failure of quasi-brittle materials such as armor ceramics. It incorporates micromechanics based damage, granular flow of the damaged material, lattice plasticity (volume preserving), and equation of state coupling. The key physical aspects of the model ares described in chapter 4. This document serves to detail the user input parameters and additional functionality that is not discussed in the paper. This document is not intended to discuss the physical implications of the input parameters or discuss the detailed physical reasoning used to develop the material

model.

B.2 Key physical equations

B.2.1 Elastic Response

We assume a decoupled representation of the Kirchoff stress tensor:

$$\boldsymbol{\tau} = \boldsymbol{\tau}_{dev} - p_s J_e \boldsymbol{I}. \tag{B.1}$$

The deviatoric stress $\boldsymbol{\tau}_{dev}$ is a linear function of the deviatoric part of the volume preserving elastic deformation as measured by $\bar{\boldsymbol{b}}_e = J_e^{-2/3} \boldsymbol{F}_e \boldsymbol{F}_e^T$:

$$\boldsymbol{\tau}_{dev} = G \left(\bar{\boldsymbol{b}}_e - \frac{1}{3} \mathrm{tr}(\bar{\boldsymbol{b}}_e) \boldsymbol{I} \right). \tag{B.2}$$

Here G is the damaged shear modulus defined as:

$$G(D) = \left(G_0^{-1} + \frac{2D}{15} \left(3Z_r + 2Z_n - 4Z_c \right) \right)^{-1}. \tag{B.3}$$

The parameters Z_n, Z_r, and Z_c are functions of the elastic moduli and relate to the compliance of an individual crack.

The volumetric response is determined by an equation of state (for most calculations, we use a Mie-Grüneisen). Damage is accounted for by scaling the computed pressure by the ratio of the damaged bulk modulus to the undamaged bulk modulus. The damaged bulk modulus is defined as:

$$K(D) = \left(K_0^{-1} + D \left(Z_n + 4Z_c \right) \right)^{-1}. \tag{B.4}$$

The definition and evolution of the damage parameter (D) is discussed next.

B.2.2 Micromechanics of Damage

We use a micromechanics based damage model where damage is defined as:

$$D = \sum_{k=1}^{N_{\text{bins}}} \omega_k \left(s_k + l_k\right)^3 . \tag{B.5}$$

In the summation the bin number k loops over the N_{bins} that are used to discretize the local flaw size distribution, ω_k is the number density of flaws per unit volume that are represented by the flaw family k, and the initial flaw size is s_k, which has grown an additional length l_k due to the applied loading history.

We use a self-consistent approach to compute the effective stress intensity factor due to both the applied load and the crack environment for the representative flaw size s_k. From that stress intensity factor (K_I) we comput the crack growth rate using:

$$\dot{l} = \frac{C_r}{\alpha_c} \left(\frac{K_I - K_{IC}}{K_I - 0.5 K_{IC}} \right)^{\gamma_c} . \tag{B.6}$$

The increased crack length is used to update the damage parameter.

B.2.3 Traditional J2 Plasticity

This portion of the model is not discussed in the paper and has not been tested extensively. It has minimal physical basis and is only included here for information purposes.

The J_2 plasticity component is an elastic-plastic material model with linear strain hardening. The plasticity module is activated with the `usePlasticity` input tag. The formulation is based on the unified Neo-Hookian model discussed in Simo's Computational Inelasticity book. The hardening modulus is defined by `hardening_modulus`. The initial yield strength is defined by `yield_stress`. The initial plastic strain is defined by `alpha`. The yield surface is defined by

$$f(\boldsymbol{\sigma}) = \|\boldsymbol{\sigma}_{dev}\| - \frac{G(D)}{G_0}\left(K\epsilon_p + \tau_0\right). \tag{B.7}$$

The factor $\frac{G}{G_0}$ corrects for the effect of damage growth where the effective yield stress decreases with damage in the same way that the shear modulus decreases with damage.

B.2.4 Granular Plasticity

There are two possible granular flow models. In both cases the flow behavior is associative to the yield surface and there is no hardening. The granular flow yield surface is determined by the input `gp_yeildSurfaceType`. Surface 1 is defined by:

$$f(\boldsymbol{\tau}) = \sqrt{\boldsymbol{\tau}_{dev} : \boldsymbol{\tau}_{dev}} + A_0\left(\frac{\mathrm{tr}(\boldsymbol{\tau})}{\sqrt{3}} - B_0\right). \tag{B.8}$$

While yield surface 2 is defined by:

$$f(\boldsymbol{\tau}) = \boldsymbol{\tau}_{dev} : \boldsymbol{\tau}_{dev} + A_0\left(\frac{\mathrm{tr}(\boldsymbol{\tau})}{\sqrt{3}} - B_0\right). \tag{B.9}$$

The default surface is surface 2. The input parameters for both surfaces are defined using the input tag `gp_A` for parameter A and `gp_cohesiveStrength` for parameter

B. The units for parameter B are units of stress for both surfaces, but for parameter A the units are stress for surface 1 and no units (order 1) for surface 2. There are no default values for these parameters and an error will be generated during problem setup if they are not provided.

A linear viscosity model is activated by setting `gp_timeConstant` to a positive value. This is the relaxation timescale for the granular flow process and has units of time. The linear viscosity model follows a Douvont-Louis type visco-plasticity model.

The granular flow algorithm sets the `p.localized` flag when bulking associated with granular flow exceeds the value provided in `gp_JGP_localize`. The default value for this is 5.0.

B.2.5 Pore Compaction

This module is turned on when granular plasticity is activated. This is an additional yield surface which depends on only the hydrostatic pressure. It is defined by:

$$f_\phi(P, J^{GP}, J) = \begin{cases} \frac{P}{P_c - P_0} - \frac{P_0}{P_c - P_0} \exp\left(-\frac{P_c - P_0}{2P_0(J_0^{GP} - 1)}(J^{GP} - J_0^{GP})\right) & P < P_0 \\ (J^{GP} - 1) - (J_0^{GP} - 1)J^2 \left(\frac{P_c - P}{P_c - P_0}\right)^2 & P_0 \leq P < P_c \\ J^{GP} - 1 & P < P_c \end{cases} . \tag{B.10}$$

This is simple porosity model with a quadratic crush behavior for pressures beyond P_0 and an exponential compaction behavior for lower pressures.

B.3 Model Input Parameters

Below is an example input specification for boron carbide that contains all of the possible input fields used in the constitutive model. Not all fields are required, and activating some fields will cause others not to be read. This example uses a Pareto distribution of flaw sizes.

```
<constitutive_model type="TongeRamesh">
 <bulk_modulus>232.0e9</bulk_modulus>
 <shear_modulus>197.0e9</shear_modulus>
 <usePlasticity> false </usePlasticity>
 <yield_stress>7.0e9</yield_stress>
 <hardening_modulus>0.0</hardening_modulus>
 <alpha> 0.0 </alpha>
 <useDamage> true </useDamage>
 <flaw_dist_numFamilies> 25 </flaw_dist_numFamilies>
 <flaw_dist_BinBias> -2.0 </flaw_dist_BinBias>
 <flaw_dist_type> pareto </flaw_dist_type>
 <flaw_dist_maxFlaw> 25e-6 </flaw_dist_maxFlaw>
 <flaw_dist_minFlaw> 1.0e-6 </flaw_dist_minFlaw>
 <flaw_dist_exponent> 2.6 </flaw_dist_exponent>
 <flaw_dist_flawDensity> 22.0e12 </flaw_dist_flawDensity>
 <bhasker_damage_KIc> 2.5e6 </bhasker_damage_KIc>
 <!-- From a friction angle of 30 degrees see HVIS paper-->
 <bhasker_damage_mu> 0.6 </bhasker_damage_mu>
 <bhasker_damage_phi> 1.04444 </bhasker_damage_phi>
 <bhasker_damage_cgamma> 1 </bhasker_damage_cgamma>
 <bhasker_damage_alpha> 5 </bhasker_damage_alpha>
 <bhasker_damage_maxDamage> 1.0 </bhasker_damage_maxDamage>
 <bhasker_damage_critDamage> 0.125 </bhasker_damage_critDamage>
 <bhasker_damage_usePlaneStrain> true </bhasker_damage_usePlaneStrain>
 <bhasker_damage_incInitialDamage> true </bhasker_damage_incInitialDamage>
 <brittle_damage_max_damage_increment> 0.001
   </brittle_damage_max_damage_increment>
 <bhasker_use_damage_timestep> false </bhasker_use_damage_timestep>
 <bhasker_damage_useOldStress> true </bhasker_damage_useOldStress>
 <!-- Granular Plasticity -->
 <useGranularPlasticity> true </useGranularPlasticity>
```

```
 <gp_timeConstant> 100e-9 </gp_timeConstant>
 <gp_yeildSurfaceType> 1 </gp_yeildSurfaceType>
 <gp_A> 0.60 </gp_A>
 <gp_cohesiveStrength> 0.1e6 </gp_cohesiveStrength>
 <gp_JGP_localize> 2.00 </gp_JGP_localize>
 <gp_Pc> 10e9 </gp_Pc>
 <gp_Pe> 100e6 </gp_Pe>
 <gp_JGPe> 2.0 </gp_JGPe>
 <useModifiedEOS>true</useModifiedEOS>
 <equation_of_state type="mie_gruneisen_temperature">
  <C_0>9.6e3</C_0>
  <!-- sqrt(232e9/2520)=sqrt(K/rho) -->
  <S_alpha>0.914</S_alpha>
  <S_2>0.0</S_2>
  <S_3>0.0</S_3>
  <Gamma_0>1.28</Gamma_0>
  <!-- Based on 2*S-1 -->
  <C_v> 962 </C_v>
  <theta_0> 294 </theta_0>
  <!-- These parameters only apply to the Temperature version-->
  <J_min> 0.5 </J_min>
  <Interpolation_Points> 50 </Interpolation_Points>
 </equation_of_state>
 <!-- random piece -->
 <flaw_dist_randomize> true </flaw_dist_randomize>
 <flaw_dist_seed> 4 </flaw_dist_seed>
 <flaw_dist_BinMethod> 7 </flaw_dist_BinMethod>
 <!-- 0, 1, or 2 -->
 <brittle_damage_printDamage>false
    </brittle_damage_printDamage>
 <bhasker_damage_dt_increaseFactor>10
    </bhasker_damage_dt_increaseFactor>
 <bhasker_damage_doFlawInteraction>true
    </bhasker_damage_doFlawInteraction>
 <useNonlocalDamage>false</useNonlocalDamage>
 <flaw_dist_Ncutoff>20</flaw_dist_Ncutoff>
 <flaw_dist_useEtaField>false</flaw_dist_useEtaField>
 <flaw_dist_etaFileName>flawDensityData.txt</flaw_dist_etaFileName>
 <flaw_dist_useSizeField>false</flaw_dist_useSizeField>
 <flaw_dist_sizeFileName>flawSizeData.txt</flaw_dist_sizeFileName>
</constitutive_model>
```

Quantity	Keyword	Default Value	units
Target damage increment	`brittle_damage_max_damage_increment`	1×10^{-4}	
Modify timestep based on damage rate	`bhasker_use_damage_timestep`	`false`	
Use damage sublooping	`bhasker_damage_useOldStress`	`false`	
Increase factor for damage timestep	`bhasker_damage_dt_increaseFactor`	10.0	
Fracture Toughness (K_{IC})	`bhasker_damage_KIc`	2×10^{-6}	stress sqrt(length)
Friction coefficient	`bhasker_damage_mu`	0.2	
Flaw angle (ϕ)	`bhasker_damage_phi`	$\frac{1}{2}\left(\pi - \text{atan}(\frac{1}{\mu})\right)$	radians
Crack growth exponent (γ_c)	`bhasker_damage_cgamma`	1.0	
Max crack speed fraction (α)	`bhasker_damage_alpha`	5.0	
Damage to start granular flow (D_c)	`bhasker_damage_critDamage`	1.0	
Maximum damage value (D_{max})	`bhasker_damage_maxDamage`	D_c	
Use plane strain	`bhasker_damage_usePlaneStrain`	`false`	
Include parent flaw damage	`bhasker_damage_incInitialDamage`	`false`	

Table B.1: Model input parameters (part 1)

Flaw number density (η)	`flaw_dist_flawDensity`	1×10^{14}	Inverse volume
Number of flaw families (N_{bins})	`flaw_dist_stdFlawSize`	10	Integer no units
Select distribution	`flaw_dist_type`	`normal`	
Enable Poisson based variability	`flaw_dist_randomize`	`false`	
Seed for Random Number Generator	`flaw_dist_seed`	0	Integer
Bin sizing method	`flaw_dist_BinMethod`	0	Integer
Bin bias exponent (Method 6 only)	`flaw_dist_BinBias`	1.0	
Flaw density variability based on series	`flaw_dist_useEtaField`	`false`	
Flaw size variability based on series	`flaw_dist_useSizeField`	`false`	
Filename for flaw density field	`flaw_dist_etaFileName`	`flawDensityData.txt`	
Filename for size density field	`flaw_dist_sizeFileName`	`flawSizeData.txt`	
Minimum flaw size (s_{min})	`flaw_dist_minFlaw`	N/A	length
Maximum flaw size (s_{max})	`flaw_dist_maxFlaw`	N/A	length
Distribution Exponent (α)	`flaw_dist_exponent`	N/A	
Mean flaw size ($\bar{s}$)	`flaw_dist_meanFlawSize`	N/A	length
Standard Deviation of flaw size (σ_s)	`flaw_dist_stdFlawSize`	N/A	length
Reference crush pressure (P_0)	`gp_P_e`	1×10^{11}	stress
Reference distension (J_0^{GP})	`gp_JGPe`	3.0	none
Consolidation pressure (P_c)	`gp_P_c`	1×10^{12}	stress

Table B.2: Summary of input parameters part(2)

B.4 Procedure for Sampling the Subscale Distribution

User defined inputs:

- Subscale distribution parameters (s_a, s_b, η_{ab}, α)
- Number of bins per particle N_{bins} - This is the number of representative flaw sizes that will be used.

B.4.1 Procedure 0: All Bins Have the Same Probability

The distribution of flaw bins is defined so that there is an equal probability of finding a flaw in each bin. The expected flaw density for each bin is the same. $\eta_{bin} = \eta_{ab}/N_b$

For each particle:

1. Sample the flaw densities for each bin: The flaw density is a random number drawn from a normal distribution with mean: η_{bin} and variance $\frac{\eta}{V}$ where V is the volume of the particle.
2. Compute the boundaries for the bins for a uniform (0,1) distribution.
3. For each bin select a uniformly distributed value from within its range (U_{bin}).

4. Compute s_{bin} using $s_{bin} = F^{-1}(U_{bin})$ where F^{-1} is the inverse CDF for the subscale distribution.

B.4.2 Procedure 1 and 2: All Bins Have the same Increment in Flaw Size

Given the number of bins N_{bin} and the average flaw density η for a bounded Pareto distribution that spans from s_{min} to s_{max} with exponent α, this procedure computes the weight of each bin (ω_k) and the representative flaw size for each bin (s_k).

The width of each bin is

$$\Delta s = \frac{s_{max} - s_{min}}{N_{bin}}. \tag{B.11}$$

The representative flaw size for the bin (s_k) is:

$$s_k = s_{min} + k\Delta s + U * \Delta s \tag{B.12}$$

Where U is a random variable drawn from a uniform distribution between 0 and 1 while k runs from 0 to $N_{bin} - 1$.

The weight of the bin (ω_k) is different for procedure 1 and 2. For procedure 1:

$$\omega_k = \eta \Delta s g(s_{k,mid}) \tag{B.13}$$

Where $g(s_{k,mid})$ is the value of the pdf evaluated at the mid point of the bin ($s_{k,mid} = s_{min} + k\Delta s + 0.5 * \Delta s$).

For procedure 2:

$$\omega_k = \max\left[0, \tilde{\eta}\right] \tag{B.14}$$

The random flaw density for the family $\tilde{\eta}$ is a normally distributed random variable with mean $\mu = \eta \Delta sg(s_k)$ and variance $\sigma^2 = \mu/V$. Here V is the volume of the material point.

B.4.3 Procedure 3 and 4

Starting with the largest flaw size in bin $k = 0$ we choose the bin size such that the expected number of flaws in the bin is 1:

$$\bar{N}_0 = 1. \tag{B.15}$$

The largest flaw that the bin covers is $s_0^h = s_{\max}$ we compute the expected bin flaw density:

$$\bar{\omega}_0 = \frac{\bar{N}_0}{V_0}. \tag{B.16}$$

Using the parent flaw density η we compute the lower bound on the flaw size for the bin by solving:

$$\bar{\omega_0} = \eta \left(G(s_0^h) - G(s_0^l) \right) \tag{B.17}$$

as:

$$s_0^l = G^{-1}\left(G(s_0^h) - \frac{\bar{\omega_0}}{\eta} \right). \tag{B.18}$$

The boundaries of the remaining bins are computed using the recursive formula:

$$\bar{\omega}_k = 2\bar{\omega}_{k-1} \tag{B.19}$$

$$s_k^h = s_{k-1}^l \tag{B.20}$$

$$s_k^l = G^{-1}\left(G(s_k^h) - \frac{\bar{\omega_k}}{\eta}\right) \tag{B.21}$$

After assigning the bin boundaries we compute the representative flaw size and the flaw density in the bin using:

$$\omega_k = \frac{\text{Pois}[\bar{\omega}_k V_0]}{V_0} \tag{B.22}$$

$$s_k = G^{-1}\left(U[F(s_k^l), F(s_k^h)]\right) \tag{B.23}$$

In procedure 3 the total CDF is always used, in procedure 4 the CDF is rescaled when computing s_k so that it covers the full range from 0 to 1 within the bin. This makes the most use of the finite precision available in pseudo random number generators.

B.4.4 Procedure 5

This is the same as procedure 2 except when there is a small number of flaws within the particle in the flaw family the flaw family density is computed by sampling a Poisson distribution. This procedure is a subset of procedure 6.

B.4.5 Procedure 6 and 7

Procedures 6 and 7 are discussed in detail in chapter 2. Procedure 6 corresponds to the weighting labeled s_A and procedure 7 corresponds to the weighting labeled s_B.

B.4.6 Assigning the Local Flaw Distribution Using a Fourier Like Process

An alternative procedure for assigning the local flaw density is a Fourier like process. The local flaw density is defined as a function of the particle centroid $\boldsymbol{x}$ using:

$$\hat{\eta}(\boldsymbol{x}) = \eta + \sum_{i=1}^{N_k} A_i \sin(\boldsymbol{k}_i \cdot \boldsymbol{x} + \phi_i). \tag{B.24}$$

The coefficients are provided as an additional input file. The file contains 5 numbers per line: the amplitude A_i, followed by the three components of $\boldsymbol{x}_i$, followed by the phase angle (in radians) ϕ_i. These quantities are separated by white space. The number of wave vectors are set be the number of lines in the file.

This Fourier like approach can also be used to shift the location of the flaw family centers, however all of the centers are shifted together. See the code listing for exactly how the shift is applied, because it varies depending on the flaw family that is used. *This shifting of the flaw bin centers has been tested to work, but was not examined in detail. Make sure it does what you think it is doing by checking the code and doing some trial simulations. Also the Poisson process and Fourier like process are mutually*

exclusive.

B.5 Model Behavior Under Homogeneous Deformation Conditions

It is easiest to illustrate the behavior of this material model by analyzing the stress history for a material point subjected to a loading path. We first consider the simple case of uniaxial stress compression. As shown in figure B.1 the stress initially rises in a linear fashion until damage begins to grow. At this pont the stress continues to rise but deviates from the linearity because as damage increases the material stiffness is decreasing. The stress reaches a maximum value when the rate of material softening exceeds the rate of loading. Once damage reaches the critical value of 0.125, we assume that there is a continuous crack path through the material and activate granular flow. Under uniaxial stress conditions, the granular material has very little strength and therefore the stress collapses rapidly.

This material model captures the rate sensitive nature of the material strength in brittle materials. Figure B.2 shows the compressive stress as a function of compressive strain for strain rates of 10^3 s^{-1}, 10^4 s^{-1}, and 10^5 s^{-1}. Both the peak stress and the strain to failure increase with increasing loading rate.

The current implementation of the granular flow model uses a single user input timescale to set the relaxation time for granular flow. The effect of the granular flow

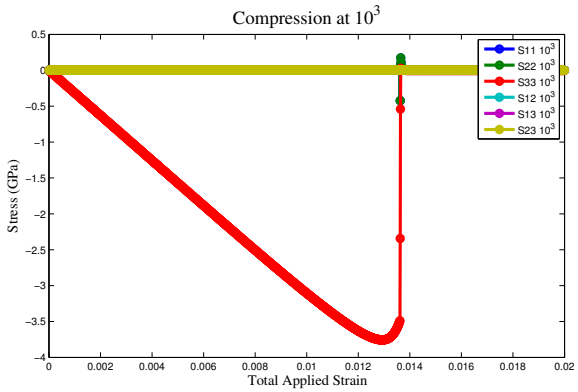

Figure B.1: All six components of stress as a function of time for nominally uniaxial stress loading at a strain rate of 1×10^3 s^{-1} for a material point with the full distribution of flaws.

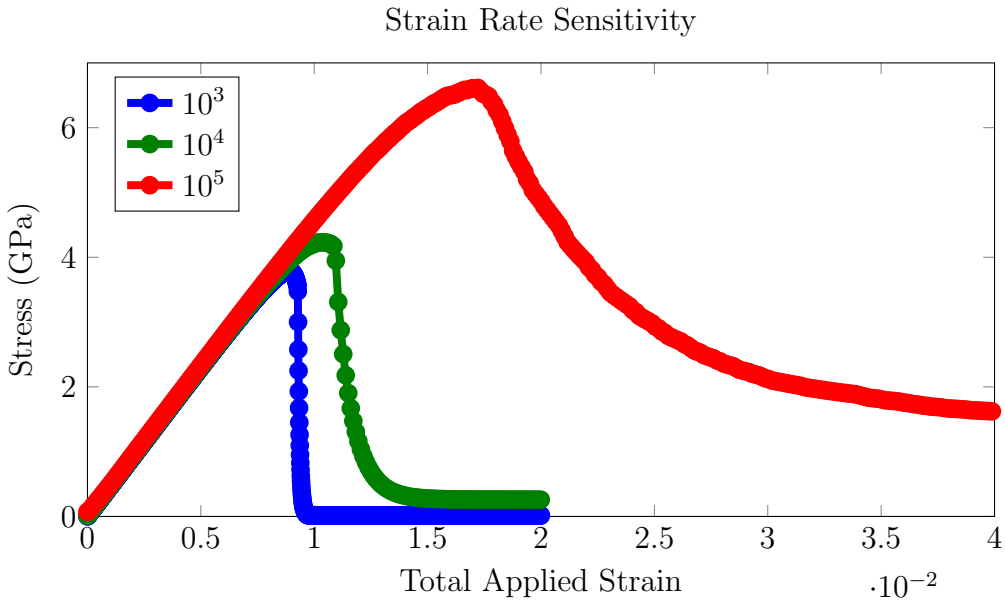

Figure B.2: Compressive stress as a function of the compressive strain fro three different strain rates. Both the peak stress and strain to failure increase with increasing strain rate.

timescale is shown in figure B.3 for a strain rate of 10^4 s^{-1}. At this strain rate a granular flow timescale of 100ns results in a noticeable kink in the stress-strain curve when damage reaches its maximum value and further damage growth is suppressed ($D = 1.0$). The material model assumes a linear strain rate sensitivity so at very high strain rates, unrealistic choices of τ_{GP} can result in unrealistic material model behavior. One approach for computing a granular flow timescale is to use a timescale close to the communication time between flaws. This would assume that the granular material consists of fragments that are about the size of flaw spacing.

Many material models use the idea of a failure surface to describe the behavior of the material ([22, 41]). We define an effective damage initiation surface as the locus of stress states required to cause the largest subscale crack to begin growth. This is done by choosing the most compressive principal stress (σ_1) and then solving for the maximum principal stress (σ_3) required to cause $K_I > K_{IC}$. To remove the effect of the flaw distribution and isolate the competition between crack interactions through the self consistent method and stable wing cracking, we simplify the problem by assuming a delta distribution of flaws with $\eta = 0.5 \times 10^9$ m^{-3} and $s = 40$ μm. Figure B.4a presents the results from this computation for different levels of damage. The blue line corresponds to the initial damage level where the wing cracks have not started to grow ($D = 3.2 \times 10^{-5}$). Under compression and small damage levels, wing cracks grow in a stable mannor where the stress required to sustain damage growth increases with damage. At a damage level close to $D = 0.047$ the interaction between

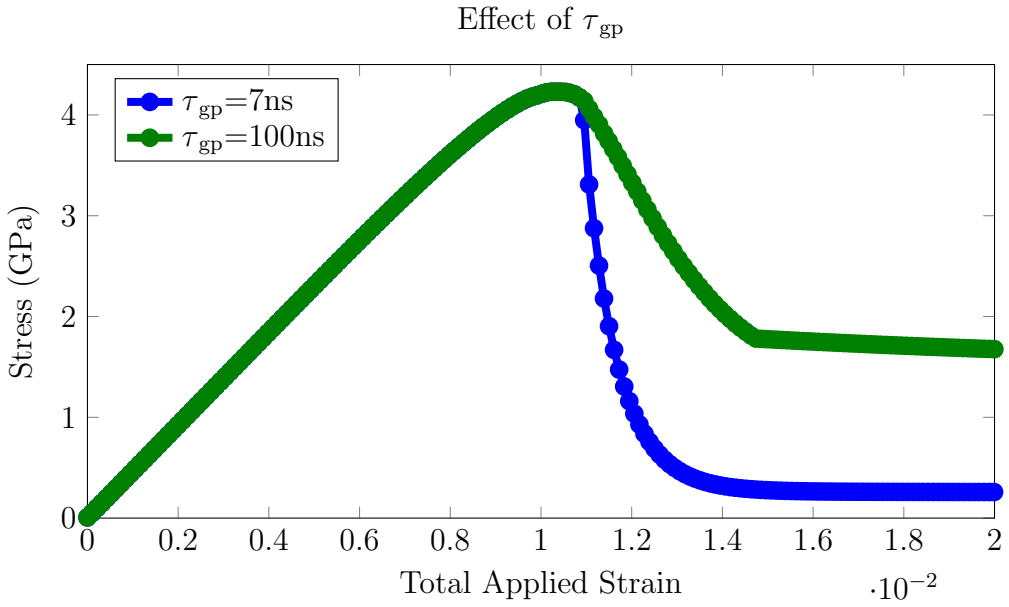

Figure B.3: Effect of the user input granular flow timescale (τ_{GP}) on the uniaxial compression stress strain curve at a strain rate of 10^4 s^{-1}. At this strain rate a granular flow timescale of 100ns results in a noticeable kink in the stress-strain curve when damage reaches its maximum value and further damage growth is suppressed ($D = 1.0$).

the cracks becomes stronger than the hardening due to the long cracks and the stress required to sustain damage growth decreases. As damage increases, from 0.047 to 1.0 the stress required to maintain damage growth decreases from the green line to the red line. This effect is shown more clearly in figure B.4b, where the uniaxial compressive stress required to sustain damage growth is plotted as a function of the damage level. The solid blue line corresponds to the damage-only regime where damage is the only active dissipation mechanism. After damage reaches 0.125, granular plasticity is enabled and the stress behavior will be the result of the competition between these two mechanisms. This region is shown with the dashed green line. Under uniaxial compression, the granular material can support almost no shear stress resulting in a rapid collapse of the stress.

The damage model relates the two extreme principal stresses, therefore the remaining principal stress may take any value between σ_1 and σ_3 without changing the damage initiation stress. Figure B.5 shows the damage initiation threshold plotted in deviatoric stress versus mean stress space for a variety of common loading paths. The axisymmetric cases represent the two limits for the middle principal stress. The biaxial compression case illustrates a limitation of the model that results from using only the extreme principal stresses. Since the model uses the two extreme principal stresses, biaxial compression with the third surface free does not increase the strength of the material beyond the uniaxial compressive strength.

The stress required to continue damage growth evolves with the damage level.

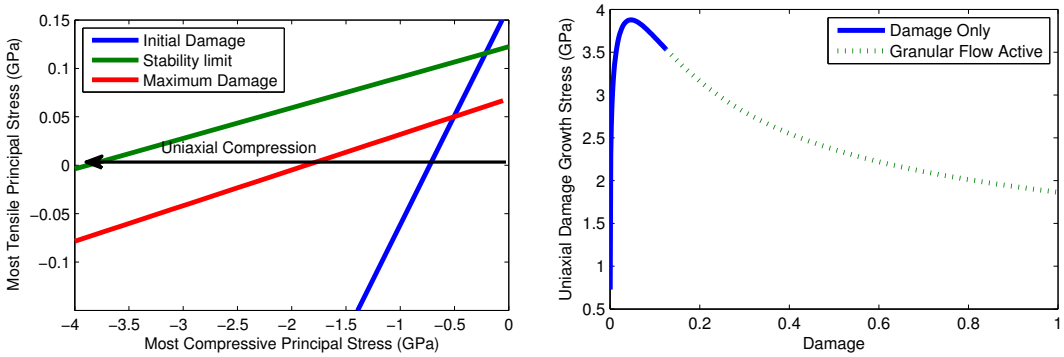

(a) Damage initiation stresses in the principal stress plane

(b) Uniaxial stress required for damage growth

Figure B.4: Subfigure (a) shows the compressive stress states beyond which damage growth occurs. The arrow indicates the path for uniaxial compression. Starting from a stress free conditions the most compressive principal stress is increased (made more negative) while the other two principal stresses remain zero. As the compressive stress increases the stress state reaches the blue line. At this point damage begins to grow stably until damage reaches a critical value and crack interactions become more important than the hardening due to lengthening wing cracks. This is also shown in subfigure (b), which plots the uniaxial compressive stress required for damage growth as a function of the damage level. In this plot the stability limit is clear where increased damage required a decreasing stress for damage growth. The rotation of the damage growth lines in subfigure (a) as damage increases is a result of the stabilizing nature of the wing cracks. Long wing cracks require less transverse compression to arrest.

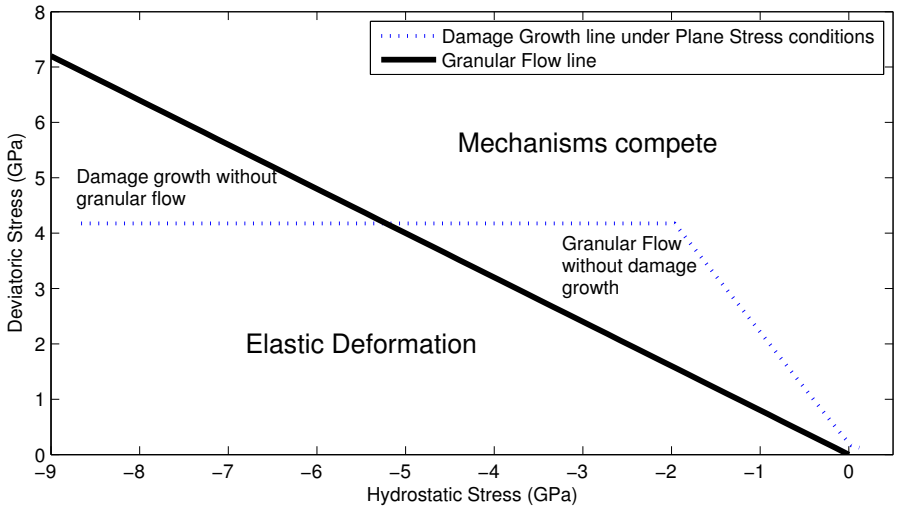

Figure B.5: Mechanism map in Hydrostatic - Deviatoric stress space for plane stress conditions showing the elastic region, a portion of stress space where damage growth is active while granular flow is suppressed, the region where granular flow suppresses damage growth, and the competition region. The break in the damage growth line is a result of assuming plane stress. In the sloped region the maximum principal stress for damage growth is tensile so the zero principal stress is the intermediate stress. In the horizontal region the intermediate stress is the other in plane stress therefore damage growth depends on the maximum compressive stress and the plane stress condition of zero out of plane stress.

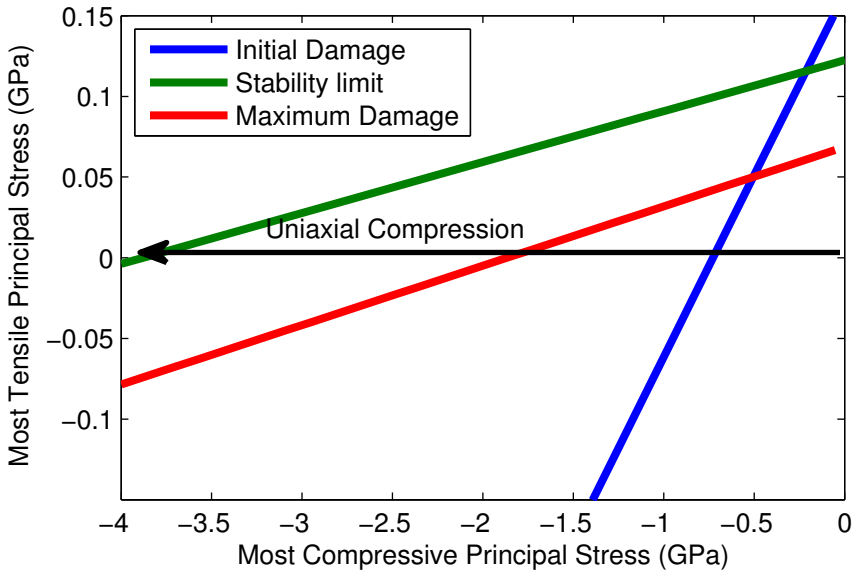

Figure B.6: Damage initiation stresses for different damage levels.

Under compression crack growth is stable until cracks begin to interact, at which point the damage growth rate accelerates and causes material failure. To illustrate this effect we plot the damage growth surface for the three damage levels of $D = 0$, $D = 0.125$, and $D = 1.0$ along with the granular flow surface in figure B.6. For the choice of $A_0 = 0.5$, the granular flow surface is inside of the damage growth surface indicating that once granular flow is activated it will take precedence over damage growth in the damage range from 0.125 to 1.0.

To illustrate the pore compaction behavior in the material model, we prescribe a deformation history consisting of hydrostatic expansion at a constant rate to a volume ratio of 1.953 in 4 μs followed by a 5 μs rest followed by hydrostatic compression to a volume ratio of 0.973 in 100μs. The resulting relationship between pressure and

distension is shown in figure B.7. The initial tension produces the initial distension. During the compaction phase, the pressure first increases at constant distension until the pressure reaches the green curve, which indicates the input pressure distension relationship. After crossing the green curve, the pressure is sufficient to crush out the porosity. The simulated pressure porosity relationship then follows the prescribed input curve indicating that the numerical implementation of the compaction process is correctly solving the equations. The distension as a function of time is shown in figure B.8. We see that the initial tensile deformation introduces the distension that is then compressed out. As shown in figure B.9, there is a significant temperature rise that results from the work done during the compression process.

The third loading path is more complicated and illustrates the key features of the granular flow model. We first apply a uniaxial strain which increases the pressure and the deviatoric stress. There is some slow damage growth during the uniaxial strain compression. After holding the uniaxial strain for 5 μs, the material is sheared at a rate of $1 \times 10^5 \mathrm{s}^{-1}$ for the next 90 μs. This shear deformation increases the deviatoric stress and causes damage to occur. The damage causes material softening that relaxes both the hydrostatic and deviatoric stresses. This is manifested as a spike in the deviatoric stress, a dip in the hydrostatic stress, and a large increase in the damage. Once damage reaches 0.125, granular flow continues to relax the deviatoric stress while increasing the pressure. This increased pressure causes an increase in the deviatoric strength until the pressure reaches a pressure that is sufficient to cause

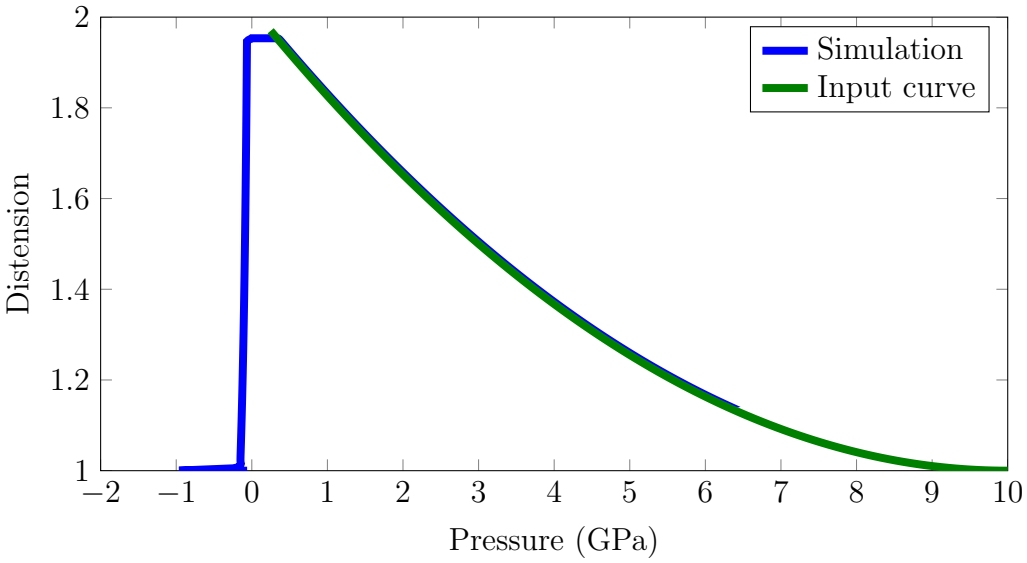

Figure B.7: Pressure-Distension relationship resulting from a simulation where the deformation was prescribed. The agreement between the input curve (shown in green) and the simulation results demonstrate that the pore compaction model is correctly solved.

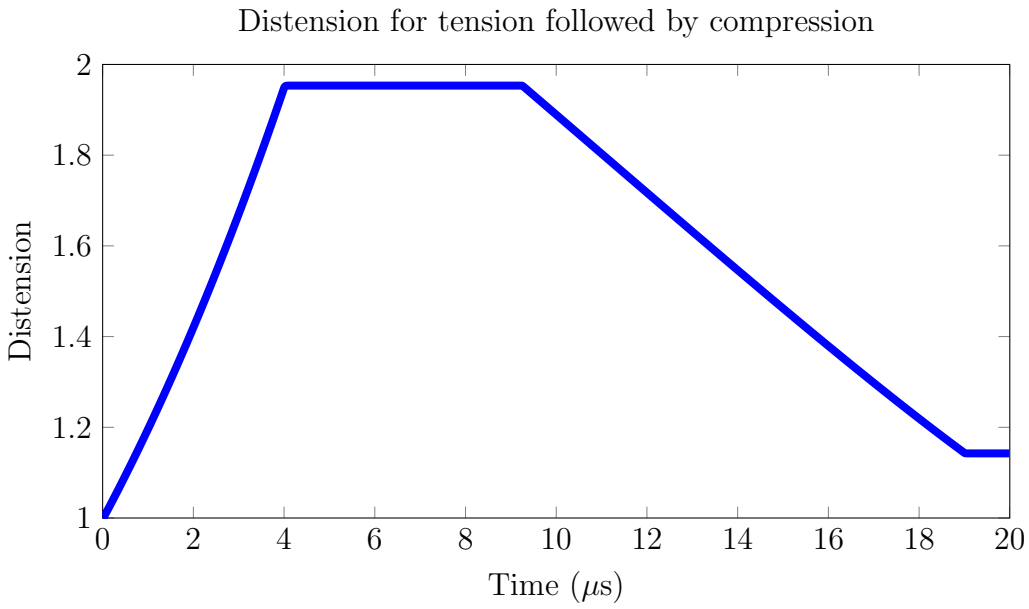

Figure B.8: Distension as a function of time for a prescribed deformation simulation where an initial hydrostatic tension is followed by compression. The tension produces the distension, which is then compressed out during the compression phase.

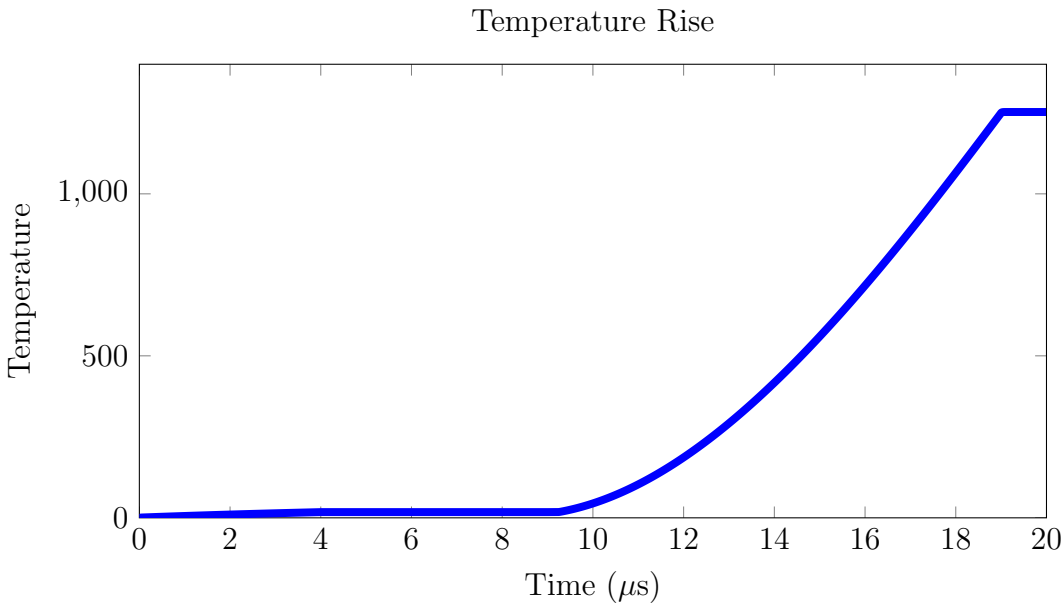

Figure B.9: Temperature rise as a function of time resulting from the energy absorbed by granular flow and the pore compaction. The majority of the heating is the result of the work done during pore compaction.

pore collapse. Once the pore collapse mechanism is activated, the material continues to flow without increasing the dilation or pressure. The next loading step from 100 μs to 150 μs is a uniaxial extension. In the final loading step the pure shear is reversed to end with the material point returned to its original shape, but their is a residual stress and dilatation. Figure B.10 shows the time history of the stress, damage, and components of granular flow.

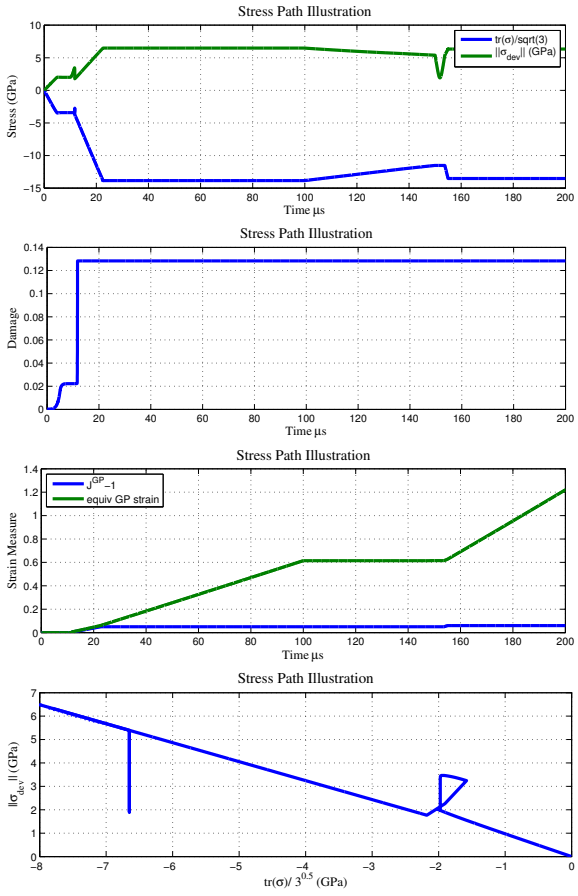

Figure B.10: Material model output for a path through stress space.

B.6 Computational Implementation of Material model in Uintah

B.6.1 Damage Evolution Calculation

We define two methods for integrating the damage evolution. The first is a simple forward Euler method where the damage growth rate is computed from the stress at the end of the previous timestep. A more complicated procedure is available by setting `bhasker_damage_useOldStress` to `false`. In this case, the damage model integration procedure first approximates the stress at the end of the time step by assuming that there is no damage growth in the time step, then calculates the damage growth rate using that approximation. If the increment in damage exceeds $\Delta D_{max} = 0.001$ (controlled by `brittle_damage_max_damage_increment`) then a sub-looping procedure is invoked to try to integrate the equation more accurately. The equations

for the sublooping are listed below.

$$\hat{\boldsymbol{\sigma}}_{n+1} = \sigma(D_n, \epsilon_{n+1}) \tag{B.25}$$

$$D_{n+1}^{test} = D_n + \Delta t \dot{D}(\hat{\boldsymbol{\sigma}}_{n+1}, D_n, l_n) \tag{B.26}$$

$$N = 10 * \lceil \frac{D_{n+1}^{test} - D_n}{\Delta D_{max}} \rceil \tag{B.27}$$

$$D_{n+1} = D_n + \sum_{k}^{N} \delta t \dot{D}^{(k)}(\sigma(D^{(k-1)}, \epsilon^k), l^{(k-1)}, D^{(k-1)}) \tag{B.28}$$

$$\delta t = \frac{\Delta t}{N} \tag{B.29}$$

$$\epsilon^k = \epsilon_n + k\delta\epsilon \tag{B.30}$$

$$\delta\epsilon = \frac{\epsilon_{n+1} - \epsilon_n}{N} \tag{B.31}$$

This sublooping procedure is only activated if the difference $D_{n+1}^{test} - D_n$ exceeds the user specified limit ΔD_{max}. If it does not exceed the limit then D_{n+1}^{test} is accepted as D_{n+1}. The constitutive model is set up so that damage growth continues until a critical damage level is reached (D_c) and at that point we assume that the energy dissipation mechanism switches from elastic softening to the relative motion of the fragmented material.

The user has the option to set the global time step for the simulation based on the time step used for the damage sub-looping calculation by setting `bhasker_use_damage_timestep` to `true`. When this is set to true the user should also set `bhasker_damage_dt_increaseFactor` to a moderately large number (the default is 10). This factor provides a way to adaptively increase the time step when the damage rate decreases. Adaptively changing the time step based on the damage growth rate can lead to *very* small time steps so

the user should use this option with caution. Activating this procedure will set the time step for the *next* time step. The current time step will not be repeated using the smaller step size.

B.6.2 Granular Plasticity

This section describes the mathematical background and the actual implementation of the granular flow calculation used for this material model. In chapter 4 the rate of deformation associated with granular flow $\boldsymbol{d}^{vp}$ is written as:

$$\boldsymbol{d}^{vp} = \dot{\lambda}\boldsymbol{m} \tag{B.32}$$

The flow direction $\boldsymbol{m}$ is

$$\frac{\partial f(\boldsymbol{\tau})}{\partial \boldsymbol{\tau}} = \frac{\boldsymbol{\tau}_{dev}}{\sqrt{\boldsymbol{\tau}_{dev} : \boldsymbol{\tau}_{dev}}} + \frac{A_0}{\sqrt{3}}\boldsymbol{I} = \boldsymbol{n} + A_0\hat{\boldsymbol{I}}. \tag{B.33}$$

The rate of granular flow $\dot{\lambda}$ is a strain like measure of the overstress $\bar{\mu}$ divided by the granular flow timescale τ_{gp}. The rate of granular flow is:

$$\dot{\lambda} = \frac{\bar{\mu}}{\tau_{gp}}. \tag{B.34}$$

We define an objective integration procedure for the elastic deformation following [58, sec. 9.3]. Starting in the material configuration, the rate of change of $\boldsymbol{C}^{vp}$ is:

$$\frac{\partial}{\partial t}\boldsymbol{C}^{vp-1} = -2\dot{\lambda}\boldsymbol{F}^{-1}\boldsymbol{m}\boldsymbol{F}^{-T}. \tag{B.35}$$

We now discretize this equation in time using an unconditionally stable backward Euler approximation:

$$\frac{\boldsymbol{C}^{vp-1}_{n+1} - \boldsymbol{C}^{vp-1}_{n}}{\Delta t} = -2\dot{\lambda}_{n+1}\boldsymbol{F}^{-1}_{n+1}\boldsymbol{m}_{n+1}\boldsymbol{F}^{-T}_{n+1} \tag{B.36}$$

$$\boldsymbol{C}^{vp-1}_{n+1} = \boldsymbol{C}^{vp-1}_{n} - 2\Delta\lambda_{n+1}\boldsymbol{F}^{-1}_{n+1}\boldsymbol{m}_{n+1}\boldsymbol{F}^{-T}_{n+1} \tag{B.37}$$

We push these equations forward into the spatial configuration using the known deformation gradient at the end of the time step ($\boldsymbol{F}_{n+1}$):

$$\boldsymbol{F}_{n+1}\boldsymbol{C}^{vp-1}_{n+1}\boldsymbol{F}^{T}_{n+1} = \boldsymbol{F}_{n+1}\left(\boldsymbol{C}^{vp-1}_{n} - 2\Delta\lambda_{n+1}\boldsymbol{F}^{-1}_{n+1}\boldsymbol{m}_{n+1}\boldsymbol{F}^{-T}_{n+1}\right)\boldsymbol{F}^{T}_{n+1} \tag{B.38}$$

$$\boldsymbol{b}^{e}{}_{n+1} = \boldsymbol{f}_{n+1}\boldsymbol{b}^{e}{}_{n}\boldsymbol{f}_{n+1} - 2\Delta\lambda_{n+1}\boldsymbol{m}_{n+1} \tag{B.39}$$

$$\left(\Delta J_{n+1}J^{e}_{n}\right)^{-2/3}\boldsymbol{b}^{e}{}_{n+1} = \left(\Delta J_{n+1}J^{e}_{n}\right)^{-2/3}\boldsymbol{f}_{n+1}\boldsymbol{b}^{e}{}_{n}\boldsymbol{f}_{n+1} - 2\Delta\lambda_{n+1}\left(\Delta J_{n+1}J^{e}_{n}\right)^{-2/3}\boldsymbol{m}_{n+1} \tag{B.40}$$

$$\Delta J^{vp}_{n+1}{}^{-2/3}\bar{\boldsymbol{b}}^{e}_{n+1} = \bar{\boldsymbol{f}}_{n+1}\bar{\boldsymbol{b}}^{e}_{n}\bar{\boldsymbol{f}}_{n+1} - 2\Delta\lambda_{n+1}\left(\Delta J_{n+1}J^{e}_{n}\right)^{-2/3}\boldsymbol{m}_{n+1} \tag{B.41}$$

Take the deviatoric part of this equation and multiply by the shear modulus:

$$\left(\Delta J^{vp}_{n+1}\right)^{-2/3} G\left(\bar{\boldsymbol{b}}^{e}_{n+1}\right)_{dev} = G\left(\bar{\boldsymbol{f}}_{n+1}\bar{\boldsymbol{b}}^{e}_{n}\bar{\boldsymbol{f}}_{n+1}\right)_{dev} - 2G\Delta\lambda_{n+1}\left(\Delta J_{n+1}J^{e}_{n}\right)^{-2/3}\boldsymbol{n}_{n+1} \tag{B.42}$$

$$\left(\Delta J^{vp}_{n+1}\right)^{-2/3}\boldsymbol{\tau}^{n+1}{}_{dev} = \boldsymbol{\tau}^{tr}_{dev} - 2G\Delta\lambda_{n+1}\left(\Delta J_{n+1}J^{e}_{n}\right)^{-2/3}\boldsymbol{n} \tag{B.43}$$

Since both ΔJ^{vp}_{n+1} and $\boldsymbol{\tau}^{n+1}_{dev}$ are unknown we recognize that $\Delta J^{vp}_{n+1} \approx 1.0$. This reduces equation (B.43) to

$$\boldsymbol{\tau}^{n+1}_{dev} = \boldsymbol{\tau}^{tr}_{dev} - 2G\Delta\lambda_{n+1}\left(\Delta J_{n+1}J^{e}_{n}\right)^{-2/3}\boldsymbol{m}_{dev} \tag{B.44}$$

For the hydrostatic portion of the stress return we use the linearization

$$\tau^m_{n+1} = \tau^m_{tr} - K\Delta\lambda_{n+1}\left(\Delta J_{n+1} J^e_n\right)^{-2/3} \mathrm{tr}(\boldsymbol{m}). \tag{B.45}$$

Here $\tau^m = \frac{1}{3}\mathrm{tr}(\boldsymbol{\tau})$ and $K = \frac{\partial \tau^m}{\partial J}$. Using equations (B.44) and (B.45) we solve for the minimum energy stress $\hat{\boldsymbol{\tau}}$ using the condition $f(\hat{\boldsymbol{\tau}}) = 0$. This is a non-linear scalar problem.

We perform the stress projection using the algorithm discussed by Rebecca Brannon in [73]. After determining the minimum energy stress $\hat{\boldsymbol{\tau}}$, we recognize that the visco-plasticity model that we selected can be integrated using [53, e.q. 5.3.9]:

$$\boldsymbol{\tau}_{n+1} = \frac{\boldsymbol{\tau}_{tr} - \frac{\Delta t}{\tau_{gp}}\hat{\boldsymbol{\tau}}}{1 - \frac{\Delta t}{\tau_{gp}}} \tag{B.46}$$

The history variables are updated using

$$\mathrm{tr}(\boldsymbol{d}^{vp}_{n+1}) = \frac{\tau^{tr}_m - \tau^{n+1}_m}{\Delta t K} \tag{B.47}$$

$$\Delta J^{vp}_{n+1} = \frac{1}{1 - \Delta t \mathrm{tr}(\boldsymbol{d}^{vp}_{n+1})} \tag{B.48}$$

$$J^{vp}_{n+1} = \Delta J^{vp}_{n+1} J^{vp}_n. \tag{B.49}$$

The deviatoric part of $\bar{\boldsymbol{b}}^e_{n+1}$ is trivially computed from the deviatoric stress using:

$$(\bar{\boldsymbol{b}}^e_{n+1})_{dev} = \frac{(\boldsymbol{\tau}_{n+1})_{dev}}{G} \tag{B.50}$$

However, $\bar{I}^e_{n+1}$ is more difficult to compute. The original algorithm uses $\bar{I}^e_{n+1} = \mathrm{tr}(\bar{\boldsymbol{b}}^e_{tr})$. This approximation does not correctly compute the strain energy in the material after plastic flow (e.g. pure shear at a constant rate of deformation, when integrated

using this approach will continue storing elastic energy even after the onset of plastic flow). The strain energy associated with volume preserving elastic deformations is $W = \frac{1}{2}G\left(\bar{I}^e - 3\right)$. We define a linearized strain energy function $\tilde{W} = \frac{1}{8G}\boldsymbol{\tau}_{dev} : \boldsymbol{\tau}_{dev}$. We then use this function to compute the ratio of the linearized strain energy in the trial state to the linearized strain energy in the final state and assume that this ratio is the same for the actual strain energies in these two states:

$$\frac{W_{n+1}}{W_{tr}} = \frac{\tilde{W}_{n+1}}{\tilde{W}_{tr}}. \tag{B.51}$$

Solving for $\bar{I}^e_{n+1}$ in terms of the known quantities $\bar{I}^e_{tr}$, $\boldsymbol{\tau}_{tr\,dev}$, and $\boldsymbol{\tau}_{n+1\,dev}$ results in an update equation for $\bar{I}^e_{n+1}$ given by:

$$\bar{I}^e_{n+1} = \left(\bar{I}^e_{tr} - 3\right)\left(\frac{||\boldsymbol{\tau}_{n+1\,dev}||^2}{||\boldsymbol{\tau}_{tr\,dev}||^2}\right) \tag{B.52}$$

Now we compute $\bar{\boldsymbol{b}}^e_{n+1}$ using:

$$\bar{\boldsymbol{b}}^e_{n+1} = \frac{\boldsymbol{\tau}_{n+1\,dev}}{G} + \frac{1}{3}\bar{I}^e_{n+1}\boldsymbol{I}. \tag{B.53}$$

The equivalent plastic strain that is accumulated is:

$$\boldsymbol{d}^{vp}_{dev} = \frac{\boldsymbol{\tau}^{tr}_{dev} - \boldsymbol{\tau}^{n+1}_{dev}}{\Delta t G} \tag{B.54}$$

B.7 Source Files Used in the Constitutive Model

This constitute model has been implemented in the Uintah computational framework. The source file containing the implementation is: `TongeRamesh.cc`. This uses the associated header file `TongeRamesh.h`. There is information regarding the specific git commit in `TongeRamesh_gitInfo.cc`. Additionally this constitutive model uses the mie-Grüneisen equation of state that is implemented in `MieGruneisenEOSTemperature.cc`. All of these files will be provided to the Uintah public repository and released under the MIT open source license. Additionally the source code is archived at the Johns Hopkins University library in digital form along with this document.

Appendix C

Supplemental File Description

There are three supplemental files included with the electronic version of this dissertation.

1. `Uintah_Tonge_ThesisVersion.tar`

2. `Tonge_Thesis_InputFiles.tar`

3. `Checksums_TongeThesis`

The first file contains a complete version of the Uintah source code listing and documentation used for this work. After extracting the tar file the documentation can be built by following the instructions in Uintah documentation. For this work the only component that needs to be built is MPM. This source code is modified from the Uintah SVN trunk as of commit `r51761`. The modified files are:

```
src/CCA/Components/MPM/ConstitutiveModel/
     .../ConstitutiveModelFactory.cc
```

```
     .../PlasticityModels/MPMEquationOfStateFactory.cc
     .../PlasticityModels/MieGruneisenEOSEnergy.cc
     .../PlasticityModels/MieGruneisenEOSTemperature.cc
     .../PlasticityModels/MieGruneisenEOSTemperature.h
     .../PlasticityModels/sub.mk
     .../TongeRamesh.cc
     .../TongeRamesh.h
     .../TongeRamesh_gitInfo.cc
     .../TongeRamesh_gitInfo.h
     .../sub.mk
src/CCA/Components/MPM/
     .../MPMFlags.cc
     .../MPMFlags.h
     .../SerialMPM.cc
src/StandAlone/inputs/UPS_SPEC
     .../constitutive_models.xml
     .../mpm_spec.xml
```

The second file contains all of the input files that were used for simulations discussed in this thesis. Using these files and the source code included in the tar file:

`Uintah_Tonge_ThesisVersion.tar`

one should be able to recreate all of the simulations that were used in this thesis.

Additionally, these input files illustrate the different options that are available for the material model and how these options are input within the Uintah framework.

The sub-folders are labeled by chapter in the Thesis. Chapter 2 discusses the sampling approach used in the Tonge-Ramesh material model to determine the local flaw distribution within a material point. The run files within this folder simulate a cube of ceramic material for a single time step. The post-processing scripts compute the total flaw distribution within the simulated volume by adding up the local flaw distributions from each of the simulated particles.

APPENDIX C. SUPPLEMENTAL FILE DESCRIPTION

Chapter 3 addresses the MPM method. The files in this folder run simulate a cylinder bouncing in a box using both the UCNH constitutive model (implemented in Uintah) and the Tonge-Ramesh material model when reduced to the elastic case. Additionally two single element problems are provided to illustrate the importance of the modifications to the plasticity algorithm discussed in the chapter.

Chapter 4 provides a number of verification tests both for a single element and for specific initial boundary value problems. These verification problems are in the Verification folder. The single element compression problems used to generate the distribution of strengths are in:

`Ch4_AlON/VariabilityTest/`

The Edge on Impact problems are in:

`Ch4_AlON/Baseline_EOI/`

and:

`Ch4_AlON/EOI_ParamStudy/`

The first folder looks at the effect of numerical resolution and the effect of material variability while the second folder contains the files used to look at the effect of granular flow and the maximum crack growth velocity.

Chapter 5 applies the model to boron carbide. There are two initial boundary value problems that were discussed in this chapter. The first is a dynamic uniaxial compression simulation. These input files are located in:

`Ch5_BoronCarbide/BoronCarbide_ParamStudy/`

The second boundary value problem is a sphere impacting a cylinder. These input files are located in:

`Ch5_BoronCarbide/Baseline_CylImpactSims/`

The submission scripts *.pbs are for the DoD open research system Copper, but could easily be adapted for use with another high performance computing system.

Chapter 6 uses the model to simulate the impact history of Eros. The multiple impact simulations are divided into 5 parts because after each impact event the material motion is damped in preparation for the next impact event. These simulations must be run sequentially. See the *.pbs files for the modifications that are made between runs to activate damping. Prior to running any of these problems, the *.pts files must be extracted by extracting the tar.gz files. All simulations in the thesis were performed using the high resolution model. To extract these points files run:

```
tar -xzvf highRes_PtsFiles_2013_11_06.tar.gz
```

One must then run the pts file splitter (pfs) utility using:

```
${PATH_TO_PFS} Eros_3ImpactSim_80m_cell_1ppc_2014-02-15.ups
```

See the Uintah documentation for more information on using pts geometry pieces. The final file contains checksum calculations for the other two tar files.

Appendix D

Workflow to Create Uintah .pts Files for Simulations in Chapter 6

In order to create the input files for the simulations in chapter 6 we started from the triangulated asteroid geometry file in the NASA Planetary Data System (PDS). This file formate is close to the Wavefront Object (*.obj) file format. Using a simple python script we add the necessary metadata to make the PDS triangulated file comply with the Wavefront object file format specification. We are then able to load the geometry file into the Blender solid modeling package.

Within Blender we sculpted the geometry to develop a model that we call "Young Eros". We then export this model as a Wavefront object file. In the next step we import that file into the visualization tool ParaView (developed by Kitware). Within ParaView we use a script to output cross-sectional images of the asteroid. We then

use the ImageMagick convert tool to fill the area inside the body in each image with a solid color. These filled images are then imported into Matlab. Within Matlab for each pixel in each slice of the stack of images we output the point if the image value of the pixel falls within a threshold range indicating that it is inside of the body. For these point the location is printed to a *.pts file that is included in the Uintah input file.

Appendix E

Other Published Works

E.1 The Mechanism of Compressive Unloading Failure in Single Crystal Quartz and Other Brittle Solids

This work was published in the International Journal of Solids and Structures in 2012 [9]. The abstract is included for completeness.

The phenomenon called unloading failure, in which the initiation and growth of cracks occurs during the removal of compressive stresses, has been observed in both uniaxial compression testing and Hertzian indentation testing of brittle materials. We have conducted finite element simulations of uniaxial com- pression experiments on single crystal quartz (specimens in which unloading failure was observed) to deter-

mine: (1) the mechanism responsible for unloading failure in brittle materials, (2) the dependence of this mechanism on friction between the specimen and loading platens, (3) the cause for the selection of specific fracture planes on which the unloading cracks propagate. The simulation results indicate that a slip-stick mechanism which is highly dependent on interface friction is responsible for the generation of tensile stress states leading to failure during unloading. The results also show that elastic anisotropy of a single crystal specimen leads to the self-selection of preferential failure planes during unloading.

E.2 A Consistent Scaling Framework for Simulating High Rate Brittle Failure Problems

This work was published in the as a part of the proceedings from the Hyper Velocity Impact Society Symposium. It represents an in-progress version of the material model presented in this work. Specifically the material mode used linear softening of the elastic moduli and did not include a transition to granular flow. The abstract is included for completeness.

We develop a material model that includes non-linear kinematics, a Mie-Gruneisen equation of state, and material failure based on an interacting microcrack dam-

age model. This material model is well suited for simulating hypervelocity impacts on brittle materials. By accounting for the subscale distribution of cracks within the material, we are able to produce a material model that does not require assumptions about how material strength scales with specimen size. This allows us to calibrate the model at laboratory scales and then apply the model under conditions that are not achievable in a laboratory setting such as asteroid impacts.

Appendix F

Summary of Work Using Smoothed Particle Hydrodynamics

F.1 History of GPUSphysics

The SPH code described in the following pages is adapted from the SPH implementation on NVidia GPU's for fluids written by Alexi Hérault, Guiseppe Bilotta, Robert A. Dalrymple and presented in Hérault et al. [105].

A more recent version of the GPUSphysics code which can run in either CPU or GPU mode called DualSPHysics can be obtained at `http://www.dual.sphysics.org/`. Our contributions to this code have been transitioned to Robert A. Dalrymple for further development and possible inclusion into the main code. Our work with GPUSphysics ended at around July of 2011 so that we could focus our efforts on developing

the material model and leverage the existing computational Uintah computational framework. The following is a summary of the state of the code including planned inclusions as of July 2011.

F.2 Model Problem

The eventual application for this code is investigating asteroid fragmentation patters. From the many types of asteroids we will focus on rocky type asteroids in the outer asteroid belt. Rocky asteroids could be made of a material similar to basalt. Typical impact velocities are in the range of 4000 m/s.

The important physics in asteroid problems are:

- Contact
- Elastic wave propagation
- Continuum damage growth and material softening
- Discrete crack growth
- Shock propagation which is driven by the material equation of state
- Plastic flow

For now we will limit the simulations to problems where the impact velocities are sufficiently low that the material equation of state can be approximated as a linear

function. We will also neglect any plastic flow and restrict the simulation to brittle materials. This is reasonable for low and moderate impact velocities.

F.3 Basic SPH Formulation:

The basic balance laws for continuum dynamics are: Conservation of linear momentum, conservation of mass, conservation of energy, and the entropy inequality.

$$\rho \frac{\mathrm{D}\boldsymbol{v}}{\mathrm{D}t} = \nabla \cdot \boldsymbol{\sigma} + \rho \boldsymbol{b} \tag{F.1}$$

$$\frac{\mathrm{D}\rho}{\mathrm{D}t} = \nabla \cdot \boldsymbol{v}\rho \tag{F.2}$$

At this point the balance of energy is trivial because there is no heat conduction and the only internal energy in the system is the elastic strain energy. The entropy inequality governs the derivation of constitutive laws and does not need to be explicitly simulated.

The Kernel approximation of a function:

$$\mathrm{A}(r) = \int \mathrm{A}(r')\mathrm{W}(r - r', h)dr' \tag{F.3}$$

$$\nabla \cdot \mathrm{A} = \sum_b A_b \frac{\mathrm{m}_b}{\rho_b} \nabla \cdot \mathrm{W} \tag{F.4}$$

APPENDIX F. SUMMARY OF WORK USING SMOOTHED PARTICLE HYDRODYNAMICS

The SPH formulation of the balance laws:

$$\frac{\mathrm{d}\boldsymbol{v}_a}{\mathrm{d}t} = -\sum_b m_b \left(\frac{\sigma_b}{\rho_b^2} + \frac{\sigma_a}{\rho_a^2} + \Pi_{ab} \right) \cdot \nabla \mathrm{W}_{ab} + \boldsymbol{b} \tag{F.5}$$

$$\frac{\mathrm{d}\rho_a}{\mathrm{d}t} = \sum_b m_b \boldsymbol{v}_{ab} \cdot \nabla_a \mathrm{W}_{ab} \tag{F.6}$$

Evolution equation for stress and strain, use the Jaumann Rate for the evolution of stress

$$\boldsymbol{\sigma} = \boldsymbol{\sigma}' - \boldsymbol{I}p \tag{F.7}$$

$$\hat{\boldsymbol{\sigma}}' = \dot{\boldsymbol{\sigma}}' - \boldsymbol{w} \cdot \boldsymbol{\sigma}' + \boldsymbol{\sigma} \cdot \boldsymbol{w} = 2\mu\dot{\boldsymbol{\epsilon}}' \tag{F.8}$$

$$\dot{\boldsymbol{\epsilon}} = \frac{1}{2}\left(\nabla \boldsymbol{v} + \nabla \boldsymbol{v}^T\right) \tag{F.9}$$

$$\boldsymbol{w} = \frac{1}{2}\left(\nabla \boldsymbol{v} - \nabla \boldsymbol{v}^T\right) \tag{F.10}$$

$$\frac{\mathrm{d}\boldsymbol{\sigma}'}{\mathrm{d}t} = \hat{\boldsymbol{\sigma}}' + \boldsymbol{w} \cdot \boldsymbol{\sigma}' - \boldsymbol{\sigma}' \cdot \boldsymbol{w} \tag{F.11}$$

$$\frac{\mathrm{d}\boldsymbol{\sigma}'}{\mathrm{d}t} = 2\mu\dot{\boldsymbol{\epsilon}}' + \boldsymbol{w} \cdot \boldsymbol{\sigma}' - \boldsymbol{\sigma}' \cdot \boldsymbol{w} \tag{F.12}$$

At this point the stress is calculated directly from the total strain and the scalar damage level. The mechanics to calculate the evolution of stress and strain independently are included in the program, but at every timestep before computing the divergence of the stress, the current value of the stress at the material point is over written using the value calculated from the strain and the damage. We have found this to be a more accurate approach and it avoids computing the rate of change of the stiffness.

$$\boldsymbol{\sigma} = 2\mu\boldsymbol{\epsilon}' + \boldsymbol{I}P(\rho) \tag{F.13}$$

Particle equations for calculating the deviatoric strain rate at particle a. The volumetric strain rate is rolled into the rate of change of the density, and it is not needed for plasticity calculations because plastic deformation is isochoric. The Jaumann stress rate is reasonable for "small" elastic strains but can introduce errors when there are large elastic strains.

$$\dot{\boldsymbol{\epsilon}}'_a = -\frac{1}{2}\sum_b \frac{m_b}{\rho_b}\Big[(\boldsymbol{v}_b - \boldsymbol{v}_a)\otimes\nabla \mathrm{W}_{ab} + ((\boldsymbol{v}_b - \boldsymbol{v}_a)\otimes\nabla \mathrm{W}_{ab})^T - \frac{2}{3}\left((\boldsymbol{v}_b - \boldsymbol{v}_a)\cdot\nabla \mathrm{W}_{ab}\right)\mathbf{I}\Big] \tag{F.14}$$

Rate of Rotation tensor calculation:

$$\mathbf{w}_a = -\frac{1}{2}\sum_b \frac{m_b}{\rho_b}\Big[(\boldsymbol{v}_b - \boldsymbol{v}_a)\otimes\nabla \mathrm{W}_{ab} - ((\boldsymbol{v}_b - \boldsymbol{v}_a)\otimes\nabla \mathrm{W}_{ab})^T\Big] \tag{F.15}$$

Calculation of the Deviatoric Stress Rate. This equation can be integrated in time to determine the deviatoric stress. The pressure is solved for using an equation of state.

$$\dot{\boldsymbol{\sigma}}'_a = 2\mu\dot{\boldsymbol{\epsilon}}' + \mathbf{w}\cdot\boldsymbol{\sigma}' - \boldsymbol{\sigma}'\cdot\mathbf{w} \tag{F.16}$$

F.4 Damping and Smoothing

This section discussed the various methods that are available to make the integration of the equations of motion behave better. Artificial viscosity smooths shock

fronts so that they can be resolved on the scale of the simulation. Moving Least Squares (MLS) recalculates the velocity and density fields to achieve higher order consistency. The Shepard filter is not implemented currently, it is a hold over from the fluids version of the code and is a filter that can exactly reproduce a constant field. XSPH is a technique of moving the particles so that they move with an average velocity of the neighboring particles. It is supposed to improve the behavior of the model in tension.

F.4.1 Artificial Viscosity

The artificial viscosity serves to smooth shock fronts and make the computation more stable. The artificial viscosity is realized as an extra internal pressure when two particles are approaching each other. It becomes large when two particles that are close to each other approach rapidly. It has three parameters. The linear viscosity term is proportional to α, the quadratic viscosity term is proportional to β, and the entire viscosity is inversely proportional to ϵ.

$$\bar{c} = \frac{c_i + c_j}{2} \tag{F.17}$$

$$\mu = \frac{h\left(\boldsymbol{v}_{ij} \cdot \boldsymbol{r}_{ij}\right)}{r^2 h^2 \epsilon} \tag{F.18}$$

$$\bar{\rho} = \frac{\rho_i + \rho_j}{2} \tag{F.19}$$

$$\Pi_{ij} = \frac{\alpha \bar{c} \mu + \beta \mu^2}{\bar{\rho}} \tag{F.20}$$

F.4.2 Moving Least Squares Filtering (MLS)

MLS is a technique to achieve a higher degree of consistency in the particle approximation than the simple kernel sum. MLS works by fitting a linear function to the particle values in the local neighborhood of the particle. The particles are weighted using the SPH kernel function, but this is a matter of convenience. The weighting function used in the MLS filtering process is not as important as it is in the SPH approximation. At this point only the velocity and density fields are smoothed using MLS. The smoothing frequency is controlled by the variable `m_simparams.mlsfreq`. If the frequency is greater than 0 then MLS filtering is performed before writing values to disk, and every mlsfreq iterations.

F.5 Boundary Conditions and Contact

F.5.1 Randles and Libersky 1996

This Formulation is implemented, but is not giving the expected results, at this point it has been abandoned in favor of a boundary formulation that can convert the boundary conditions to an effective acceleration of the particle. The reference for this boundary formulation is : Randles and Libersky [106]

This boundary formulation is a generalization of the ghost particle method. By assuming appropriate properties for the ghost particles, Randles and Libersky were

able to derive an interpolation procedure for specifying the particle properties for particles that are closest to the boundary. The formulation is as follows:

The kernel summation is broken up into three portions:

If each body in the simulation is given a color (object id in SPHysics) then the boundaries can be identified as follows:

$$\Psi_a = \sum_{b\in\mathbb{I}} \Psi_b \frac{m_b}{\rho_b} W_{ab} + \sum_{b\in\mathbb{B}} \Psi_b \frac{m_b}{\rho_b} W_{ab} + \sum_{b\in\mathbb{E}} \Psi_b \frac{m_b}{\rho_b} W_{ab}$$

$$\Psi_a < \Psi_{\text{obj.}}$$

Now we can write the SPH approximation for the particle property f as:

$$f_a = \sum_{b\in\mathbb{I}} \frac{m_b}{\rho_b} f_b \mathrm{W}_{ab} + \sum_{b\in\mathbb{B}} \frac{m_b}{\rho_b} f_b \mathrm{W}_{ab} + \sum_{b\in\mathbb{E}} \frac{m_b}{\rho_b} f_b \mathrm{W}_{ab}$$

Assuming that all exterior particles have the desired boundary condition, and the mass and density of particle a:

$$f_a = \sum_{b\in\mathbb{I}} \frac{m_b}{\rho_b} f_b \mathrm{W}_{ab} + \sum_{b\in\mathbb{B}} \frac{m_b}{\rho_b} f_b \mathrm{W}_{ab} + \frac{m_a}{\rho_a} f_{bc} \sum_{b\in\mathbb{E}} \mathrm{W}_{ab}$$

Assuming all boundary particles have the same f as particle a

$$f_a = \sum_{b\in\mathbb{I}} \frac{m_b}{\rho_b} f_b \mathrm{W}_{ab} + f_a \sum_{b\in\mathbb{B}} \frac{m_b}{\rho_b} \mathrm{W}_{ab} + \frac{m_a}{\rho_a} f_{bc} \sum_{b\in\mathbb{E}} \mathrm{W}_{ab}$$

Now take the Kernel estimate of one and multiply by f_{bc}

$$f_{bc} = f_{bc} \sum_{b\in\mathbb{I}} \frac{m_b}{\rho_b} \mathrm{W}_{ab} + f_{bc} \sum_{b\in\mathbb{B}} \frac{m_b}{\rho_b} \mathrm{W}_{ab} + \frac{m_a}{\rho_a} f_{bc} \sum_{b\in\mathbb{E}} \mathrm{W}_{ab}$$

Subtract the 2 equations and solve for f_a:

$$f_a = f_{bc} + \frac{\sum_{b\in\mathbb{I}} \frac{m_b}{\rho_b} \left(f_b - f_{bc}\right) \mathrm{W}_{ab}}{1 - \sum_{b\in\mathbb{B}} \frac{m_b}{\rho_b} \mathrm{W}_{ab}}$$

The method outlined above to identify boundary particles and calculate boundary normals is used, but the application of boundary conditions using the above method does not work at this point

Since the time that the 1996 paper was written Randles and Libersky have adopted stress points to carry field variable information while SPH points carry the kinematic information. By insuring that all particles have a suitable set of neighbors they claim to have been able to eliminate the tensile instability. They also derive a method for applying boundary conditions that follows a procedure similar to the above technique. Libersky and Randles [107], Randles and Libersky [108], Randles et al. [109], Randles and Libersky [110]

F.5.2 Lennard Jones

This is a scheme for calculating the equivalent force applied to a fluid/solid particle as it approaches a boundary particle. This method is consistent with ideas of interacting particles, but the translation to continuum mechanics is less straight forward. It might be difficult to apply tensile stresses, since this is generally a repulsive force.

The Lennard Jones force applied to a particle is given by:

$$f = d\left[\left(\frac{r_0}{r}\right)^{p_1} - \left(\frac{r_0}{r}\right)^{p_2}\right]\boldsymbol{r} \tag{F.21}$$

This force acts on a line connecting the centers of the two interacting particles. As

such it will conserve linear and angular momentum exactly. There are 2 disadvantages of this approach to contact boundaries:

- Boundaries are "soft", the force applied to an approaching particle depends on how close it gets
- Given sufficient momentum a particle could penetrate a boundary, when this happens, there is no grantee that the net force on the particle will be out of the body that it has penetrated. This can result in some alien particles being locked in a host body.
- Since the applied force depends on the separation distance, creating a simulation where there is initial contact is difficult. If the particles are too close then they will introduce compressive stresses (like a loaded spring), but if they are too far apart, there can be some rigid body motion before the effects of contact are established

F.5.3 Immersed Boundary Method

The principal behind this boundary formulation is to calculate the force that must be applied to the particle in order to insure that the particle has the desired velocity after the time integration step. After calculating the internal forces acting on the particle a particle has a proposed acceleration $\dot{\boldsymbol{v}}$. Because of the integration scheme the relative normal velocity at the end of the time step (v_{cont}) will be:

$$\boldsymbol{v}_i^{n+1} = \boldsymbol{v}_i^n + \Delta t \left(\boldsymbol{f}_{int} + \boldsymbol{b} + \boldsymbol{f}_{bound} + \boldsymbol{f}_{cont} \right) \tag{F.22}$$

This logic can be applied both to contact and boundaries with a specified velocity. The specified velocity is straight forward with some special cases depending on the type of boundary. A wall type boundary should specify the velocity only in the direction normal to the wall, while a clamped boundary can specify the velocity in all directions.

$$\boldsymbol{v}_i^{n+1} = v_{bound} \boldsymbol{n}_{bound} \tag{F.23}$$

$$v_{bound} \boldsymbol{n}_{bound} = \boldsymbol{v}_i + \Delta t \boldsymbol{f}_i \tag{F.24}$$

$$v_{bound} = \left(\boldsymbol{v}_i + \Delta t \left(\boldsymbol{f}_i^{int} + \boldsymbol{f}_i^{bound} \right) \right) \cdot \boldsymbol{n}_{bound} \tag{F.25}$$

$$\Delta t \boldsymbol{f}_i^{bound} \cdot \boldsymbol{n}_{bound} = v_{bound} - \boldsymbol{v}_i \cdot \boldsymbol{n}_{bound} - \Delta t \boldsymbol{f}_i^{int} \cdot \boldsymbol{n}_{bound} \tag{F.26}$$

$$\boldsymbol{f}_{bound} = \left(\frac{v_{bound} - \boldsymbol{v}_i \cdot \boldsymbol{n}_{bound}}{\Delta t} - \boldsymbol{f}_i^{int} \cdot \boldsymbol{n}_{bound} \right) \boldsymbol{n}_{bound} \tag{F.27}$$

For a contact boundary the condition is that at the end of the time step the relative normal velocity between the two surfaces should be 0. This is equivalent to frictionless contact. Boundary normals are computed during the internal force (divergence of stress) calculation loop.

$$\boldsymbol{v}_{ij} = \boldsymbol{v}_i - \boldsymbol{v}_j \tag{F.28}$$

$$v_{cont} = \max\left(0, \boldsymbol{v}_{ij} \cdot \boldsymbol{n}_i\right) \tag{F.29}$$

$$0 = \left(\boldsymbol{v}_i^n + \boldsymbol{f}_i \Delta t\right) \cdot \boldsymbol{n}_i - \left(\boldsymbol{v}_j^n + \boldsymbol{f}_j \Delta t\right) \cdot \boldsymbol{n}_i \tag{F.30}$$

$$0 = v_{cont} + \boldsymbol{f}_i \Delta t \cdot \boldsymbol{n}_i - \boldsymbol{f}_j \Delta t \cdot \boldsymbol{n}_j \tag{F.31}$$

$$v_{cont} = -2\boldsymbol{f}_i \Delta t \cdot \boldsymbol{n}_i \tag{F.32}$$

$$\boldsymbol{f}_{cont} = \left(\frac{v_{cont}}{-2\Delta t} - \boldsymbol{f}_i^{int} \cdot \boldsymbol{n}_i\right) \boldsymbol{n}_i \tag{F.33}$$

The set of equations above describes how two particles should interact if there are no other particles in the area. The challenge comes in defining how particle i should incorporate the effect of multiple alien particles j. There are 2 approaches for calculating the effective velocity and normal of the approaching body.

1. Use the kernel weighted average of the approaching particle normals and velocities.

$$v_i^{cont} = \frac{\sum_{j \in \mathrm{B}} \boldsymbol{v}_{ij} \frac{m_j}{\rho_j} \mathrm{W}_{ij} \cdot \left(\frac{\boldsymbol{n}_i - \frac{\sum_{j \in \mathrm{B}} \boldsymbol{n}_j \mathrm{W}_{ij}}{\left|\sum_{j \in \mathrm{B}} \boldsymbol{n}_j \mathrm{W}_{ij}\right|}}{\left| \boldsymbol{n}_i - \frac{\sum_{j \in \mathrm{B}} \boldsymbol{n}_j \mathrm{W}_{ij}}{\left|\sum_{j \in \mathrm{B}} \boldsymbol{n}_j \mathrm{W}_{ij}\right|} \right|} \right)}{\sum_{j \in \mathrm{B}} \frac{m_j}{\rho_j} \mathrm{W}_{ij}}$$

2. Use the kernel sum of the approaching particle normals and velocities.

$$v_i^{cont} = \kappa \left[\sum_{j \in \mathrm{B}} \boldsymbol{v}_{ij} \frac{m_j}{\rho_j} \mathrm{W}_{ij} \cdot \left(\frac{\boldsymbol{n}_i - \frac{\sum_{j \in \mathrm{B}} \boldsymbol{n}_j \mathrm{W}_{ij}}{\left|\sum_{j \in \mathrm{B}} \boldsymbol{n}_j \mathrm{W}_{ij}\right|}}{\left| \boldsymbol{n}_i - \frac{\sum_{j \in \mathrm{B}} \boldsymbol{n}_j \mathrm{W}_{ij}}{\left|\sum_{j \in \mathrm{B}} \boldsymbol{n}_j \mathrm{W}_{ij}\right|} \right|} \right) \right]$$

The kernel estimate of the alien normal does not take into account the neighboring particle volume. This is not correct, but it should not be affecting the results because all particles should have the same volume

These two methods are similar, but differ in the magnitude of the velocity that would be detected when a single alien particle enters the domain of influence of the boundary particle. With the first approach the two particles immediately feel each other and interact, while in the second case the influence that the particles exert on each other increases as they get closer (proportional to the kernel function).

F.6 Continuum Damage

The continuum damage model provides a mechanism for softening the material in response to increasing strain. There are two parts to the model in the way that we have developed the program to this point. There is a damage evolution calculation. This calculation determines the rate a damage accumulation due to the applied stress. The second part is how the level of damage effects the stress state. Given the total strain and the current state of the damage at a location $\boldsymbol{x}$ what is the stress at that location. This assumes that the strain energy density is a function of both the strain and the damage state. Traditionally in SPH the evolution of stress is calculated and tracked and strain is not tracked. For history dependent damage models we believe that strain is a more fundamental measure of the material state.

F.6.1 Damage Evolution

F.6.1.1 Benz and Asphaug

The Benz and Asphaug damage model postulates that each flaw in a material has an associated activation strain. The rate of growth of damage is proportional to the number of activated flaws in the computational volume. This is an extension of the Grady Kipp damage model. Benz and Asphaug just made the flaws in the Grady Kipp model explicit. Since damage can only grow at a finite rate, a system that is driven at a sufficient rate can activate multiple flaws in a computational volume. This leads to a rate dependent strength of the material.

$$\frac{dD}{dt}^{1/3} = n\frac{C_g}{R_s}$$

Where D is the damage measure, n is the number of active flaws, C_g is the crack growth speed, and R_s is the radius of the computational volume.

F.6.1.2 Threshold Stress

The threshold stress model takes 4 parameters: a tensile damage threshold, a tensile damage rate, a compressive damage threshold, and a compressive damage rate. The model is that when the the maximum principal stress exceeds the tensile damage threshold then damage grows at the tensile damage rate. If the maximum principal stress does not exceed the tensile damage threshold, then the minimum principal stress is compared to the compressive damage threshold. If the minimum

principal stress (maximum compression) exceeds the compressive damage threshold, then damage grows at the compressive damage rate.

$$\dot{D} = \begin{cases} \dot{D}_t & \sigma_1 > \sigma_t \\ \dot{D}_c & \sigma_3 < -\sigma_c \\ 0 & \text{Otherwise} \end{cases} \tag{F.34}$$

Where σ_1 is the most tensile principal stress, σ_3 is the most compressive, $\dot{D}_t$ and $\dot{D}_c$ are the tensile and compressive damage rates, and σ_t and σ_c are the tensile and compressive strengths.

F.6.1.3 Deshpande and Evans

The Deshpande and Evans damage model Deshpande and Evans [19] is based on the micromechanics of an array of interacting microcracks. This is a generalization of the work done by Ashby and Sammis.

From the micromechanics of an array of cracks the following quantities can be

defined:

$$D = \frac{4}{3}\pi \left(l + \alpha a\right)^3 f \tag{F.35}$$

$$c_1 = \frac{1}{\pi^2 \alpha^{3/2} \left[\left(\frac{D}{D_0}\right)^{1/3} - 1 + \left(\frac{\beta}{\alpha}\right)\right]^{3/2}} \tag{F.36}$$

$$c_2 = 1 + 2\left[\left(\frac{D}{D_0}\right)^{1/3} - 1\right]^2 \left(\frac{D_0^{2/3}}{1 - D^{2/3}}\right) \tag{F.37}$$

$$c_3 = 2\alpha^2 \pi^{3/2} \left[\left(\frac{D}{D_0}\right)^{1/3} - 1\right]^2 \tag{F.38}$$

$$A_1 = \pi \sqrt{\frac{\beta}{3}} \left[\left(1 + \mu^2\right)^{1/2} - \mu\right] \tag{F.39}$$

$$A_3 = \pi \sqrt{\frac{\beta}{3}} \left[\left(1 + \mu^2\right)^{1/2} + \mu\right] \tag{F.40}$$

$$A = c_1 \left(c_2 A_3 - c_2 A_1 + c_3\right) \tag{F.41}$$

$$B = \frac{c_1}{\sqrt{3}} (c_2 A_3 + c_2 A_1 + c_3) \tag{F.42}$$

$$C = A + \gamma \sqrt{\alpha \left(\frac{D}{D_0}\right)^{1/3}} \tag{F.43}$$

$$E^2 = \frac{B^2 C^2}{C^2 - A2} \tag{F.44}$$

The stress intensity and strain energy density are parametrized in terms of the hydrostatic stress and the equivalent stress.

$$\sigma_m = \frac{\sigma_{kk}}{3} \tag{F.45}$$

$$S_{ij} = \sigma_{ij} - \delta_{ij}\sigma_m \tag{F.46}$$

$$\sigma_e = \sqrt{\frac{3}{2} S_{ij} S_{ij}} \tag{F.47}$$

$$\lambda \equiv \frac{\sigma_m}{\sigma_e} \tag{F.48}$$

The mode one stress intensity factor is:

$$\frac{K_I}{\sqrt{\pi a}} = \begin{cases} 0 & \lambda \leq -\frac{B}{A} \\ A\sigma_m + B\sigma_e & -\frac{B}{A} < \lambda \leq \frac{AB}{C^2 - A^2} \\ (C^2\sigma_m^2 + E^2\sigma_e^2)^{\frac{1}{2}} & \lambda > \frac{AB}{C^2 - A^2} \end{cases} \tag{F.49}$$

The crack growth rate, which defines the damage growth rate is:

$$\dot{l} = \min\left[\dot{l}_0 \left(\frac{K_I}{K_{IC}}\right)^m, \sqrt{\frac{G}{\rho_0}}\right] \tag{F.50}$$

$$\dot{D} = 3^{\frac{2}{3}} (4\pi f)^{\frac{1}{3}} D^{\frac{2}{3}} \dot{l} \tag{F.51}$$

Up to this point has been implemented. $\dot{D}$ can be calculated using the Deshpande and Evans 2008 model. The rest of this section describes the remainder of the Deshpande and Evans model which has not been implemented. This damage model is enabled by setting `m_physparams.damageMdl=DESHPANDE_EVANS_2008`

The strain energy density is the sum of the strain energy required to deform the pristene material, and the energy absorbed by the cracks as they grow. Deshpande

and Evans [19] calculates the energy absorbed by the cracks by integrating the stress intensity factor. One assumption that they make during the derivation is that the ratio of $\frac{l}{a}$ is a constant. In a 2011 paper they abandon the idea that the elastic strain energy density depends on both the damage state and the strain favor of decomposing the strain rate into elastic, plastic, and granular flow portions. We like this approach but have not implemented it yet.

$$
\begin{aligned}
W_0 &= \frac{1}{4G}\left[\frac{2}{3}\sigma_e^2 + \frac{3(1-2\nu)}{1+\nu}\sigma_m^2\right] \\
W &= \begin{cases} W_0 & \lambda \leq -\frac{B}{A} \\ W_0 + \frac{\pi D}{4\alpha^3 G(1+\nu)}\left(A\sigma_m + B\sigma_e\right)^2 & -\frac{B}{A} < \lambda \leq \frac{AB}{C^2-A^2} \\ W_0 + \frac{\pi D}{4\alpha^3 G(1+\nu)}\left(C^2\sigma_m^2 + E^2\sigma_e^2\right) & \lambda > \frac{AB}{C^2-A^2} \end{cases}
\end{aligned}
\tag{F.52}
$$

The strain can be calculated by taking the derivitive of the strain energy density.

$$
\begin{aligned}
\epsilon_{ij} &= \frac{\partial W}{\partial \sigma_{ij}} \\
&= \frac{\partial W}{\partial \sigma_m}\frac{\partial \sigma_m}{\partial \sigma_{ij}} + \frac{\partial W}{\partial \sigma_e}\frac{\partial \sigma_e}{\partial \sigma_{ij}}
\end{aligned}
\tag{F.53}
$$

To make the derivation cleaner define:

$$
\xi = \frac{\pi D_0}{\alpha^3} \tag{F.54}
$$

For regime 1 the material is isotropic linear elastic so the constitutive relation is:

$$
\epsilon_{ij} = \frac{\sigma_{kk}\delta_{ij}}{3K} + \frac{\sigma_{ij} - \frac{\sigma_{kk}}{3}\delta_{ij}}{2G} \tag{F.55}
$$

This system of equations can be inverted to get:

$$
\sigma_{ij} = K\epsilon_{kk}\delta_{ij} + 2G\left(\epsilon_{ij} - \frac{1}{3}\epsilon_{kk}\delta_{ij}\right) \tag{F.56}
$$

For regime 2:

$$\epsilon_{ij} = \left[\frac{1}{3K} + \frac{\xi A^2}{3(2G)(1+\nu)}\right]\frac{1}{3}\sigma_{kk}\delta_{ij} + \left[\frac{\xi AB}{3(2G)(1+\nu)}\right]\sigma_e\delta_{ij} + \left[\frac{1}{2G} + \frac{3\xi B(A\lambda+B)}{4G(1+\nu)}\right]S_{ij} \tag{F.57}$$

For regime 3:

$$\epsilon_{ij} = \left[\frac{1}{3K} + \frac{\xi C^2}{3(2G)(1+\nu)}\right]\frac{1}{3}\sigma_{kk}\delta_{ij} + \left[\frac{1}{2G} + \frac{3\xi E^2}{4G(1+\nu)}\right]S_{ij} \tag{F.58}$$

This model has been updated by a 2011 paper in Journal of the American Ceramics Socity. The major change in the paper is how the effect of the damage is incorporated into the constitutive law. The model above includes the effect of microcracking in the elastic behavior of the material. The derivitive of the strain energy density with respect to stress gives the strain. In the updated model the elastic responce of the material is the elastic responce of the undamaged material and the damage is represented using a granular flow plastifity model. The cohesive strength of the granular medium is degraded from the material yeild strength with $D = D_0$ to a minimum value that depends on the characteristic slope of the material. The granular flow can introduce the dilitation that is observed, but it is a parameter in the model. The model does not naturally predict the dilitation. This approach is reasonable and probably quite effective for high levels of damage, but it is probably not as accurate at very low damage levels, for the low levels of damage we will probably have to use Kachanov's approach.

F.6.2 Calculating Stress From Strain and Damage

F.6.2.1 Linear Softening

$$\boldsymbol{\sigma} = \mathbb{C} : \boldsymbol{\epsilon}$$

$$\boldsymbol{\sigma}^d = (1 - D)\boldsymbol{\sigma}$$

F.6.2.2 Linear Softening of Shear Modulus and Bulk Softening Depending on Stress

$$\boldsymbol{\sigma} = \mathbb{C} : \boldsymbol{\epsilon}$$

$$\boldsymbol{\sigma} = \sigma_h \boldsymbol{I} + \boldsymbol{\sigma}_{dev}$$

$$\sigma_h^d = \begin{cases} (1 - D)\sigma_h & \sigma_h > 0 \\ \sigma_h & \text{otherwise} \end{cases}$$

$$\boldsymbol{\sigma}_{dev}^d = (1 - D)\boldsymbol{\sigma}_{dev}$$

$$\boldsymbol{\sigma}^d = \boldsymbol{\sigma}_{dev}^d + \sigma_h^d \boldsymbol{I}$$

This is the currently implemented model

F.6.2.3 Principal Stress Softening

$$\boldsymbol{\sigma} = \mathbb{C} : \boldsymbol{\epsilon}$$

$$\boldsymbol{\sigma} = \sum_k \sigma_k \boldsymbol{N_k} \otimes \boldsymbol{N_k}$$

$$\sigma_k^d = \begin{cases} (1-D)\sigma_k & \sigma_k > 0 \\ \sigma_k & \text{otherwise} \end{cases}$$

$$\boldsymbol{\sigma}^d = \sum_k \sigma_k^d \boldsymbol{N_k} \otimes \boldsymbol{N_k}$$

F.6.2.4 Kachanov Damage Strain Calculation

This is a model that is based on the crack kinematics and introduces a crack compliance tensor. They assume an additive decomposition of the elastic strain and the damage strain.

$$\boldsymbol{\epsilon} = \boldsymbol{S} : \boldsymbol{\sigma} + \Delta\boldsymbol{\epsilon}$$

$$\Delta\boldsymbol{\epsilon} = \boldsymbol{H} : \boldsymbol{\sigma}$$

$$\boldsymbol{\sigma} = (\boldsymbol{S} + \boldsymbol{H})^{-1} : \boldsymbol{\epsilon}$$

For wing cracks we can approximate the initial flaw and the wing crack with an ellipse. The flat ellipse has the following compliance tensor:

APPENDIX F. SUMMARY OF WORK USING SMOOTHED PARTICLE HYDRODYNAMICS

$\boldsymbol{n} \equiv$ Normal to the initial penny flaw

$\boldsymbol{m} \equiv$ Direction of largest compressive principal strain

$c \equiv$ Initial diameter of the flaw

$\pm l\boldsymbol{m} \equiv$ Wing Crack Growth

$\boldsymbol{s} \equiv$ Normal in the plane of the initial flaw

$\boldsymbol{t} \equiv$ Normal in the plane of the initial flaw

$$\boldsymbol{t} = \alpha \boldsymbol{m} \times \boldsymbol{n}$$

$$\boldsymbol{s} = \boldsymbol{n} \times \boldsymbol{t}$$

$b\boldsymbol{t}' \equiv$ Minor axis of ellipse

$a\boldsymbol{s}' \equiv$ Major axis of ellipse

$$a\boldsymbol{s}' = c\boldsymbol{s} + l\boldsymbol{m}$$

$$b\boldsymbol{t}' = c\boldsymbol{t}$$

$$\boldsymbol{n}' = \boldsymbol{t}' \times \boldsymbol{s}'$$

$$\boldsymbol{H} = \frac{1}{V}\boldsymbol{n}\otimes\boldsymbol{B}\otimes\boldsymbol{n}$$

$$\boldsymbol{B} = \xi\left[\boldsymbol{n}\otimes\boldsymbol{n} + \frac{\eta+\zeta}{2\xi}\left(\boldsymbol{I}-\boldsymbol{n}\otimes\boldsymbol{n}\right) + \frac{\eta-\zeta}{2\xi}\left(\boldsymbol{t}\otimes\boldsymbol{t}-\boldsymbol{s}\otimes\boldsymbol{s}\right)\right]$$

$$\xi = \frac{8(1-\nu^2)}{3E}\frac{\pi a b^2}{E(k)}$$

$$\eta = \frac{8(1-\nu^2)}{3E}\frac{\pi a b^2}{Q(k)}$$

$$\zeta = \frac{8(1-\nu^2)}{3E}\frac{\pi a b^2}{R(k)}$$

$$k = \sqrt{1-\left(\frac{b}{a}\right)^2}$$

$$Q(k,\nu) = k^{-2}\left[\left(k^2+\nu-\nu k^2\right)E(k) - \nu(1-k^2)K(k)\right]$$

$$R(k,\nu) = k^{-2}\left[\left(k^2-\nu\right)E(k) - \nu(1-k^2)K(k)\right]$$

$$E(k) = \int_0^{\pi/2}\sqrt{1-k^2\sin^2\phi}\mathrm{d}\phi \text{ Complete elliptic integral of the second kind}$$

$$K(k) = \text{ Complete elliptic integral of the first kind}$$

F.7 Stochastic Effects

F.7.1 Benz and Asphaug Full Implementation

In this model the pdf of activation strains for the flaws is discritized into a series of bins(N_f). Then these activation strains are distributed amongst the computational particles randomly. All computational particles must have at least one flaw, but they could have more than one. The result of this assignment method is that on agerage

the number of flaws that are required scales with $N_p \log N_p$ which results an very large memory usages at high particle densities. Most of these flaws will never be activated.

F.7.2 Benz and Asphaug Constant Number of Flaws

This model is similar to the previously described one, except a predetermined number of flaws are permitted in each particle. The particle is assigned flaws starting with the largest flaw in the distribution and moving to successively smaller flaws until the maximum number of flaws in the particle is reached. If the smallest flaw size is reached before the particle has all of the needed flaws, then the remaining flaws are assigned to a very small size which should not be activated during the simulation.

F.7.3 Threshold Stress

The compressive and tensile strength can be taken from a 3 parameter Weibull distribution. The damage growth rates at this point are fixed at a fraction of the shear wave speed.

F.7.4 Deshpande and Evans

There are two parameters in the Deshpande and Evans damage model, the flaw density and the flaw size. The flaw density can be sampled by assuming that the number of flaws in a computational volume is given by a Poisson Random variable.

The flaw density can then be computed as the number of flaws divided by the computational volume.

F.8 Damage Modeling Modifications Apr 4 2011 to June 8 2011

Assumed Damaged Constitutive Law:

$$\boldsymbol{\sigma} = \mathbb{C} : \boldsymbol{\epsilon}$$

$$\boldsymbol{\sigma} = \sigma_h \boldsymbol{I} + \boldsymbol{\sigma}_{dev}$$

$$\sigma_h^d = \begin{cases} (1-D)\sigma_h & \sigma_h > 0 \\ \sigma_h & \text{otherwise} \end{cases}$$

$$\boldsymbol{\sigma}_{dev}^d = (1-D)\boldsymbol{\sigma}_{dev}$$

$$\boldsymbol{\sigma}^d = \boldsymbol{\sigma}_{dev}^d + \sigma_h^d \boldsymbol{I}$$

This consititutive law is implimented in rate form using:

$$\dot{\boldsymbol{\epsilon}}' = \dot{\boldsymbol{\epsilon}}'_{el} + \dot{\boldsymbol{\epsilon}}'_d + \dot{\boldsymbol{\epsilon}}'_p \tag{F.59}$$

$$\dot{\boldsymbol{\epsilon}}'_d = \dot{D}\boldsymbol{\epsilon} + D\dot{\boldsymbol{\epsilon}} \tag{F.60}$$

$$\dot{\boldsymbol{\sigma}}' = 2\mu\left(\dot{\boldsymbol{\epsilon}}' - \dot{\boldsymbol{\epsilon}}'_d - \dot{\boldsymbol{\epsilon}}'_p\right) \tag{F.61}$$

Particle equations for calculating the deviatoric strain rate at particle a. The volumetric strain rate is rolled into the rate of change of the density, and it is not needed for plasticity calculations because plastic deformation is isochoric.

$$\dot{\boldsymbol{\epsilon}}'_a = -\frac{1}{2}\sum_b \frac{m_b}{\rho_b}\Big[(\boldsymbol{v}_b - \boldsymbol{v}_a)\otimes\nabla \mathrm{W}_{ab} + ((\boldsymbol{v}_b - \boldsymbol{v}_a)\otimes\nabla \mathrm{W}_{ab})^T - \frac{2}{3}\left((\boldsymbol{v}_b - \boldsymbol{v}_a)\cdot\nabla \mathrm{W}_{ab}\right)\mathbf{I}\Big] \quad \text{(F.62)}$$

Rate of Rotation tensor calculation:

$$\mathbf{w}_a = -\frac{1}{2}\sum_b \frac{m_b}{\rho_b}\left[(\boldsymbol{v}_b - \boldsymbol{v}_a)\otimes\nabla \mathrm{W}_{ab} - ((\boldsymbol{v}_b - \boldsymbol{v}_a)\otimes\nabla \mathrm{W}_{ab})^T\right] \quad \text{(F.63)}$$

The internal force acting on a particle is:

$$\frac{\mathrm{d}\boldsymbol{v}_a}{\mathrm{d}t} = -\sum_b m_b\left(\frac{\sigma_b}{\rho_b^2} + \frac{\sigma_a}{\rho_a^2} + \Pi_{ab}\right)\cdot\nabla \mathrm{W}_{ab} \quad \text{(F.64)}$$

The force on particle a due to particle b $\boldsymbol{f}_{ab}$ is given by:

$$\boldsymbol{f}_{ab} = -m_a m_b\left(\frac{\boldsymbol{\sigma}_b}{\rho_b^2} + \frac{\boldsymbol{\sigma}_a}{\rho_a^2}\right)\boldsymbol{r}_{ab} f(r_{ab}) \quad \text{(F.65)}$$

$$\boldsymbol{r}_{ab} = \boldsymbol{r}_a - \boldsymbol{r}_b \quad \text{(F.66)}$$

$$f(r) = \begin{cases} \frac{3}{4\pi h^4}\frac{-4+3\frac{r}{h}}{h} & \frac{r}{h} < 1 \\ \frac{3}{4\pi h^4}\frac{\left(-2+\frac{r}{h}\right)^2}{r} & \frac{r}{h} < 2 \\ 0 & \text{otherwise} \end{cases} \quad \text{(F.67)}$$

Now adding damage and writing the equation in indicial form (i and j are used for dimensional indexes and a and b are used for particle indexes).

$$f_i^{ab} = -m_a m_b \left(\begin{array}{c} \dfrac{2\mu\left((1-D_b)\epsilon_{ij}^b - P(\rho_b,\ D_b)\delta_{ij}\right)}{\rho_b^2} \\ + \dfrac{2\mu\left((1-D_a)\epsilon_{ij}^a - P(\rho_a,\ D_a)\delta_{ij}\right)}{\rho_a^2} \end{array} \right) r_i^{ab} f(r_{ab}) \tag{F.68}$$

F.9 Another Constitutive Model That was Discussed

F.9.1 Kinematic Assumption

$$\boldsymbol{d} = \frac{1}{2}\left(\nabla \boldsymbol{v} + \nabla \boldsymbol{v}^T\right) \tag{F.69}$$

$$\boldsymbol{w} = \frac{1}{2}\left(\nabla \boldsymbol{v} - \nabla \boldsymbol{v}^T\right) \tag{F.70}$$

Assume an additive decomposition of the rate of deformation tensor

$$\boldsymbol{d} = \boldsymbol{d}^{el} + \boldsymbol{d}^{*} + \boldsymbol{d}^{vp} \tag{F.71}$$

Where $\boldsymbol{d}$ is the total rate of deformation, $\boldsymbol{d}^{el}$ is the elastic rate of deformation, $\boldsymbol{d}^{vp}$ is the viscoplastic rate of deformation, $\boldsymbol{d}^{*}$ is the damage rate of deformation.

We can solve for the elastic rate of deformation as:

$$\boldsymbol{d}^{el} = \boldsymbol{d} - \boldsymbol{d}^{*} - \boldsymbol{d}^{vp} \tag{F.72}$$

We will be using the Jaumann stress rate:

$$\hat{\boldsymbol{\sigma}} = \dot{\boldsymbol{\sigma}} - \boldsymbol{w} \cdot \boldsymbol{\sigma} + \boldsymbol{\sigma} \cdot \boldsymbol{w} \tag{F.73}$$

Where $\boldsymbol{w}$ is the antisymmetric part of the velocity gradient.

F.9.2 Constitutive Law

The constitutive law is specified by prescribing $\hat{\boldsymbol{\sigma}}$, $\boldsymbol{d}^{*}$, and $\boldsymbol{d}^{vp}$.

F.9.2.1 Viscoplastic Flow Law

Assume that the material is a Elastic-Viscoplastic material so that there is always some plastic flow, but only substantial flow when there are sufficiently large stresses.

$$\boldsymbol{d}^{vp} = \begin{cases} \frac{g(\sigma_{eq})\boldsymbol{S}}{\bar{\sigma}} & \bar{\sigma} > 0 \\ 0 & \text{otherwise} \end{cases} \tag{F.74}$$

Where:

$$\boldsymbol{S} = \boldsymbol{\sigma} - \operatorname{tr}(\boldsymbol{\sigma})\,\boldsymbol{I}$$

$$\bar{\sigma} = \sqrt{\boldsymbol{S} : \boldsymbol{S}}$$

$$g(\bar{\sigma}) = \dot{\epsilon_0} \exp\left(\frac{\bar{\sigma}}{\sigma_0}\right)$$

When $D = 1$ this transitions to a Mohr-Coulomb type behavior.

F.9.2.2 Damage Strain Rate

There are three components to $\boldsymbol{d}^*$

$$\boldsymbol{d}^* = \begin{cases} \frac{\dot{\alpha}}{\bar{\sigma}}\boldsymbol{S} + \dot{\beta}\left(\mathrm{tr}\left(\boldsymbol{\sigma}\right)\right)\boldsymbol{I} + h\left(\boldsymbol{S}\right)\boldsymbol{I} & \bar{\sigma} > \sigma_s \text{ and } P < P_s \\ 0 & \text{otherwise} \end{cases} \tag{F.75}$$

Where:

$$\sigma_s = \begin{cases} \sigma_2 + f_1 P & P < P_s \\ \sigma_f & P \geq P_s \end{cases} \tag{F.76}$$

To determine α use Jamie's scaling result which must be translated from the uniaxial stress case to working with the deviatoric stresses.

$$\frac{\sigma_s}{\sigma_1} = 1 + \left(\frac{\dot{\epsilon}}{\dot{\epsilon}_1}\right)^{\frac{2}{3}} \tag{F.77}$$

Assuming $\sigma_s = \bar{\sigma}$ and $\dot{\epsilon} = \dot{\alpha}$

$$\dot{\alpha} = \dot{\epsilon}_1 \left(\frac{\bar{\sigma}}{\sigma_1} - 1\right)^{\frac{3}{2}} \tag{F.78}$$

Also use Jamie's scaling law to derive $\dot{\beta}$, but the way that it was written in the meeting has an issue:

$$\dot{\beta} = \begin{cases} C_0\dot{\alpha} & P < P_t \\ 0 & \text{otherwise} \end{cases} \tag{F.79}$$

When $P < P_t$, $\bar{\sigma} = 0$ so $\dot{\alpha} = 0$. We should re-derive the hydrostatic behavior from the scaling law as:

$$\dot{\beta} = \begin{cases} \dot{\epsilon_0}\left(\frac{P}{P_t} - 1\right)^{\frac{3}{2}} & P < P_t \\ 0 & \text{otherwise} \end{cases} \tag{F.80}$$

For bulking due to shearing:

$$h(\boldsymbol{S}) = \begin{cases} C_1 \frac{\bar{\sigma}}{\sigma_3} & \int_0^t \operatorname{tr}(\boldsymbol{d}^*)\, dt < B_c \\ 0 & \text{otherwise} \end{cases} \tag{F.81}$$

For $D = 1$, $\boldsymbol{d}^* = \boldsymbol{0}$

F.9.2.3 Jaumann Stress Rate

This relation quantifies the elastic response of the damaged material. First we define the scalar damage variable as:

$$D = \int_0^t \sqrt{d^*_{dev} : d^*_{dev}} dt \tag{F.82}$$

And assume isotropic elastic response and isotropic damage:

$$\hat{\boldsymbol{\sigma}} = 2\left(\mu_0 - \mu_1 D\right) \boldsymbol{d}^{el}_{dev} + \left(K_0 - K_1 D\right) \operatorname{tr}\left(\boldsymbol{d}^{el}\right) \boldsymbol{I} \tag{F.83}$$

F.9.3 Model Parameters

The parameters in this model are:

- $\dot{\epsilon}_0$: The reference strain rate for plastic flow
- σ_0: The reference stress for plastic flow
- P_s: The pressure that shuts down the wing cracking mechanism
- σ_f: The deviatoric stress at which the wing cracking mechanism is shut down because of pressure. This is not independent.

- f_1: Slope of the line in equivalent stress - pressure space that describes failure due to the wing cracking mechanism.
- σ_2: Uniaxial compressive strength due to wing cracking
- σ_1: Reference strength for scaling in Jamie's model
- $\dot{\epsilon_1}$: Reference strain rate for scaling in Jamie's model
- P_t: Transition pressure to allow damage dilatation $P_t = \frac{-\sigma_2}{f_1}$.
- σ_3: Normalizing stress for bulking due to shear stress.
- C_1: Bulking rate coefficient
- B_c: Maximum dilatation for shear bulking to be active
- μ_0: Undamaged shear modulus
- μ_1: slope for degrading shear modulus with damage
- K_0: Undamaged Bulk Modulus
- K_1: Slope for degrading bulk modulus

F.9.4 Rework Damage Strain Rate Normalization

Start with assuming a relationship between stress, strain, and damage:

$$\boldsymbol{\sigma} = \mu_0 \left(1 - \frac{\mu_1}{\mu_0} D\right)^{\alpha} \operatorname{dev}(\boldsymbol{\epsilon}) + K_0 \left(1 - \frac{K_1}{K_0} D\right)^{\beta} \operatorname{tr}(\boldsymbol{\epsilon}) \boldsymbol{I} \tag{F.84}$$

Differentiating with respect to time:

$$\hat{\boldsymbol{\sigma}} = \mu_0 \left(1 - \frac{\mu_1}{\mu_0} D\right)^{\alpha} \overset{\cdot}{\overline{\text{dev}\left(\boldsymbol{\epsilon}\right)}} + \mu_0 \alpha \left(1 - \frac{\mu_1}{\mu_0} D\right)^{(\alpha-1)} \left(-\frac{\mu_1}{\mu_0} \dot{D}\right) \text{dev}\left(\boldsymbol{\epsilon}\right) + K_0 \left(1 - \frac{K_1}{K_0} D\right)^{\beta} \overset{\cdot}{\overline{\text{tr}\left(\boldsymbol{\epsilon}\right)}} \boldsymbol{I} + K_0 \beta \left(1 - \frac{K_1}{K_0} D\right)^{(\beta-1)} \left(-\frac{k_1}{K_0} \dot{D}\right) \text{tr}\left(\boldsymbol{\epsilon}\right) \boldsymbol{I} \quad \text{(F.85)}$$

Using the substitution

$$\dot{\bar{\boldsymbol{\epsilon}}} = \boldsymbol{d} \quad \text{(F.86)}$$

And collecting similar terms:

$$\hat{\boldsymbol{\sigma}} = \mu_0 \left(1 - \frac{\mu_1}{\mu_0} D\right)^{\alpha} \left(\text{dev}\left(\boldsymbol{d}\right) - \frac{\alpha \frac{\mu_1}{\mu_0} \text{dev}\left(\boldsymbol{\epsilon}\right) \dot{D}}{1 - \frac{\mu_1}{\mu_0}}\right) + K_0 \left(1 - \frac{K_1}{K_0} D\right)^{\beta} \left(\text{tr}\left(\boldsymbol{d}\right) - \frac{\beta \frac{K_1}{K_0} \text{tr}\left(\boldsymbol{\epsilon}\right) \dot{D}}{1 - \frac{K_1}{K_0}}\right) \quad \text{(F.87)}$$

Using (F.84) to solve for tr($\boldsymbol{\epsilon}$ and dev($\boldsymbol{\epsilon}$:

$$\text{dev}\left(\boldsymbol{\epsilon}\right) = \frac{\text{dev}\left(\boldsymbol{\sigma}\right)}{\mu_0 \left(-\frac{\mu_1}{\mu_0} D\right)^{\alpha}} \quad \text{(F.88)}$$

$$\text{tr}\left(\boldsymbol{\epsilon}\right) = \frac{\text{tr}\left(\boldsymbol{\sigma}\right)}{3K_0 \left(-\frac{K_1}{K_0} D\right)^{\beta}} \quad \text{(F.89)}$$

$$\quad \text{(F.90)}$$

Let:

$$\text{dev}\left(\boldsymbol{d}^*\right) = \frac{\alpha \mu_1 \text{dev}\left(\boldsymbol{\sigma}\right)}{\mu_0 \left(1 - \frac{\mu_1}{\mu_0} D\right)^{\alpha+1} \mu_0} \dot{D} \quad \text{(F.91)}$$

$$\text{tr}\left(\boldsymbol{d}^*\right) = \frac{\beta K_1 \text{tr}\left(\boldsymbol{\sigma}\right)}{K_0 \left(1 - \frac{K_1}{K_0} D\right)^{\beta+1} K_0} \dot{D} \quad \text{(F.92)}$$

$$\quad \text{(F.93)}$$

Substituting gives:

$$\hat{\boldsymbol{\sigma}} = \mu_0 \left(1 - \frac{\mu_1}{\mu_0} D\right)^{\alpha} \left(\operatorname{dev}(\boldsymbol{d}) - \operatorname{dev}(\boldsymbol{d}^*)\right) + K_0 \left(1 - \frac{K_1}{K_0} D\right)^{\beta} \left(\operatorname{tr}(\boldsymbol{d}) - \operatorname{tr}(\boldsymbol{d}^*)\right) \quad \text{(F.94)}$$

The damage growth rate ($\dot{D}$) can be calculated from the scaling work that Jamie developed.

Starting from:

$$\frac{\sigma_f}{\sigma_0} = 1 + \left(\frac{\dot{\epsilon}}{\dot{\epsilon}_0}\right)^{\frac{2}{3}} \quad \text{(F.95)}$$

And solving for the strain rate:

$$\dot{\epsilon}_{eq} = \dot{\epsilon}_0 \left(\frac{\sigma_{eq}}{\sigma_0} - 1\right)^{\frac{3}{2}} \quad \text{(F.96)}$$

Equation (F.96) relates a scalar measure of the strain rate to the applied stress. This equation takes care of the rate effects. Since the tensorial damage rate of deformation has the form given in equation (F.75) a scalar equation for the damage rate $\dot{D}$ can complete the deviatoric part of the damage flow rule. For now the equivilent stress

is the Von-Miesis stress and equivilent strain rate has a similar form.

$$\begin{aligned}
\boldsymbol{S} &= \operatorname{dev}(\boldsymbol{\sigma}) \\
\sigma_{eq} &= \sqrt{\frac{2}{3}\boldsymbol{S}:\boldsymbol{S}} \\
\dot{\epsilon}_{eq} &= \sqrt{\frac{2}{3}\left(\operatorname{dev}\left(\boldsymbol{d}^*\right):\operatorname{dev}\left(\boldsymbol{d}^*\right)\right)} \\
\dot{\epsilon}_{eq} &= \sqrt{\frac{2}{3}\left(\frac{\alpha\mu_1\boldsymbol{S}}{\mu_0\left(1-\frac{\mu_1}{\mu_0}D\right)^{\alpha+1}\mu_0}\dot{D}:\frac{\alpha\mu_1\boldsymbol{S}}{\mu_0\left(1-\frac{\mu_1}{\mu_0}D\right)^{\alpha+1}\mu_0}\dot{D}\right)} \\
\dot{\epsilon}_{eq} &= \sqrt{\frac{2}{3}\left(\left(\frac{\alpha\mu_1}{\mu_0\left(1-\frac{\mu_1}{\mu_0}D\right)^{\alpha+1}\mu_0}\dot{D}\right)^2\boldsymbol{S}:\boldsymbol{S}\right)} \\
\dot{\epsilon}_{eq} &= \left(\frac{\alpha\mu_1}{\mu_0\left(1-\frac{\mu_1}{\mu_0}D\right)^{\alpha+1}\mu_0}\dot{D}\right)\sqrt{\frac{2}{3}\left(\boldsymbol{S}:\boldsymbol{S}\right)} \\
\dot{\epsilon}_{eq} &= \frac{\alpha\mu_1\sigma_{eq}}{\mu_0\left(1-\frac{\mu_1}{\mu_0}D\right)^{\alpha+1}\mu_0}\dot{D}
\end{aligned}$$

Solving for $\dot{D}$ gives:

$$\dot{D} = \frac{\dot{\epsilon}_0\left(\frac{\sigma_{eq}}{\sigma_0}-1\right)^{\frac{3}{2}}}{\frac{\alpha\mu_1\sigma_{eq}}{\mu_0\left(1-\frac{\mu_1}{\mu_0}D\right)^{\alpha+1}\mu_0}} \tag{F.97}$$

Simplifying:

$$\dot{D} = \frac{\dot{\epsilon}_0\left(\frac{\sigma_{eq}}{\sigma_0}-1\right)^{\frac{3}{2}}\mu_0^2\left(1-\frac{\mu_1}{\mu_0}D\right)^{\alpha+1}}{\alpha\mu_1\sigma_{eq}} \tag{F.98}$$

Equation (F.98) gives a stress dependent damage growth rate. This damage growth rate is the rate term for the damage strain rate. However equation (F.98) was derived based on a normalizing stress in uniaxial compression. From Guangli's work we know that the strength of the material is a strong function on the applied pressure, as

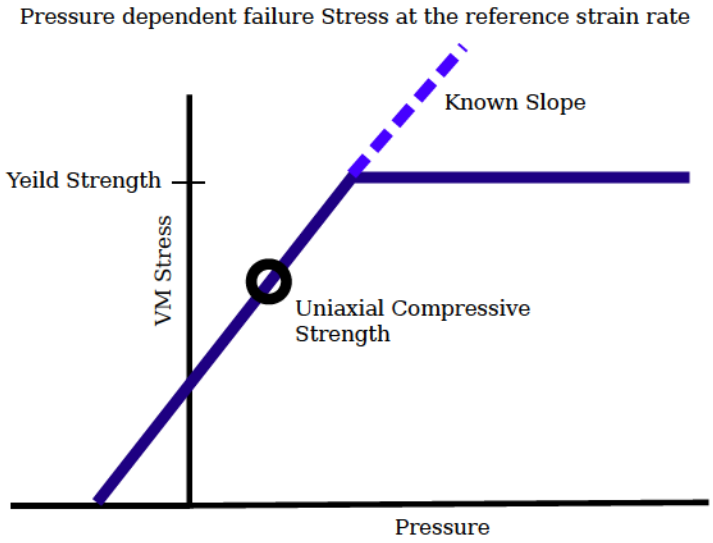

Figure F.1: Summary of Gunagli's Pressure dependent strength

shown in figure F.1. This can be accounted for by assigning a normalizing stress that is a function of pressure. Let $\sigma_0 = \sigma_s(P)$:

$$\sigma_s = \begin{cases} \sigma_2 + f_1\left(P - \frac{\sigma_2}{3}\right) & P > P_t \\ P_t & \text{otherwise} \end{cases} \tag{F.99}$$

We need to make sure that we am not in a position of dividing by 0. Maybe we should be looking at when $P < 0$ using the pressure to calculate the damage rate and when the pressure is positive using the deviatoric stress. For the region where $\sigma_{eq} > 0$ and $P < P_t$ I will need a condition where the deviatoric stress helps accelerate the damage rate. Also when the damage rate is controlled by the pressure the bulk modulus should be used for normalization. Bulking can be controlled based on the damage rate and the deviatoric stress.

Bibliography

[1] Junwei Liu, Lori Graham-Brady, and K. T. Ramesh. Erratum to "an interacting micro-crack damage model for failure of brittle materials under compression". *Journal of the Mechanics and Physics of Solids*, 2014.

[2] E. Love and D.L. Sulsky. An unconditionally stable, energy–momentum consistent implementation of the material-point method. *Computer Methods in Applied Mechanics and Engineering*, 195:3903–3925, 2006.

[3] S. Chocron, C.E. Anderson Jr., K.A. Dannemann, A.E. Nicholls, and N.L. King. Intact and predamaged boron carbide strength under moderate confinement pressures. *Journal of the American Ceramic Society*, 95(1):350–357, 2012.

[4] B. Paliwal and K. T. Ramesh. Effect of crack growth dynamics on the rate-sensitive behavior of hot-pressed boron carbide. *Scripta Materialia*, 57(6):481–484, 2007.

[5] Martin Jutzi, Patrick Michel, Kensuke Hiraoka, Akiko M. Nakamura, and Willy

BIBLIOGRAPHY

Benz. Numerical simulations of impacts involving porous bodies: Ii. comparison with laboratory experiments. *Icarus*, 201(2):802 – 813, 2009.

[6] L.E. Schwer. An overview of the ptc 60/v&v 10: Guide for verification and validation in computational solid mechanics: Transmitted by l. e. schwer, chair ptc 60v&v 10. *Engineering with Computers*, 23(4):245–252, 2007.

[7] N. Moës, J. Dolbow, and T. Belytschko. A finite element method for crack growth without remeshing. *International Journal for Numerical Methods in Engineering*, 46(1):131–150, 1999.

[8] M. L. Falk, A. Needleman, and J. R. Rice. A critical evaluation of cohesive zone models of dynamic fracture. *J. Phys. IV France*, 2001.

[9] A.L. Tonge, J. Kimberley, and K.T. Ramesh. The mechanism of compressive unloading failure in single crystal quartz and other brittle solids. *International Journal of Solids and Structures*, 49(26):3923–3934, 2012.

[10] B. Paliwal and K.T. Ramesh. An interacting micro-crack damage model for failure of brittle materials under compression. *Journal of the Mechanics and Physics of Solids*, 56(3):896–923, 2008.

[11] V. Grechka and M. Kachanov. Effective elasticity of rocks with closely spaced and intersecting cracks. *Geophysics*, 71(3):D85–D91, 2006.

[12] Chengyi Huang and Ghatu Subhash. Influence of lateral confinement on dynamic damage evolution during uniaxial compressive response of brittle solids. *Journal of the Mechanics and Physics of Solids*, 51(6):1089 – 1105, 2003.

[13] S. Sarva and S. Nemat-Nasser. Dynamic compressive strength of silicon carbide under uniaxial compression. *Materials Science and Engineering A*, 317(1-2): 140–144, 2001.

[14] M Basista and D Gross. The sliding crack model of brittle deformation: An internal variable approach. *International Journal of Solids and Structures*, 35 (5-6):487–509, 1998.

[15] S. Nemat-Nasser and M. Obata. Microcrack model of dilatancy in brittle materials. *Journal of Applied Mechanics, Transactions ASME*, 55(1):24–35, 1988.

[16] M.F. Ashby and S.D. Hallam (Née Cooksley). The failure of brittle solids containing small cracks under compressive stress states. *Acta Metallurgica*, 34 (3):497–510, 1986.

[17] S. Nemat-Nasser and H. Horii. Compression-induced nonplanar crack extension with application to splitting, exfoliation, and rockburst. *Journal of Geophysical Research*, 87(B8):6805–6821, 1982.

[18] Vikram S. Deshpande, E. A. Nell Gamble, Brett G. Compton, Robert M. McMeeking, Anthony G. Evans, and Frank W. Zok. A constitutive descrip-

tion of the inelastic response of ceramics. *Journal of the American Ceramic Society*, 94:s204–s214, 2011.

[19] V. S. Deshpande and A. G. Evans. Inelastic deformation and energy dissipation in ceramics: A mechanism-based constitutive model. *Journal of the Mechanics and Physics of Solids*, 56(10):3077–3100, 10 2008.

[20] H. Deng and S. Nemat-Nasser. Microcrack arrays in isotropic solids. *Mechanics of Materials*, 13(1):15–36, 1992.

[21] J. Kimberley, K.T. Ramesh, and N.P. Daphalapurkar. A scaling law for the dynamic strength of brittle solids. *Acta Materialia*, 61(9):3509–3521, 2013.

[22] R.M. Brannon, A.F. Fossum, and O.E. Strack. Kayenta: Theory and user's guide. Technical Report SAND2009-2282, Sandia National Laboratories, 2009.

[23] Karl Terzaghi, Ralph B. Peck, and Gholamreza Mesri. *Soil Mechanics in Engineering Practice - Third Addition*. John Wiley & Sons, Inc., 1996.

[24] Jose E. Andrade, Qiushi Chen, Phong H. Le, Carlos F. Avila, and T. Matthew Evans. On the rheology of dilative granular media: Bridging solid- and fluid-like behavior. *Journal of the Mechanics and Physics of Solids*, 60(6):1122 – 1136, 2012.

[25] D.A. Shockey, A.H. Marchand, S.R. Skaggs, G.E. Cort, M.W. Burkett, and

R. Parker. Failure phenomenology of confined ceramic targets and impacting rods. *International Journal of Impact Engineering*, 9(3):263–275, 1990.

[26] J.K. Dienes. A statistical theory of fragmentation processes. *Mechanics of Materials*, 4(3-4):325–335, 1985.

[27] Benjamin A. Gailly and Horacio D. Espinosa. Modelling of failure mode transition in ballistic penetration with a continuum model describing microcracking and flow of pulverized media. *International Journal for Numerical Methods in Engineering*, 54(3):365–398, 2002.

[28] J.K. Dienes, Q.H. Zuo, and J.D. Kershner. Impact initiation of explosives and propellants via statistical crack mechanics. *Journal of the Mechanics and Physics of Solids*, 54(6):1237–1275, 2006.

[29] J.D. Clayton. Deformation, fracture, and fragmentation in brittle geologic solids. *International Journal of Fracture*, 163(1-2):151–172, 2010.

[30] H. Deng and S. Nemat-Nasser. Dynamic damage evolution in brittle solids. *Mechanics of Materials*, 14(2):83–103, 1992.

[31] H. Deng and S. Nemat-Nasser. Dynamic damage evolution of solids in compression: microcracking, plastic flow, and brittle-ductile transition. *Journal of Engineering Materials and Technology, Transactions of the ASME*, 116(3): 286–289, 1994.

BIBLIOGRAPHY

[32] V.S. Deshpande, R.M. McMeeking, H.N.G. Wadley, and A.G. Evans. Constitutive model for predicting dynamic interactions between soil ejecta and structural panels. *Journal of the Mechanics and Physics of Solids*, 57(8):1139 – 1164, 2009.

[33] Lori Graham-Brady. Statistical characterization of meso-scale uniaxial compressive strength in brittle materials with randomly occurring flaws. *International Journal of Solids and Structures*, 47(18–19):2398 – 2413, 2010.

[34] J.F. Molinari, G. Gazonas, R. Raghupathy, A. Rusinek, and F. Zhou. The cohesive element approach to dynamic fragmentation: The question of energy convergence. *International Journal for Numerical Methods in Engineering*, 69 (3):484–503, 2007.

[35] H.W. Meyer Jr. and R.M. Brannon. A model for statistical variation of fracture properties in a continuum mechanics code. *International Journal of Impact Engineering*, 42:48–58, 2012.

[36] R.M. Brannon and T.J. Gowen. Aleatory quantile surfaces in damage mechanics. *Journal of the European Ceramic Society*, 2014.

[37] C. Daux, N. Moës, J. Dolbow, N. Sukumar, and T. Belytschko. Arbitrary branched and intersecting cracks with the extended finite element method. *International Journal for Numerical Methods in Engineering*, 48(12):1741–1760, 2000.

BIBLIOGRAPHY

[38] R. Radovitzky, A. Seagraves, M. Tupek, and L. Noels. A scalable 3d fracture and fragmentation algorithm based on a hybrid, discontinuous galerkin, cohesive element method. *Computer Methods in Applied Mechanics and Engineering*, 200 (1-4):326–344, 2011.

[39] A. Pandolfi and M. Ortiz. An eigenerosion approach to brittle fracture. *International Journal for Numerical Methods in Engineering*, 92(8):694–714, 2012.

[40] Timothy J. Holmquist and Gordon R. Johnson. A computational constitutive model for glass subjected to large strains, high strain rates and high pressures. *Journal of Applied Mechanics*, 78(5):051003, 2011.

[41] G.R. Johnson, T.J. Holmquist, and S.R. Beissel. Response of aluminum nitride (including a phase change) to large strains, high strain rates, and high pressures. *Journal of Applied Physics*, 94(3):1639–1646, 2003.

[42] G. R. Johnson and T. J. Holmquist. An improved computatonal constitutive model for brittle materials. *High Pressure Science and Technology*, pages 981–984, 1993.

[43] Elmar Strassburger, Parimal Patel, James W. McCauley, and Douglas W. Templeton. Visualization of wave propagation and impact damage in a polycrystalline transparent ceramic - alon. In *22nd International Symposium on Ballistics*, 2005.

[44] Michael Bakas, James W. McCauley, Victor Greenhut, Dale Niesz, Richard Haber, and Bruce West. Quantitative analysis of inclusion distributions in hot pressed silicon carbide. *International Journal of Impact Engineering*, 50(0):40 – 48, 2012.

[45] Somnoth Ghosh and D. Dimiduk, editors. *Computational Methods for Microstructure-Property Relations*. Springer NY, 1 edition, 2011.

[46] B Budiansky and R. J. O'Connell. Elastic moduli of a cracked solid. *International Journal of Solids and Structures*, 12(2):81 – 97, 1976.

[47] Donald E. Knuth. *The art of computer programming*, volume 2. Semi-numerical algorithms of *Addison-Westley series in computer science and information processing*. Reading, Mass., Addison-Westley Pub. Co., 2nd edition, 1970.

[48] J. E. Bishop and O. E. Strack. A statistical method for verifying mesh convergence in monte carlo simulations with application to fragmentation. *International Journal for Numerical Methods in Engineering*, 88(3):279–306, 2011.

[49] D. Sulsky, Z. Chen, and H.L. Schreyer. A particle method for history-dependent materials. *Computer Methods in Applied Mechanics and Engineering*, 118(1-2): 179–196, 1994.

[50] A Sadeghirad, R.M. Brannon, and J.E. Guilkey. Second-order convected particle domain interpolation (cpdi2) with enrichment for weak discontinuities at

material interfaces. *International Journal for Numerical Methods in Engineering*, 95(11):928–952, 2013.

[51] A. Sadeghirad, R.M. Brannon, and J. Burghardt. A convected particle domain interpolation technique to extend applicability of the material point method for problems involving massive deformations. *International Journal for Numerical Methods in Engineering*, 86(12):1435–1456, 2011.

[52] Steve Parker, J. Davison de St. Germain, John Schmidt, Todd Harman, James Guilkey, and Many Others. Uintah Website, 2011.

[53] J. C. Simo and T.J.R Hughes. *Computational Inelasticity*, volume 7 of *Interdisciplinary Applied Mathematics*. Springer, 2 edition, 2000.

[54] M.D. Bolton. Strength and dilatancy of sands. *Geotechnique*, 36(1):65–78, 1986.

[55] E. Strassburger. Visualization of impact damage in ceramics using the edge-on impact technique. *International Journal of Applied Ceramic Technology*, 1(3): 235–242, 2004.

[56] E. Strassburger, P. Patel, J.W. McCauley, and D.W. Templeton. High-speed photographic study of wave propagation and impact damage in fused silica and alon using the edge-on impact (eoi) method. In *AIP Conference Proceedings*, volume 845 II, pages 892–895, 2006.

[57] B. Leavy, E. Strack, R. Brannon, R. Jensen, and J. Houskamp. Simulation

of experimental variability with spatially heterogeneous models. In *Society for Experimental Mechanics - SEM Annual Conference and Exposition on Experimental and Applied Mechanics*, volume 4, pages 2290–2292, 2009.

[58] J.C. Simo and M. Ortiz. A unified approach to finite deformation elastoplastic analysis based on the use of hyperelastic constitutive equations. *Computer Methods in Applied Mechanics and Engineering*, 49(2):221–245, 1985.

[59] M. Carroll and A.C. Holt. Suggested modification of the p- model for porous materials. *Journal of Applied Physics*, 43(2):759–761, 1972.

[60] D.S Drumheller. *Introduction to Wave Propagation in Nonlinear Fluids and Solids*. Cambridge University Press, 1998.

[61] F. Armero and J.C. Simo. A priori stability estimates and unconditionally stable product formula algorithms for nonlinear coupled thermoplasticity. *International Journal of Plasticity*, 9(6):749 – 782, 1993.

[62] J. VonNeumann and R.D. Richtmyer. A method for the numerical calculation of hydrodynamic shocks. *Journal of Applied Physics*, 21(3):232–237, 1950.

[63] V. Grechka and M. Kachanov. Effective elasticity of fractured rocks: A snapshot of the work in progress. *Geophysics*, 71(6), 2006.

[64] B. Paliwal, K.T. Ramesh, and J.W. McCauley. Direct observation of the dy-

namic compressive failure of a transparent polycrystalline ceramic (aion). *Journal of the American Ceramic Society*, 89(7):2128–2133, 2006.

[65] David James Macon, Rebecca Moss Brannon, and Otto Erik Strack. Plastic cap evolution law derived from induced transverse isotropy in dilatational triaxial compression. Technical Report SAND2014-1217, Sandia National Laboratories, Sandia National Laboratories (SNL), Albuquerque, NM, and Livermore, CA (United States), 2014.

[66] L.B. Freund. Crack propagation in an elastic solid subjected to general loading-ii. non-uniform rate of extension. *Journal of the Mechanics and Physics of Solids*, 20(3):141–152, 1972.

[67] B. Paliwal, K.T. Ramesh, J.W. McCauley, and M. Chen. Dynamic compressive failure of alon under controlled planar confinement. *Journal of the American Ceramic Society*, 91(11):3619–3629, 2008.

[68] W. Chen and H. Luo. Dynamic compressive responses of intact and damaged ceramics from a single split hopkinson pressure bar experiment. *Experimental Mechanics*, 44(3):295–299, 2004.

[69] S. Chocron, C.E. Anderson Jr., K.A. Dannemann, and A.E. Nicholls. Pressure effects on the compressive response of confined intact and damaged soda-lime glass. *Experimental Mechanics*, 53(1):77–89, 2013.

[70] Huiyang Luo, Weinong W. Chen, and A. M. Rajendran. Dynamic compressive response of damaged and interlocked sic–n ceramics. *Journal of the American Ceramic Society*, 89(1):266–273, 2006.

[71] X. Nie and W.W. Chen. The influence of temperature and confinement pressure on the dynamic response of damaged borosilicate glass. In Jeffery Swab, editor, *Advances in Ceramic Armor VII : Ceramic Engineering and Science Proceedings*, volume 32:5, pages 3–10. Wiley, 2011.

[72] B.E. Martin, M.E. Kabir, and W. Chen. Undrained high-pressure and high strain-rate response of dry sand under triaxial loading. *International Journal of Impact Engineering*, 54:51–63, 2013.

[73] RebeccaM. Brannon. Elements of phenomenological plasticity: Geometrical insight, computational algorithms, and topics in shock physics. In Yasuyuki Horie, editor, *ShockWave Science and Technology Reference Library*, ShockWave Science and Technology Reference Library, chapter Elements of Phenomenological Plasticity: Geometrical Insight, Computational Algorithms, and Topics in Shock Physics, pages 189–274. Springer Berlin Heidelberg, 2007.

[74] D.R. Curran, L. Seaman, T. Cooper, and D.A. Shockey. Micromechanical model for comminution and granular flow of brittle material under high strain rate application to penetration of ceramic targets. *International Journal of Impact Engineering*, 13(1):53 – 83, 1993.

[75] P.C. Wallstedt and J.E. Guilkey. An evaluation of explicit time integration schemes for use with the generalized interpolation material point method. *Journal of Computational Physics*, 227(22):9628–9642, 2008.

[76] R.B. Leavy, J.D. Clayton, O.E. Strack, R.M. Brannon, and E. Strassburger. Edge on impact simulations and experiments. In *Hyper Velocity Impact Society Symposium Procedings*, volume 58, pages 445–452, 2013.

[77] J.C. Lasalvia, M.J. Normandia, H.T. Miller, and D.E. MacKenzie. Sphere impact induced damage in ceramics: Ii. armor-grade b 4c and wc. In *2005 Ceramics Engineering and Science Proceedings*, volume 26, pages 183–192, 2005.

[78] T. J. Vogler, W. D. Reinhart, and L. C. Chhabildas. Dynamic behavior of boron carbide. *Journal of Applied Physics*, 95(8):4173–4183, 2004.

[79] Y. Zhang, T. Mashimo, Y. Uemura, M. Uchino, M. Kodama, K. Shibata, K. Fukuoka, M. Kikuchi, T. Kobayashi, and T. Sekine. Shock compression behaviors of boron carbide (b4c). *Journal of Applied Physics*, 100(11):–, 2006.

[80] Dattatraya P. Dandekar. Shock response of boron carbide. Technical Report ARL-TR-2456, Army Research Laboratory, Aberdeen Proving Ground, MD 21005-5066, April 2001.

[81] F. Thevenot. Boron carbide-a comprehensive review. *Journal of the European Ceramic Society*, 6(4):205–225, 1990.

[82] H. Wang and K.T. Ramesh. Dynamic strength and fragmentation of hot-pressed silicon carbide under uniaxial compression. *Acta Materialia*, 52(2):355–367, 2004.

[83] Guruswami Ravichandran and Ghatuparthi Subhash. Critical appraisal of limiting strain rates for compression testing of ceramics in a split hopkinson pressure bar. *Journal of the American Ceramic Society*, 77(1):263–267, 1994.

[84] K.J. Frutschy and R.J. Clifton. High-temperature pressure-shear plate impact experiments using pure tungsten carbide impactors. *Experimental Mechanics*, 38(2):116–125, 1998.

[85] Dattatraya P. Dandekar and Dennis E. Grady. Shock equation of state and dynamic strength of tungsten carbide. *AIP Conference Proceedings*, 620(1): 783–786, 2002.

[86] Marc A. Meyers. *Dynamic Behavior of Materials*. John Wiley & Sons, 1994.

[87] N. Guy, D.M. Seyedi, and F. Hild. A probabilistic nonlocal model for crack initiation and propagation in heterogeneous brittle materials. *International Journal for Numerical Methods in Engineering*, 90(8):1053–1072, 2012.

[88] R.B. Leavy, R.M. Brannon, and O.E. Strack. The use of sphere indentation experiments to characterize ceramic damage models. *International Journal of Applied Ceramic Technology*, 7(5):606–615, 2010.

BIBLIOGRAPHY

[89] E.A. Gamble, B.G. Compton, and F.W. Zok. Impact response of layered steel–alumina targets. *Mechanics of Materials*, 60(0):80 – 92, 2013.

[90] O. E. Strack, R.B. Leavy, and R.M. Brannon. Aleatory uncertainty and scale effects in computational damage models for failure and fragmentation. *International Journal for Numerical Methods in Engineering*, TBD(TBD), 2014.

[91] D.L. Buczkowski, O.S. Barnouin-Jha, and L.M. Prockter. 433 eros lineaments: Global mapping and analysis. *Icarus*, 193(1):39–52, 2008.

[92] P.C. Thomas and M.S. Robinson. Seismic resurfacing by a single impact on the asteroid 433 eros. *Nature*, 436(7049):366–369, 2005.

[93] S.L. Wilkison, M.S. Robinson, P.C. Thomas, J. Veverka, T.J. McCoy, S.L. Murchie, L.M. Prockter, and D.K. Yeomans. An estimate of eros's porosity and implications for internal structure. *Icarus*, 155(1):94–103, 2002.

[94] M. Jutzi, W Benz, and P Michel. Numerical simulations of impacts involving porous bodies. i. implementing sub-resolution porosity in a 3d sph hydrocode. *Icarus*, 198(1):242–255, 2008.

[95] Kevin R. Housen and Keith A. Holsapple. Scale effects in strength-dominated collisions of rocky asteroids. *Icarus*, 142(1):21 – 33, 1999.

[96] Thomas J. Ahrens and Mary L. Johnson. Shock wave data for rocks. *Rock Physics and Phase Relations*, 1995.

[97] Andrew L. Tonge, Jamie Kimberley, and K. T. Ramesh. A consistent scaling framework for simulating high rate brittle failure problems. *Procedia Engineering*, 2012.

[98] M.R. Balme, V. Rocchi, C. Jones, P.R. Sammonds, P.G. Meredith, and S. Boon. Fracture toughness measurements on igneous rocks using a high-pressure, high-temperature rock fracture mechanics cell. *Journal of Volcanology and Geothermal Research*, 132(2-3):159–172, 2004.

[99] Eugene C. Robertson. Thermal properties of rocks. Geological survey, United Stated Department of the Interior, http://pubs.usgs.gov/of/1988/0441/report.pdf, 1988.

[100] S.G. Bardenhagen and E.M. Kober. The generalized interpolation material point method. *CMES - Computer Modeling in Engineering and Sciences*, 5(6): 477–495, 2004.

[101] A. L. Tonge, O.S. Barnouin, and K. T. Ramesh. A new pressure dependent damage and flow model applied to numerical simulations of psyche formation on eros (433). In *Lunar and Planatary Science Conference*, 2013.

[102] Gareth S. Collins, H. Jay Melosh, and Boris A. Ivanov. Modeling damage and deformation in impact simulations. *Meteoritics & Planetary Science*, 39(2): 217–231, 2004.

[103] K. A. Holsapple and R. M. Schmidt. On the scaling of crater dimensions: 2. impact processes. *Journal of Geophysical Research: Solid Earth*, 87(B3):1849–1870, 1982.

[104] E. Asphaug. Survival of the weakest. *Nature*, 402(6758):127–128, 1999.

[105] A.a Hérault, G.b Bilotta, and R.A.c Dalrymple. Sph on gpu with cuda. *Journal of Hydraulic Research*, 48(SUPPL. 1):74–79, 2010.

[106] P. W. Randles and L. D. Libersky. Smoothed particle hydrodynamics: Some recent improvements and applications. *Computer Methods in Applied Mechanics and Engineering*, 139(1-4):375–408, DEC 15 1996.

[107] L. D. Libersky and P. W. Randles. Shocks and discontinuities in particle methods. *Shock Compression of Condensed Matter - 2005, Pts 1 and 2*, 845:1089–1092, 2006.

[108] P. W. Randles and L. D. Libersky. Boundary conditions for a dual particle method. *Computers & Structures*, 83(17-18):1476–1486, JUN 2005.

[109] P. W. Randles, A. G. Petschek, L. D. Libersky, and C. T. Dyka. Stability of dpd and sph. *Meshfree Methods for Partial Equations*, 26:339–357, 2003.

[110] P. W. Randles and L. D. Libersky. Normalized sph with stress points. *International Journal for Numerical Methods in Engineering*, 48(10):1445–1462, 2000.

Vita

Andrew Tonge was born on June 4, 1985 in Waterville Maine. He obtained is Bachelor's of Science from the University of Maine in May of 2008. While at the University of Maine he was introduced to academic research at the Advanced Engineered Wood Composites as an undergraduate. After graduating, he spent a year in an applied engineering position at General Dynamics in Groton Connecticut.

Andy joined K.T. Ramesh's lab in August of 2009 to work on the dynamic failure of materials. From 2010 to 2012 he was an NSF IGERT Trainee as a part of the Modeling Complex Systems IGERT program. In 2012 he received an Alex Charters Scholar award from the Hyper Velocity Impact Society, and in 2014 he was recognized as a Future Leader by the American Ceramics Society as a part of the Future Leaders Program at the Ceramics Leadership Summit. He is continuing his research career as an ORISE postdoctoral fellow at the Army Research Laboratory.